TECHNISCHE UNIVERSITÄT MÜNCHEN

Physik-Department
Lehrstuhl für Funktionelle Materialien

Morphology of polymer-based films for organic photovoltaics

Matthias A. Ruderer

Vollständiger Abdruck der von der Fakultät für Physik der Technischen Universität München zur Erlangung des akademischen Grades eines

Doktors der Naturwissenschaften (Dr. rer. nat.)

genehmigten Dissertation.

Vorsitzender: Univ.-Prof. Dr. Martin Zacharias
Prüfer der Dissertation:
1. Univ.-Prof. Dr. Peter Müller-Buschbaum
2. Univ.-Prof. Jonathan J. Finley, Ph. D.

Die Dissertation wurde am 04.04.2012 bei der Technischen Universität München eingereicht und durch die Fakultät für Physik am 22.05.2012 angenommen.

Was du für den Gipfel hältst, ist nur eine Stufe.
Istud, quod tu summum putas, gradus est.
Seneca

Abstract

In this thesis, polymer-based films are examined for applications in organic photovoltaics. Polymer-fullerene, polymer-polymer and diblock copolymer systems are characterized as active layer materials. The focus is on experimental parameters influencing the morphology formation of the active layer in organic solar cells. Scattering and imaging techniques provide a complete understanding of the internal structure on different length scales which is compared to spectroscopic and photovoltaic properties. The morphologies of all systems are sensitive to changes of the environmental conditions during organic solar cell preparation. These changes result in an altered photovoltaic performance. In particular, the influence of annealing, blending, composition, solvent and additional components are investigated. This thesis demonstrates different possibilities to tune the morphology of the active layer.

In dieser Dissertation werden polymerbasierte Schichten für die Verwendung in der organischen Photovoltaik untersucht. Polymer-Fulleren, Polymer-Polymer und Diblock Copolymer Systeme werden als aktive Schicht verwendet und untersucht. Hierbei wird besonderes Augenmerk auf die experimentellen Parameter gelegt, die die strukturelle Anordnung in der aktiven Schicht in organischen Solarzellen beeinflussen. Ein Gesamtverständnis der inneren Struktur auf verschiedenen Längenskalen wird aus Streumethoden und abbildende Messungen erzielt und mit den spektroskopischen und photovoltaischen Eigenschaften verglichen. Die Morphologie aller Systeme ist empfindlich auf Änderungen der experimentellen Bedingungen während der Herstellung organischen Solarzellen empfindlich. Diese Änderungen spiegeln sich in der Effizienz der Solarzellen wieder. Insbesondere wird der Einfluss von Tempern, Mischen, Mischungsverhältnissen, Lösungsmitteln und zusätzlichen Komponenten untersucht. Diese Dissertation zeigt verschiedene Möglichkeiten auf, die innere Struktur der aktiven Schicht einzustellen.

Contents

Chapter 1

Introduction

The sun is the fundamental energy source of most renewable energies including wind and hydro power as well as biomass. The stored kinetic and potential energies are used in power plants to generate electricity. Besides this indirect energy generation, energy can also be directly extracted from solar radiation using either thermal energy or the photovoltaic effect.
The photovoltaic effect describes the creation of a voltage due to excitation of electrons in a semiconducting material via light absorption. In a solar cell, this effect is used to generate electrical power. Classical solar cells made of inorganic semiconductors, such as silicon, use the internal electric field created by a p-n junction to separate the created electron-hole pairs. Monocrystalline solar cells have a power conversion efficiency up to 25%.[1] However, this type of solar cells, although widely used, needs energy consuming production steps and stable encapsulations to shield the rigid cells from environmental harm. As a consequence, the energetic amortization period of conventional solar cells is rather large.

Semiconducting organic materials have established themselves as a new class of materials which promises to overcome these drawbacks in so-called organic solar cells. These new materials are solution processable and cheap, large scale production will become possible, using for example printing technologies. In addition, the mechanical flexibility of organic materials makes a variety of new applications feasible, e.g. on 3-dimensionally shaped surfaces or in solar fibers. The most efficient organic solar cells are polymer-based systems with at least one component of the active layer being a semiconducting polymer. The active layer is the part of an organic solar cell which converts light to electricity. Organic solar cells have already reached efficiencies up to 10% in 2011.[1]
First conductive organic materials were synthesized in the 19^{th} century.[2] A significant upturn started with the publication of Shirakawa et al. about polyacetylenes [3] and the

corresponding Nobel prize in Chemistry in 2000. From that time onward, basic research on the development and application of conductive organic materials increased rapidly. In particular, the possibility to synthesize numerous different semiconducting polymers with different absorption ranges and electronic properties has given rise to optimization.[4] However, so far no general rule has been developed on how an optimum semiconducting polymer for photovoltaic applications is assembled. Compared to their inorganic counterparts, new challenges like a relatively high exciton binding energy and the short diffusion length of excitons have to be faced. To overcome these, the tailoring of the internal morphology of the active layer is as important as the electronic properties of the polymers. Employing only one type of organic semiconductor as active layer results in an organic solar cell with extremly low efficiencies as the excitons decay before they contribute to charge carriers.[5] The introduction of a second material in a bilayer device opens the possibility for efficient exciton dissociation and therefore the power conversion efficiency increases.[6] The main breakthrough occurred with the bulk heterojuntion concept which is realized by a blend of two components.[7, 8] Such a bulk heterojunction morphology is seen to be optimum if it forms an interpenetrating network with structural length scales in the range of the exciton diffusion length which is typically on the nanometer scale. However, the bulk heterojunction morphology cannot be controlled directly but evolves from a self-assembly process. Therefore, the environmental conditions, the exact preparation history and the applied materials define the resulting morphology which is in most cases not in structural equilibrium.[9] In particular, the structural disorder of polymers makes it impossible to predict the structure as well as the electronic behavior and finally, the power conversion efficiency. Rather novel approaches are diblock copolymers consisting of two semiconducting polymers which should form more predictable structures. However, up to now the power conversion efficiencies of devices from diblock copolymers are still low.[10]

In this thesis the morphology of polymer-based films used as active layers in organic solar cells is investigated. The focus is on the influence of external parameters - such as materials, composition, solvents and annealing - on the formation of the morphology on different length scales and its influence on spectroscopic properties and photovoltaic performance. The morphology of the active layer is probed with imaging and scattering techniques. The following general questions are addressed in this thesis: How can the morphology of the active layer in an organic solar cell be controlled? To what extend is the morphology influencing the efficiency of the active layer? Is there a general rule which can be translated to different material combinations?

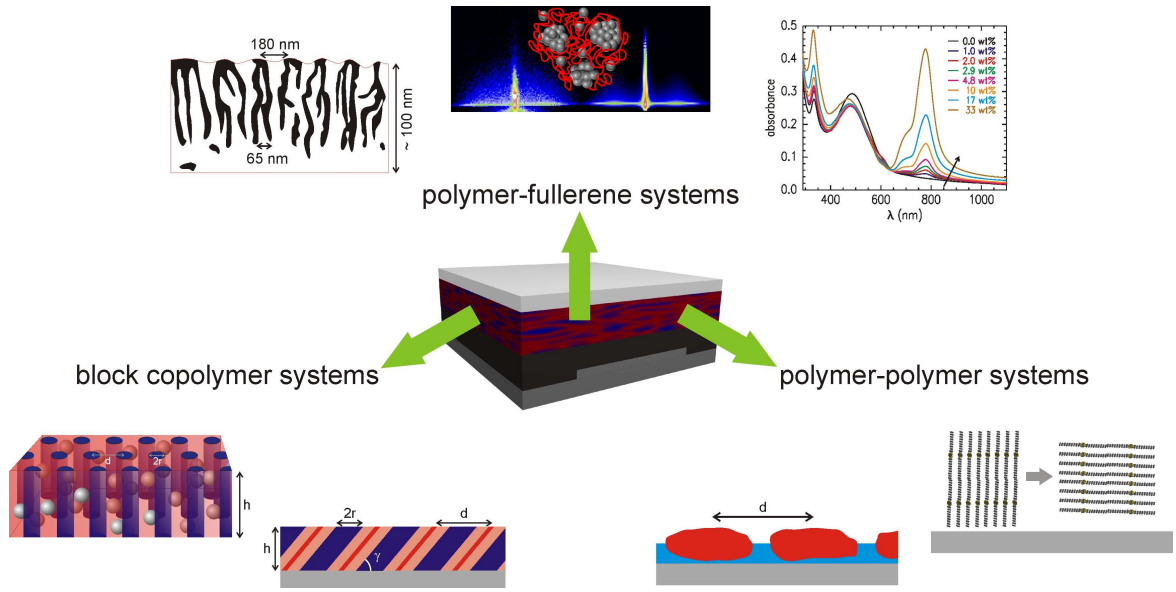

Figure 1.1: *Schematic illustration of an organic solar cell (center) with the active layer displaying a bulk heterojunction morphology (red and blue). Surrounding, an overview of the different material combinations characterized within the framework of this thesis. The different topics are detailed in the text.*

In the center of figure 1.1 a schematic illustration of an organic solar cell is shown. The multilayer architecture including electrodes and a blocking layer is necessary to obtain reasonable efficiencies. In this thesis, the morphology of the active layer, depicted in red and blue, made up of different material combinations is characterized. For the polymer-fullerene systems (chapter 5) the influence of the used solvent on the overall morphology is investigated while all other external parameters remain unchanged. Additionally, the composition of the two components is varied and special focus is put on the molecular miscibility of the fullerene component in the polymer phase. The effect of expanding the absorption range with an additional component is studied and its influence on the morphology of the active layer and photovoltaic performance is probed.
Besides the most efficient polymer-fullerene systems, polymer-polymer systems are a further promising approach (chapter 6). The impact of modifying the annealing conditions and the composition on the morphology of the active layer is investigated. Furthermore, the influence of blending two polymers on the resulting morphology is discussed with a view to photovoltaic performance.
Finally, a diblock copolymer with one semiconducting block is investigated as a model system for the active layer in organic solar cells (chapter 7). The combination of a partly semiconducting diblock copolymer with inorganic semiconducting nanoparticles is introduced as a novel approach in organic photovoltaics. In addition, tuning of the morphology

with incorporation of an additional polymeric component is analyzed.

To provide a background the next chapter (chapter 2) covers the theoretical aspects of the principle processes occurring in an organic solar cell and the phase separation and crystallization in polymer blends. Also, the fundamentals of scattering as the main characterization technique in this thesis are presented. Thereafter, the applied investigation methods (chapter 3) and the sample preparation including the different materials (chapter 4) are introduced. In the main part of this thesis, the experimental results on polymer-fullerene (chapter 5), polymer-polymer (chapter 6) and diblock copolymer (chapter 7) systems are described and discussed. Finally, a conclusion and an outlook complete this thesis (chapter 8).

Chapter 2

Theoretical aspects

Before starting with the experimental part, this chapter comprises the theoretical background for the experimental studies and interpretations presented in this thesis. First of all, the device physics of organic solar cells are discussed in section 2.1. For this purpose, the individual steps from the initial light absorption to the final charge extraction are covered. In the second section, the theories for phase separation of polymer blends with focus on rod like polymers and polymer crystallization are introduced. The final section addresses the basic principles of X-ray and neutron scattering with emphasis on grazing incident scattering techniques for structural investigations of thin polymer film systems.

2.1 Organic photovoltaics

Organic photovoltaics describes the class of optoelectronic devices which convert light to electricity using carbon based molecules. Depending on the definition, organic photovoltaics covers solar cells purely made of organic compounds as well as hybrid solar cells which combine organic and inorganic materials. In this thesis, organic photovoltaics refers only to systems in which the so-called active layer contains just organic compounds, i.e. organic semiconductors. The active layer is the part of an organic solar cell in which light is converted to electricity. Furthermore, the systems investigated in this thesis are polymer-based, meaning that at least one component of the active layer is a polymer. The basic principles such as the setup of a typical organic solar cell and an overview of the charge carrier generation process in the active layer are introduced in section 2.1.1. The single steps of the charge carrier generation process in an organic solar cell, i.e. the device physics, are described in the following sections. First, light absorption and the formation of excitons (section 2.1.2), followed by the exciton diffusion (section 2.1.3) and dissociation (section 2.1.4) are discussed. To obtain the full generation process, the charge carrier transport to the electrodes (section 2.1.5) and the charge carrier extraction at the

electrodes (section 2.1.6) are introduced. A description of the different loss mechanisms occurring during these processes completes the chapter (section 2.1.7).

2.1.1 Basic principles

Organic photovoltaic devices consist typically of a multilayer setup (figure 2.1). A solar cell is confined by two electrodes which are necessary for charge extraction. For the bottom electrode, transparent conducting materials like transparent conducting oxides (TCO), graphene or carbon nanotubes on a transparent solid support (glass or flexible foil) are used. The top electrode consists typically of a metal layer. Next to the electrodes, blocking layers and optical spacers are installed to improve the solar cell efficiency.[11] The main layer is the active layer in which the incident light is actually converted to charge carriers. The light enters the solar cell through the transparent bottom electrode and is absorbed in the active layer. The preparation of the solar cells investigated in this thesis can be found in chapter 4.5.

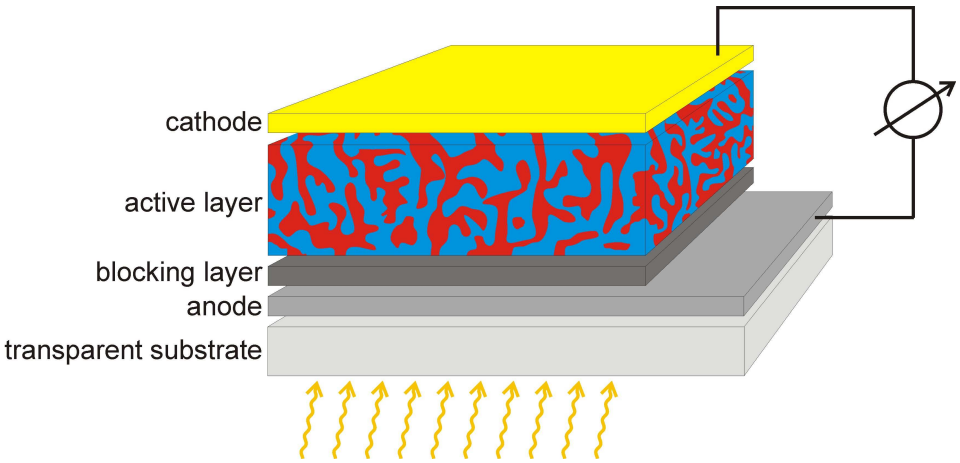

Figure 2.1: *Device architecture of a typical organic photovoltaic device. The light enters the solar cell through the transparent substrate.*

The active layer of an organic photovoltaic device is composed of organic semiconductors which are carbon-based molecules with semiconducting properties. In polymer-based solar cells as investigated in this thesis at least one component of the active layer is a semiconducting polymer. While most polymers are colorless insulators, polymers exist which are semiconducting or even conducting, e.g. doped polyacetylene. Most semiconducting polymers are conjugated polymers such as polythiophenes, polyphenylenevinylenes and polypyrrols. Conjugated polymers have a backbone which consists of alternating single and double bonds resulting in binding and anti-binding states in the molecule. These

states form the so-called highest occupied molecular orbital (HOMO) and the lowest unoccupied molecular orbital (LUMO) with an energy gap E_g in the range of 1.5 eV to 3 eV. Consequently, most conjugated polymers are colored.[12]
Due to the high exciton binding energies ($\sim$ 0.5 eV)[13, 14, 15] and the short exciton diffusion length ($\sim$ 10 nm)[16] in organic semiconductors, the charge carrier generation is a multi-step process. In figure 2.2 these steps are shown schematically. A photon is absorbed by an organic semiconductor and an exciton is generated. Due to the high exciton binding energy, the probability of exciton dissociation in the pure material is very low. Therefore, a second material has to be introduced whereby an interface between an n-type and a p-type material is formed. The exciton has to diffuse to this interface to dissociate. The generated charge carriers are transported through percolation paths in the corresponding materials to the electrodes. At the electrodes the charge carriers are extracted.[16, 17] The details on each of the processes are described in the following sections.

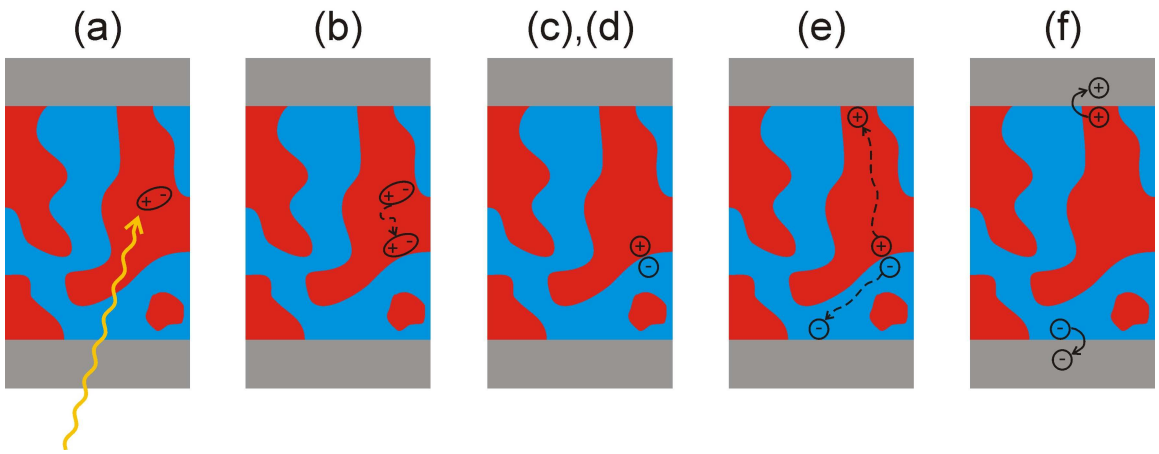

Figure 2.2: *Illustration of the charge carrier generation process: (a) absorption, (b) exciton diffusion, (c),(d) exciton dissociation, (e) charge transport and (f) charge extraction. The electrodes are depicted in gray and the n-type and the p-type materials in the active layer in blue and in red, respectively.*

Due to the limitations given by the high exciton binding energy and the short exciton diffusion length, active layers consisting of a bulk heterojunction structure, i.e. an interpenetrating blend of two organic semiconductors, are found to show much higher efficiencies than bilayer systems. The bulk heterojunction concept enables an active layer with a thickness on the order of 100 nm to have efficient absorption and internal structural length scales in the range of the exciton diffusion length.[8, 18, 7] Therefore, the detailed morphology of the active layer is of high importance.

2.1.2 Absorption

The first step of the charge carrier generation process in every solar cell is the absorption of a photon by exciting an electron (figure 2.2(a)). In the case of organic materials, the electron is excited from the HOMO to the LUMO. Therefore, the energy of the incident photon $E = h\nu = hc/\lambda$ has to be larger than E_g in order to be absorbed. The probability of absorption of a photon by exciting an electron from a lower electronic state l to an upper electronic state u, B_{lu}, can be derived from Einstein's coefficients for absorption and gives

$$B_{lu} = \frac{c}{n_0} \int \frac{\sigma(\nu)}{h\nu} \mathrm{d}\nu \tag{2.1}$$

where c/n_0 describes the speed of light in a material with refractive index n_0, h is Planck's constant and ν the frequency of the photons. $\sigma(\nu)$ is the cross section to capture a photon. This cross section is proportional to the extinction coefficient $\epsilon(\nu)$.[19]

$$\sigma(\nu) \propto \epsilon(\nu) \tag{2.2}$$

The extinction coefficient $\epsilon(\nu)$ is the imaginary part of the complex refractive index and describes the attenuation of light in a material. If scattering can be neglected, $\epsilon(\nu)$ is equal the absorption coefficient $\alpha(\nu)$ of the material.[19]

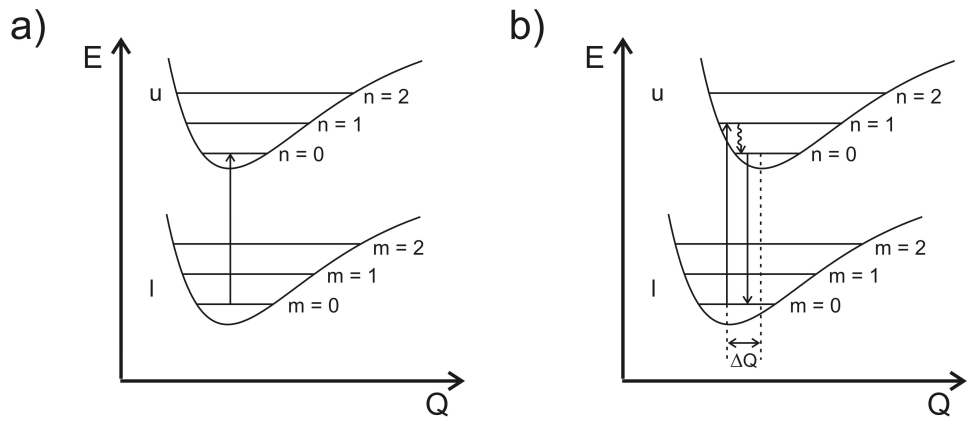

Figure 2.3: *Band profile of a lower (l) and an upper (u) electronic state including the corresponding vibrational levels m and n, respectively. Excitation of a molecule a) in the case of an unchanged molecular structure and b) in the case of some change ΔQ of the molecular structure. Q is a displacement coordinate, E the energy.*

The shape of the absorption spectrum of an organic molecule as a function of the wavelength is defined by the type of monomer. For organic molecules the absorption spectra consist not only of a sharp peak but also reveal further fine structure from vibrational

excitations. This fine structure results from alteration of the molecular structure due to the electronic excitation in an organic molecule, i.e. an expansion of the chemical bonds occurs.[20] In figure 2.3 two different electronic states of a molecule are shown including vibrational modes. Following the Franck-Condon principle, electronic transitions are much faster than the motion of the nuclei. Consequently, in a molecule the electronic transitions in figure 2.3 are drawn as vertical lines. In the case of an electronic excitation with no spacial displacement (figure 2.3a), the excitation occurs from the lowest vibrational state $m = 0$ of the lower electronic level l to the lowest vibrational state $n = 0$ of the upper electronic level u. The absorption spectrum in this case consists of a single peak with a certain width due to the life time of the excited state. However, in organic materials the electronic excitation is connected to a certain spatial displacement (figure 2.3b). Consequently, transitions to different vibrational states n are possible. The transition probability is given by the overlap of the wavefunctions of the initial and the final state. The absorption spectrum in this case shows a certain fine structure (see figure 2.4).[12]
The absorption spectra of molecules with varying numbers n_p of the same monomer show the same shape but with increasing n_p the absorption spectrum is red shifted.[21]

$$\omega(n_p) = \omega_0 + \frac{\Delta\omega}{n_p} \tag{2.3}$$

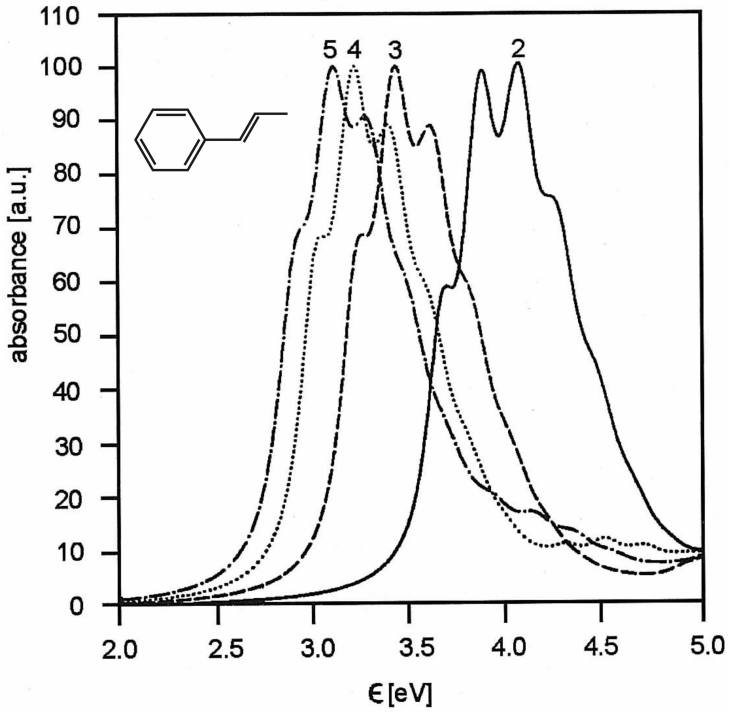

Figure 2.4: *Optical absorbance spectra of phenylene vinylene oligomers with two-, three-, four- and five-ring structure. The monomeric unit is shown in the inset. From Cornil et al.[21]*

where $\omega(n_p)$ is the absorption frequency. In figure 2.4 the optical absorption spectra of phenylene vinylene oligomers with different numbers of monomers are shown. With increasing number of monomers, the spectrum exhibits a red shift.[21, 12] Due to the extension of the π-electron system, the binding and anti-binding states form a band-like structure and the energy gap decreases with increasing π-electron system. Consequently, a higher number of electrons results in a red-shift of the absorption spectrum.
In the case of conjugated polymers, the position of the absorption is given by the intrachain ordering or conjugation length Λ which describes the length of the undisturbed conjugation in a polymer chain. Due to kinks, defects etc. of the polymer backbone, the conjugation length is much shorter than the length of the polymer chain (figure 2.5).[12]

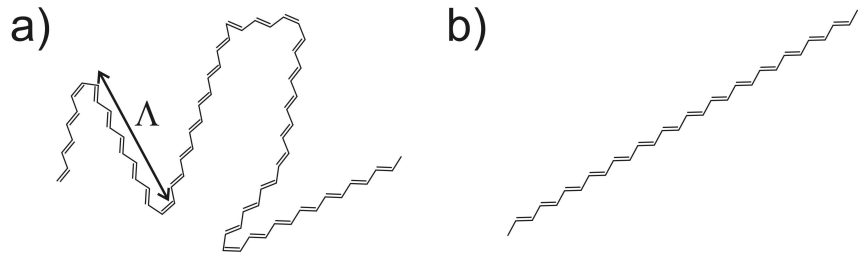

Figure 2.5: *Illustration of the spectroscopic-unit concept (see section 2.1.3) by the introduction of structural disorder (a) compared to a one-dimensional semiconductor (b). The structural disorder is described by the so called conjugation length* Λ.

The absorption of a photon excites an electron with a remaining hole. Most likely the electron and the hole form a Coulomb-bond electron-hole pair, called exciton. In organic molecules a Frenkel exciton which resides on one polymer chain is created. Due to spin conservation electrons and holes have an opposite spin and a singlet exciton is generated. Excitons which are located on different chains are called charge-transfer excitons. The binding energy of excitons in polymers is typically on the order of 0.5 eV [13, 14, 15], and the excitons are extended over several monomer units.[22] In contrast to the Wannier-Mott excitons found in inorganic semiconductors with binding energies of about 20 meV, excitons in polymers cannot be dissociated at room temperature. In figure 2.6 the schematic representation of a crystal lattice with Wannier-Mott, charge-transfer and Frenkel excitons is shown. However, an organic semiconductor typically is only partly ordered and figure 2.6 cannot directly be applied for organic semiconductors. Nevertheless, figure 2.6 gives a sufficient overview of different exciton types.

Besides the intrachain order as described above also interchain interactions can influence the absorption spectrum of an organic material. When two molecules approach each other, they interact and influence their electronic properties. These electronic proper-

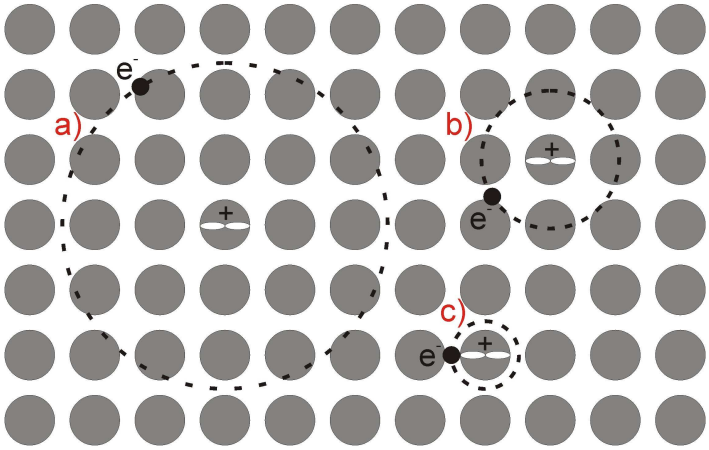

Figure 2.6: *Illustration of a crystal lattice where the gray circles depict the atoms on a lattice with different types of excitons: a) Wannier-Mott exciton, b) charge-transfer exciton and c) Frenkel exciton. The holes are illustrated as a empty orbital (white).*

ties are mainly determined by electron exchange and Coulomb interactions. Therefore, electronic excitations are coupled with the vibrational modes of the molecules and the absorption spectrum is altered depending on the type of molecular aggregation. Two main types of ordering exist, J- and H-aggregates (figure 2.7). In J- and H-aggregates, dipoles are arranged in-line and parallel, respectively. A detailed description can be found in reference [20].

It was found that the conjugated polymer P3HT can be treated as a weakly coupled H-aggregate which dominates the absorption and emission spectra. From the relative absorbance of the 0-0 and 0-1 vibronic peaks A_{0-0}/A_{0-1} the free exciton bandwidth W can be extracted. The free exciton band width W is decreasing with increasing conjugation length and therefore an indication for changes in intrachain ordering.[23]

$$\frac{A_{0-0}}{A_{0-1}} \approx \frac{n_{0-0}}{n_{0-1}} \left(\frac{1 - 0.24W/E_p}{1 + 0.073W/E_p} \right) \tag{2.4}$$

where n_{0-0} and n_{0-1} are the real part of the refractive index at the 0-0 and 0-1 peaks, respectively. In P3HT, the phonon energy of the main oscillator coupled to the electronic transition is $E_p = 0.18$ eV and the ratio of the refractive indices n_{0-0}/n_{0-1} is assumed to be 0.97.[24] In this thesis the weakly coupled H-aggregate model is used to estimate the ratio of unaggregated and aggregated P3HT chains following the analysis of Gao et al.[25]

2.1.3 Exciton diffusion

An exciton is a mobile quasi-particle with no charge, thus it does not contribute to the charge transport. Therefore, the exciton has to dissociate which typically occurs at an interface as the exciton's binding energy is considerably higher than room temperature. As most excitons are not created in the vicinity of an interface, excitons have to diffuse to such an interface. The motion of excitons happens via energy transfer processes between a donor molecule and an acceptor molecule. In the case of exciton diffusion in one polymer phase, the donor molecule is the site where the excitation is located and the acceptor molecule is the site to which the excitation is transfered. Energy migration describes the process of movement involving several energy transfer processes.

Energy Transfer

The energy transfer consists of two main processes, namely the trivial energy transfer process (figure 2.8a) and the Förster transfer also known as resonant transfer process (figure 2.8b). In the case of the trivial energy transfer process, which is also called photon reabsorption, the donor molecule emits a photon by fluorescence and an acceptor molecule absorbs the photon, thereby creating a new excitation. The transfer rate $K^{ET}_{D\to A}$ of the photon reabsorbtion from a donor molecule D to an acceptor molecule A is

$$K^{ET}_{D\to A} \propto R^{-2} \tag{2.5}$$

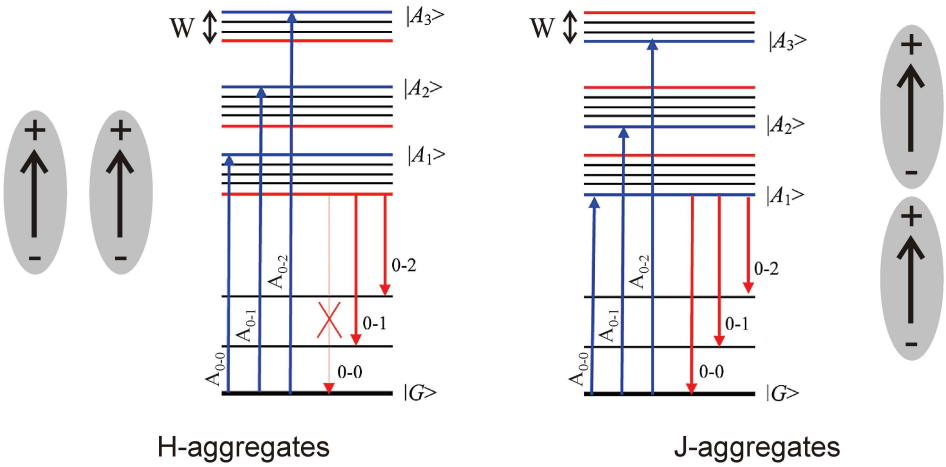

Figure 2.7: *Schematic presentation of the alignment of two dipoles depicted as black arrows in gray ellipses in H- and J- aggregates. The corresponding level diagrams for weakly coupled H- and J-aggregates are shown. The absorption ($A_{0-(v+1)}$) and the emission (0-(v+1)) transitions are depicted in blue and red, respectively. The vibrationless ground state and the v-th vibronic band are depicted as $|G\rangle$ and $|A_{v+1}\rangle$. The free exciton bandwidth is given by W. The figure is adapted from reference [20].*

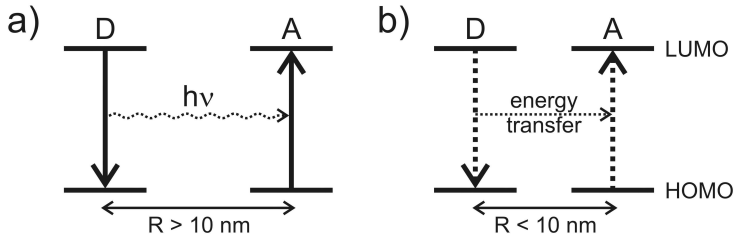

Figure 2.8: *Band diagrams describing a) the trivial energy transfer process and b) the resonant transfer process from a donor molecule D to an acceptor molecule A.*

where R is the distance between donor and acceptor molecule. The trivial energy transfer process is dominating at larger distances (R >10 nm). The apparent lifetime of the excitation is extended by this process.[19]

The Förster transfer, also known as fluorescence resonance energy transfer (FRET), is a radiationless energy transfer from D to A by dipole-dipole coupling. It was originally developed for diluted dye molecules, but is applicable to extended conjugated polymers by means of the spectroscopic-unit concept. This concept assumes the segmentation of the conjugated π-system by structural defects which break the translation symmetry. The segmentation is expressed by the conjugation length Λ. In figure 2.5 the spectroscopic-unit concept is demonstrated schematically.[26] The transfer rate $K_{D\to A}^{FRET}$ for the Förster transfer is

$$K_{D\to A}^{FRET} = \frac{1}{\tau_D}\left(\frac{R_0}{R}\right)^6 \tag{2.6}$$

where τ_D is the natural lifetime of the donor and R again describes the distance between D and A. R_0 is the critical transfer distance at which the energy transfer rate is equal to the radiative decay rate τ_D^{-1}:[19]

$$R_0^6 \propto \kappa^2 \int \lambda^4 f_D(\lambda)\epsilon_A(\lambda)\mathrm{d}\lambda \tag{2.7}$$

where $f_D(\lambda)$ is the normalized donor emission spectrum depending on the wavelength λ and $\epsilon_A(\lambda)$ the normalized acceptor extinction coefficient. The dipole orientation factor κ describes the dipole orientation between the D and A molecules:

$$\kappa = (\cos\theta_{DA} - 3\cos\theta_D\cos\theta_A)^2 \tag{2.8}$$

where θ_{DA} is the angle between the dipoles of the D and A molecules and θ_D and θ_A are the angles between the corresponding dipoles and the connecting vector of molecule D and A. From parallel to perpendicular arrangement, κ varies from 4 to 0. Consequently, for the FRET process the following requirements have to be fulfilled: For parallel dipoles of the donor and acceptor molecules, the transfer rate $K_{D\to A}^{FRET}$ is maximum. In addition,

the emission spectrum of the donor has to overlap with the absorption spectrum of the acceptor. Finally, due to the $K_{D\to A}^{FRET} \propto R^{-6}$ dependency the distance between the molecules has to be sufficiently low ($R < 10$ nm).

Energy Migration

The exciton diffusion or movement is described by the energy migration process which is composed of several energy transfer steps. Therefore, exciton diffusion can be interpreted as a random hopping-like motion starting at position x_0 (figure 2.9). The final distance or diffusion length l_D is much smaller than the total covered distance. The diffusion length is given by

$$l_D = \sqrt{ZD\tau_D} \tag{2.9}$$

where Z is a parameter describing the dimensionality d of the diffusion: $Z = 2d$. D is the diffusion coefficient and τ_D the exciton lifetime which is in the range of ns.[27] For conjugated polymers, an exciton diffusion length of 4-14 nm is found in literature.[28, 22] In the case of the fullerene C_{60}, the exciton diffusion length is $l_D = 40$ nm.[29]

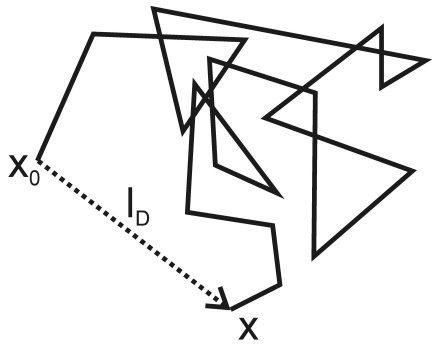

Figure 2.9: *The exciton diffusion as a random hopping-like motion, where the final distance l_D is much smaller than the total covered distance. x_0 and x denote the starting and the end point of the random walk, respectively.*

2.1.4 Exciton dissociation

After reaching the interface between the electron acceptor phase and the electron donor phase[1], the excitons dissociate in a two step process. In the following, the exciton dissociation is described for an exciton which is initially generated in the donor material. This is the general case for polymer:fullerene systems as the majority of the photons are

[1] In this case donor and acceptor materials are defined by their band structure and describe the hole and electron conducting materials, respectively. The naming should not to be confused with the naming in section 2.1.3, where the energy transfer process in the case of exciton diffusion was described.

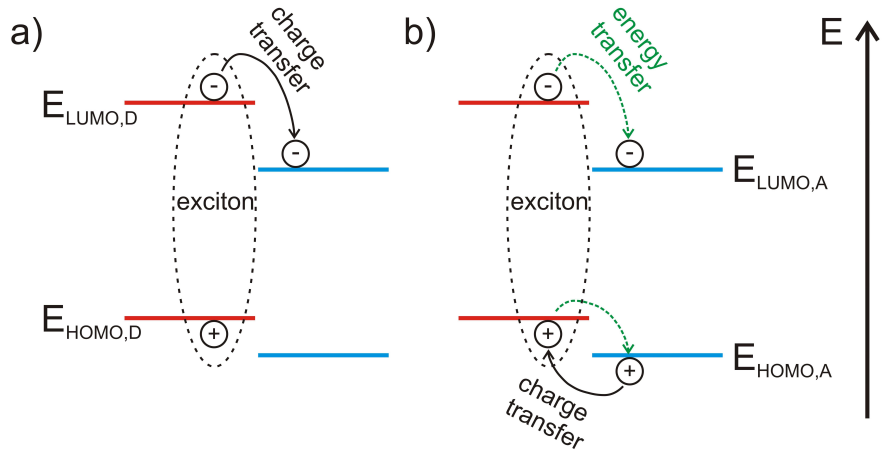

Figure 2.10: *The HOMO and LUMO energy levels of an acceptor (blue) and donor (red) interface neglecting band bending. The exciton dissociation occurs either by a) direct charge transfer or b) initial energy transfer followed by charge transfer.*

absorbed in the polymer, i.e. the electron donor, with a typical absorption range in the visible regime. In contrast, fullerenes absorb in the UV regime which has a small overlap with the solar spectrum. The inverted case exists as well and can be described in a similar way.[16, 17]

For an efficient exciton dissociation the HOMO and LUMO energy levels of the acceptor and donor materials have to match as shown in figure 2.10. When an exciton reaches the interface between electronically matching materials, the dissociation is very fast ($\sim$ 10 fs for polymer:fullerene systems), i.e. much faster than any decay process.[30, 31] Consequently, the efficiency of exciton dissociation is almost unity provided the exciton reaches such an interface. The process can occur in two ways, by direct charge transfer (figure 2.10a) or by an initial energy transfer followed by a subsequent charge transfer (figure 2.10b). After either charge transfer, the negative and positive charge carriers reside on the acceptor and on the donor, respectively. In the presented cases, the charge carriers consist of polarons. Polarons are quasiparticles consisting of a charge and the caused polarization of the surrounding. However, the polarons are still Coulomb bound as a so-called polaron pair, which constitutes an intermediate step between the exciton and the free charges. To gain free charges, the polaron pair has to be separated.[16]

To describe the polaron pair dissociation, the Braun-Onsager model is commonly used. This model treats the separation of two oppositely charged ions assisted by an electric field.[32, 33] The bound polaron pair can either recombine to the ground state with a rate $k_f \propto \tau_f^{-1}$, where τ_f is the lifetime of the polaron pair, or it can dissociate with a rate k_d (figure 2.11). There is also a chance given by the rate k_r that free polarons form a polaron

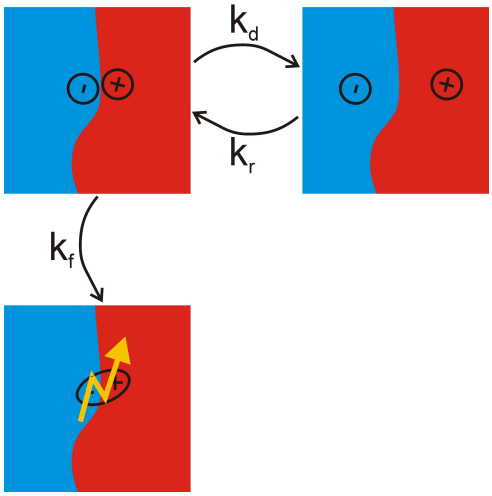

Figure 2.11: *Illustration of a polaron pair at the donor-acceptor interface with the rate k_f for recombination to the ground state, the dissociation rate k_d and the rate k_r for polaron pair formation from free polarons.*

pair again. The polaron pair-separation yield $P(F)$ depending on the electrical field F [33] is given by

$$P(F) = \frac{k_d(F)}{k_d(F) + k_f} \tag{2.10}$$

with the field-dependent dissociation rate

$$k_d(F) = \frac{3\gamma}{4\pi r_{pp}^3} \exp\left(-\frac{E_b}{kT}\right) \frac{J_1\left(2\sqrt{-2b}\right)}{\sqrt{-2b}} \tag{2.11}$$

where $\gamma = q\mu/\epsilon\epsilon_0$ is the Langevin recombination factor [19] with the elementary charge q, the sum of hole and electron charge carrier mobilities μ and the effective dielectric constant of the organic semiconductor system $\epsilon\epsilon_0$. r_{pp} is the initial polaron-pair radius, $E_b \propto 1/r_{pp}$ the Coulombic binding energy of the polaron pair, kT the thermal energy, J_1 the Bessel function of order one and b the reduced field with $b = q^3F/(8\pi\epsilon\epsilon_0(kT)^2)$. Thus, the polaron pair-separation yield $P(F)$ can be expressed as

$$P(F) = \frac{\kappa_d(F)}{\kappa_d(F) + (\mu\tau_f)^{-1}} \tag{2.12}$$

where $\kappa_d(F)$ is used as substitution with $k_d(F) = \mu\kappa_d(F)$.[17] Consequently, the polaron-pair separation yield $P(F)$ strongly depends the charge carrier mobilities μ and the polaron-pair lifetime τ_f. For systems with high mobilities and long polaron-pair life times, the charge carrier generation at the acceptor-donor interface is most efficient.[17]

2.1.5 Charge carrier transport

The free charge carriers, i.e. the polarons, have to be transported to the respective electrodes. Organic semiconductors are highly disordered and therefore band transport as in crystalline semiconductors with long-range order does not take place. Instead, the electrical transport occurs by hopping from one localized state to the next. This hopping process happens when the wavefunctions of neighboring sites overlap only weakly. Hopping is a combination of tunneling from one site to another and a thermally activated process. The hopping rate ν_{ij} for a local charge transport from site i to site j was described by Marcus [34, 35]:

$$\nu_{ij} = \frac{|I_{ij}|}{\hbar}\sqrt{\frac{\pi}{\xi kT}}\exp\left(-\frac{(\Delta G_{ij}+\xi)^2}{4\xi kT}\right) \tag{2.13}$$

where $\hbar$ is the reduced Planck constant, kT the thermal energy and ξ the reorganization energy accounting for the polaron relaxation. I_{ij} stands for the transfer integral which describes the overlap of the wave functions of the sites i and j and is proportional to the tunneling rate. ΔG_{ij} is the energy difference of two sites i and j. The density of states is typically given by an exponential or gaussian distribution in disordered systems.[16]
Another description of the hopping rate is the Miller-Abrahams hopping rate in which the tunneling and thermal activation contribution are more obvious.[36]

$$\nu_{ij} = \nu_0 \exp\left(-\gamma' r_{ij}\right)\begin{cases}\exp\left(-\frac{\Delta E_{ij}}{kT}\right) & \Delta E_{ij} > 0 \ \text{ (hopping up)},\\ 1 & \Delta E_{ij} \leq 0 \ \text{ (hopping down)}\end{cases} \tag{2.14}$$

where ν_0 is the maximum hopping rate, γ' the inverse localization radius which is proportional to the transfer integral and r_{ij} the distance between the sites i and j. The tunneling contribution is described by the first exponential expression. The thermal activation contribution for hops upwards in energy is given by a Boltzmann term where ΔE_{ij} is the energy difference between the sites i and j.
Both models describe only the mesoscopic hopping transport but not directly the macroscopic behavior. However, these models were used in combination with Master equations [37, 38] and Monte Carlo simulations [39, 40] to simulate the macroscopic charge transport. Bässler applied the Miller-Abrahams hopping rate in Monte Carlo simulations in which he used a Gaussian distributed density of states.[40] The found charge carrier mobility μ_{GMD} in Bässlers Gaussian disorder model depends on the temperature T and on the field F. The parametric fit is given by

$$\mu_{GMD} = \mu_\infty \exp\left(-\left(\frac{2\sigma}{3kT}\right)^2 + C\left(\left(\frac{\sigma}{kT}\right)^2 - \Sigma\right)F^{1/2}\right) \tag{2.15}$$

where σ is the energetic width of the Gaussian distribution of the density of states, also called disorder parameter. The corresponding spatial disorder is given by Σ. C and $2/3$ are

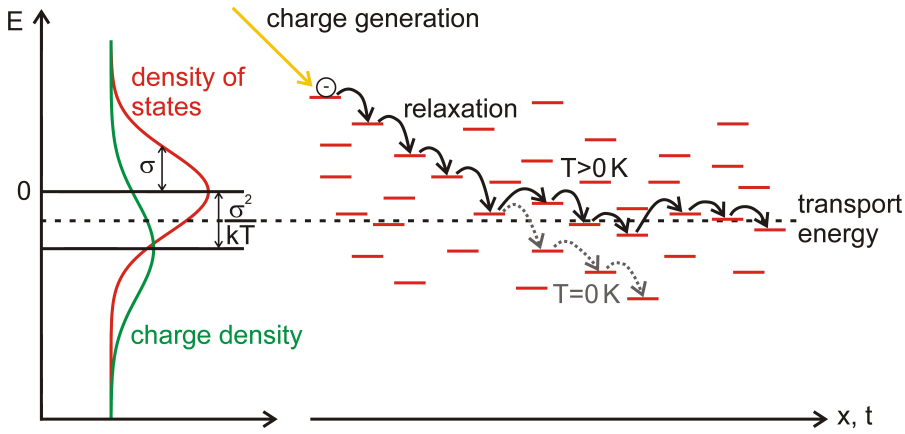

Figure 2.12: *Presentation of the concept of transport energy. A Gaussian distribution of the density of states and of the charge density are assumed. The charge transport in time t and space x by hopping takes place around the transport energy.*

scaling factors of the parametric fit. The introduced parametric Gaussian disorder model is commonly used to describe experimental results. The $\ln \mu \propto F^{1/2}$ and $\ln \mu \propto 1/T^2$ dependencies were both found in experiments.[41, 42]

To describe the charge transport in an organic semiconductor as band transport plus trapping, the so-called concept of transport energy is used (figure 2.12).[16] A Gaussian distribution of the density of states with a width σ is assumed for a disordered organic material. The charge density thermalizes by $-\sigma^2/kT$ and a transport energy can be defined. Around this transport energy (indicated by the dashed line in figure 2.12), the charge carrier transport by hopping takes place. The charge carriers are created at higher energies, relax to a quasi-equilibrium and are transported along the transport energy level. Below the transport energy, charges get immobile and do not contribute to charge transport anymore. As a result, disordered organic semiconductors can be treated as trap-rich inorganic semiconductor.[16]
The parametric models described above refer to charge transport in single materials only. However, a model for the charge transport in material combinations is still missing and the Gaussian disorder model is currently used to simulate charge transport in material combinations.[16]

2.1.6 Charge carrier extraction

After reaching the organic semiconductor-metal interface the charge carriers have to be extracted. This process is strongly affected by the device architecture. In addition, the

charge carrier concentration, which is influenced by the recombination at the interface of organic semiconductor and metal electrode, is an important aspect. So far, there is not much experimental knowledge about charge extraction.[16]
Typically, the field-dependent photocurrent is modeled to obtain information on the charge carrier extraction. However, the charge carrier generation also depends on the electric field. Therefore, an independent experimental approach is not possible. Mihailetchi et al.[43] were able to model the photocurrent by a combination of the Braun-Onsager model (section 2.1.4) and the Sokel and Huges model analytically.[44] The photocurrent after Sokel and Huges is given by

$$J_{ph,SH} = J_{ph,max}\left(\frac{\exp(qV/kT)+1}{\exp(qV/kT)-1} - \frac{2kT}{q}\right) \tag{2.16}$$

where $J_{ph,max}$ is the maximum photocurrent, V the internal voltage and kT/q the thermal voltage with q the elementary charge. The most important result is that the equation (2.16) depends on the voltage across the device. In comparison, the polaron pair dissociation is field-dependent.[16]
Further mechanisms influencing charge carrier extraction are imbalanced hole and electron mobilities or surface recombinations.[16, 45]

2.1.7 Loss mechanisms

Besides the understanding of the single processes in an organic photovoltaic cell, also the knowledge of the different loss mechanism is important. In figure 2.13 different loss mechanism (i-vi), which occur in an organic solar cell, are shown.

After generation of an exciton by light absorption, the exciton will recombine (figure 2.13 process (i)) if no interface is reached during the exciton lifetime τ_D. As mentioned before, the lifetime of an exciton τ_D is typically in the range of ns.[27]
The recombination of two or more free polarons, can be divided in a first-order and a second-order recombination, also called geminate and non-geminate recombination, respectively. A geminate recombination occurs when the positive and negative polarons have a common precursor state. Consequently, the recombination occurring during polaron-pair dissociation is of geminate nature (figure 2.13 process (ii)).[16] This loss mechanism is taking place when the polaron-pair dissociation is too slow, i.e. in systems with low charge carrier mobilities and short polaron-pair lifetimes (see section 2.1.4).
Recombination of two already separated polarons is of non-geminate nature as the two participating polarons do not have a common precursor state (figure 2.13 process (iii)).[16]
In an organic solar cell, two charge carriers typically form a polaron-pair before recombining. The charge carrier dynamics are given by the continuity equation. Taking into

account that the recombination of mobile charges depends on the number of charges and including the polaron-pair formation as an intermediate state, the continuity equation can be written as

$$\frac{\mathrm{d}n}{\mathrm{d}t} = -\frac{1}{q}\frac{\mathrm{d}j_n}{\mathrm{d}x} + PG_{pp} - (1-P)R \tag{2.17}$$

where n is the electron concentration, q the elementary charge and j_n the electron current. P is the polaron-pair dissociation rate given by equation (2.10) and G_{pp} the polaron pair generation rate. t and x are the time and the position.[16] The recombination of free polarons in materials with a low mobility is described by the Langevin recombination rate R [46, 19]:

$$R = \gamma(np - n_i^2) \tag{2.18}$$

where p is the hole concentration, n_i^2 the intrinsic carrier concentration and γ the Langevin recombination prefactor (see section 2.1.4). The recombination is a two step process with the primary finding of the partners (step 1) followed by the actual recombination (step 2). In organic materials the recombination rate is limited by step 1 due to the low carrier mobilities. Consequently, the Langevin recombination prefactor can be described by

$$\gamma = \frac{q}{\epsilon_r \epsilon_0}(\mu_e + \mu_h) \tag{2.19}$$

with the effective dielectric constant $\epsilon_r\epsilon_0$ and the electron and hole mobilities μ_e and μ_h.[16]

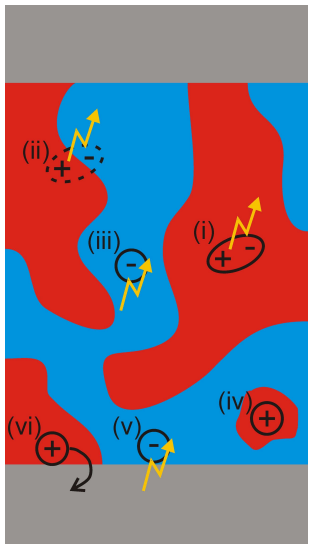

Figure 2.13: *Illustration of the loss mechanism (i)-(vi) occurring in an organic solar cell with an electron acceptor (blue) and donor (red). Recombinations are depicted as yellow arrows. The bottom and top electrodes (gray) are the cathode and anode, respectively. The processes (i)-(vi) are described in the text.*

Besides the recombination of two free polarons, process (iii) in figure 2.13 refers also to the recombination of a mobile charge carrier with a trapped one. In this case, the order of recombination depends on the concentration of trapped charge carriers. If the density of trapped charges is high, i.e. higher than the mobile charge density, a recombination is considered as a first order process because the density of trapped charges is hardly diminished. In contrast one refers to the recombination as a second order process if the trapped charge carrier density is similar or smaller than the mobile charge carrier density.[16]
Further losses occur due to trapping either in a deep energetic state with a very low escape probability or at structural defects as depicted as process (iv) in figure 2.13. A structural defect is an isolated phase of one material with no connection to an electrode. These charges will be trapped until recombination with a mobile charge occurs.
Finally, polarons reaching an electrode can still recombine and therefore diminish the photovoltaic performance. On the one hand charge recombination at the electrode interface can occur (figure 2.13 process (v)). Scott et al. reported on this so-called surface recombination in detail.[45] On the other hand charge extraction at the wrong electrode (process (vi) in figure 2.13) can happen in systems with contact between the electron conducting material with the anode or the hole conducting material with the cathode.
All described loss mechanisms reduce the efficiency of an organic solar cell.

2.2 Polymer crystallization and phase separation

Due to the intrinsic electronic properties of organic semiconductors, in particular the high exciton binding energy and the short exciton diffusion length as well as the charge carrier transport mechanisms (chapter 2.1), the inner morphology of the active layer in an organic solar cell is of utmost importance. Firstly, the arrangement of the single polymer chains is crucial for the charge carrier mobility. The mobility is orders of magnitudes higher in crystalline regions of the polymer than in the amorphous parts.[47] Therefore, the principles of polymer crystallization are described in section 2.2.1. Furthermore, on mesoscopic length scales the phase separation of the electron donor and acceptor materials in a bulk heterojunction is important. The phase separation of polymers in general and of rod-like polymers in particular is introduced in section 2.2.2. In addition, the structural evolution of polymer blends with the two competing ordering processes, phase separation and crystallization, is described (section 2.2.2.3).

2.2.1 Polymer crystallization

In contrast to small organic molecules or oligomers, crystallizable polymers do not form complete crystals but exist in a semicrystalline state. This state, which is not a thermally

equilibrated state but is kinetically determined, consists of polymer crystals separated by amorphous regions of the same polymer. A full crystallization of polymers is hindered by a high entropic activation barrier which results from the need of complete disentanglement of the coiled polymer chains before crystallization. As a complete disentanglement takes very long, only semicrystalline structures form. A further reason for only partly crystallized polymers is the polydispersity. The crystallinity ϕ_c of polymers is defined as the volume fraction of the crystalline part:

$$\phi_c = \frac{v_c}{v_a + v_c} \tag{2.20}$$

where v_c and v_a are the volumes occupied by the crystalline and amorphous phases, respectively. In the amorphous parts mainly chain ends, entangled chains, impurities and other defects are found. Polymer crystals have a layered structure with a layer thickness d_c (Figure 2.14) and can extend laterally, i.e. perpendicular to the polymer chains, over several micrometers. The crystal thickness d_c depends on the crystallization temperature T_c but was found to be independent of the molecular weight M_w of the polymer.[48] Thus, polymers form crystalline lamellae with a thickness d_c and lateral expansion up to micrometers. Macroscopically, these lamellae arrange in so-called spherulites. However, in organic photovoltaics which needs structural ordering on the order of 10 nm the formation of spherulites is counterproductive and therefore avoided. In this section therefore only the early stages of crystal formation are described and the spherulite structure is omitted. Polymers can crystallize when they are supercooled, i.e. the crystallization temperature T_c lies between the glass transition temperature T_g and the melting temperature T_m. The mechanism of crystal formation, i.e. the growth kinetics, was initially described by the Lauritzen-Hoffman (LH) model.[49] However, during the last two decades experimental results raised doubts about the LH model and new models were suggested.[50, 51, 52, 53, 54] Nowadays the multistage model proposed by Strobl [12, 55] is widely accepted and is presented in this thesis. It has to be mentioned that the validity is still debated and the multistage model is not generally accepted yet.

2.2.1.1 Nucleation

Polymer crystallization from an amorphous melt starts with the formation of nuclei. First, particles with an enhanced inner order are formed due to thermal fluctuations. Depending on the size, these particles, so-called embryos, disappear again or form nuclei from which crystal growth starts. The nucleation rate is described by τ_{nuc}^{-1} which is proportional to the volume v of the crystallizable domain.[56]

$$\tau_{nuc} \propto v^{-1} \tag{2.21}$$

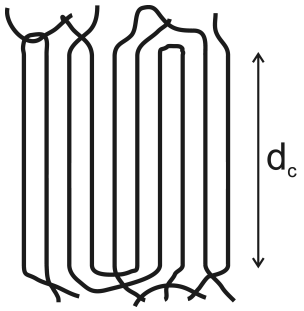

Figure 2.14: *Sketch of a polymeric crystal with thickness d_c. The lines depict the polymer backbone.*

In addition, the nucleation rate is an exponential function of the temperature.[57]

$$\tau_{nuc}^{-1} \propto \exp\left(-\frac{\Delta U + \Delta F_c}{k_B T}\right) \tag{2.22}$$

where k_B is the Boltzmann constant and ΔU an activation energy barrier for diffusion across the phase boundary which describes the sluggishness of the polymer at low temperatures. The gain in free energy due to the formation of nuclei is given by the critical free energy barrier for primary nucleation ΔF_c which is dominant at high temperatures.[58] Consequently, a maximum nucleation rate is found for mediate temperatures which is changing with chain length.[59] The fast intramolecular nucleation, where only one folded molecule is contributing to the nucleus formation, and the extremely slow intermolecular nucleation, where the nucleus consists of stretched stems from different molecules, are reported on as extreme paths of polymer crystal nucleation.[60]

2.2.1.2 Growth kinetics

From the formed nuclei or from nucleating agents, e.g. impurities, the crystal starts to grow. It has been experimentally shown that the crystallization and melting of polymers in bulk can be described by different laws using three controlling temperatures.[12] Therefore, crystallization is not the reverse process of melting and vice versa. An intermediate phase, the so called "mesophase", was introduced to explain the existence of three controlling temperatures instead of one. Consequently, in the crystal formation process of polymers three different phases exist, namely the amorphous melt (here denoted with a), the mesomorphic (m) and the crystalline phase (c). The transition between these three phases is described by the following three controlling temperatures: T_{am}^{∞} describes the transition from the melt to the mesomorphic phase, T_{ac}^{∞} the transition from the melt to the crystalline phase (equilibrium melting point) and T_{mc}^{∞} represents a virtual transition

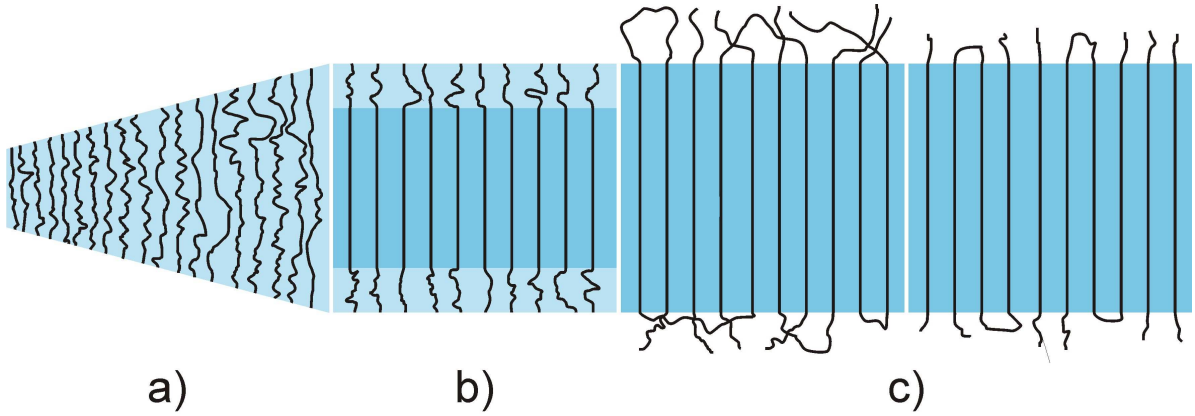

Figure 2.15: *The crystallization process in the multistage model by Strobl [55] is described as a) growing of a mesomorphic layer, b) solidification by core crystallization and c) stabilization by surface ordering.*

between the mesomorphic and the crystalline phase whereas

$$T_{am}^{\infty} < T_{ac}^{\infty} < T_{mc}^{\infty}. \tag{2.23}$$

From a thermodynamic view, this means that the chemical potential of the polymer in the mesophase and the crystalline phase drops at T_{am}^{∞} and T_{ac}^{∞} below the chemical potential of the melt, respectively.

In Figure 2.15 the crystallization process within a multistage model is shown schematically. Between the crystal phase and the melt a thin mesophase forms which is stabilized by epitaxial forces[2]. Defects are already rejected from the mesophase which is spontaneously thickening due to high inner mobility. At a critical thickness the core region solidifies and forms a block. In a final step, the chains at the surface of the block order and therefore stabilize the crystal.[12]

Based on this model, Strobl [50, 62] constructed a thermodynamic multiphase scheme. The phase diagram in Figure 2.16 deals with four phases: the amorphous melt, the mesophase and the crystalline phase which is divided into two limiting forms to account for the stabilization process: the native crystal (c_n) and the stabilized crystal (c_s). The stable regions with their transition lines are shown as functions of the temperature T and the inverse crystal thickness $1/n$. n is the number of subunits, e.g. monomers, in one stem or rod. So the crystal thickness is defined as $d_c = n\Delta a$ with the length of the subunit Δa.

At the transition lines the adjacent phases are in equilibrium and this leads to

$$T_{ac}^{\infty} - T \approx \frac{2\sigma_{ac_s} T_{ac}^{\infty}}{\Delta h_{ac}} \frac{1}{n} \tag{2.24}$$

[2]Epitaxial forces is the term for orienting molecular forces at the interface of two media which are driving forces required for epitaxial growth.[61]

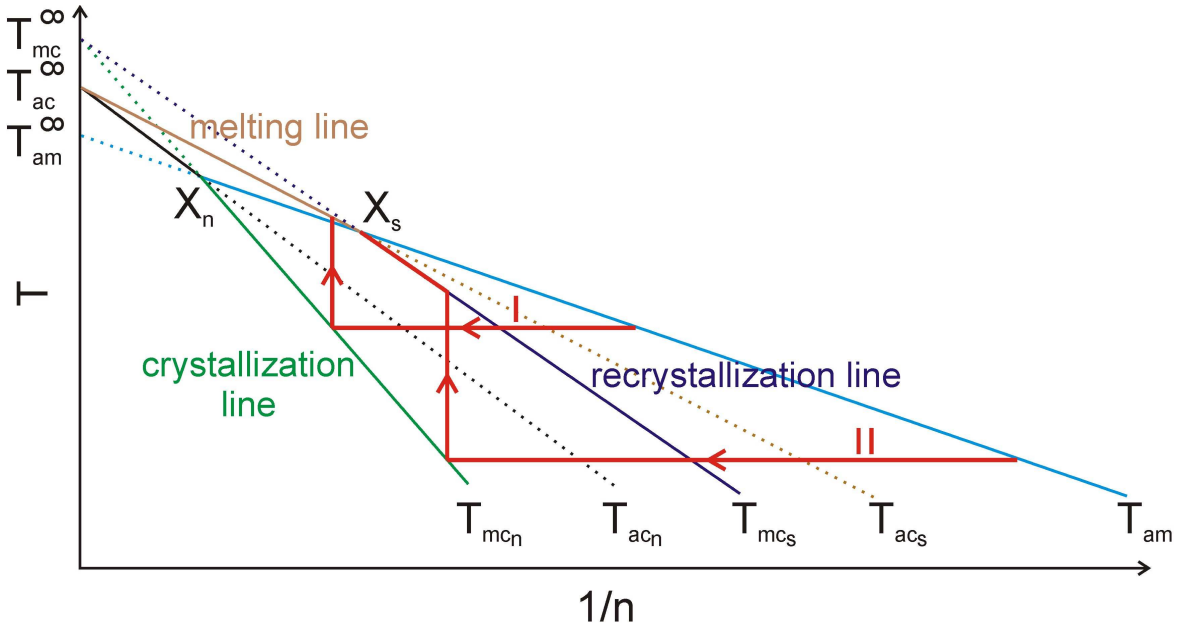

Figure 2.16: *T/n^{-1} phase diagram of layered polymer crystals in an amorphous melt. The transition lines separating the four phases, namely melt (a), mesophase (m), native crystals (c_n) and stabilized crystals (c_s) are described by equations (2.24) to (2.27).*

as the theoretical expression of the melting line. σ_{ac_s} denotes the surface free energy of a stabilized crystal and Δh_{ac} the heat of fusion. Equation (2.24) is the Gibbs-Thomson equation describing the reduction of the melting temperature due to excess free energy of the fold crystal surface. For the crystallization line one obtains

$$T_{mc}^{\infty} - T \approx \frac{(2\sigma_{ac_n} - 2\sigma_{am})T_{mc}^{\infty}}{\Delta h_{mc}} \frac{1}{n} \tag{2.25}$$

and for the recrystallization line

$$T_{mc}^{\infty} - T \approx \frac{(2\sigma_{ac_s} - 2\sigma_{am})T_{mc}^{\infty}}{\Delta h_{mc}} \frac{1}{n}. \tag{2.26}$$

σ_{ac_n}, σ_{ac_s}, σ_{am} and Δh_{mc} denote the corresponding surface free energies and the heat of fusion, respectively. While the equilibrium melting temperature T_{ac}^{∞} is decreasing with the incorporation of co-units or diluents (impurities), the crystallization and recrystallization lines were found to be independent of impurities. Equation (2.27) describes the transition from the melt to the mesophase.

$$T_{am}^{\infty} - T \approx \frac{2\sigma_{am}T_{am}^{\infty}}{\Delta h_{am}} \frac{1}{n} \tag{2.27}$$

where σ_{am} is the surface free energy and Δh_{am} the heat of fusion. Above the temperature T_{am}^{∞} the mesophase does not exist. At the triple points X_n (X_s) the free energy of the

melt, the mesomorphic layer and the native (stabilized) crystals are equal.[50, 62]
In Figure 2.16 two scenarios of isothermal annealing with subsequent heating (red solid lines) are demonstrated. Both scenarios start identically: chains from the melt are attached to the front of a mesomorphic layer which is spontaneously thickening until it reaches the crystallization line and native crystals are formed and stabilized. The crystal thickness depends on the crystallization temperature. In scenario I (high crystallization temperatures) heating does not affect the crystal thickness and the crystals melt when reaching the melting line. At low crystallization temperatures (scenario II) the crystal thickness is increasing when the recrystallization line is reached. Further heating ends at the triple point X_s and the crystals melt. Consequently, all systems crystallized at low temperatures melt at the same point (X_s) when heated.[50, 62]

2.2.1.3 Lateral growth

While the crystal thickness is defined by the crystallization temperature, the lateral size of the crystalline lamellae is, in principle, not limited. The crystalline lamellae consist of crystalline blocks which merge during growth. The lateral dimensions of the blocks are proportional to the crystal thickness d_c. The lateral growth rate can be described with

$$u = u_0 \exp\left(-\frac{T_A^*}{T}\right) \exp\left(-\frac{T_G}{T_{am}^\infty - T}\right). \tag{2.28}$$

The first exponential expression dominates the growth rate at low temperatures and is following an Arrhenius law with an effective activation temperature T_A^*. At low temperatures the segmental mobility of the melt is decisive. With increasing temperature the segmental mobility is enhanced and therefore also the growth rate u increases. At higher temperatures an activation barrier is emerging which has an entropic nature (second exponential expression). This barrier is due to straightening of a coiled chain in the melt before it can attach to the mesomorphic layer. With higher supercooling below T_{am}^∞ the growth rate u is increasing. T_G is a parameter which is proportional to the inverse temperature T^{-1} and is determined by the heat of fusion and the surface free energies of the fold surface and the growth front.[12]

2.2.1.4 Secondary crystallization

After the crystallization at a chosen temperature is finished, secondary crystallization begins upon cooling down to room temperature. While surface crystallization and melting as one process for secondary crystallization has been found for only a few polymers

so far, the insertion mode is the standard process occurring and will be described here. During annealing at a certain crystallization temperature, crystalline lamellae with a constant thickness form. In the amorphous regions between the crystallites, the defect density is increased and a region with an extension of d_{min} exists into which no crystalline lamella can enter. The distances d between two crystalline lamellae are in the range of $d_{min} < d < 2d_{min}$. At lower temperatures, crystalline lamellae with smaller thicknesses can form which grow between the initial crystalline lamellae. The lamella thickness is decreasing with decreasing temperature.[12]

2.2.2 Phase separation

In applied polymer science, the combination of two or more different polymers is used to obtain materials with new properties such as increased mechanical stability.[12] In the case of conducting polymers the combination of an n-type and a p-type polymer is necessary to achieve organic photovoltaic devices with reasonable performance.[30] Typically two polymers are not miscible on a molecular level but phase separate. For the thermodynamic phase behavior the change in free energy due to mixing, the so-called Gibbs free energy of mixing ΔG_{mix}, has to be considered. In section 2.2.2.1, the thermodynamics of polymer solutions and polymer blends containing standard coil-like polymers is described using a mean-field approach. To account for conjugated polymers, the theory is extended for blends of a coil-like polymer and a rod-like polymer (section 2.2.2.2). The section is completed by the description of the influence of crystallization on the phase separation behavior (section 2.2.2.3).

2.2.2.1 Phase separation of coil-like polymers

Flory [63] and Huggins [64] analyzed the thermodynamics of polymer solutions and polymer blends using a mean-field approach. In a mean-field approach, the pair-interactions in a many-body problem are replaced by a single body system in an external field. The phase behavior is derived from the Gibbs free energy of mixing ΔG_{mix} of two components A and B:

$$\Delta G_{mix} = G_{AB} - (G_A + G_B) \tag{2.29}$$

where G_A, G_B and G_{AB} are the Gibbs free energies of the pure components A and B and of the mixture, respectively. The free energy can be expressed by the sum of the change of entropy ΔS_{mix} and the change of enthalpy ΔE_{mix} due to mixing of A and B.

$$\Delta G_{mix} = -T\Delta S_{mix} + \Delta E_{mix} \tag{2.30}$$

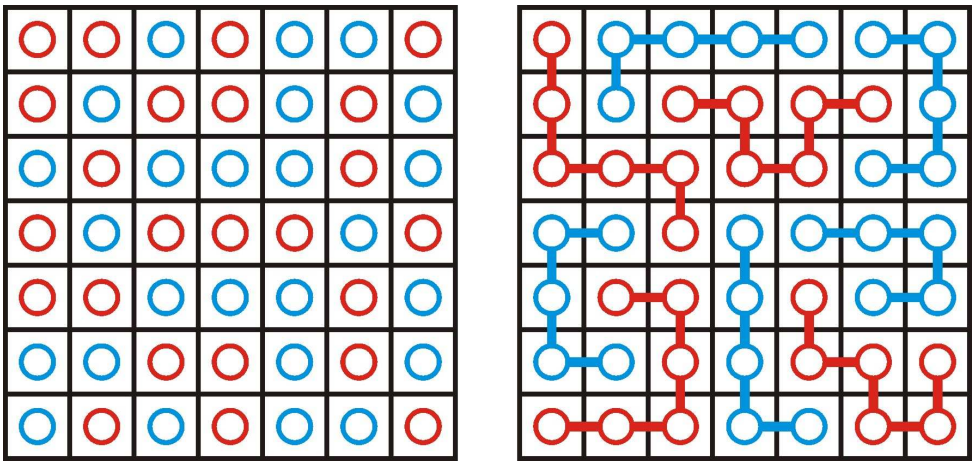

Figure 2.17: *Lattice model of a mixture of two low molecular components (left) and two polymers (right).*

As the combinatorial possibilities of the mixture is increased compared to the pure components, the entropy is increasing with mixing. In addition, the interaction between the two components influences the enthalpy of the system.[12]

Entropic contribution

To obtain the change in entropy ΔS_{mix}, a rigid lattice framework is used. In figure 2.17 the lattice models for mixtures of two low molecular components (left) and two polymers (right) on a lattice are shown. The lattice model requires that all sites are occupied and no double entry of a lattice site exist. From the number of possible arrangements Ω the entropy can be calculated by $S = k_B \ln(\Omega)$ with the Boltzmann constant k_B.
The change in entropy due to mixing given by $\Delta S_{mix} = S_{AB} - (S_A + S_B)$ is

$$\Delta S_{mix} = -k_B n \left[\frac{\phi_A}{N_A} \ln \phi_A + \frac{\phi_B}{N_B} \ln \phi_B \right] \tag{2.31}$$

with N_i the degree of polymerization and ϕ_i the volume ratio of component $i \in$ [A,B]. n is the total number of molecules on the lattice. As there is no free volume considered in this model, $\phi_A + \phi_B$ is unity. Depending on the values used for N_i, equation (2.31) describes mixtures of low molecular components ($N_A = N_B = 1$) and of two polymers ($N_A > 1$, $N_B > 1$) as well as polymer solutions ($N_A = 1$, $N_B > 1$). From mixtures of low molecular components to polymer-polymer mixtures the entropy is reduced due to less combinatorial possibilities.[12]

Enthalpic contribution

The enthalpic contribution to the Gibbs free energy describes the interaction between the

monomers of the two components. The change in enthalpy due to mixing is given by

$$\Delta E = nk_BT\chi\phi_A\phi_B \tag{2.32}$$

where χ is the Flory-Huggins interaction parameter:

$$\chi = \frac{z\Delta\epsilon}{k_BT} \tag{2.33}$$

with the lattice coordination number z and the excess exchange interaction energy $\Delta\epsilon$:

$$\Delta\epsilon = \epsilon_{AB} - \frac{\epsilon_{AA} + \epsilon_{BB}}{2} \tag{2.34}$$

where ϵ_{ij} is the segmental attractive nearest-neighbor van der Waals interaction energy between segments i and j. In the Flory-Huggins theory χ is inversely proportional to the temperature.[12]
Entering equations (2.31) and (2.32) into equation (2.30) gives the change in Gibbs free energy ΔG_{mix} due to mixing normalized to one mole ($n = N$):

$$\Delta G_{mix} = RT\left[\frac{\phi_A}{N_A}\ln\phi_A + \frac{\phi_B}{N_B}\ln\phi_B + \chi\phi_A\phi_B\right] \tag{2.35}$$

where $R = k_BN$ and N is Avogadros number.

Flory-Huggins interaction parameter

The mean-field formalism of the Flory-Huggins model assumes an incompressible system and the Flory-Huggins interaction parameter χ to be independent of pressure, composition, molecular weight and chain architecture. From experimental investigations an effective χ of the type

$$\chi = \chi_S + \chi_H/T \tag{2.36}$$

is found. As a result the Flory-Huggins interaction parameter shows not only an enthalpic behavior (χ_H) but contains also an entropic contribution χ_S.[12]

Phase diagram

In figure 2.18a the Gibbs free energy of mixing depending on the polymer ratio $\Delta G_{mix}(\phi_A)$ is plotted for different temperatures. From the trajectory of $\Delta G_{mix}(\phi_A)$ the stability of a mixture at a certain temperature can be determined. For high temperatures (T_4 and T_5) a homogeneous mixture is stable. When the temperature is decreased (T_1 to T_3) phase separation occurs. The transition line, the so-called binodal, from a homogeneous phase to a separated phase is given by the ϕ' and ϕ'' of the $\Delta G_{mix}(\phi_A)$ trajectories for different temperatures (solid line in figure 2.18b). ϕ' and ϕ'' are obtained from a tangent construction. Starting from a mixture at a given temperature with a polymer ratio of

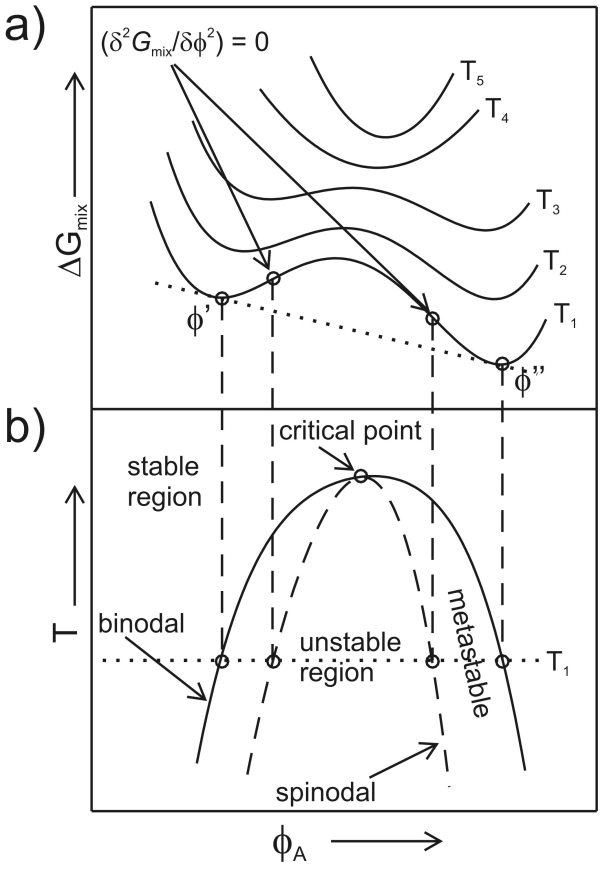

Figure 2.18: *a) The blend ratio dependent free energies $\Delta G_{mix}(\phi_A)$ for different temperatures T (eq. 2.35). ϕ' and ϕ'' are obtained from a tangent construction (dotted line). The temperature increases from T_1 to T_5. b) The phase diagram derived from the tangential construction (binodal) and the second derivative (spinodal) of the free energies for different temperatures.*

$\phi' < \phi_A < \phi''$ the mixture will phase separate into two phases with the polymer ratios of ϕ' and ϕ'', respectively. The sum of the Gibbs free energies of these two phases is lower than of the initial mixture as the straight line between the two minima lies below $\Delta G_{mix}(\phi_A)$. Depending on the starting blend ratio the phase separation occurs spontaneously (spinodal decomposition) or needs a nucleation step (metastable phase). The transition line, called spinodal, between the separated phase and the metastable phase (dashed line in fig. 2.18b) is obtained where the second derivative of $\Delta G_{mix}(\phi_A)$ is equal to 0.[12]

The common point of the binodal and spinodal transition lines is the so called critical point given by the third derivative of $\Delta G_{mix}(\phi_A)$. The critical interaction parameter χ_c and the critical mixing ratio ϕ_c are given by

$$\chi_c = \frac{1}{2N_B}\left(1 + \sqrt{\frac{N_B}{N_A}}\right)^2 \tag{2.37}$$

and

$$\phi_c = \frac{1}{\sqrt{N_B/N_A} + 1}. \tag{2.38}$$

At the critical point a second order phase transition occurs. In the case of $N_A = N_B = N$ the phase diagram is symmetric and $\phi_c = 0.5$. In addition, $N\chi_c = 2$ gives the condition

for the miscibility gap.[12]

2.2.2.2 Phase separation of coil- and rod-like polymers

The Flory-Huggins model describes the phase behavior of polymer blends of coil-like polymers. However, most conjugated polymers used in organic electronics are rod-like and tend to crystallize. Therefore, corrections have to be applied to the original Flory-Huggins theory to account for the rod-like nature of polymers. In the following section, a modified model for the phase behavior of a blend containing a coil- and a rod-like polymer is discussed.[65]

We assume a mixture of a coil-like polymer and a rod-like polymer denoted by A and R, respectively. To account for the rod-like polymer, chains consisting of m rod-like segments of the same length x_R are introduced. The segments are freely jointed. In addition, a parameter y denotes the disorientation. y/x_R is a measure for the degree of disorder whereas $y = x_R$ is the limit of complete disorder. The contour length of the coil-like polymer is x_A. Therefore, x_A and mx_R are interpreted as the degrees of polymerization of the coil-like and the rod-like polymer, respectively. For the following calculations it is assumed that the rod-like polymer orders perfectly in its pure state. Applying the lattice model and adding the enthalpic contribution, the Gibbs free energy of mixing is given as [65]

$$\frac{\Delta G_{mix}}{RT} = \frac{\phi_A}{x_A}\ln\phi_A + \frac{\phi_R}{mx_R}\ln\phi_R + \chi\phi_A\phi_R + \Delta g_{orient} \tag{2.39}$$

with

$$\begin{aligned}\Delta g_{orient} = \frac{\phi_R}{mx_R}\ln\left(\frac{1}{mx_R}\right) - \left[1-\phi_R\left(1-\frac{y}{x_R}\right)\right]\ln\left[1-\phi_R\left(1-\frac{y}{x_R}\right)\right] \\ -\frac{\phi_R}{mx_R}(m\ln y^2 - my + 1)\end{aligned} \tag{2.40}$$

where ϕ_A and ϕ_R are the volume fractions of the coil-like and the rod-like polymers, respectively. χ is the Flory-Huggins interaction parameter. For a completely disordered rod-like component, $y = x_R$ or rather $y/x_R = 1$, follows $\Delta g_{orient} = 0$. In this case, equation (2.39) is equal to the original Flory-Huggins equation (2.35). The miscibility limit of a blend of a coil-like and a rod-like polymer is given by the spinodal [65]:

$$\frac{\partial^2 \Delta G_{mix}}{\partial \phi_R^2} = 0. \tag{2.41}$$

The spinodal is obtained setting the second derivative of equation (2.39) zero.[65]

$$\frac{1}{\phi_A x_A} + \frac{1}{\phi_R m x_R} - 2\chi - \frac{(1-(y/x_R))^2}{1-\phi_R(1-(y/x_R))} = 0 \tag{2.42}$$

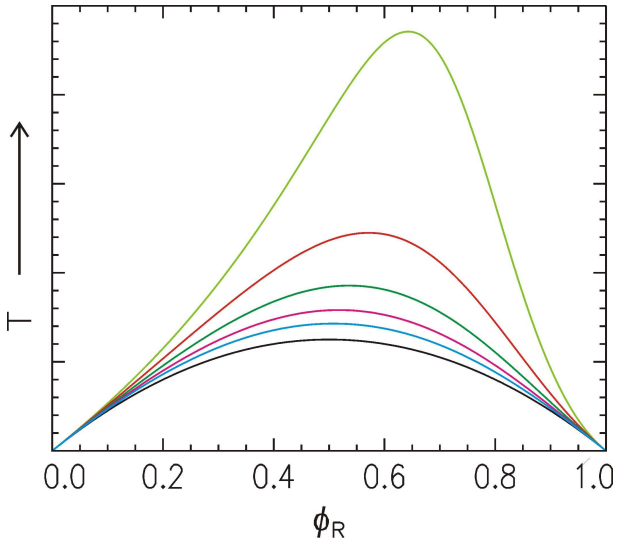

Figure 2.19: *The calculated spinodals of a symmetric blend containing a rod-like and coil-like polymer as a function of the content of the rod-like polymer ϕ_R for different degrees of disorder $y/x_R = 0.2$ (light green), 0.3 (red), 0.4 (dark green), 0.5 (magenta), 0.6 (cyan) and 1 (black) using equation (2.42). $x_A = mx_R = 2.5$.*

In figure 2.19 the spinodals of a symmetric blend containing a rod-like and a coil-like polymer for different degrees of disorder y/x_R are plotted using equation (2.42) with the proportionality $\chi \propto 1/T$. The case of a coil-coil polymer blend is represented by the limit of the degree of disorder $y/x_R = 1$ (black line in figure 2.19). With decreasing degree of disorder y/x_R or rather increasing order of the rod-like polymer the miscibility limit shifts to higher temperatures. Consequently, polymer blends containing a rod-like polymer phase separate easier than standard coil-coil polymer blends. Therefore, blends with decreasing degree of disorder y/x_R of the rod-like polymer are less miscible. In addition, the spinodal gets more asymmetric for decreasing degree of disorder y/x_R. Thus, the influence of the degree of disorder y/x_R is less decisive for lower contents of the rod-like component ϕ_R.

2.2.2.3 Phase separation of crystallizing polymers

In a polymer blend with one crystallizing component, the structural evolution is dominated either by the phase separation or the crystallization process depending on the experimental conditions. In figure 2.20, a schematic phase diagram of a blend of an amorphous and a crystalline polymer is shown. Besides the lines for binodal and spinodal phase transition, also the melting temperature of the crystalline polymer $T_m(\phi_A)$ which depends on the blend ratio ϕ_A is plotted. With the aid of different routes (A, B, C, D), typical structure evolutions are obtained.

We start in the stable region, i.e. both polymers are compatible and mixed. As long as the temperature T is well above the melting temperature $T_m(\phi_A)$, the crystallizing polymer is still amorphous and the blend behaves like a standard blend of two amorphous polymers. Below the melting temperature $T_m(\phi_A)$ (routes A and B), the structural length is defined by the dominating process. Is the phase separation process faster than the crystallization process the crystal size, e.g. the size of a spherulite, is limited by the structural length of the phase separation. In the inverted case, the crystal size is larger than the structure of the phase separation. Depending on the route (A or B), phase separation occurs via spinodal decomposition or by nucleation and growth. However, during crystallization the content of the crystallizing component in the phase surrounding the crystal is getting lower and therefore the crystallization process is hindered. Typically, a crystalline polymer does not crystallize if its content is below 50 %. However, due to the phase separation process, regions with a higher content of the crystallizable polymer will develop and therefore crystalline nuclei form and crystallization starts.[66]

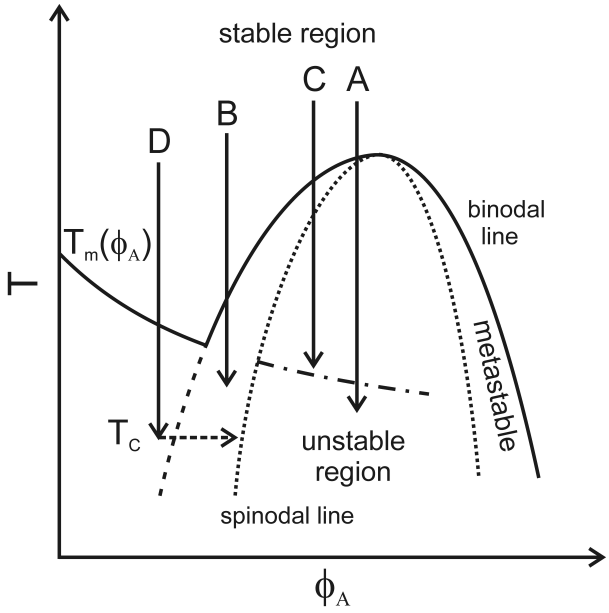

Figure 2.20: *Schematic temperature-concentration phase diagram of a blend of an amorphous and a crystalline polymer including spinodal and binodal lines as well as the melting line $T_m(\phi_A)$ of the crystalline component. The arrows labeled with A, B, C and D describe different routes of temperature quenching from the melt. T_C is the crystallization temperature in route D.*

The route C represents the case in which phase separation induces crystallization. A blend at a temperature slightly above $T_m(\phi_A)$ and in the unstable regions starts to phase separate. Therefore, the blend ratio changes locally. As $T_m(\phi_A)$ depends on the blend

ratio, it can occur that one phase reaches a blend ratio which has a melting temperature above the actual temperature. Consequently, crystallization starts in this phase.[66]
The inverted case, crystallization induced phase separation, is described by route D. A blend below $T_m(\phi_A)$ but still in the stable, i.e. homogeneous, region starts to crystallize. During the crystallization process, impurities, i.e. in this case also the amorphous component, are rejected from the crystals (see section 2.2.1). Consequently, the blend ratio at the growth front of the crystal, i.e. the surrounding phase, is shifted to a blend with a higher content of the amorphous component. If the blend ratio of the surrounding phase shifts into the unstable region phase separation starts.[66]

2.3 Scattering methods

The structure in the active layer of an organic solar cell is crucial for its photovoltaic performance as described in section 2.1. Neutron and X-ray scattering techniques are powerful tools to determine the structures formed by phase separation and crystallization processes (section 2.2). This section introduces the basic principles of elastic scattering, i.e. the wavelength of the incident wave before and after the scattering event is constant (section 2.3.1). The main techniques applied in this thesis are reflectivity (section 2.3.2) and grazing incidence scattering (section 2.3.3) experiments. The properties of soft X-rays as a new possibility for grazing incidence scattering is discussed in section 2.3.4. To probe crystalline structures, an introduction to diffraction in particular in reflection geometry is given in section 2.3.5.

2.3.1 Basic principles

The physical process of scattering describes the deflection of an electromagnetic wave or a particle at an object or in matter.[67] In this thesis, X-ray and neutron scattering are used to probe the structure of soft matter. In the following section, the basic principles of scattering are introduced for X-rays. However, the final description can also be applied for neutron scattering. Therefore, the characteristics of neutrons are introduced for the techniques which also use neutrons (sections 2.3.2 and 2.3.3).
The electric field vector of a plane electromagnetic wave is

$$\vec{E}(\vec{r}) = \vec{E}_0 \exp[i\vec{k}_i\vec{r}] \tag{2.43}$$

where $\vec{E}_0$ involves the amplitude and the polarization, $\vec{k}_i$ is the wavevector and $\vec{r}$ the position vector. The modulus of the wavevector is $k = \left|\vec{k}_i\right| = 2\pi/\lambda$ with the wavelength

λ. The propagation of an electromagnetic wave is described by the Hemholtz equation

$$\Delta\vec{E}(\vec{r}) + k^2 n^2(\vec{r})\vec{E}(\vec{r}) = 0 \tag{2.44}$$

where $n(\vec{r})$ is the position dependent refractive index.[67] The refractive index is

$$n(\vec{r}) = 1 - \delta(\vec{r}) + \mathrm{i}\beta(\vec{r}) \tag{2.45}$$

with the dispersion

$$\delta(\vec{r}) = \frac{\lambda^2}{2\pi} r_e \rho(\vec{r}) \sum_{j=1}^{N} \frac{f_j^0 + f_j'(E)}{Z} \tag{2.46}$$

and the absorption

$$\beta(\vec{r}) = \frac{\lambda^2}{2\pi} r_e \rho(\vec{r}) \sum_{j=1}^{N} \frac{f_j''(E)}{Z} = \frac{\lambda}{4\pi}\mu(\vec{r}). \tag{2.47}$$

$r_e = e^2/(4\pi\epsilon_0 mc^2)$ is the classical electron radius and $\rho(\vec{r})$ the position dependent electron density.[68] The dispersion $\delta(\vec{r})$ and the absorption $\beta(\vec{r})$ are expressed by the sum over N atoms per unit volume where Z is the number of electrons in the unit volume and $f_j = f_j^0 + f_j'(E) + f_j''(E)$ the complex expression of the forced oscillator strength of the atom j.[67] For small scattering vectors $\vec{q} = \vec{k_f} - \vec{k_i}$ with $\vec{k_i}$ and $\vec{k_f}$ the wavevectors of incident and exiting X-rays, respectively, f_j^0 can be expressed by the number of electrons of the atom j. In the case of X-rays, $n(\vec{r})$ of matter is slightly smaller than 1 and therefore total reflection occurs at small angles.[3] In the following, the refractive index n of a material is assumed to be independent of the position in this material. Therefore, the dispersion and absorption of a material are expressed by δ and β. The angle of total reflection is given by $\alpha_c \approx \sqrt{2\delta}$ as δ is on the order of 10^{-6}. In addition, for small incident and exit angles the influence of periodic crystal structures on the scattered intensity is irrelevant.

The absorption for hard X-rays in soft matter is typically $\beta \approx 10^{-8}$ and therefore plays a minor role for thin films. The penetration depth Λ is in the range of several nicrometers for soft matter. In the case of soft X-rays the absorption is much higher. Its influence on scattering is discussed in section 2.3.4.

In figure 2.21 the principle scattering setup for reflection geometry is shown. The coordinate system is defined by the sample and the incident wavevector $\vec{k_i}$. The scattering plane is spanned by the x- and z-axes. The exiting wavevector $\vec{k_f}$ can be described by the exit out-of-plane angle ψ_f and the exit angle α_f.

[3] For X-rays angles are measured towards the surface.

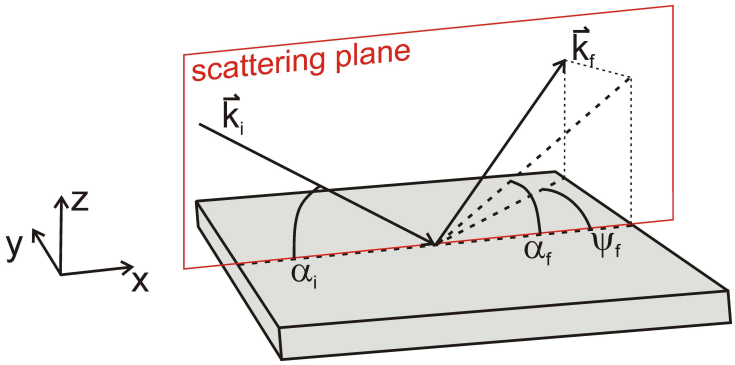

Figure 2.21: *Principle scattering setup in reflection geometry with incident and exiting beam defined by $\vec{k_i}$ and $\vec{k_f}$, respectively. The incident angle α_i and exit angle α_f lie in the scattering plane (red), the out-of plane angle ψ_f in the sample plane.*

2.3.2 Reflectivity

In X-ray reflectivity (XRR) the specular scattering as a function of the incident angle α_i is recorded, i.e. the incident angle is equal to the exit angle and the out-of plane angle is 0. Consequently, the scattering vector $\vec{q}$ is normal to the sample plane and therefore only the q_z component is different from 0.[67]

$$q_z = \frac{4\pi}{\lambda} \sin(\alpha_i) \tag{2.48}$$

In this geometry, the electron density distribution perpendicular to the sample plane, i.e. in z direction, is probed. At a single interface between two materials with different n the incident beam is partly reflected and partly transmitted. The angle of the transmitted beam α_t is given by Snell's law and the ratio of the amplitudes of the reflected and transmitted beams by the Fresnel reflection coefficient r^F and the Fresnel transmission coefficient t^F. The reflectivity and transmission are defined by $R^F = |r^F|^2$ and $T^F = |t^F|^2$.[67]

However, for the analysis of most reflectivity curves a single interface is not sufficient for the description. Typical sample systems are polymer films on substrates whereas the polymer film often reveals an inner layering. Therefore, an approach with N layers each with its refractive index $n_j(z)$ and a thickness d_j is used to model the reflectivity. The confining layers are infinite in thickness and represent in most cases air and the substrate. For the interface between layer j and $j+1$ the ratio of reflectivity and transmission $X_j = R_j/T_j$ is calculated. The final reflectivity is given by R_1. For the calculation of R_1 initially a matrix formalism was used but a more efficient and widely applied recursive algorithm was developed by Parratt.[69]

So far, interfacial roughness was neglected and perfectly smooth interfaces were assumed.

The deviations from a smooth interface are typically expressed by the root mean square roughness σ_{rms} which is defined by

$$\sigma_{rms} = \sqrt{\frac{1}{N_{\sigma_{rms}}} \sum_{i=1}^{N_{\sigma_{rms}}} \Delta z_i^2} \tag{2.49}$$

where $N_{\sigma_{rms}}$ is the number of sampling points along the interface and Δz_i is the deviation from the mean interface at the sampling point i. The roughness can be included in the Parratt algorithm using the Névot-Croce factor expressed by an exponential function to correct the Fresnel reflection coefficients.[70] For roughnesses in the range of the film thickness the correction reaches its limit. A detailed description of the derivation of the X-ray reflectivity scattering theory can be found elsewhere.[67]
In figure 2.22 the calculated reflectivity of a polystyrene (PS) film on a silicon (Si) substrate is shown as an example. At low incident angles α_i and accordingly at small q_z values, the reflectivity is unity as the conditions for total reflection ($\alpha_i < \alpha_c$) are fulfilled. For $\alpha_i = \alpha_c$ the reflectivity shows a minimum and a steep decrease for PS and Si, respectively. The intensity decreases with a q^{-4}-dependence whereas the higher the roughness the steeper the decrease in reflectivity. The oscillations, so called Kiessig-fringes, at higher q_z represent the film thickness. The film thickness d and the periodicity Δq_z of the Kiessig-fringes are related by $d \approx 2\pi/\Delta q_z$.[71] To extract a profile of the refractive index from the reflectivity, the data has to be fitted, typically using a program based on the Parratt algorithm.[69, 72]

Neutrons

Other than X-rays, neutrons do not interact with the electron cloud of atoms or molecules but are scattered by the nuclei. In the case of the reflectivity geometry, the interaction of a neutron with a nucleus can be described by a one-dimensional Schrödinger equation determining the z-component of the neutron wave function $\psi_n(z)$.[73]

$$\left[-\frac{\hbar}{2m_n}\Delta + V(z)\right]\psi_n(z) = E\psi_n(z) \tag{2.50}$$

where $\hbar$ is the reduced Planck's constant, m_n the rest mass of the neutron and $V(z)$ the potential. A similar theory to the X-ray case can be used to describe the neutron reflectivity due to the analogy of the potential $V(z)$ to the Helmholtz equation (2.44). The potential $V(z)$ is

$$V(z) = -\frac{\hbar k_n^2 n_n^2(z)}{2m_n} + E \tag{2.51}$$

where k_n is the wave vector of the plane wave solution of the Schrödinger equation. The main difference to the X-ray case is the derivation of n_n which is the scattering length

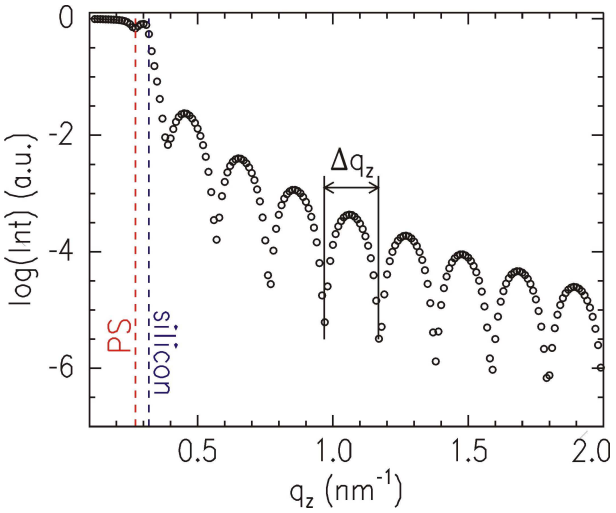

Figure 2.22: *Calculated reflectivity curve of a polystyrene (PS) film on a silicon substrate. The critical q_z values of PS and silicon are highlighted. The distance between the minima of the Kissing fringes is Δq_z.*

density (SLD) for neutrons rather than the refractive index. The SLD for a molecule is defined as

$$n_n = \frac{\sum_k B_k}{v_{mol}} \tag{2.52}$$

with the bound scattering lengths of the atoms in the molecule B_k and the molecular volume v_{mol}.[74] B_k can be expressed as a complex number to account also for absorption.

$$B_j = B'_j + \mathrm{i}B''_j \tag{2.53}$$

To account for the similarities to X-ray, it is common to express the SLD with

$$n_n = 1 - \delta_n + \mathrm{i}\beta_n. \tag{2.54}$$

However, for most elements the neutron absorption β_n is very small and typically neglected in literature.[75] In addition, δ_n is referred to SLD.[76] As neutrons interact with the atomic nucleus, δ_n can be altered by changing the isotope of one atom without changing the chemical properties of that molecule. A typical approach is the exchange of hydrogen atoms with deuterium atoms which is known as deuteration.

2.3.3 Grazing incidence small angle scattering

Besides specular scattering, also diffuse scattering occurs from rough interfaces which is not recorded in a reflectivity experiment. In addition to simple interface roughness as

introduced in section 2.3.2, also regular lateral structures contribute to diffuse scattering. The contribution of regular lateral structures to the diffuse scattering cannot be expressed by simple roughness. Typically, the diffuse scattering of interfaces is recorded in grazing incidence geometry (see figure 2.21 with $\alpha_i < 1$). In such a setup the incident angle α_i is fixed. The scattered intensity is typically recorded with a two-dimensional (2d) detector in which every pixel can be assigned to the out-of-plane angle Ψ_f and the exit angle α_f. The scattering vector $\vec{q}$ is thus given by

$$\vec{q} = \frac{2\pi}{\lambda} \begin{pmatrix} \cos(\Psi_f)\cos(\alpha_f) - \cos(\alpha_i) \\ \sin(\Psi_f)\cos(\alpha_f) \\ \sin(\alpha_i) + \sin(\alpha_f) \end{pmatrix}. \tag{2.55}$$

In the grazing incidence small angle scattering (GISAS) case, the q_x component is negligible as the angles are typically very small.[77]
Commonly the diffuse scattering is treated by the distorted wave Born approximation (DWBA).[78, 79] In this framework, the scattering process is considered as a perturbation of an ideal system. First-order perturbation theory is used to calculate the scattering cross section. Smooth interfaces are therefore used as the ideal system and the roughness and lateral structures are perturbations. The differential cross section is given by

$$\frac{\mathrm{d}\sigma}{\mathrm{d}\Omega} = \frac{C\pi^2}{\lambda^4} \left(1 - n^2\right)^2 \left|t_i^F\right|^2 \left|t_f^F\right|^2 P_{diff}(\vec{q}) \propto P_{diff}(\vec{q}) \tag{2.56}$$

where C is the illuminated surface area, $t_{i,f}^F$ the Fresnel transmission coefficients and $P_{diff}(\vec{q})$ the diffuse scattering factor.[68] The Fresnel transmission coefficients have a maximum for the incident or the exit angle equal to the critical angle of the probed material. This maximum gives rise to the so called Yoneda peak in the scattered intensity in a GISAS experiment which is material sensitive.[80] However, the Fresnel transmission coefficients act only as overall scaling factors and the scattered intensity is proportional to $P_{diff}(\vec{q})$.[81]
To describe a certain GISAS scattering pattern, objects with a certain size as well as an interference function are used. In the approximation of N identical objects with a random orientation, the diffuse scattering factor $P_{diff}(\vec{q})$ is given by

$$P_{diff}(\vec{q}) \propto NS(\vec{q}) \left|F(\vec{q})\right|^2 \tag{2.57}$$

where $S(\vec{q})$ is the interference function describing the spatial arrangement of the objects and $F(\vec{q})$ the object form factor which is the Fourier transformation of the electron density distribution of the object.[82]
In this thesis this approximation is used to analyze the scattering data when only the q_y information is of interest. Thus, just lateral structural information is extracted. This

simplification is typically referred to as effective surface approximation.[77]
For a comprehensive analysis of the 2d scattered intensity, further contributions have to be taken into account. Thus, as modeling objects cylinders are used. To describe the scattering of polymer films, cylinders are the common approach due to the typical rotational isotropy of the investigated samples. To describe the spatial arrangement of the objects, a one-dimensional paracrystal (1DDL) is chosen as the interference function $S(\vec{q})$. In a paracrystal objects are arranged periodically and the deviation of the exact position is increasing with the distance from the origin. Therefore, short-range order rather than long-range order is found. In a 1DDL, the arrangement is independent of the direction in the system, so no two-dimensional ordering appears.[83]
So far, no size distribution of the objects is taken into account. A common approximation is the local monodisperse approximation (LMA) to include different object sizes. The LMA acts on the assumption that in local domains which have the size of the coherence length of the beam only monodisperse objects, i.e. of one size, are found. As a consequence, the overall scattered intensity can be calculated by the sum of the scattered intensity of each of these domains.[73]
The approach discussed above is still not sufficient to describe a GISAS experiment. In the framework of the DWBA, three further contributions which include reflections before and/or after the scattering event have to be included. The final corrected form factor is the sum over all contributions whereas the reflections are expressed by the Fresnel reflection coefficients r^F including roughness corrections.[84] However, this approach only describes scattering at objects arranged on a substrate. In this thesis, mainly polymer blends on a substrate are investigated with GISAS. To analyze these systems, objects embedded in a polymer matrix are used which makes further corrections necessary (see figure 2.23). For data simulation the program IsGISAXS is used.[85]

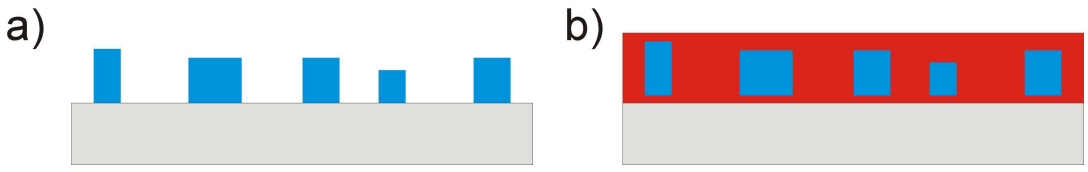

Figure 2.23: *Models for GISAS data analysis: a) Objects (blue) on a substrate (gray) and b) objects (blue) in a matrix (red) on a substrate (gray).*

Neutrons

Similar to the reflectivity experiments, GISAS can also be performed with neutrons. For neutrons the theory detailed above is still applicable. This is because the vectorial propagation equation for X-rays reduces to a Helmholtz equation in the DWBA approach

as polarization effects of the X-rays are negligible for small scattering angles. Due to the similarities of the Helmholtz equation and the Schrödinger equation which describes neutron scattering, the same theory can be used for both, X-rays and neutrons.

2.3.4 Soft X-ray scattering

Soft X-rays are electromagnetic waves in the energy range from 50 to 2000 eV.[86] The propagation of soft X-rays and the refractive index can be described as shown in section 2.3.1. However, compared to hard X-rays and neutrons, the absorption of soft X-rays in matter is much higher. In figure 2.24 the cross-sections of X-rays in carbon as a function of energy is shown. In the case of soft X-rays, the absorption dominates and the incoherent scattering, i.e. inelastic or Compton scattering, is negligible. Consequently, the absorption has a high contribution to the scattering contrast of two materials which can be expressed by the differences of dispersion and absorption of these materials:

$$\Delta\delta^2 + \Delta\beta^2 = (\delta_2 - \delta_1)^2 + (\beta_2 - \beta_1)^2 \tag{2.58}$$

where $\delta_{1,2}$ is the dispersion and $\beta_{1,2}$ the absorption of a material 1 and 2.[86]

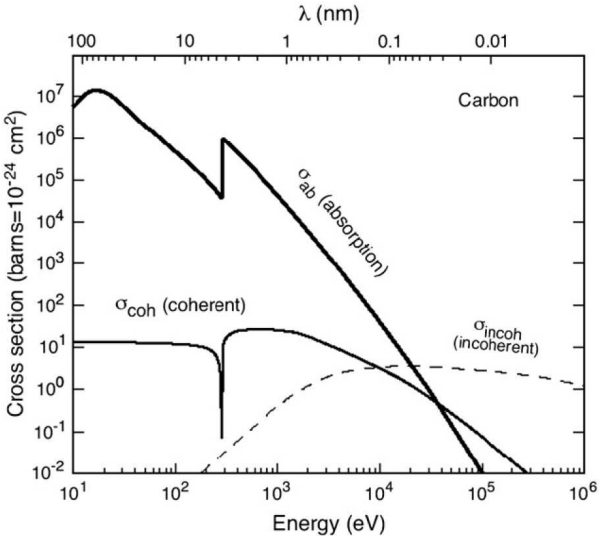

Figure 2.24: *The energy dependent X-ray cross sections for carbon. The coherent, incoherent and absorption cross sections are shown. Figure taken from reference [86].*

Around the absorption edge of an atom (e.g. 285 eV for carbon), the absorption and the dispersion undergo dramatic changes with the X-ray energy (see figure 2.24). These changes can be modeled with a damped forced oscillator in a semi-classical model of atoms. Such an oscillator shows a maximum in amplitude when the natural frequency is

equal to the driving frequency, i.e. in this case the X-ray energy. This resonance results in the term 'resonant scattering' for scattering at the absorption edge. At the absorption edge a core electron is excited into an empty state and therefore this edge is element specific. Above all, also the chemical environment of the atom, i.e. the chemical bonds to other atoms, changes the exact position and shape of the absorption edge. Thus, the energy dependent absorption and dispersion change from molecule to molecule although the building blocks are the same atoms. In the case of resonant soft X-ray scattering (RSoXS), this behavior is used to vary the scattering contrast by changing the X-ray energy.[86]

Soft X-ray near edge X-ray absorption fine structure (NEXAFS) spectroscopy is typically used to obtain the energy dependent absorption $\beta(E)$ and dispersion $\delta(E)$ spectra of organic molecules. In NEXAFS spectroscopy, the absorption $\beta(E)$ of the soft X-rays is measured as a function of energy. For a detailed description refer to [87]. The dispersion $\delta(E)$ is related to the absorption $\beta(E)$ via the Kramers-Kronig relation [88]:

$$\delta(\omega) - 1 = \frac{2}{\pi} P \int_0^\infty \frac{\omega' \beta(\omega')}{\omega'^2 - \omega^2} \mathrm{d}\omega' \tag{2.59}$$

where ω is the frequency and P the Cauchy principal value. To calculate the dispersion $\delta(E)$ correctly, $\beta(E)$ has to be known from 0 to infinity. Thus, $\beta(E)$ is measured around the absorption edge and then extended by tabulated values from Henke et al.[89][4] The dispersion $\delta(E)$ can be negative around the absorption edge with the consequence that no critical reflection angle exists in this range.[86]

By changing the X-ray energy not only the contrast in a scattering experiment can be tuned but also the penetration depth Λ can be altered. Therefore, surface or rather bulk sensitivity can be selected. Λ is defined as the depth at which $I = I_0/\mathrm{e}$ with the initial intensity I_0 is fulfilled. Using Lambert-Beers law $I(z) = I_0 \mathrm{e}^{-\alpha z}$ and the relation for the absorption coefficient $\alpha = 4\pi\beta/\lambda$, the penetration depth is given by

$$\Lambda = \frac{\lambda}{4\pi\beta}. \tag{2.60}$$

The so called information depth is half the penetration depth as in a scattering experiment the X-ray beam has to exit the sample after the scattering event to be detected.

In this thesis, soft X-rays are used in RSoXS experiments in grazing incidence geometry for the first time.[5] The basic setup is in principle identical to the GISAS experiments. However, the DWBA is not sufficient to analyze the grazing incidence RSoXS experiments. The main problem is that the DWBA neglects the influence of polarization.[73] For soft

[4]For the calculation of $\delta(E)$ the program KKcalc from Dr. Benjamin Watts, PSI (Switzerland), was used.

[5]So far no publications on grazing incidence RSoXS experiments are existing.

X-rays the dispersion and absorption depend strongly on the polarization.[90] In addition, so far no theory exists which is dealing with the analysis of grazing incidence RSoXS. In this thesis, the approximation

$$d = \frac{2\pi}{q} \tag{2.61}$$

with the component of the scattering vector q and the corresponding structural length scale d is used to analyze the scattering data.

2.3.5 Diffraction

So far, only scattering methods probing mesoscopic structures are introduced. To investigate crystalline structures, i.e. ordered structures on atomic length scales, X-ray diffraction (XRD) is used. A monochromatic X-ray beam is scattered at different lattice planes in a crystal. The scattered X-rays interfere and give rise to a maximum if the so-called Bragg condition is fulfilled. In figure 2.25 the diffraction of parallel X-rays by two lattice planes is shown. Due to the path difference s of the two rays, constructive and destructive interference occurs depending on the angle θ. For constructive interference Bragg's law has to be fulfilled:[91]

$$n\lambda = 2d_{hkl} \sin\theta \tag{2.62}$$

where d_{hkl} is the distance of the hkl-lattice planes. The definition of the reciprocal lattice can be found in reference [92].

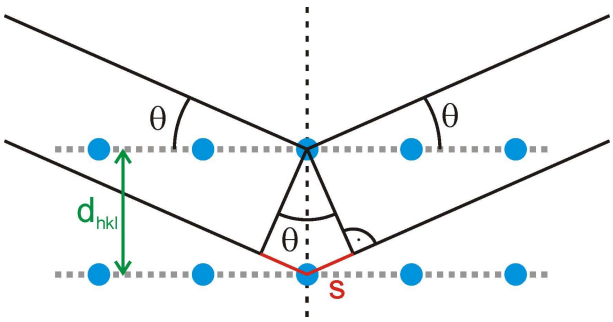

Figure 2.25: *Scattering of X-rays (black solid lines) at two lattice planes (gray doted lines). The distance of the lattice planes d_{hkl} (green), the incident angle θ and the path difference s (red) are shown.*

If the sample consists of an assembly of small crystallites with isotropic orientations it is referred to as a powder and can be investigated with powder diffraction. In powder diffraction, a monochromatic X-ray beam is scattered at the crystallites in the powder

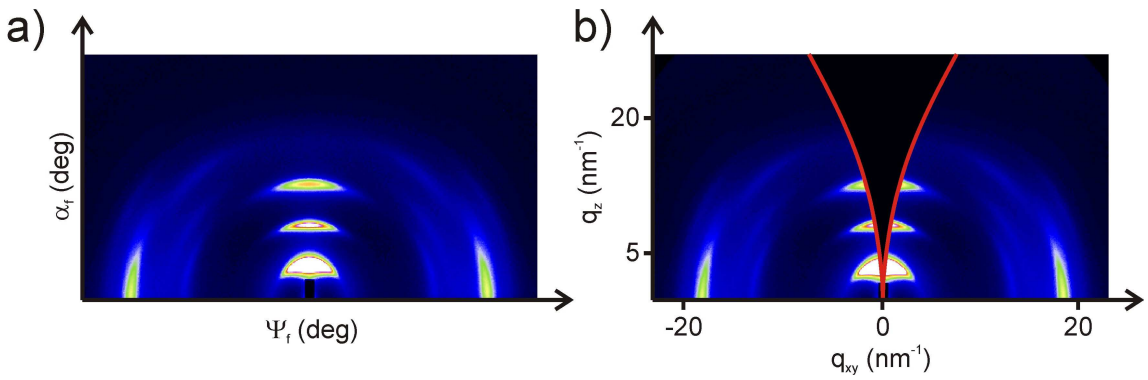

Figure 2.26: *a) 2d GIWAXS data of a crystalline P3HT film as recorded by a 2d detector. b) The same 2d GIWAXS data as a function of q_{xy} and q_z. The inaccessible q-range is highlighted by red borders.*

and gives rise to a circular Bragg peak under an angle of 2θ, a so-called Debye-Scherrer ring. Each Bragg peak refers to a set of hkl-lattice planes which fulfill Bragg's law at this angle. Besides the lattice plane distance d_{hkl}, the spatial dimensions of the crystallite in hkl-direction D_{hkl} can be determined from the width of the corresponding Bragg peak via the Scherrer equation

$$D_{hkl} = \frac{K\lambda}{\Delta(2\theta)\cos\theta_0} \tag{2.63}$$

where K is the Scherrer form factor which is approximately 1, λ the wavelength and $\Delta(2\theta_0)$ the FWHM of the Bragg peak at the angle $2\theta_0$.[91] The transformation of the Scherrer equation from angle in coordinates of the scattering vector $\vec{q}$ results in

$$D_{hkl} = \frac{2\pi}{\Delta q_{hkl}} \tag{2.64}$$

where Δq_{hkl} is the integral linewidth[6] of the Bragg peak.[93, 12] Besides the decreasing crystal size also the distribution of the lattice constant as well as the resolution of the scattering setup broadens the Bragg peaks. Consequently, the crystal size obtained from the Scherrer equation is only a lower limit. In the case of structural investigations of crystalline structures in polymers, wide angle X-ray scattering (WAXS) which is in principal identical with powder diffraction is used.

Grazing incidence wide angle X-ray scattering (GIWAXS) probes the crystalline structures in thin semicrystalline polymer films. The setup is equal to the GISAS setup (Figure 2.21) but recording large scattering angles rather than small angles. The Bragg peaks in the 2d scattering data are detected as a function of $q_{xy} = \sqrt{q_x^2 + q_y^2}$ and q_z with the q-components defined as in equation (2.55). As the incident angle α_i is kept constant, in a GIWAXS experiment not the full q-range is accessible. Figure 2.26 shows the 2d scattering

[6]The integral linewidth is defined as the area of the Bragg peak divided by its amplitude.

data as recorded with a 2d detector (a) and the 2d scattering pattern as a function of q_{xy} and q_z (b). The inaccessible q-range is highlighted by red borders. To measure a Bragg peak with the only non-zero component being q_z, the Bragg peak has to fulfill $\alpha_i = \alpha_f$. However, only for pole figure analysis when one is interested in the azimuthal distribution of a Bragg peak, a measurement under the $\alpha_i = \alpha_f$ condition is necessary. For systems investigated in this thesis one measurement at a fixed α_i is sufficient for the analysis as the main Bragg peaks emerge at small angles. Further intensity corrections have to be applied to account for the flat detector. In the case of a flat detector the distances from the sample to different pixels on the detector vary and therefore an intensity correction is required.[94]

In this thesis, not large polymer crystals but small polymer crystallites embedded in an amorphous polymer matrix are probed (see section 2.2.1). Due to the thin film geometry with substrate interfaces etc., crystallites show preferential orientations. Consequently, Bragg peaks in a GIWAXS experiment are rather peaks than circles like in powder diffraction experiments and therefore the main orientation of the crystallites regarding the substrate can be extracted. Lattice planes oriented parallel and perpendicular to the substrate reveal Bragg peaks in q_z and q_{xy} direction, respectively.

Chapter 3

Characterization methods

The focus of this thesis is to correlate structural properties of polymer-based films for photovoltaic applications with their photovoltaic performance and spectroscopic behavior. Necessary methods to study these systems are spectroscopic and electronic methods (section 3.1) as well as structural characterization techniques (section 3.2). This chapter introduces the instruments and the corresponding data analysis of both characterization fields used in this thesis.

3.1 Spectroscopic and electronic characterization

Spectroscopic characterization with UV/Vis (section 3.1.1) and photoluminescence (section 3.1.2) are used to detect basic material properties like absorption but also to obtain information on charge carrier recombination and molecular ordering. To determine the photovoltaic performance, IV-curves are measured in dark and under solar illumination (section 3.1.3).

3.1.1 UV/Vis spectroscopy

Absorption measurements are carried out with the UV/Vis spectrometer Lambda 35 (PerkinElmer). Two lamps with complementary spectra provide light with a wavelength range from 190 nm to 1100 nm. A deuterium lamp and a halogen lamp are used in the UV and visible wavelength region, respectively. At a wavelength of 326 nm the lamps are automatically switched. An optical grating and a slit system provide a monochromatic light beam. The beam is split before it is transmitted through a sample which typically consists of a polymer film on a transparent substrate, usually a glass slide. The second light beam is used as a reference beam which measures the transmission of the substrate simultaneously. The transmitted light beams are each detected with a photo diode. The

spectra presented in this thesis are recorded with a velocity of 120 nm/min and a slit width of 1 nm. Since the substrate, i.e. the glass slide, absorbs almost all light with a wavelength below 290 nm, the recorded wavelength range is restricted from 290 nm to 1100 nm. The spectrometer is controlled with the software UV-Winlab (PerkinElmer).
The obtained transmitted intensity is the ratio of the sample and the reference, i.e. the pristine substrate. The transmission spectra are converted to the wavelength dependent absorbance $A(\lambda)$ by using Lambert-Beer's law.

$$A(\lambda) = -\log_{10}\left(\frac{I_t(\lambda)}{I_0(\lambda)}\right) = \alpha(\lambda) h \log_{10} \mathrm{e} \tag{3.1}$$

with the initial and transmitted intensities $I_0(\lambda)$ and $I_t(\lambda)$, the linear absorption coefficient $\alpha(\lambda)$ and the film thickness h. For samples with known thicknesses h the linear absorption coefficient $\alpha(\lambda)$ is calculated and presented. Due to the linearity of the absorption coefficient $\alpha(\lambda)$, absorption measurements are also used to determine the thickness of polymer films.
Besides the light absorption also structural information can be extracted from the measured spectra. The position of the main absorption peak of conjugated polymers is a measure for inter- and intramolecular ordering of the conjugated polymer. In addition, vibronic states arise as additional features, such as shoulders or peaks, in the absorption spectra if the conjugated polymer is crystalline. For a detailed analysis in the case of P3HT the weakly coupled H-aggregate model is applied (section 2.1.2).

3.1.2 Photoluminescence spectroscopy

Most conjugated polymers also show photoluminescence (PL). After absorption of light these polymers emit photons at higher wavelength. The fluorescence spectrometer LS55 (PerkinElmer) is used to detect the PL signal of the investigated systems. Therefore, the sample is illuminated with monochromatic light. The light source is a Xenon discharge lamp with a pulse width at half height of < 10 µs. The excitation monochromator (optical grating) with a wavelength range of 200 nm to 800 nm is set to a wavelength at or near the maximum absorption peak of the probed material, e.g. at 485 nm for P3HT. The sample is illuminated and the emitted signal is recorded under an angle of 90°. The emission monochromator (optical grating) has a wavelength range of 200 nm to 900 nm. A red-sensitive Hamamatsu R928 photomultiplier detects the signal. The scan speed is set to 500 nm/min and the slits are adjusted in such a way that the photomultiplier does not saturate. The fluorescence spectrometer is controlled by the software FL WinLab (PerkinElmer).
In contrast to the absorption measurements (section 3.1.1), silicon is chosen as substrate

as glass slides reveal a strong own PL signal due to the containing boron atoms. Because of a missing intensity calibration standard, the measurements are performed directly one after each other to be able to compare different samples.
The PL intensity is a measure for exciton dissociation. If the PL signal of a conjugated polymer blend is quenched compared to the homopolymer, this is an indication for exciton dissociation. The shape of the PL spectrum reveals information on the molecular ordering of conjugated polymers. Shoulder-like features correspond to crystalline portions of the conjugated polymer.

3.1.3 IV characterization

The photovoltaic performance is determined by measuring IV-curves in dark and under illuminated conditions (figure 3.1). The IV-curves are recorded with a Keithley 2400 sourcemeter which is controlled by an internally developed software based on Testpoint v6. The measurements are performed in a voltage range from -1 V to 1 V with increments of 0.01 V and a delay of 0.01 s. For illumination the solar simulator SolarConstant (K. H. Steuernagel Lichttechnik GmbH) with an AM1.5 solar spectrum is used according to standard test conditions. A halide lamp with rare earth metals provides a light spectrum close to the solar spectrum and with a tunable light intensity. If not mentioned otherwise an intensity of 1000 W/cm^2 is used for characterization. The intensity is calibrated with a silicon based calibration solar cell (WPVS-ID 3, ISE). For a homogeneous sample illumination the solar simulator is equipped with a reflector system and a borosilicate filter with integrated diffuser.

The samples are placed 320 mm above the diffuser and only the measured electrode is illuminated to avoid degradation of the other parts of the organic solar cell. The measured

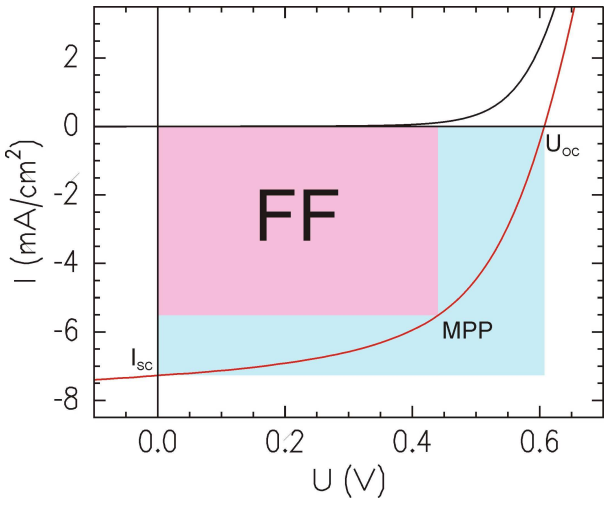

Figure 3.1: *Exemplary IV-curve measured in dark (black solid line) and under illumination (red solid line). The rectangles spanned by MPP (light red) and U_{OC} and I_{SC} (light blue) are depicted.*

current is normalized by the size of the electrode. From the IV-curves under illumination the open circuit voltage U_{OC}, the short circuit current I_{SC} and the fill factor FF are extracted. U_{OC} and I_{SC} are the intercept of the IV-curve with the voltage and the current axes, respectively.
The fill factor is the ratio of the power at the maximum power point P_{MPP} and the product of U_{OC} and I_{SC} and is therefore a measure for the quality of the solar cell, i.e. for recombination and resistive losses. The maximum power point is defined as the point where $P = UI$ is maximum. A descriptive presentation of FF is the ratio of the rectangles spanned by the maximum power point on the one hand (red rectangle in figure 3.1) and the open circuit voltage U_{OC} and the short circuit current I_{SC} on the other hand (blue rectangle in figure 3.1). An ideal solar cell with a high FF reveals an IV-curve with an almost rectangular shape, i.e. the solar cell has a low series and a high parallel resistance.[1] U_{OC} in an organic solar cell mainly depends on the material system used.[16] I_{SC} depends on the charge carrier generation and recombination (see section 2.1).
The solar cell efficiency η is defined as the ratio of the extracted power P_{out} and the power that is put in, P_{in}, in this case the illumination power $P_{AM1.5}$. Then η is given by

$$\eta = \frac{P_{out}}{P_{in}} = \frac{I_{SC}U_{OC}FF}{P_{AM1.5}}. \tag{3.2}$$

3.2 Structural characterization

Structural characterization techniques can be divided in two classes. One class contains real space techniques such as optical microscopy (section 3.2.1) and atomic force microscopy (AFM) (section 3.2.2) which image surface structures directly on different length scales. The second class covers methods which reveal structural information in reciprocal space, such as scattering techniques. Reciprocal information does not give a direct image of the probed structure but contains averaged information on length scales and form factors. In this section reflectivity (section 3.2.3) and grazing incidence scattering techniques (section 3.2.4) using X-rays and neutrons are introduced. Furthermore, near edge X-ray absorption fine structure (NEXAFS) spectroscopy is presented to obtain the refractive index of polymers in the soft X-ray regime.

3.2.1 Optical microscopy

Optical microscopy is used for quality assurance of the sample preparation, for determination of the electrode size of solar cells and for characterization of structures in the

[1] The series and parallel resistances can be obtained from the slopes of the IV-curve at the intercepts with the x-axis and the y-axis, respectively.

micrometer range. An Axiolab A microscope (Carl Zeiss) in combination with a PixeLink USB Capture BE 2.6 CCD camera and five different objectives with magnifications from 1.25× to 100× are used. The recorded images have a size of 1280×1024 pixels. At a magnification of 100× one pixel is equivalent to 80 nm. However, the actual resolution is 570 nm at this magnification for a wavelength $\lambda = 700$ nm.

3.2.2 Atomic force microscopy

The atomic force microscopy (AFM) Autoprobe CP Research (Veeco Metrology Group) is used to probe the topography of thin polymer films on the nanometer scale. A gold covered, conical shaped silicon tip with a curvature radius of 10 nm (Ultralever canitlevers) is mounted on the bottom side of a triangular silicon cantilever with a force constant of 2.1 N/m. Its resonance frequency is 80 kHz. When the tip is approaching the sample surface the cantilever deflects due to forces between the tip and the surface. A laser is focused on the top side of the cantilever and reflected to a multiple segment photo diode which detects the cantilever deflection.
By recording force-distance curves the mechanical properties of the sample surface on nanoscale are probed. However, in this thesis AFM is used to probe the topography by scanning the tip over the sample surface. Therefore, the tip is excited by a piezoelectric drive with a frequency ω and the sample is moved horizontally below the tip at a sample-tip distance below 100 nm. The changes in amplitude, frequency and phase of the cantilever are detected and a feedback software controls the sample holder to keep the sample-tip distance constant. Furthermore, the software records these changes and calculates topography and phase images.
It is assumed that the sample-tip potential follows a simple Lennard-Jones potential with a short range repulsive and a long range attractive part. Depending on the sample-tip distance three different scanning modes exist: the contact, tapping and non-contact mode. In this thesis the tapping mode is chosen as the operating mode which is working at large distance and therefore in the attractive regime of the potential. The excitation frequency is set above the resonant frequency corresponding to non-contact mode conditions. But, since the tip is still repeatedly touching the surface, the measurement is performed under tapping conditions. The topography image is obtained by keeping the amplitude of the cantilever constant.
The images are recorded with sizes from 1×1 µm up to 20×20 µm. Every image consists of 256 line scans which are collected to form a 2d image. To obtain representative information every sample is measured at several positions. For a quantitative analysis the rms-roughness (equation (2.49)) and the power spectral density (PSD) are determined.[95] For this purpose a Fourier transformation of the 2d images is carried out and radially av-

eraged. The PSD curves of different scan sizes of one sample surface are merged to one master curve. The PSD master curve exhibits lateral, characteristic structures of the sample surface in reciprocal space and is therefore suitable to be directly compared with scattering data.[96]

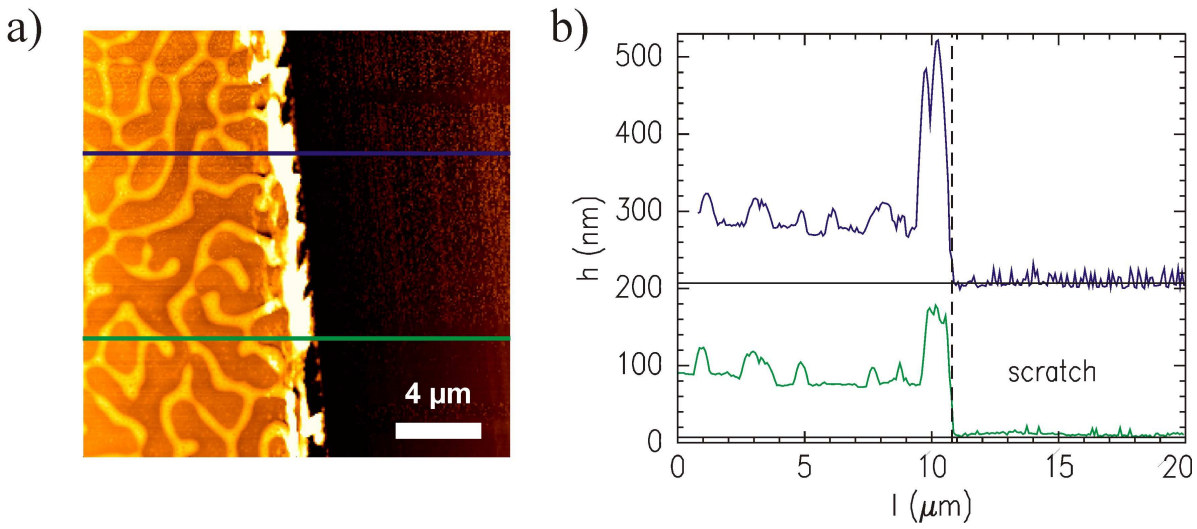

Figure 3.2: *a) Exemplary, scratched AFM image (20 × 20 μm^2) of a polymer blend with pronounced surface structures. The positions at which the line cuts are taken are highlighted with blue and green solid lines. b) The corresponding line cuts. The solid lines represent the substrate surface and the dashed line the edge of the scratch.*

For polymer films with pronounced surface structures AFM is used to determine the film thickness which cannot be determined by scattering techniques due to the high surface roughness. To measure the film thickness, the polymer film is scratched with a needle in such a way that the polymer is fully removed while the substrate is not harmed. Typically this is unproblematic since the substrate is much harder than the polymer film. The AFM image is taken at the edge of the scratch to probe the polymer surface and the substrate in one run. In figure 3.2a an AFM image of such a scratch is shown. To determine the film thickness, line cuts perpendicular to the scratch are performed (figure 3.2b). The film thickness is obtained by the difference in height of the polymer surface and the substrate. Special attention has to be paid to the correct flattening of the image to avoid deviations from the true film thickness.

3.2.3 Reflectivity

Reflectivity measurements with X-rays and neutrons are performed to reveal the thickness, surface roughness and the vertical material composition of thin films. The theoretical

description can be found in section 2.3.2.
The analyses for both X-ray and neutron reflectivity curves are performed with the software Parratt32 version 1.6.0 using the Parratt algorithm.[72, 69] Parratt32 calculates the reflectivity from an initially assumed refractive index profile and compares the calculated curve with the measured curve. Iteratively, the refractive index profile is altered until a fit to the data is obtained. The final refractive index profile is transformed to the electron density profile from which a vertical material distribution is evaluated. Besides the material distribution also the film thickness and the roughness are obtained from the fitting.
For better illustration the vertical material profiles of two component systems are translated into a gray scale code. The gray scale code follows a linear dependence in which black corresponds to 100% of one component and white to 100% of the other component. The corresponding software code (Visual basic) can be found in reference [97].

3.2.3.1 X-ray reflectivity (XRR)

The XRR experiments are performed at the diffractometer D 5000 (Siemens) at the chair E21 of Professor Böni. The laboratory X-ray source uses a Cu target with a voltage of 40 kV and a current of 30 mA. The X-ray beam with a wavelength of λ=0.154 nm (Cu K_α line) is collimated by a slit system and focused onto the sample. The sample is mounted on a vacuum stage and a knife edge collimator which is directly placed above the sample defines the illuminated surface area (beam footprint). The reflected beam passes a monochromator and is detected with a scintillation counter. The XRR curve is measured in three angular regimes. For small angles (typically up to about 0.5°) an automatic beam absorber is used to prevent the detector from saturation. At higher angles the beam absorber is removed. The accumulation time per data point increases from regime to regime. Typically the incident angle α_i is varied from 0° to 6°. The reflected intensity is recorded as a function of α_i. The three curves are merged and normalized before fitting.

3.2.3.2 Neutron reflectivity (NR)

For special sample systems NR is used to detect the vertical material profile. In this thesis NR experiments are performed at the REFSANS beamline at the neutron source FRM2.[98, 99] In contrast to reflectivity setups using a monochromatic beam, at REFSANS a white beam with the time-of-flight (TOF) mode is applied. To measure a reflectivity curve at a TOF instrument, not the incident angle is changed but neutrons with different wavelengths are used. As neutrons with different wavelength have different velocities the wavelength is determined by measuring the time which has elapsed from the point where the neutrons leave the chopper system to the point at which the neutrons arrive at the detector.

For the reflectivity curves measured at REFSANS neutrons with wavelengths from 0.22 nm to 2.2 nm are used. A 2d ^{3}He-detector detects the neutrons. To obtain a reflectivity curve up to q_z =1.5 nm^{-1}, measurements at three different incident angles α_i, 0.6°, 1.6° and 2.8°, are performed and the single curves are merged to form a master curve. $\Delta\lambda/\lambda$ is set to 1.5% for the first two angles and to 10% for the last angle. The data treatment before fitting is carried out with the programs Nestor Standard Edition (GKSS) and DART (GKSS).

3.2.4 Grazing incidence scattering

To detect the diffuse scattering of thin film samples, typically grazing incidence scattering (GIS) methods are applied. In GIS the sample-detector distance (SDD) defines the scattering angle and therefore the resolvable length scales. In figure 3.3 the principle setup of a GIS experiment is shown. Structures on molecular length scales (0.2 nm) up to structures in the micrometer range can be resolved. The theoretical background of GIS for X-rays and neutrons is introduced in sections 2.3.5 and 2.3.3.

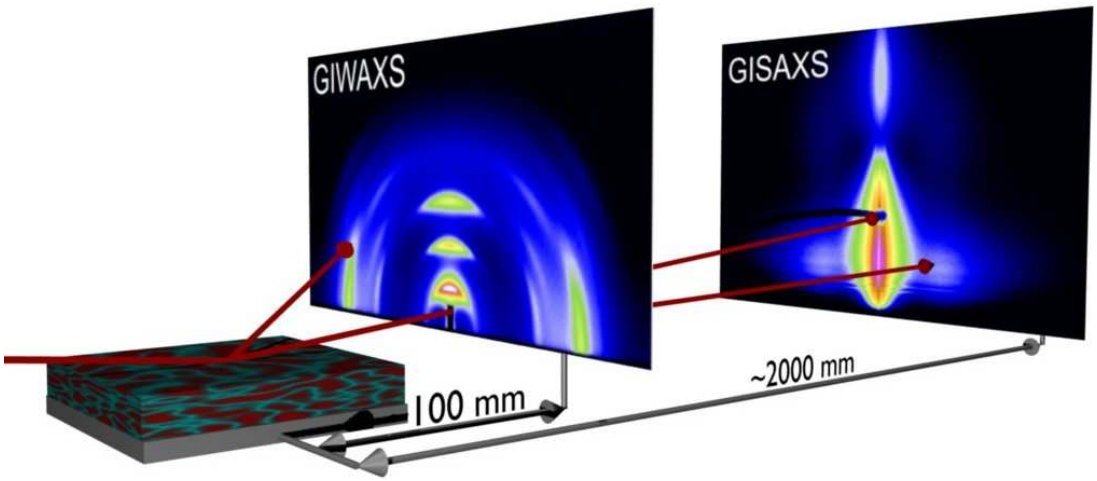

Figure 3.3: *Schematic grazing incidence scattering setup. The X-ray beam (red) impinges on a sample. The 2d detector records the scattered intensity. Depending on the sample-detector distance different length scales are resolved. Exemplary scattering data for grazing incidence wide angle X-ray scattering (GIWAXS) and grazing incidence small angle X-ray scattering (GISAXS) setups are shown.*

3.2.4.1 Grazing incidence small angle X-ray scattering (GISAXS)

GISAXS experiments are performed at the synchrotron beamline BW4 of the DORISIII storage ring (HASYLAB at DESY) in Hamburg. The wavelength is set to 0.138 nm and the SDD to about 200 cm resulting in resolvable length scales from 5 nm to 1.5 µm. The

scattered data is recorded with a MARCCD detector (2048×2048 pixel) with a pixel size of 79.1 µm. The direct and specular beams are blocked by two point like beamstops to avoid detector damage. An assembly of beryllium compound refractive lenses focuses the beam to 30x40 µm^2 at the sample position.[100] The incident angle is typically set to about 0.4° which is above the critical angle of the investigated materials and assures a full penetration of the polymer film.[81]

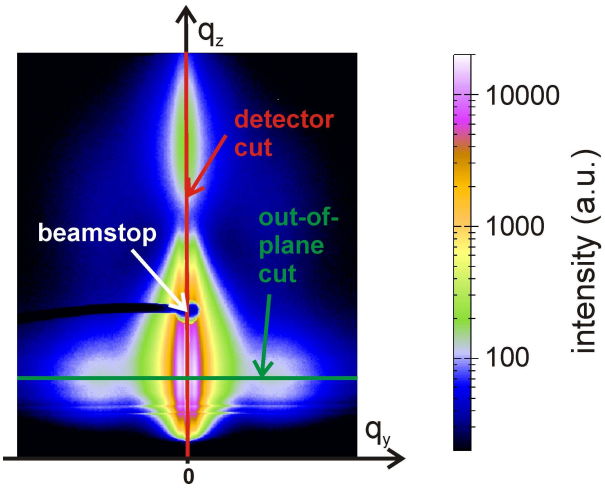

Figure 3.4: *Exemplary 2d GISAXS data with the positions highlighted at which the detector cut (red) and the out-of-plane cut (green) are typically taken. The specular beam stop is marked.*

For the analysis of the GISAXS data horizontal (out-of-plane cuts) and vertical (detector cuts) cuts are examined with the detector cuts and the out-of-plane cuts taken at $q_y = 0$ nm^{-1} and at the critical angle of the investigated materials, respectively (figure 3.4). The cuts are fitted concerning the effective surface approximation or with IsGISAXS within the DWBA (see section 2.3.3).

Effective surface approximation

The effective surface approximation is used to fit out-of-plane cuts.[77] Detector cuts cannot be fitted with the effective surface approximation. The data is fitted by two Lorentzian functions where the positions give the structure sizes using the relation $d = 2\pi q_y$ and the width the distribution or polydispersity of the structure sizes. In addition, the effective surface approximation includes a constant background and a resolution function which is a Lorentzian function with position zero. Although this approximation is a mathematical approach and all correlations between interfaces are neglected, the resulting length scales are a good approximation of the real system.

IsGISAXS

For a 2d simulation of GISAS data or fitting of both cuts, i.e. out-of-plane and detector

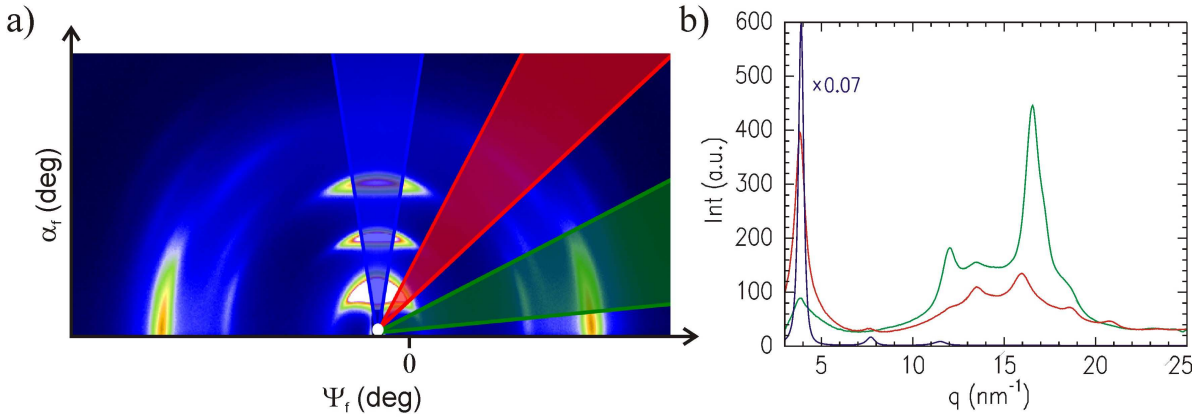

Figure 3.5: *a) Exemplary 2d GIWAXS data of P3HT with highlighted integration areas. b) The corresponding sector integrals. The blue sector integral is multiplied by 0.07 for clarity of presentation.*

cuts, the program IsGISAXS is used.[85] Therefore, a simplified model with objects embedded in a film supported by a substrate is chosen. As the investigated systems have rotational symmetry regarding the normal of the sample surface, cylinders are a good estimation as object type. Each cylinder is defined by its radius and height including their respective distributions. As interference function, i.e. structure factor, a 1d paracrystal (1DDL) is applied which includes a structure size and its distribution (section 2.3.3). Up to three different objects with a certain probability are used to fit the GISAS data in this thesis. Further, parameters are the refractive indices of the substrate, film and objects, and the film thickness.

3.2.4.2 Grazing incidence wide angle X-ray scattering (GIWAXS)

A molecular resolution (from 0.2 nm to 6 nm) is achieved by GIWAXS experiments with a typical SDD on the order of 10 cm. The complete GISAXS signal is blocked by a rod-like beamstop. The incident angle is set to 0.2°. The alignment procedure is described elsewhere.[101] For background subtraction a bare silicon or glass substrate is measured. To extract information on lattice constants, crystal sizes and crystallinity, sector integrals are taken from the 2d scattering images. The resulting Bragg peaks are fitted with Gaussian functions.

For the experiments performed at BW4 the detector, wavelength and focusing setup are identical to the GISAXS setup described above.

Further GIWAXS experiments are performed at the beamline 7.3.3 of the advanced light source (ALS) at the LBNL in Berkeley (USA). A wavelength of 0.124 nm is chosen there. The scattered intensity is recorded by a four quadrant Quantum CCD X-ray detector (ADSC) with 2304×2304 pixels of size 81.6×81.6 µm^2.

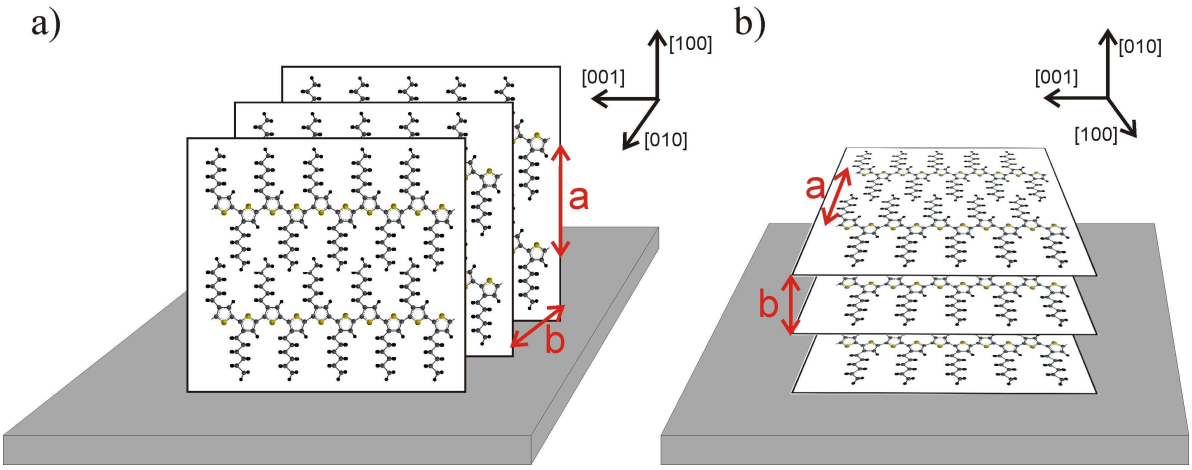

Figure 3.6: *Schematic representation of P3HT crystals in a) edge-on and b) face-on orientation with respect to the substrate. The lattice constants a and b as well as the crystal directions [100], [010] and [001] are depicted.*

For a quantitative analysis sector integrals are taken. In figure 3.5a the 2d GIWAXS data of a crystalline P3HT film is shown. The integration areas for three different sector integrals are highlighted. The corresponding sector integrals are presented in figure 3.5b. From the position and the width of the Bragg reflections, i.e. the peaks in the sector integrals, the lattice constants and the crystal sizes can be extracted, respectively (section 2.3.5). The GIWAXS data presented in this thesis exhibit only Bragg reflections in horizontal and vertical direction. Thus, only sector integrals in these directions are shown. From the intensity ratio the main orientation of the polymer crystals regarding the substrate is extracted.

In figure 3.6 the most common orientations, edge-on and face-on orientation, are depicted for P3HT. P3HT forms so-called conjugation planes depicted as white sheets in figure 3.6. The crystal directions [100], [010] and [001] correspond to the directions along the side chains, perpendicular to the conjugation planes and along the polymer backbone, respectively. The distance of the polymer backbones in the conjugation plane is the lattice constant a. The conjugation planes are separated by the lattice constant b. For polymers other than P3HT investigated in this thesis, an equivalent corresponding notation is used.

3.2.4.3 Grazing incidence small angle neutron scattering (GISANS)

GISANS experiments are carried out at the large dynamic range small-angle diffractometer D22 at the Institute Laue-Langevin (ILL) in Grenoble. The wavelength is set to 0.6 nm with a resolution of $\Delta\lambda/\lambda$ =10%. The collimation length and the SDD are chosen to be 17.6 m and 11.2 m, respectively. Therefore, structural length scales from 15 nm to

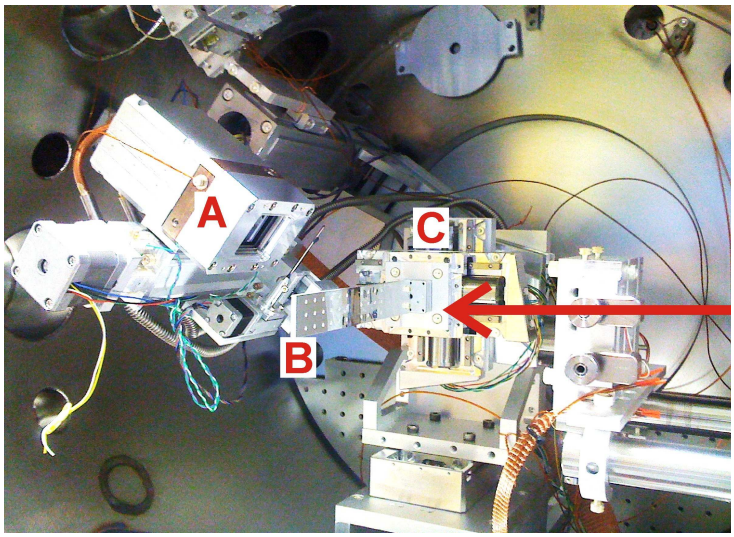

Figure 3.7: *Photo of the vacuum chamber at the beamline 11.0.1.2 of the ALS with detector (A), sample holder (B) and sample goniometer (C). The incident X-ray beam is depicted as the red arrow.[103]*

800 nm are resolvable. The signal is recorded with a ^{3}He large area multidetector (1 m^2) with a pixel size of 8×8 mm^2.[102]
The GISANS data are fitted using the effective surface approximation or IsGISAXS (section 3.2.4.1). For the IsGISAXS the scattering length densities (SLD) δ_n have to be converted into the corresponding refractive indices δ using the following equation:

$$\delta = \frac{\lambda^2}{2\pi}\delta_n \tag{3.3}$$

with the wavelength λ. In addition, the wavelength distribution of the neutrons has to be taken into account.

3.2.4.4 Grazing incidence resonant soft X-ray scattering (GI-RSoXS)

GISAXS measurements with soft X-rays (GI-RSoXS) are performed at the synchrotron beamline 11.0.1.2 of the ALS.[103] Due to the high absorption of soft X-rays in air, the full setup, including sample and detector, is kept in high vacuum (figure 3.7). The energy of the X-rays is altered from 280 eV to 320 eV which corresponds to wavelengths from 4.4 nm to 3.9 nm. The intensity of the primary beam as a function of the energy is plotted in figure 3.8. The minimum in intensity at the absorption edge of carbon (285 eV) is due to the carbon contamination of the optics in the beam path. Due to the long wavelengths of soft X-rays a SDD of 18.5 cm is sufficient to probe length scales in the range from 21 nm to more than 2 µm. An in-vacuum CCD camera with 2048×2048 pixel (pixel size of 13 × 13 µm^2) is used as detector. Since the whole setup is installed in a vacuum

chamber several samples are mounted at once to avoid extensive venting and pumping of the chamber. The measuring time of one scattering pattern is on the order of 1 s or less.[86]

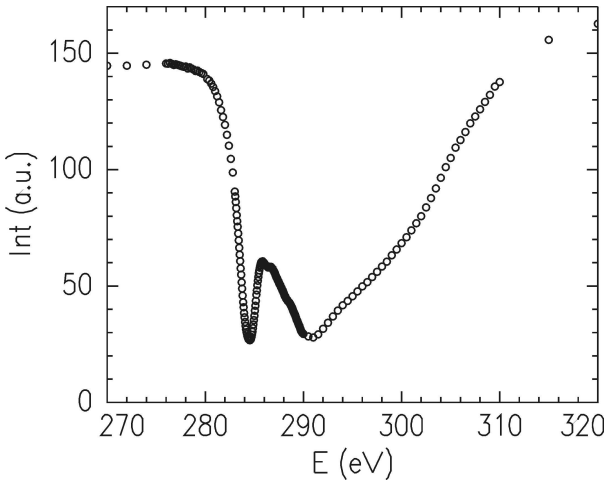

Figure 3.8: *Energy dependent X-ray intensity at the beamline 11.0.1.2 of the Advanced Light Source (ALS) at the LBNL in Berkeley (USA).*

3.2.5 Near edge X-ray absorption fine structure spectroscopy

To obtain the refractive index of polymers for electromagnetic radiation near the absorption edge (section 2.3.4), near edge X-ray absorption fine structure (NEXAFS) spectra of polymer films are measured at the synchrotron beamline 11.0.1.2.[103] The sample environment is identical to the GI-RSoXS setup described above.

NEXAFS spectra are typically obtained in two ways, either by transmission or by electron yield measurements. In this thesis, the NEXAFS spectra are obtained by the latter method. Thus, the sample is connected to a picoammeter and secondary electrons created by Auger electrons are detected. In figure 3.9 the Auger-effect is shown schematically. When soft X-rays are absorbed, a core electron is excited above the vacuum level and a hole remains. An electron from a higher shell can now fill this core hole. Due to the energy gain, either a photon is emitted or another electron is excited above the vacuum level by a non-radiative transition. The latter process is the so-called Auger decay and the excited electron is an Auger-electron. For soft X-rays the Auger decay is the dominant process to fill the core holes. The Auger electrons create secondary electrons which are then detected in a electron yield measurement. The resulting X-ray energy dependent current is a direct measure for the absorption process.[104] The polymer films are prepared on SiN membranes and measured in transmission geometry. The spectra are corrected for the signal of the pure substrate.[87]

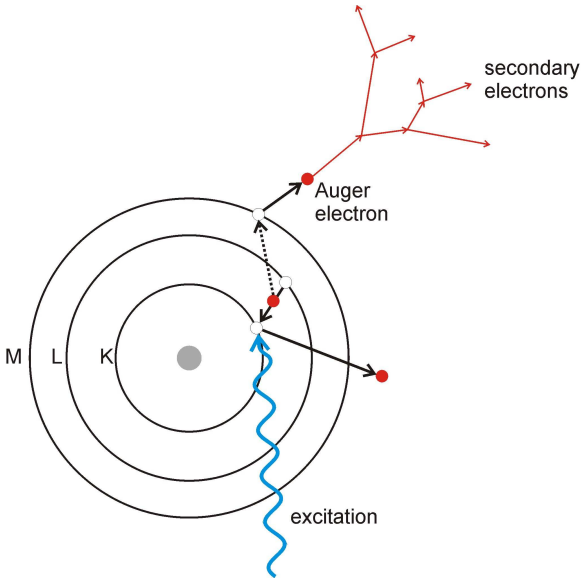

Figure 3.9: *Schematic presentation of the Auger-effect. Electrons and nucleus are depicted as red and gray spheres, respectively. The K, L and M shells are depicted. Holes are shown as open circles. Electron motions, radiative and non-radiative transitions are marked as solid, wavy and dotted arrows, respectively. The creation of secondary electrons is pictured with red arrows.*

Besides the determination of the refractive index, NEXAFS spectra are also used in this thesis to obtain the exact composition of blended polymer films.

Chapter 4

Sample preparation

The preparation of samples which are investigated in this thesis is described in this chapter. The reproducibility and comparability of the sample preparation is of fundamental importance. First, the examined materials (section 4.1) and the substrate cleaning methods including different substrate types (section 4.2) are introduced. In section 4.3 the applied coating techniques of polymer solutions and metal electrodes are presented. Most systems require annealing steps as post production treatment which are subsequently described (section 4.4). Finally, the preparation steps for an organic solar cell are specified (section 4.5).

4.1 Materials

The investigated materials can be divided into different groups: electron donors and acceptors, block copolymers and additives. As electron donors two polythiophene derivatives were selected whereas as electron acceptors two cyano derivatives of poly(p-phenylene-vinylene) (PPV) and a polyfluorene copolymer as well as a derivative of the buckminster fullerene were used. Furthermore a photoactive diblock copolymer was investigated. Nanoparticles, dyes and a standard non-conducting homopolymer were applied as additives. For the solar cell preparation additional polymers were needed as a blocking layer. The detailed parameters for all materials such as molecular weight M_W, polydispersity d_p, purity and the supplier are listed in table 4.1.

Electron donor

The semiconducting polymers poly(3-hexylthiophene-2,5-diyl) (P3HT) and poly(3-octylthiophene-2,5-diyl) (P3OT) consist of a backbone of thiophene rings with an alkyl side chain and are typically used as electron donors in organic solar cells. Both polymers differ just in the length of the alkyl side chain whereas the side chain of P3HT and P3OT consist

material	supplier	M_n	M_w	p_d	purity
P3HT	American Dye Source Inc.	16470	28000	1.7	n.a.
P3HT	Rieke Metals Inc.	n.a.	50000	n.a.	>99%
P3OT	Sigma Aldrich	34000	n.a.	n.a.	n.a.
CN-PPV	Sigma Aldrich	n.a.	29000[a]	n.a.	n.a.
MEH-CN-PPV	Sigma Aldrich	n.a.	25000[a]	n.a.	n.a.
F8TBT	CDT Inc.	n.a.	54000	n.a.	n.a.
PCBM	Nano-C Inc.	910.88	n.a.	n.a.	98.5%
d5-PCBM	American Dye Source Inc.	915.91	n.a.	n.a.	99.5%
P(S-b-PP)	Polymer Source Inc.	5700-2900	n.a.	1.14	n.a.
d8-PS	Polymer Source Inc.	2200	2400	1.07	n.a.
OPc	Sigma Aldrich	1091.38	n.a.	n.a.	95%
PEDOT:PSS	Sigma Aldrich	n.a.	n.a.	n.a.	n.a.

Table 4.1: *Known details such as the supplier, the molecular weights M_n and M_w, the polydispersity p_d and the purity of the organic compounds used in this thesis. The molecular weight is given in g/mol. [a] The molecular weight of CN-PPV and MEH-CN-PPV were determined in this thesis via the spin coating method described in section 4.3. CDT Inc. stands for Cambridge Display Technology Inc.*

of 6 and 8 carbon atoms, respectively. The difference in the side chain alters not only the electronic structure but also the solubility of the polymers. Both polymers are soluble in organic solvents. In figure 4.1 the molecular structures are shown.

Electron acceptor

As electron acceptors semiconducting polymers and a small organic molecule were used. Poly(2,5-di(hexyloxy)cyanoterephthalyliden) (CN-PPV) and poly(5-(2-(ethylhexyloxy)-2-methoxy-cyanoterephthalyliden) (MEH-CN-PPV) are two different derivatives of PPV. The backbone is altered by a cyano group which influences the electronic band structure and results in electron accepting polymers which are used in organic photovoltaics.[105, 106, 107] Both polymers differ only in the attached side chains whereas linear and branched side chains are attached to the backbones of CN-PPV and MEH-CN-PPV, respectively. Additionally, the polyfluorene copolymer poly((9,9-dioctylfluorene)-2,7-diyl-alt-[4,7-bis(3-hexylthien-5-yl)-2,1,3-benzothiadiazole]-2',2"-diyl) (F8TBT) is used as electron acceptor. These electron acceptors are soluble in organic solvents (figure 4.1).
In figure 4.2 the molecular structure of [6,6]-phenyl-C_{61}-butyric acid methyl ester, a derivative of the buckminster fullerene, is depicted. Due to the attached side chain PCBM is soluble in organic solvents. In combination with the electron donor P3HT, PCBM is the most widely investigated material system used in organic photovoltaics.

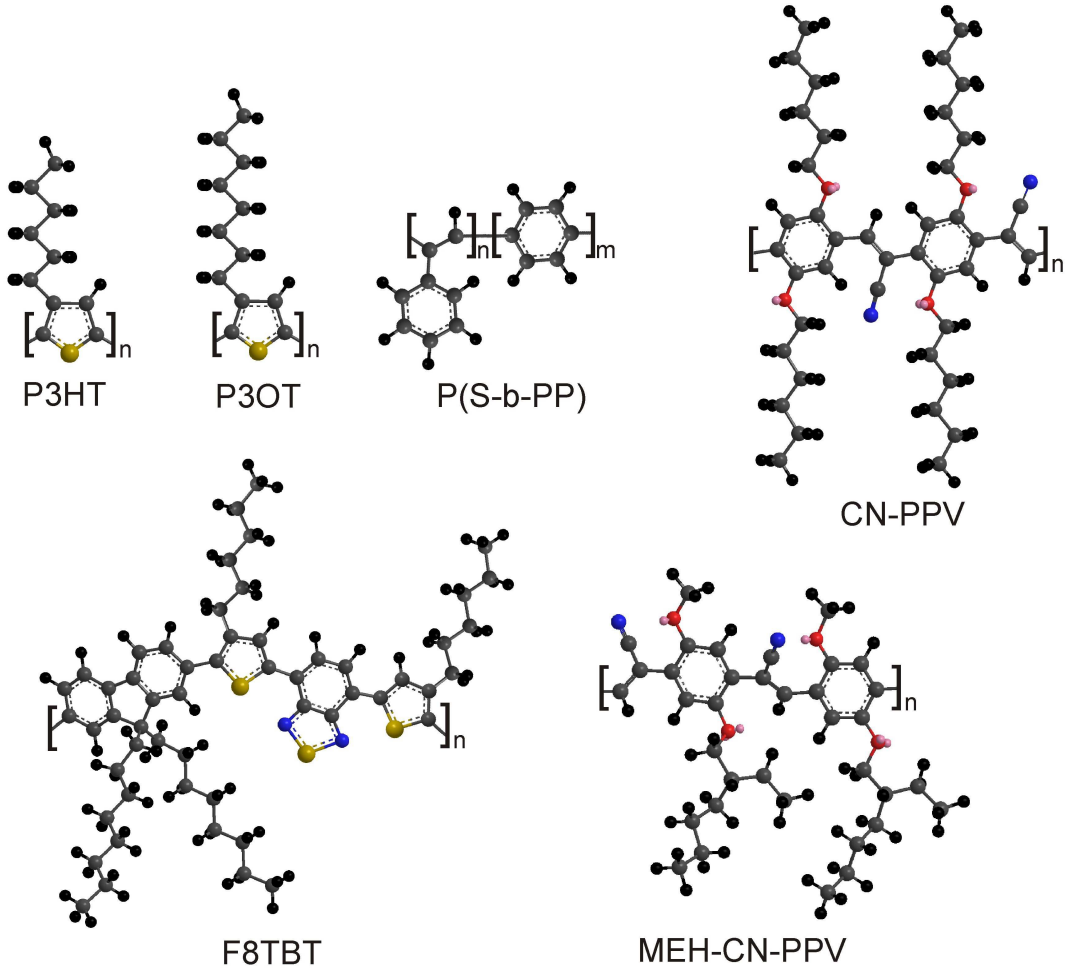

Figure 4.1: *The chemical structure of the photoactive polymers used in this thesis. The atoms are depicted with different colors: hydrogen (black), carbon (grey), nitrogen (blue), oxygen (red) and sulfur (yellow).*

Block copolymer

The photoactive diblock copolymer poly(styrene-b-para-phenylene) P(S-b-PP) is a so called rod-coil like copolymer. One block consists of the standard coil-like polymer polystyrene (PS). The photoactive block is the rod-like polymer poly(para-phenylene) (PPP) which is built up of phenyl rings with no side chains. In contrast to the insoluble homopolymer PPP the block copolymer P(S-b-PP) is soluble in organic solvents. The chemical structure is displayed in figure 4.1.

Additives

To modify the morphology as well as other properties such as the absorption of thin poly-

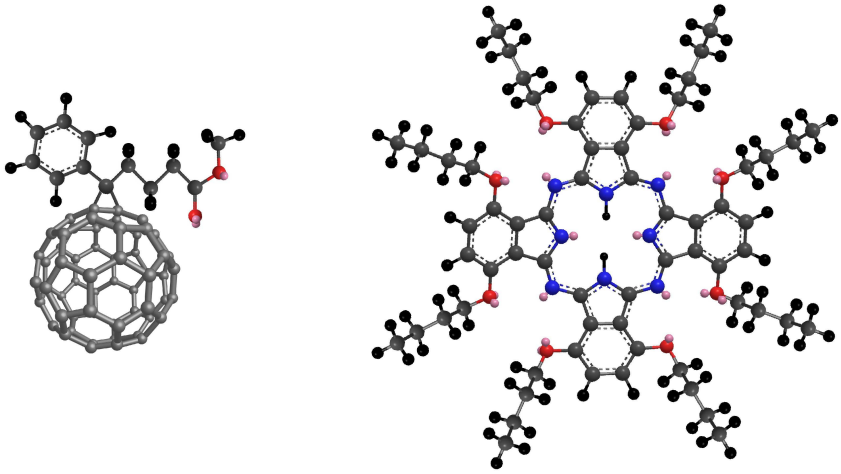

Figure 4.2: *The chemical structure of PCBM (left) and of the dye OPc (right).*

mer films, additives can be introduced in a system. In this work, three different types of additives were used, namely dyes, polymers and nanoparticles.
The dye 1,4,8,11,15,18,22,25-octabutoxy-29H,31H-phthalocyanine (OPc) is a derviative of phthalocyanine (figure 4.2). Phthalocyanines are typically used in dye sensitized solar cells to absorb light.[108] In this thesis, OPC was utilized to extend the absorption range of an organic solar cell to higher wavelengths.
To modify the structure of the block copolymer P(S-b-PP), deuterated polystyrene (d8-PS) was selected as an additive. The deuteration improved the contrast when the system was investigated with neutron scattering techniques (figure 4.1).
Besides organic additives, also inorganic materials can be incorporated in organic systems. A typical approach is to employ nanoparticles as their length scales are on the same order of magnitude as those of the polymer structures. In this work, titania nanoparticles[1] are used. The anatase titania nanoparticles have a size of 10 nm and the surface is modified with 4-tert-butylcatechol (TBC).

Blocking layer

Besides the active layer and the electrode materials, at least one additional layer is necessary to prepare organic solar cells with a reasonable performance. This additional layer is typically an electron blocking layer which prevents short cuts in organic solar cells. The most prominent blocking layer is a mixture of poly(3,4-ethylenedioxythiophene) (PEDOT) and poly(styrenesulfonate) (PSS) (figure 4.3) which is used for organic solar cell prepara-

[1]The nanoparticles were synthesized by Johann Szeifert from the Bein group at the LMU München.[109]

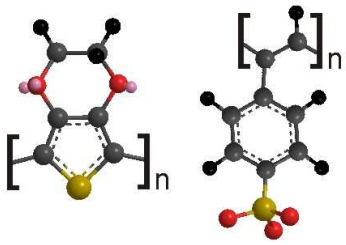

Figure 4.3: *The chemical structure of the single components of the electron blocking material, PEDOT (left) and PSS (right).*

tion in this work. The material mixture is commercially available as a dispersion in water with a concentration of 0.5 wt% (PEDOT) and 0.8 wt% (PSS) (Sigma Aldrich, product number 483095). The conductivity is given as 1 S/cm.

4.2 Substrates

Depending on the investigated material system and the investigation technique different types of substrates and treatments are required for the thin polymer film preparation. In this thesis, for most systems glass and silicon substrates were used. The glass substrates with a size of $3.6 \times 7.6 \times 1$ mm^3 were purchased from Carl Roth GmbH and fulfill the requirements of ISO 8037/1. The p-doped silicon substrates were purchased from Si-Mat as wafers with a diameter of 100 mm and a thickness of (525 ± 25) μm. Glass as well as silicon substrates were cut in sizes ranging from 20×20 mm^2 to 70×70 mm^2 according to the required sample size. In the case of glass slides a glass cutter with a hard metal rosette was used to scratch the back side of the substrate. For silicon substrates a diamond cutter was used for scratching. Afterwards, both types of substrates were carefully broken over a sharp edge avoiding to scratch the front side and bend the substrate.
In the case of photoelectric characterization, transparent conducting substrates are required. Therefore, indium tin oxide (ITO) coated glass slides (Solems S. A.) with a size of 2.2×2.2 mm^2 were selected. In addition, fluorine doped tin oxide (FTO) coated on sodalime glass (TCO10-10, Solaronix SA), which are transparent conducting substrates, were chosen to compare the influence of different types of substrates on the morphology. All substrates cannot be used as received from the supplier as the surface properties are undefined. To obtain a controllable substrate surface the substrates have to undergo a defined cleaning procedure. Glass and silicon substrates were cleaned using an acidic bath based on sulfuric acid or hydrofluoric acid (HF). In this thesis, the expression acidic cleaning is used for the method based on sulfuric acid. ITO and FTO coated substrates were

chemical	amount
H_2O (DI)	22.5 ml
H_2O_2 (30 %)	35 ml
H_2SO_4 (96 %)	82.5 ml

Table 4.2: *The composition of the acid bath used for substrate cleaning.[111]*

cleaned with different solvents since these substrates are unstable against acid. Before cleaning, the ITO substrates these had to be patterned when used for organic solar cell preparation.

Acidic cleaning

The precut substrates were blown clear with dry oil-free nitrogen to remove dust particles. Afterwards, the substrates were placed in a sample holder which was immersed into an acid bath for 15 min. The acid bath was kept at a temperature of 80 °C. The composition of the acid bath is shown in Table 4.2. Thereafter, the substrates were transferred to a bath of deionized water and each substrate was thoroughly rinsed with deionized water ($\approx$ 250 ml). The substrates were subsequently blown dry with dry oil-free nitrogen and were stored in petri dishes until usage which occurred on the same day.[110] The contact angle was found to be $(4.5 \pm 0.3)^\circ$ for this cleaning procedure.

HF cleaning

For the block copolymer systems the silicon substrates were cleaned with HF to ensure a substrate which is chemically nonselective to neither block. For this reason, the silicon substrates were immersed into a 19 % HF bath for 2 min. Afterwards, the substrates were rinsed with deionized water and blown dry with dry oil-free nitrogen. By this method the natural oxide was removed completely. The substrates were coated directly after the HF cleaning.

ITO and FTO substrate treatment

The ITO substrates were mainly used for the preparation of organic solar cells. Therefore, the ITO coating had to be patterned before cleaning (see figure 4.5a,b). For this reason, the ITO part, which has to be preserved, was covered with an adhesive tape. The uncovered parts were coated with a mixture of zinc powder and water. Hydrochloric acid (19 %) was dripped on the zinc paste and the ITO was etched away. The substrate was subsequently rinsed with deionized water. The successful removal of the ITO was checked by measuring the resistance of the substrate surface with an ohmmeter. Subsequently,

the adhesive tape was removed.
The patterned ITO substrates and the FTO substrates were cleaned using different solvents. The following procedure was consecutively performed for Alconox solution, ethanol, acetone and isopropanol. The Alconox solution consisted of the powdered precision cleaner *Alconox* dissolved in deionized water with a concentration of 16 mg/ml. Therefore, the substrates were immersed into each solvent separately and put into an ultrasonic bath for 10 min, afterwards the substrates were rinsed with the same solvent and blown dry with dry oil-free nitrogen.
After the final drying, the substrates which were used for solar cell preparation were treated with oxygen plasma (Plasma System Nano, Diener Electronics) for 10 min at a power of 240 W. The pressure was set to 0.1 mbar and the working pressure to 0.4 mbar. The full organic solar cell preparation is described in section 4.5.

4.3 Coating methods

The big advantage of soluble organic compounds is the solution processiblity. Thin polymer films can easily be prepared with techniques such as spin coating, solution casting, doctor blading, dip coating, inkjet printing, roll-to-roll printing etc. In the case of organic electronics, printing techniques seem to be very promising for cheap large scale production. However, in research, spin coating is one of the main procedures used which will be introduced in this chapter in detail. The deposition of metal layers as electrodes will be described subsequently.

Solution preparation
First of all, the organic compound had to be dissolved in the required solvent. For this reason, the organic compound was weighed in a cleaned welted glass. Afterwards, the required amount of solvent was added. The welted glasses were closed with a cap and sealed with Paratape. To improve the dissolving of the organic compound, the solution was either stirred with a magnetic stirrer or put on a shaker. For some organic compounds, in particular at high concentrations, heating the solution was necessary to dissolve the materials completely.
Solutions containing two or more components were prepared by dissolving the compounds separately and subsequently mixing the single solutions. Thereby, the mixing ratio of the compounds wa adjusted more precisely. In the case of P3HT:PCBM mixtures, PCBM was dissolved first and the solution was used to dissolve P3HT afterwards. This procedure was necessary due to the lower solubility limit of PCBM.

PEDOT:PSS was purchased as a dispersion in water. To achieve a homogeneous dispersion PEDOT:PSS was put into an ultrasonic bath for 10 min and filtered with a 5 μm PTFE filter before spin coating. Also P(S-b-PP) had to be filtered with a 0.2 μm PTFE filter to achieve a smooth homogeneous polymer film.

Spin coating

All organic thin films were prepared by the spin coating technique. For this purpose, the solution with a defined concentration c_0 was put onto a cleaned substrate in such a way that the surface was fully covered. Directly afterwards, the substrate rotation started with a selected rotational speed ω. A thin homogeneous film formed. The resulting thickness is described by

$$d = A\omega^{-1/2}c_0M^{1/4} \tag{4.1}$$

with the rotational speed ω, the initial concentration of the solution c_0, the molecular weight of the used polymer M and an experimental parameter A.[112, 113] The experimental parameter A depends on the spin coater used and the environmental conditions. The thickness can be controlled by changing the concentration of the solution, the molecular weight of the polymer and the rotational speed. While the rotational speed is limited by the spin coater itself and the molecular weight by the available polymers, the concentration can be varied over a large range and is simply limited by the solubility of the materials used. Therefore, in this work the thickness is controlled by changing the concentration of the solution.

Equation 4.1 is only valid for the concentration range in which the viscosity of the polymer solution is negligible. The concentration-thickness dependence can be divided into three regimes. At very low concentrations the polymer chains do not entangle and no homogeneous film is created by spin coating. This concentration regime can be used to prepare nanostructured polymer templates as shown in the case of the photoactive polymer polypyrrol (PPy).[114] For higher concentrations the polymer chains entangle and equation 4.1 is valid, i.e. a linear concentration thickness dependence is found. In the third regime, the concentration thickness dependence is still linear but with an increased slope. In this regime, the viscosity has to be taken into account.

Schubert et al. have also used equation 4.1 to determine the molecular weight of polystyrene after calibrating the experimental parameter A with a polystyrene of a known molecular weight. In this work, this dependence was applied to estimate the molecular weights of MEH-CN-PPV and CN-PPV which were not known from the supplier. The parameter A was calibrated with P3HT and P3OT. Thin polymers films were made from polymer solutions with different concentrations via spin coating. While for P3HT and MEH-CN-PPV were dissolved in trichloromethan, tetrahydrofuran was used for P3OT

and CN-PPV. In Figures 4.4a and b the concentration dependent thickness of thin films of P3HT, MEH-CN-PPV, P3OT and CN-PPV are plotted. All four polymers show a linear relation corresponding to the second concentration regime described above (eq. 4.1). The same spin coater with comparable environmental conditions was taken for the sample preparation. In addition, the same solvents were used for the corresponding polymers and the molecular weigths of P3HT and P3OT are known (Tab. 4.1). Consequently, the molecular weights of MEH-CN-PPV $M_{MEH-CN-PPV}$ and of CN-PPV M_{CN-PPV} can be estimated. $M_{MEH-CN-PPV}$ and M_{CN-PPV} were found to be 25000 g/mol and 29000 g/mol, respectively.

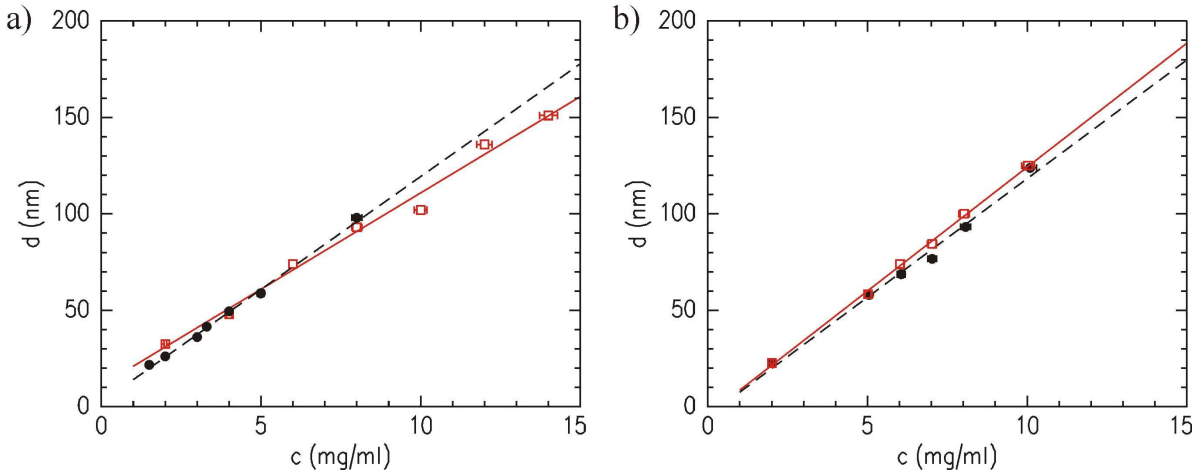

Figure 4.4: *Concentration dependent thickness of thin films of a) P3HT (red open squares) and MEH-CN-PPV (black closed circles) and b) P3OT (red open squares) and CN-PPV (black closed circles). The error bars concerning the thickness are smaller than the symbol size. The red solid (P3HT and P3OT) and black dashed lines (MEH-CN-PPV and CN-PPV) are linear fits to the data.*

Thermal evaporation

An aluminum layer was thermally evaporated as the top electrode of the organic solar cells. For this purpose, an evaporation chamber was used. The deposition was carried out at a pressure of about $2 \cdot 10^{-6}$ mbar. The evaporation was stopped as soon as the Al contacts got non-transparent which corresponds to a thickness of about 100 nm. When preparing solar cells, masks were used which created eight contacts per solar cell. Each contact had a size of approximately 1.5 mm^2 (figure 4.5e).

4.4 Annealing

In most cases, and particularly after spin coating, thin polymer films are in a non-equilibrium morphology. Moreover, the installed structure is most likely not ideal for organic photovoltaics. Annealing increases mobility of the polymer chains such that rearrangements are taking place, resulting in an altered morphology. The polymer chains can rearrange on different length scales. Rod like polymers, like most conducting polymers, will crystallize. In the case of polymer blends, phase separation will proceed. For block copolymers the microphaseseparation develops with annealing. In general, different types of annealing are possible. In this thesis thermal and solvent annnealing were used.

Thermal annealing
Thermal annealing is one of the most common annealing procedures. The sample was heated up to a chosen temperature for a specific amount of time. Besides the final annealing temperature and duration of heating also the heating and cooling rate influence the resulting state of the system. Thermal annealing was performed in a vacuum oven, on a hot plate in air and for sensitive samples in an inert gas atmosphere to avoid degradation. In addition to the structural changes, thermal annealing also removed residual solvent from the polymer films.

Solvent annealing
The second procedure was annealing in a saturated solvent atmosphere. To allow for solvent annealing, the samples were placed in a sealed environment of defined volume, i.e. in a desiccator, with a reservoir of solvent. After a defined time, the desiccator was opened and the samples were removed. This procedure was applied to the block copolymer system.

4.5 Solar cells

An organic solar cell consists of a multi-layer architecture including electrodes, a blocking layer and the active layer. In Figure 4.5 the main steps during solar cell preparation are shown schematically. As substrate a transparent solid support, in this thesis glass, coated with a thin ITO layer was used (figure 4.5a). The ITO layer which is acting as the electrode was patterned and cleaned as described in section 4.2 (figure 4.5b). On top of the ITO, a thin layer of PEDOT:PSS was spin coated (2000 rpm for 60 s) as an electron blocking layer with a typical thickness of 70 nm. For further drying, the PEDOT:PSS layer was thermally annealed on a hot-plate at 150 °C for 10 min under ambient conditions (figure 4.5c). The active layer, e.g. P3HT:PCBM, was deposited via spin coating (2000 rpm for 30 s) onto

the blocking layer (figure 4.5d). The top electrode material, aluminum, was thermally evaporated onto the active layer as described in section 4.3. As a final step the solar cell was thermally annealed at 140 °C for 10 min. Since the active layer is sensitive to oxidation the annealing was performed on a hot-plate in an inert gas atmosphere (figure 4.5e).

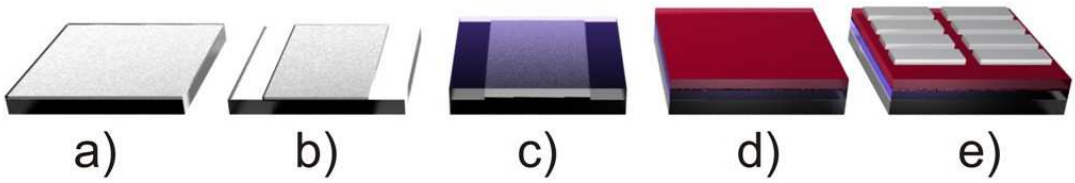

Figure 4.5: *Schematic representation of the main steps during organic solar cell preparation: a) ITO substrate as received, b) patterned ITO substrate, c) with the blocking layer PEDOT:PSS, d) after deposition of the active layer and e) the entire organic solar cell with the top electrode.*

Chapter 5

Characterization of polymer-fullerene systems

At present, the most efficient organic photovoltaic (OPV) devices consist of a conjugated polymer and fullerene derivatives.[115, 116, 1] The most prominent material combination is P3HT:PCBM as it has been the most efficient system for several years. Consequently, P3HT:PCBM solar cells are the most extensively studied devices in OPVs.[117] Therefore, P3HT:PCBM bulk heterojunction systems evolved into the standard system in basic OPV research although meanwhile new, more efficient donor and acceptor materials have been synthesized.[11, 116]

The internal morphology of bulk heterojunction systems is crucial due to their intrinsic material properties, such as high exciton binding energy and short exciton diffusion length, as described in section 2.1.1. The creation of bulk heterojunction films for the active layer is typically a solution-based and, therefore, a self-assembly process. Thus, the formation of the morphology cannot be controlled directly, but is influenced by external parameters, such as the molecular structure and the blend ratio of the used materials, the solvent and post-production treatments. The overall goal is to adjust the external parameters to obtain an optimized morphology which fits the requirements best. However, the final optimum structure is usually far from equilibrium.[9]

While in literature most morphological investigations are based on imaging techniques which are typically limited to several μm^2, in this thesis scattering is the main technique for structural characterization. Scattering gives not a direct image of the morphology but an averaged structural information. The probed area, over which structural information is averaged, is in the range of several tens of mm^2 and has therefore a typical size of an electrode of a research solar cell. Consequently, results from two methods averaging over similar areas are compared, i.e. when the photovoltaic performance is compared with the structural information obtained from scattering experiments.

In this chapter, the morphology formation of P3HT:PCBM bulk heterojunction films as the active layer in OPV devices is characterized. The focus is put on the influence of external parameters. The absorption of P3HT and PCBM is introduced and possibilities to extend it to higher wavelengths are illustrated (section 5.1). The first investigated parameter influencing the morphology is the used solvent. The photovoltaic performance is compared with structural models obtained from several investigation methods including imaging as well as scattering techniques (section 5.2). In section 5.3 the impact of the blend ratio on the molecular structure in particular on the molecular solubility of PCBM in the P3HT phase is discussed. Finally, the disturbance of an additional dye molecule on the developed P3HT:PCBM morphology in comparison with the photovoltaic performance is presented (section 5.4).
Results of this chapter have been published in references [118, 119, 120].

5.1 Spectral properties of P3HT and PCBM

The absorption coefficient spectra of as-spun and annealed P3HT and PCBM are shown in figure 5.1a. The spectra are obtained from absorption measurements normalized by the thickness determined with X-ray reflectivity (XRR) (figure 5.1b). The thicknesses of PCBM and P3HT are retrieved from fitting XRR data.

PCBM absorbs mainly in the UV region with a maximum at 335 nm and hardly overlaps with the solar spectrum. Therefore, the contribution of PCBM to the photovoltaic

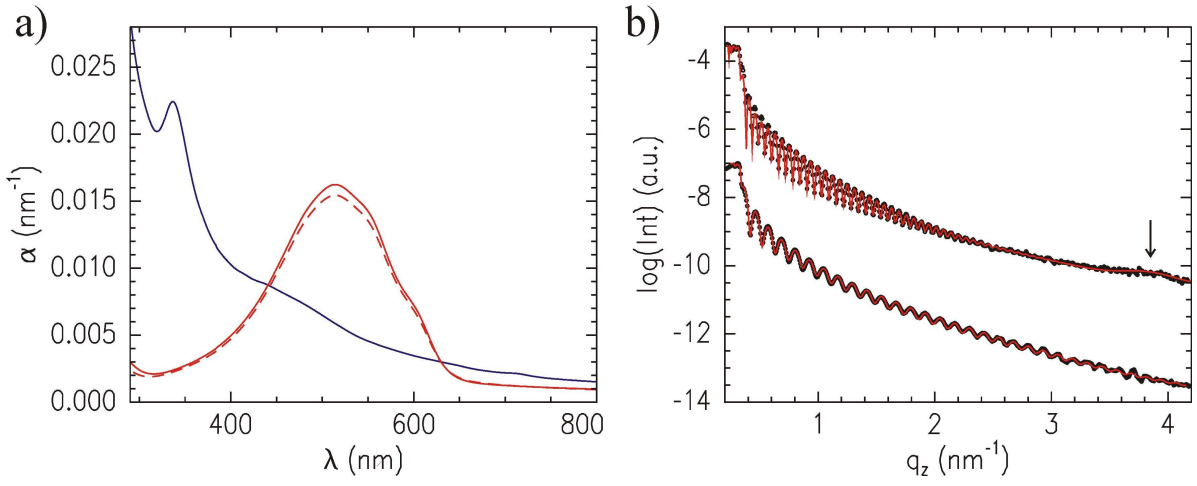

Figure 5.1: *a) Wavelength dependent absorption coefficient $\alpha(\lambda)$ of as-spun (red dashed line) and annealed (red solid line) P3HT and PCBM (blue line) films. b) X-ray reflectivity data (symbols) with fits (red line) of PCBM and as-spun P3HT (from bottom to top). The P3HT (100) Bragg peak is indicated by an arrow. The curves are shifted along the y-axis for clarity.*

performance is limited. In the case of P3HT with the main absorption peak at 510 nm, the absorption spectrum overlaps with the maximum of the solar spectrum. The peak position depends on the intra- and interchain order of the polymer.[25] Thus, a change in peak position is a sign for structural variation in the probed P3HT film. For example, an increase in conjugation length or in π-π-stacking results in a red shifted absorption peak.[25] Two additional features in the P3HT spectrum are the shoulders at 550 nm and 600 nm which occur due to vibrational excitations and arise if the P3HT film is crystalline. The comparison of as-spun and annealed P3HT films (dashed and solid lines, respectively) show only a slight increase of the shoulder-like features. Consequently, thermal annealing does not improve the crystallinity much or rather, the as-spun film reveals already a certain crystallinity. The main peak of P3HT exhibits a high absorption coefficient of 0.016 nm^{-1}. For comparison, a 100 nm thick film of a material with an absorption coefficient of 0.016 nm^{-1} at a certain wavelength absorbs already 80% of the incoming light with this wavelength. Almost no absorption for wavelengths above 650 nm takes place.
In addition to the film thickness, the XRR data reveal also information on the molecular ordering of P3HT. The (100) Bragg peak around 4 nm^{-1} is observed (figure 5.1b). A detailed discussion on the crystalline ordering of P3HT follows in the next sections.

5.2 Influence of solvent and annealing

For poly(2-meth-oxy-5-(3,7-dimethyloctyloxy)]-1,4-(phenylenevinylene):PCBM (MDMO-PPV:PCBM) based solar cells, Shaheen et al.[121] found a strong influence of the used solvent on the photovoltaic performance. Solar cells cast from chlorobenzene solution revealed an efficiency of 2.5% in comparison to 0.9% for cells made from toluene solution. The authors related this behavior to the difference in surface morphology probed with AFM. While the systems made from toluene solution showed surface structures on the order of 500 nm, the films obtained from chlorobenzene solution exhibited 100 nm structures. Further investigations of the topography and cross sections revealed similar structure sizes for both systems using high resolution scanning electron microscopy (SEM). In addition, for the toluene-cast samples big PCBM clusters were covered with a MDMO-PPV skin.[122] Both studies related the difference in photovoltaic performance to the morphology of the chlorobenzene-cast system with its smaller length scales.
Several other studies investigated the influence of solvents used to cast the active layer of an organic solar cell on the photovoltaic performance. Different systems, also including all-polymer systems, showed an influence on performance and improvements were always related to the optimized morphology.[11, 123, 124, 125] Furthermore, this dependency was

also found for systems made from solvent mixtures.[126, 127] Generally, systems cast from solutions with higher boiling-point solvents seem to be advantageous for the photovoltaic performance. However, a detailed structural investigation on multiple length scales and with high statistic relevance is still missing.
In this section, the morphologies of P3HT:PCBM bulk heterojunction films cast from chloroform, toluene, chlorobenzene and xylene as active layer are characterized and compared to findings from spectral and efficiency measurements. Throughout this section, the data obtained from films made from different solvents are color coded. For chloroform, toluene, chlorobenzene and xylene the colors red, cyan, green and blue are used, respectively. The films are prepared via spin coating. Besides the influence of the used solvents, also the effect of thermal annealing at 140 °C for 10 min in an inert gas atmosphere is investigated.

5.2.1 Solvent-dependent spectral characterization

As expected, the photovoltaic performance for P3HT:PCBM bulk heterojunction films is found to depend on the solvent used for spin coating. In figure 5.2 the corresponding current-voltage (IV) curves under AM1.5G illumination (74 mW/cm^2) are shown. The light intensity corresponds to the direct solar light intensity when the diffusive part is neglected. The extracted photovoltaic parameters are summarized in table 5.1. While for the system made from chloroform solution a low efficiency of 0.4% is measured, the films made from toluene, chlorobenzene and xylene reveal higher efficiencies of about 2.5%. The main differences are found in the short-circuit current I_{SC} and the fill factor FF. However, the open-circuit voltage U_{OC} is almost identical as the open-circuit voltage is mainly defined by the material combination used in organic solar cells. The low fill factor $FF = 18\%$ of the solar cell made from chloroform is due to the s-shape of the IV-curve which can be related to an interfacial barrier.[128] In the case of the organic solar cells made from toluene, chlorobenzene and xylene, the photovoltaic performances are in the same range and no significant difference is observeds.

The efficiencies are rather low compared to literature. For comparison, an organic solar cell prepared from chlorobenzene solution and characterized under AM1.5G illumination with the standard intensity of 100 mW/cm^2 is also shown in figure 5.2. This solar cell revealed an efficiency of 3.3% which is moderate, as compared with high performance organic solar cells made from P3HT:PCBM. The investigated solar cells are prepared at ambient conditions and with the simplest device architecture to keep the influence of additional blocking layers etc. as low as possible (see section 4.5). Therefore, an efficiency of 3.3% matches well with most efficiencies published for P3HT:PCBM systems.[117]
The initial solution concentrations of the solvents are adapted in such a way that the

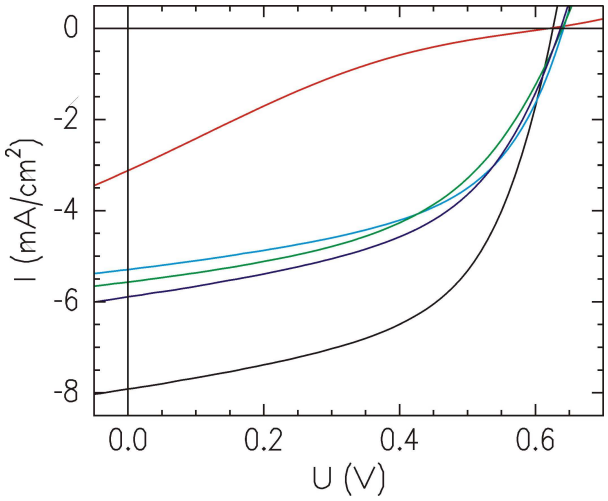

Figure 5.2: *Current-voltage curves of P3HT:PCBM bulk heterojunction solar cells cast from chloroform (red), toluene (cyan), chlorobenzene (green) and xylene (blue) solutions under AM1.5G illumination (74 mW/cm²). For comparison a current-voltage curve of a P3HT:PCBM bulk heterojunction solar cell cast from chlorobenzene solution under AM1.5G illumination (100 mW/cm²) is shown (black solid line).*

solvent	I_{SC} [mA/cm²]	U_{OC} [V]	FF [%]	η [%]
chloroform	3.1	0.62	18	0.46
toluene	5.3	0.64	52	2.4
chlorobenzene	5.6	0.64	49	2.4
xylene	5.9	0.64	50	2.6

Table 5.1: *Short-circuit current (I_{SC}), open-circuit voltage (U_{OC}), fill factor (FF) and efficiency (η) obtained from the IV-curves in figure 5.2.*

resulting film thickness of all active layers is constant at about 95 nm. For solutions made of chloroform, toluene, chlorobenzene and xylene the concentrations for spin coating are set to 7 mg/mL, 18 mg/mL, 24 mg/mL and 24 mg/mL, respectively. Consequently, the inner film structure has to be the decisive factor defining the photovoltaic performance as the same material system with the identical environment is used.

The wavelength-dependent absorption coefficient of the P3HT:PCBM films made from different solvents (figure 5.3a) show features from both components, P3HT and PCBM (compare figure 5.1). The spectra follow a linear superposition of the P3HT and PCBM spectra with no additional features. Therefore, no significant ground-state charge transfer occurs.[123] Only small deviations are observed in the curves from samples made from different solvents. The absorption coefficient of the main absorption peak of P3HT in the P3HT:PCBM blend is about 0.008 nm^{-1} which is half the value of pure P3HT (section 5.1) due to the blend ratio of 1:1. No shoulder-like features in the P3HT absorption spectrum are visible. Therefore, P3HT in as-spun P3HT:PCBM films seems to be amorphous. So, when compared to the absorption data from pure P3HT (section 5.1), which already showed the shoulder-like features, this is a strong indication that PCBM hinders

the crystallization of P3HT during spin coating. After thermal annealing, the contribution from PCBM is unaffected whereas a change in the P3HT absorption behavior is observed. The shoulder-like features appear and the position of the main absorption peak is red-shifted. Consequently, P3HT is ordering during thermal annealing. The conjugation length is increased and P3HT crystallites are formed.

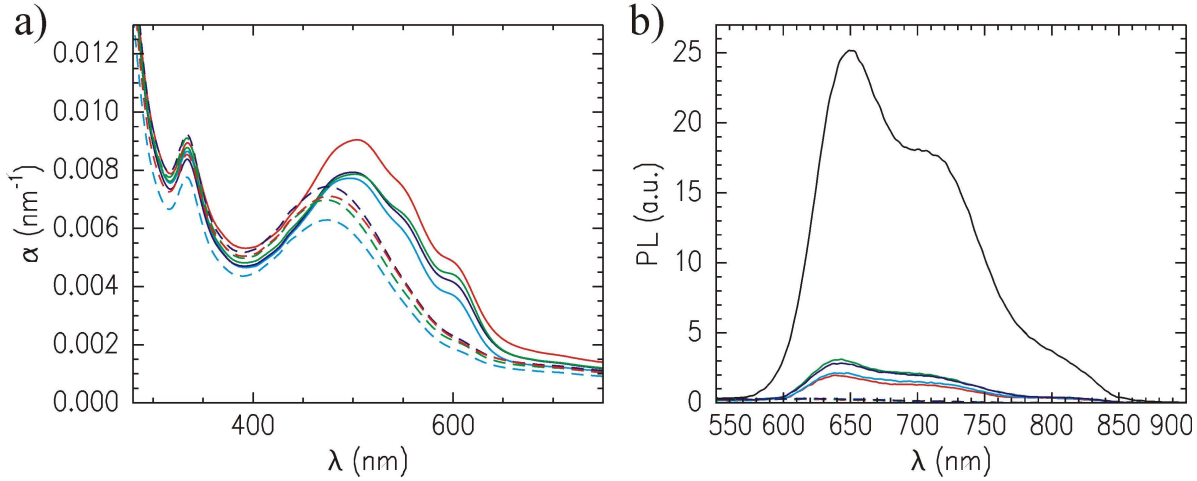

Figure 5.3: *a) Wavelength dependent absorption coefficient $\alpha(\lambda)$ and b) photoluminescence PL of as-spun (dashed lines) and annealed (solid lines) P3HT:PCBM bulk heterojunction films cast from chloroform (red), toluene (cyan), chlorobenzene (green) and xylene (blue) solutions. b) The photoluminescence of a pristine P3HT film (black solid line) is shown for comparison.*

In figure 5.3b the photoluminescence spectra of pure P3HT, as-spun and annealed P3HT:PCBM bulk heterojunction films are shown. The photoluminescence (PL) signal of pure P3HT results from generated excitons which decay radiatively. In the case of the as-spun P3HT:PCBM, the PL signal is completely quenched (dashes lines in figure 5.3b) indicating that all excitons are dissociated and decay non-radiatively afterwards. Therefore, P3HT and PCBM have to be intermixed on a molecular level. When the system is annealed, the PL signal increases slightly which means that a radiative decay of excitons is occurring again. Thus, pure P3HT domains have to be formed which are sufficiently big that a generated exciton does not reach a PCBM molecule and decays radiatively within the P3HT domain. The pure P3HT phases can form either due to phase separation of P3HT and PCBM or due to P3HT crystallization in which the PCBM molecules are ejected from the crystal. Nevertheless, most excitons are dissociated as the PL signal is still one order of magnitude lower compared to pure P3HT.

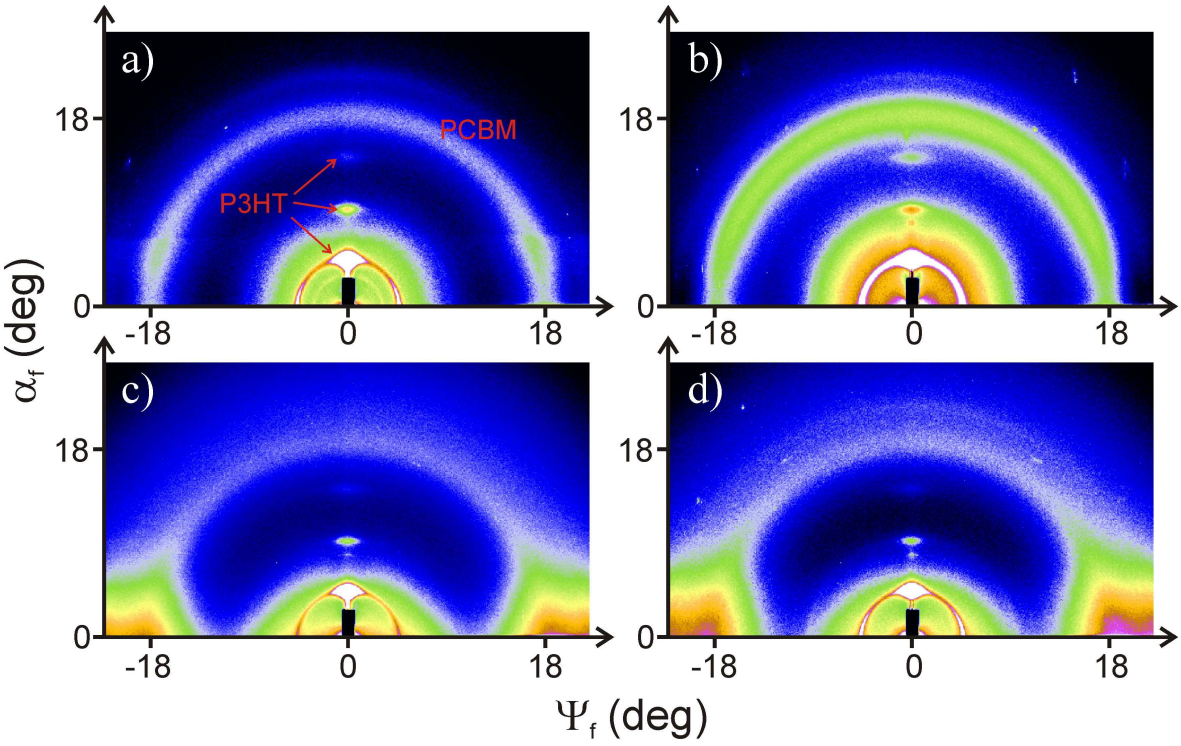

Figure 5.4: *2d GIWAXS data of annealed P3HT:PCBM films cast from chloroform (a), toluene (b), chlorobenzene (c) and xylene (d) solutions. The features corresponding to P3HT and PCBM are highlighted (a). The linear color code spans an intensity range of 80-650 (a,b), 80-550 (c) and 80-350 (d), respectively.*

5.2.2 Crystallization process and cluster formation

Absorption measurements give already an indication that P3HT crystallizes due to thermal annealing. For a more quantitative analysis the P3HT:PCBM bulk heterojunction films are investigated with grazing incidence wide angle scattering (GIWAXS) to obtain lattice constants and crystal sizes for P3HT crystals. For the definition of P3HT crystals in terms of crystalline orientation and nomenclature see section 3.2.4.2. The 2d scattering data of the annealed P3HT:PCBM films (figure 5.4) reveal distinct Bragg reflections of P3HT which are most pronounced in vertical directions. In addition, a broad ring-like feature of PCBM is observed for all systems. Therefore, the PCBM crystals have as powder-like distribution, i.e. no preferential orientation is existing. The vertical and horizontal sector integrals of the GIWAXS measurements are shown in figure 5.5 for a quantitative analysis. In all curves, contributions of crystalline PCBM are observabed. Consequently, PCBM is already aggregated in as-spun films but the aggregation seems to be independent of the solvent and of thermal annealing. For the as-spun films, no signal from P3HT crystallites is visible (dashed lines) indicating that in these as-spun

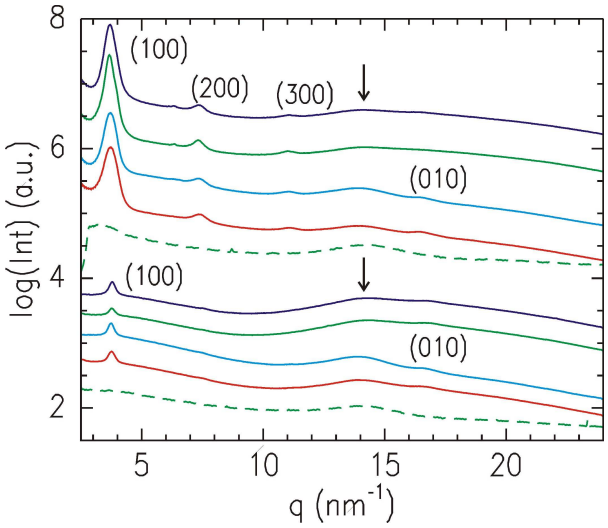

Figure 5.5: *Vertical (upper five curves) and horizontal (lower five curves) sector integrals of GIWAXS measurements of as-spun (dashed lines) and annealed (solid lines) P3HT:PCBM bulk heterojunction films cast from chloroform (red), toluene (cyan), chlorobenzene (green) and xylene (blue) solutions. Bragg peaks are indicated. The PCBM contribution is indicated by arrows. The curves are shifted along the y-axis for clarity.*

P3HT:PCBM films no P3HT crystallites exist. This confirms the findings from the absorption data which showed no vibrational excitations in the as-spun P3HT:PCBM films. It is well known that pure P3HT already crystallizes during spin coating. Consequently, PCBM hinders P3HT crystallization which has already been indicated by the absorption measurements.

The sector integrals of the annealed P3HT:PCBM films reveal strong Bragg peaks which are assigned to P3HT lattice orientations as indicated in figure 5.5. For the vertical cuts the (100) peak and its two higher orders are visible. The (100) reflection is also observed in the horizontal sector integrals, but with much lower intensity, and no higher orders appear. In addition, the (010) signal is detected with low intensity in the vertical as well as in the horizontal sector integrals. As the intensity of the (100) signal is more pronounced in the vertical than in the horizontal direction, the main orientation of the P3HT crystallites regarding the substrate is edge-on. It was reported that the orientation of crystals in a P3HT homopolymer film depends on spinning speed amongst others.[129]

For a quantitative analysis the Bragg reflections in the sector integrals are fitted with Gaussian functions. From the position, the lattice constant is extracted (see table 5.2). The lattice constants are found to be 1.7 nm (100) and 0.38 nm (010) for both the vertical and horizontal sector integrals independent of the solvent used. These values are in good agreement with literature.[130, 131, 132]

The width of the Gaussian fit provides information on the corresponding dimensions of the crystallites via the Scherrer equation (2.64). However, since also the distribution of the lattice constant and the resolution of the scattering setup broaden the peak width, this yields only a lower limit. The crystal size is not determined in (010) direction as the (010) reflection is not sufficiently pronounced for the evaluation of the crystal size. In

solvent	**lattice constant [nm]**			
	(100) v	(010) v	(100) h	(010) h
chloroform	1.69	0.38	1.67	0.38
toluene	1.69	0.38	1.68	0.38
chlorobenzene	1.70	-	1.66	0.37
xylene	1.71	-	1.67	0.37

Table 5.2: *Lattice constant of P3HT crystallites in annealed P3HT:PCBM films made from different solvents. The data are obtained from vertical (v) and horizontal (h) sector integrals of GIWAXS measurements. The uncertainty obtained from the Gaussian fits to the Bragg peaks is below 0.1%.*

table 5.3 the crystal sizes perpendicular and parallel to the substrate are shown depending on the solvent used for coating. The crystallites are larger for solvents with higher boiling points. For the major part of the crystallites, i.e. edge-on oriented crystallites, the crystal size increases from 12.6 nm to 22.0 nm with increasing boiling point of the solvent. This corresponds to a stacking from 7 to 13 lattice planes. As seen from the (100) reflection in the horizontal sector integral, also face-on P3HT crystals are present in the films. The face-on P3HT crystals show an increase in size from 20.5 nm to 30.6 nm corresponding to 12 and 18 lattice planes, respectively. The difference in P3HT crystal dimensions in vertical and horizontal direction is due to the confinement of the top and bottom interfaces which reduces the vertical crystal sizes.
The solvent-dependent crystal sizes are attributed to the higher boiling points of the solvents which results in a lower evaporation rate. Preordering and residual solvents influence the crystal size. Although no crystalline phases are visible for the as-spun systems, preordering is taking place. The preordering is more distinctive for the systems cast from solvents with higher boiling points as the drying time is increased. In addition, it was recently found that residual solvents in conducting polymer films exist and increase the diffusive mobility of PCBM.[133] Hence, residual solvents in the P3HT:PCBM films after the spin coating process have to be taken into account as it will influence the mobility of the molecules in the film. Furthermore, the amount of residual solvent increases with the boiling point. Consequently, the used solvent influences the ordering also during thermal annealing. In summary, both, the preordering and the chain mobility, increases with the boiling point. Therefore, larger crystals arise from systems cast from solvents with higher boiling points.

For P3HT:PCBM solar cells, thermal annealing is absolutely necessary to obtain cells with a reasonable performance. P3HT:PCBM solar cells without thermal annealing reached efficiencies on the order of only 0.4%. The increase in efficiency is, amongst oth-

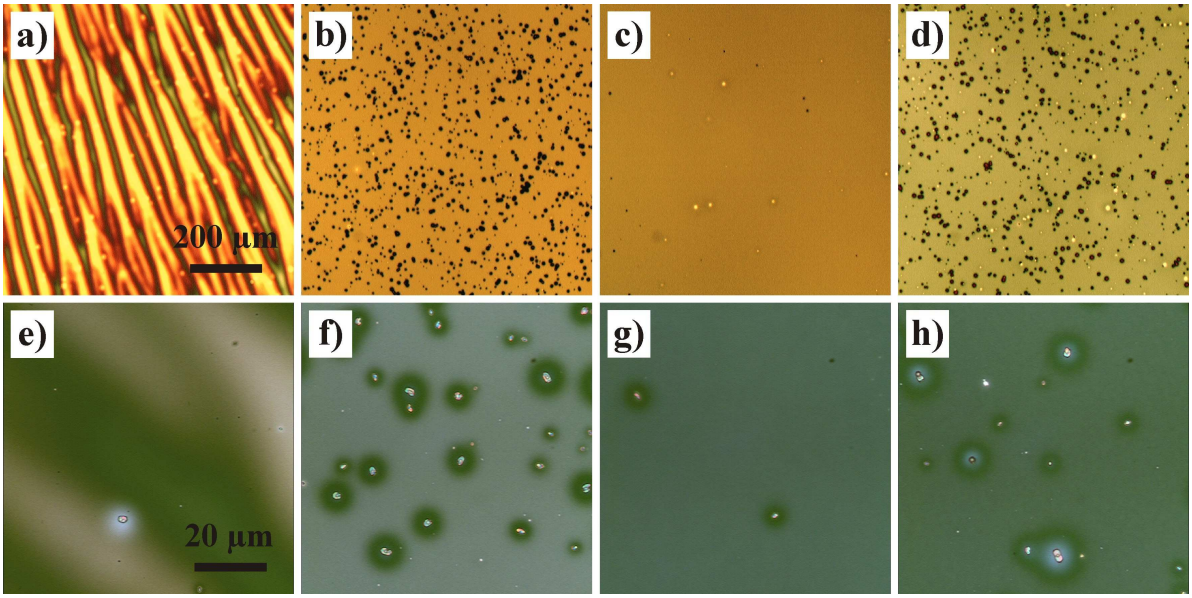

Figure 5.6: *Optical micrographs of P3HT:PCBM bulk heterojunction films cast from chloroform (a,e), toluene (b,f), chlorobenzene (c,g) and xylene (d,h) solutions. The micrograps are taken at magnifications of 10× (a-d) and 100× (e-h). The scale bars are valid for all micrographs with a magnification of 10× and 100×, respectively.*

ers, attributed to the crystallization of P3HT and the accordingly higher charge carrier mobility. Consequently, larger P3HT crystallites should result in enhanced photovoltaic performance. However, it is not sufficient to explain the observed difference in photovoltaic performance of the P3HT:PCBM solar cells made from different solvents by the change in crystal size only. Rather, above a minimum crystal size the effect on the photovoltaic performance seems to become less dominant or is canceled out by other factors. However, for the solar cell with the lowest efficiency (made from chloroform), also the crystal size is found to be smallest.

Besides the partial crystallization of P3HT and the aggregation of PCBM, PCBM forms also big agglomerates due to thermal annealing. Although there is no change of the PCBM features in the GIWAXS data observed, optical microscopy reveals PCBM cluster formation due to thermal annealing (figure 5.6). The PCBM clusters appear as bright dots surrounded by a dark rim. No clusters are found for the as-spun systems. The bright dots are attributed to the PCBM clusters while the dark rim is the PCBM depletion region. The PCBM cluster formation was described in detail by Zhong et al.[134] AFM investigations showed that the clusters grow in both, lateral and vertical, directions with a dominating growth in height. In addition, the surrounding depletion region exhibited a lower thickness which explains the difference in color. For lower magnifications (figure 5.6a-d) only the depletion regions are visible as dark regions and the PCBM clusters

solvent	T_B [°C]	**solubility of PCBM [mg/mL]**	**crystal size [nm]**	
			(100) v	(100) h
chloroform	61	25	12.6	20.5
toluene	111	10	13.6	24.5
chlorobenzene	131	25	16.0	23.6
xylene	140	5-15	22.0	30.6

Table 5.3: *Boiling points T_B of the various solvents and PCBM solubilities in these solvents.[135] Crystal sizes of P3HT crystallites in annealed P3HT:PCBM films made from different solvents. The data are obtained from vertical (v) and horizontal (h) sector integrals of GIWAXS measurements. The uncertainty for the crystal size obtained from the Gaussian fits to the Bragg peaks is below 1%.*

are not resolved.

The PCBM cluster formation in P3HT:PCBM films is found to be solvent dependent. The films made from chloroform and chlorobenzene show no or just very few clusters. However, films cast from toluene and xylene exhibit a higher density of PCBM clusters which reveals a solubility driven cluster formation. The solubility of PCBM in different solvents is shown in table 5.3. While for chloroform and chlorobenzene a solubility of 25 mg/mL is reported, toluene and xylene dissolve PCBM much worse.[135] Troshin et al. studied the cluster formation of several fullerene derivatives in P3HT:PCBM films made from chlorobenzene with optical microscopy.[136] Cluster formation was just found for fullerene derivatives which revealed a solubility lower than 20 mg/mL. This limit is also applicable to the findings in this thesis and confirms this solubility limit as a more general rule. Nevertheless, PCBM cluster formation alone does not yet explain the found photovoltaic behavior of the solar cells as well.

Besides the presence of PCBM clusters, the optical micrographs (figure 5.6) reveal a wavy structure of the P3HT:PCBM film cast from chloroform while the surface of films cast from the other solvents is smooth on the micrometer range.

5.2.3 Lateral structures

More important than structures on the micrometer range is the morphology on the nanometer scale in P3HT:PCBM bulk heterojunction systems, as these length scales are in accordance with the exciton diffusion length and therefore crucial for the charge carrier generation. In figure 5.7 AFM topography images of annealed P3HT:PCBM films cast from chloroform, toluene, chlorobenzene and xylene are shown. The surface roughness is about 1 nm for all investigated films which reveal a structure on the nanometer range.

For a quantitative analysis, the AFM images are Fourier transformed. In figure 5.8a the 2d Fourier transformation of an AFM image of a P3HT:PCBM film made from chlorobenzene is shown as an example. The characteristic length scale arises as a ring in the 2d Fourier transformation. Power spectral density (PSD) curves are obtained (figure 5.8b). The PSD curves show characteristic lateral surface structures which appear as peak or shoulder-like features. The PSD curves can be compared directly with scattering curves. For P3HT:PCBM films cast from chloroform, toluene, chlorobenzene and xylene, lateral surface structures of about 500 nm, 400 nm, 180 nm and 600 nm are revealed. The found structures are far above the exciton diffusion length and therefore very disadvantageous. However, these length scales refer to surface structures only and do not necessarily resemble the inner film morphologies. In addition, from the small surface roughness it is known that the surface structures are not very pronounced. In contrast to the difference in surface structure of MDMO-PPV:PCBM systems cast of toluene and xylene[121, 122], the structures found for P3HT and PCBM are very similar.

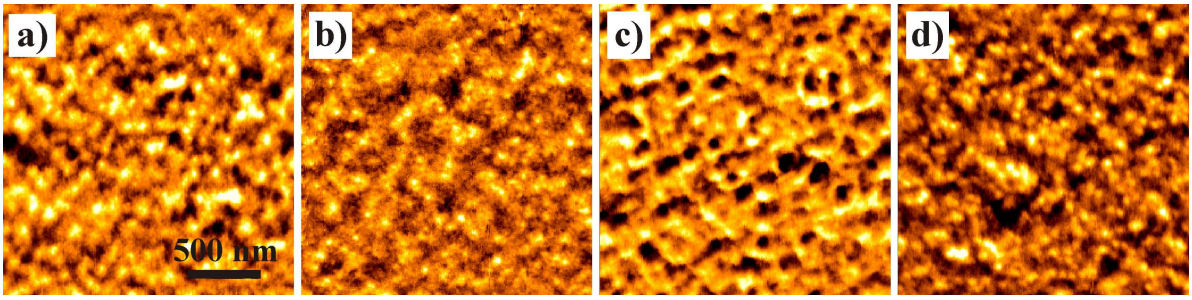

Figure 5.7: *Atomic force microscopy images (scan size 2×2 μm^2) of P3HT:PCBM bulk heterojunction films cast from chloroform (a), toluene (b), chlorobenzene (c) and xylene (d) solutions. The color range covers 3.5 (a), 6.0 (b), 8.0 (c) and 1.0 nm (d).*

Moreover, the topography images of AFM measurements picture the surface only with limited statistics due to their limited size in the µm-range. Nevertheless, images are taken at different position to enhance their significance. In addition, the extracted information is restricted to surface structures.

To obtain structural information with higher statistics and about the inner film morphology, grazing incidence small angle X-ray scattering measurements (GISAXS) of as-spun and annealed P3HT:PCBM films made from different solvents are performed. In figure 5.9a the detector cuts of the GISAXS data are shown. The detector cuts reveal information on vertical material distributions in the measured films. For the systems cast from chloroform (red), the curves are dominated by a broadened specular peak which is due to big surface structures. These structures are also seen in the optical micrograph

(figure 5.6a). Therefore, no further information is accessible. For the other solvents, features like the Yoneda peak (at $\alpha_f + \alpha_i \approx 0.5°$), correlated roughness, i.e. oscillations between the Yoneda and the specular peak, and shoulder-like features at angles above 0.8° are seen. The Yoneda peak position is material sensitive and does not change for the different solvents as the material system P3HT:PCBM is the same for all the samples. However, its shape changes slightly due to thermal annealing. Correlated roughness arises when two parallel interfaces show correlated structures, i.e. the structure of one interface follows the underlying interface. The correlation does not change with heating. The most interesting features are the shoulders at high angles which are an indication for enrichment layers. As the shoulders are visible for all detector cuts and change due to thermal annealing, these enrichment layers exist in as-spun and in an altered way also in annealed P3HT:PCBM bulk heterojunction films. For a quantitative analysis and a clear conclusion, X-ray reflectivity measurements are better suited to determine enrichment layers (see section 5.2.4).

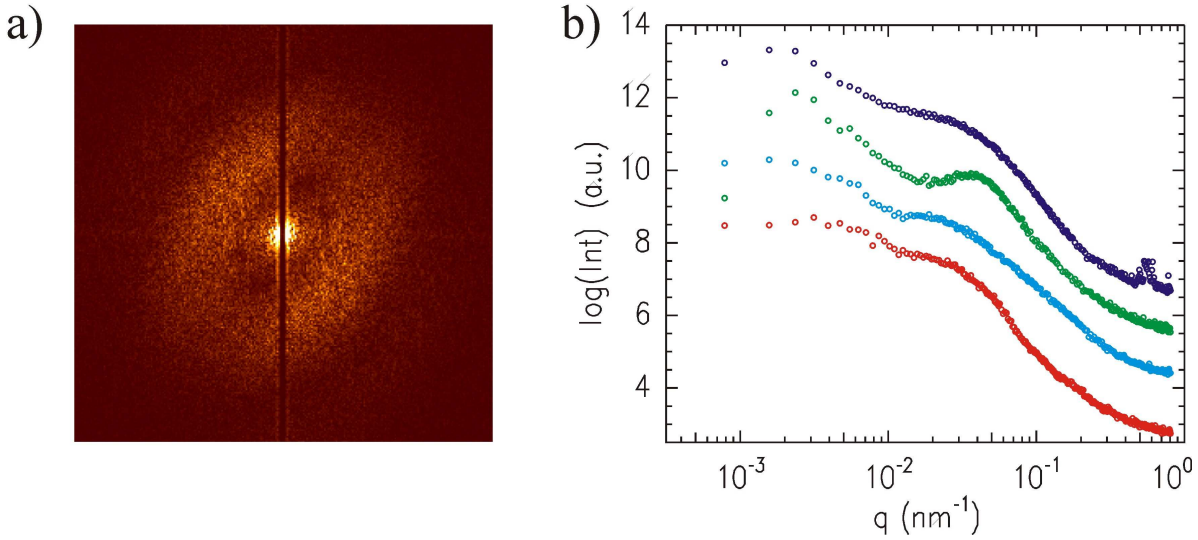

Figure 5.8: *a) 2d Fourier transformation of a 8×8 μm^2 AFM image of a P3HT:PCBM bulk heterojunction film cast from chlorobenzene. b) Power spectral density curves obtained from AFM images (scan sizes 1×1 μm^2 to 8×8 μm^2) of P3HT:PCBM bulk heterojunction films cast from chloroform (red), toluene (cyan), chlorobenzene (green) and xylene (blue). The peak at $q = 0.6$ nm^{-1} (blue curve) is an artifact originating from the AFM measurement. The curves are shifted along the y-axis for clarity.*

Out-of-plane cuts of the GISAXS data (figure 5.9) comprise information on lateral structures comparable to PSD curves, but also on the inner film morphology rather than the surface structures. The out-of-plane cuts are fitted using the effective interface approximation model within the DWBA (section 2.3.3). Again, peaks or shoulder-like features rep-

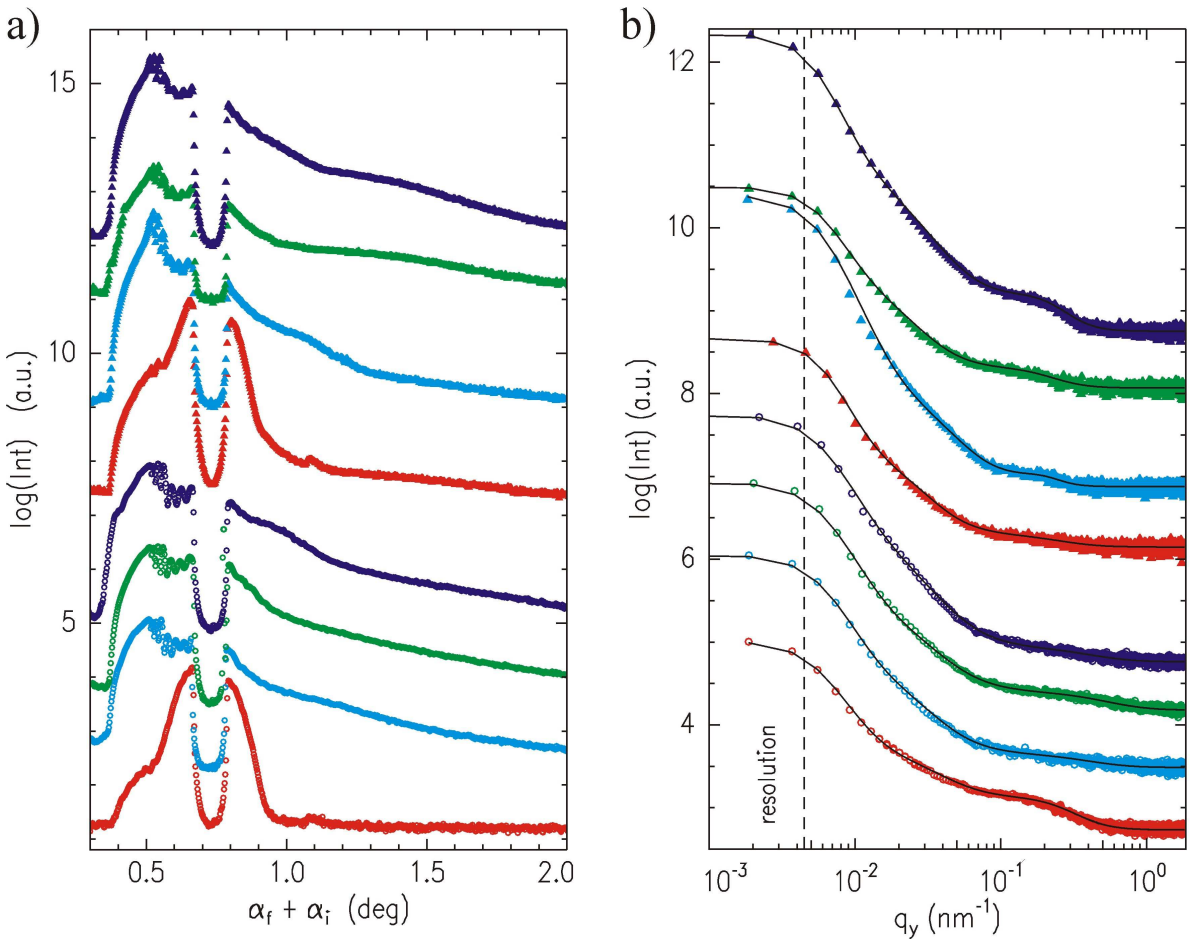

Figure 5.9: *a) Logarithmic plot of detector cuts and b) double-logarithmic plot of out-of-plane cuts taken at the critical angles of PCBM of 2d GISAXS measurements from as-spun (lower four curves, circles) and annealed (upper four curves, triangles) P3HT:PCBM bulk heterojunction films cast from chloroform (red), toluene (cyan), chlorobenzene (green) and xylene (blue) solutions. b) The solid lines are fits to the data using the effective surface approximation model. The dashed line indicates the resolution limit. The curves are shifted along the y-axis for clarity.*

resent characteristic lateral structure sizes. In the case of as-pun P3HT:PCBM films made from different solvents, except for chloroform, no characteristic length scales are found, but rather many different broadly distributed ones which corresponds to widely intermixed phases. This observation for the as-spun films is in accordance with the PL data which revealed molecular intermixing (section 5.2.1). For the films cast from chloroform solution, a structure size of 53 nm is detected. However, the phases are not pure as the PL signal is quenched. Intermixed phases were also found for other systems. For example, in the case of the all-polymer system poly(9,9'-dioctylfluorene-co-bis(N,N'-(4,butylphenyl))bis(N,N'-phenyl-1,4-phenylene)diamine):poly(9,9'-dioctylfluorene-co-benzothiadiazole) (PFB:F8BT) phases containing significant amounts of both components were revealed, using scanning

transmission X-ray microscopy (STXM) with a resolution of 50 nm.[137] These phases purified with increasing drying time.
The structural length in P3HT:PCBM films cast from chloroform gets broadly distributed due to thermal annealing. As the PL signal is increasing, the phases purify, but without a characteristic length scale. In the case of films made from toluene, chlorobenzene and xylene, more defined structure sizes of 35 nm, 65 nm and 44 nm are observed. Therefore, the P3HT:PCBM systems phase separate and coarsen, which is in agreement with the PL data. These length scales are larger than the exciton diffusion length. However, a larger length scale is not necessarily disadvantageous as there is always a balance between smaller and larger structures required. While small structures are needed for an efficient exciton dissociation, larger structures minimize the recombination during the charge carrier transport to the electrodes after dissociation (section 6.1). For example, an optimal structural length scale of 100 nm was found for the system P3HT:F8TBT.[138] In addition, it has to be noted that the structure sizes determined from GISAXS differ totally from the topography probed with AFM. The surface structures are not observed in the scattering data as the structures are not very pronounced concerning height differences. Consequently, it is not sufficient to measure the surface topography and conclude then on the inner film morphology without actually measuring it.

5.2.4 Vertical material composition

To gain a full understanding of the morphology in a bulk heterojunction film, a detailed knowledge of the vertical material composition is necessary. Therefore, X-ray reflectivity (XRR) measurements are performed which detect a vertical material composition profile with a sub-nanometer resolution.[139] In figure 5.10 the XRR curves of as-spun and annealed P3HT:PCBM films cast from different solvents are shown. The region of total reflection including the material sensitive critical angles at low q_z appears independent of the used solvent and the thermal annealing. As the used materials are identical for all investigated systems, no deviation in the critical angle is expected. For a more detailed quantitative analysis the XRR data are fitted with the Parratt algorithm (section 2.3.2). From the fitting, film thicknesses of about (95 ± 7) nm are revealed for all films. Slight changes of 1-2 nm are found due to annealing of the film. The roughnesses are found to be around 0.4 nm except for the as-spun film made from xylene which has a roughness of 2 nm. The roughnesses differ slightly from the roughnesses found by AFM measurements (section 5.2.3). While AFM probes just an area of several tens of μm^2, the illuminated area in an XRR experiment is one order of magnitude larger. As a consequence, a deviation in roughness can occur. Besides the film thickness, the refractive index profile is extracted from the fitting. The presence of the residual solvents do not influence the

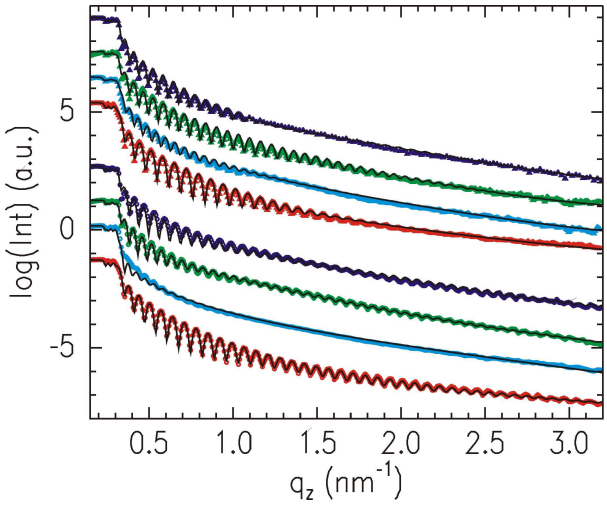

Figure 5.10: *X-ray reflectivity data (symbols) with fits (solid lines) of as-spun (lower four curves, circles) and annealed (upper four curves, triangles) P3HT:PCBM bulk heterojunction films cast from chloroform (red), toluene (cyan), chlorobenzene (green) and xylene (blue) solutions. The curves are shifted along the y-axis for clarity.*

determination of the refractive index profile as their refractive indices are similar to that of P3HT and the amount is very small. Actually, soft X-rays or neutrons have to be used to determine the amount of residual solvents in polymer films.[140, 141]

The refractive index profile is transfered to a material composition profile which contains information of the material composition, i.e. PCBM content in the P3HT:PCBM film, as a function of depth. To illustrate the vertical material profile in a more demonstrative way, a grayscale-coded presentation is chosen.[142] Therefore, pure P3HT and PCBM are depicted as white and black, respectively. The grayscaling is following a linear dependence from white to black for linearly increasing PCBM content. In an ideal vertical material composition of a P3HT:PCBM solar cell, the hole and electron conducting materials are at the hole and electron extracting electrodes, respectively. That means that PCBM (black) should be at the top aluminum electrode and P3HT (white) at the bottom ITO electrode. In addition, a vertical composition gradient might improve charge-carrier transport to the electrodes.[143] Consequently, from bottom to top such an ideal profile would show a continuous transition from white to black in a grayscale-coded presentation.

In figure 5.11 vertical material composition profiles of as-spun and annealed P3HT:PCBM bulk heterojunction films in a grayscale presentation are shown. It has to be noted that no lateral structures can be detected by XRR and are therefore not included in this presentation. All profiles reveal vertical segregation of P3HT and PCBM which are strongly depending on the solvent. While films cast from chloroform show enrichment of P3HT and PCBM at the top and bottom, respectively, the films made from the other solvents reveal a reversed composition. The arrangement in the chloroform case is inversed compared to the ideal profile and therefore very disadvantageous for photovoltaic performance. The thermal annealing further amplifies this inverse structure. This type of enrichment results in an interfacial barrier concerning charge transport and therefore explains the s-shaped

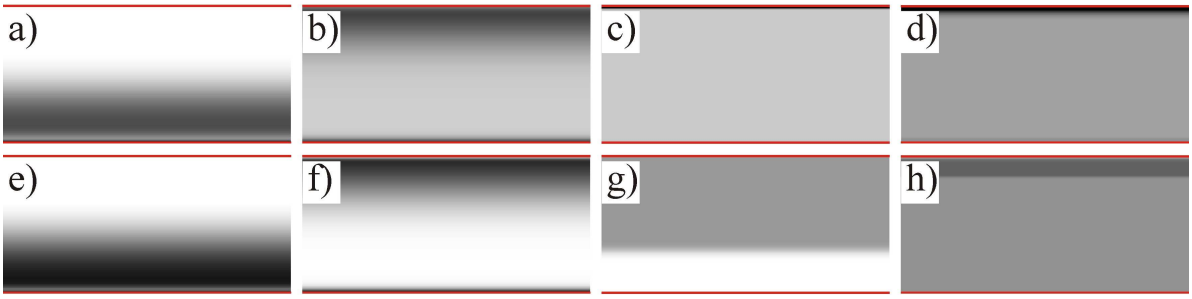

Figure 5.11: *Grayscale-coded material composition profiles of as-spun (a-d) and annealed (e-h) P3HT:PCBM bulk heterojunction films cast from chloroform (a,e), toluene (b,f), chlorobenzene (c,g) and xylene (d,h) solutions. Black and white correspond to pure PCBM and P3HT material, respectively. The substrate (bottom) and the air (top) interface are depicted as red lines.*

IV-curves when measuring the photovoltaic performance (figure 5.2).

The as-spun film made from toluene exhibits a gradual transition from a PCBM layer at the top to an intermixed layer at the bottom. Thermal annealing enhances this gradient with a pure P3HT layer forming at the bottom. In addition, PCBM enriches at the very bottom. In the case of chlorobenzene, a homogeneous film with a 2 nm thin PCBM enriched top layer is detected after spin coating. The PCBM top layer vanishes due to annealing and a bilayered system is developing. The thinner bottom layer contains mainly P3HT while the top part is a mixture of P3HT and PCBM. Finally, the P3HT:PCBM film cast from xylene is initially also a homogeneous mixture with a 5 nm PCBM top layer. After annealing the main part of the film is still homogeneously mixed but the top layer smears over. In addition, there is an indication that after annealing all films reveal a very thin top layer of P3HT. However, its thickness is not detectable as the signal from the top layer is convoluted with the surface roughness. The formation of the additional P3HT layer is energetically driven as the surface free energy of P3HT (26.9 mJ/cm^2) is smaller than that of PCBM (38.2 mJ/cm^2).[144, 145] However, the systems are far from equlibrium, even after 10 min of thermal annealing, and the solvent still influences the evolution of the morphology.[9, 142]

Compared to the vertical material composition of the films made from chloroform, the films cast from the other solvents reveal the correct material arrangement concerning charge transport. Nevertheless, there are still deviations which should favor the films made from toluene and chlorobenzene due to the P3HT enrichment at the bottom which acts as a kind of blocking layer. This type of layer is missing in the case of the films cast from xylene. A further improvement could be reached by adding an additional pure PCBM layer on top as shown by Kumar et al.[146]

Investigations of the influence of thermal annealing and different casting conditions, like

spinning speed, on the vertical material composition were reported. P3HT:PCBM bulk heterojunction films cast from chlorobenzene were characterized with neutron reflectivity. [147, 148] Both studies found a P3HT layer near the surface as expected from the surface free energies. In addition, enriched PCBM was revealed at the bottom layer. However, the detailed near surface structure was not in agreement with each other. Also the influence of thermal annealing showed different effects. A study with ellipsometry also probed the vertical material composition in P3HT:PCBM bulk heterojunction films in dependence of spinning speed, annealing and substrate type.[149] The authors revealed also enriched P3HT at the surface and PCBM at the bottom. However, the detected material composition profiles are found to be linear which is in contrast to other findings and might be a result of the low depth resolution of ellipsometry.
In this thesis, no enrichment of PCBM at the substrate, except for the films cast from chloroform, is found. Also the surface enrichment is different. Consequently, all investigated systems are far from structural equilibrium and at different states of the vertical morphology evolution. All reported studies used different types and times of annealing, different blend ratios, different film thicknesses etc. which makes a direct comparison impossible. It seems that the detailed vertical material composition is very sensitive to the experimental protocol in terms of the used preparation method and annealing steps.

5.2.5 Results

In figure 5.12 the results from AFM, GISAXS and XRR measurements are summarized in schematic morphologies for annealed P3HT:PCBM bulk heterojunction films cast from different solvents. Only pure phases of P3HT (white) and PCBM (black) are pictured and phases with a molecular mixture of P3HT and PCBM, as found recently, are not resolved with these experiments and therefore neglected. The subject of molecularly dissolved PCBM in P3HT phases is addressed in section 5.3.

For films made from chloroform a bilayer structure is found with the disadvantageous inverse arrangement, i.e. the hole conducting material, P3HT, is enriched at the electron extracting electrode, aluminum. Therefore, the found IV-characteristics shows the s-shape due the interfacial barrier. No characteristic lateral structures are found in the inner film region. Consequently, the bad photovoltaic performance is mainly due to the inverse vertical material composition.
On the contrary, the films made of toluene, cholorbenzene and xylene show the correct vertical material composition. Nevertheless, the exact arrangement is different. The films cast from xylene seem to be disadvantageous as features like dominating enrichment layers are missing and short cuts seem to be possible. However, these films show the largest P3HT crystals. In the case of lateral structures, the film made from toluene reveals the

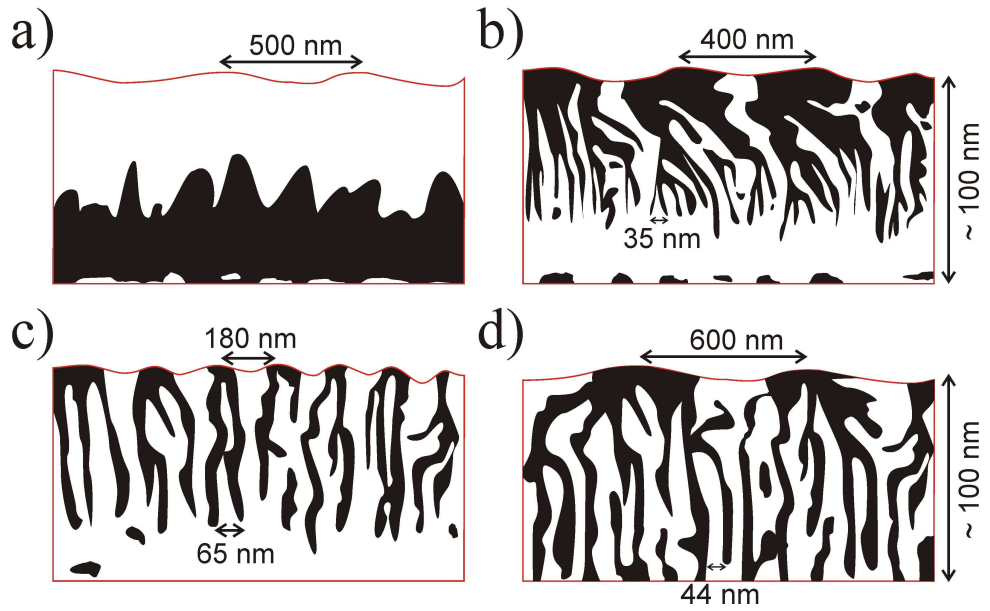

Figure 5.12: *Schematic morphologies of annealed P3HT:PCBM bulk heterojunction films cast from chloroform (a), toluene (b), chlorobenzene (c) and xylene (d) solutions as reconstructed from AFM, GISAXS and XRR analysis. Black and white correspond to pure PCBM and P3HT phases, respectively. Prominent length scales are indicated. The illustration of the films are streched and therefore structures seem more elongated as they are assumed to be.*

smallest size, but additional PCBM is found at the bottom electrode. And finally, the film made using chlorobenzene has a bottom P3HT layer but a considerably higher lateral structure size.

Nevertheless, all these systems show a very similar photovoltaic behavior. It seems that the different problems, i.e. large lateral length scales, missing enrichment layers or small crystal sizes, and the advantageous features observed in the different P3HT:PCBM films cancel each other out concerning photovoltaic performance. However, the exact knowledge of the morphology of the active layer makes it possible to identify different ways for improvement of the structure and thus the photovoltaic performance.

From the finding that the topography does not coincide with the inner film morphology and similar photovoltaic behavior, it has to be concluded that it is not possible to deduce from the photovoltaic characterization and topography measurements on the inner film morphology. In summary, similar IV-curves can result from totally different morphologies.

5.3 Influence of composition

In the previous section, the influence of solvent and thermal annealing on the the morphology of P3HT:PCBM bulk heterojunction films as active layer in a photovoltaic device has

been discussed. The characterization and data analysis is performed under the assumption that just pure phases of P3HT and PCBM exist, i.e. molecular intermixing of P3HT is neglected. However, recent investigations on systems of conjugated polymers with PCBM revealed an intermixing of both components on the molecular scale.[150, 151, 152, 153] These studies probed the molecular miscibility and diffusion of PCBM in different conjugated polymers. It was shown that P3HT and PCBM intermix on a molecular level and that PCBM diffusion is a very fast process. These investigations were performed on bilayer and strongly phase separated systems. In the following section, the morphology of P3HT:PCBM bulk heterojunction films as a function of the blend ratio is probed. The usage of GISANS makes it possible to detect object, structure and domain sizes as well as the molecularly dissolved PCBM ratio.
P3HT:PCBM bulk heterojunction films with a thickness of about 300 nm (profilometer measurements) are prepared via spin coating from chlorobenzene solution and annealed at 140 °C for 10 min in an inert gas atmosphere. blend ratios with a PCBM content of 9 wt%, 25 wt%, 33 wt%, 50 wt% and 67 wt% are used.

5.3.1 Spectral characterization

The wavelength-dependent absorbance of annealed P3HT:PCBM films with different blend ratios reveals features from both P3HT and PCBM (figure 5.13a). As the exact film thicknesses are unknown the absorption coefficient α cannot be calculated from the absorbance spectra. However, from the main P3HT peak intensity A_{P3HT} the film thickness d can be estimated. Using the corresponding absorption coefficient $\alpha_{P3HT} = 0.016$ nm^{-1} of pure P3HT from figure 5.1 and the blend ratio ϕ_{PCBM} of the P3HT:PCBM films the thickness d can be calculated with

$$d = \frac{A_{P3HT}}{\alpha_{P3HT}(1 - \phi_{PCBM})\lg(\mathrm{e})}. \tag{5.1}$$

A thickness of (305 ± 15) nm is revealed for all blend ratios. The thicknesses are in good agreement with the results from measurements with a profilometer.

The PCBM peak position at 335 nm does not change with varying PCBM content. The main P3HT peak at around 500 nm shifts to lower wavelength with increasing PCBM content which is due to an increase of the energy gap, i.e. due to a decrease of the π-electron system. Intra- as well as intermolecular order influence the π-electron system. While the former refers to the conjugation length of a polymer chain, the later describes polymer chain crystallization. The decreased order in both results in a blue shift of the main absorption peak.[25] Furthermore, the absorbance curves reveal shoulder-like features at 550 nm and 600 nm for all blend ratios which is attributed to crystalline P3HT. Hence, P3HT crystallizes in films with different PCBM content but its order is also disturbed

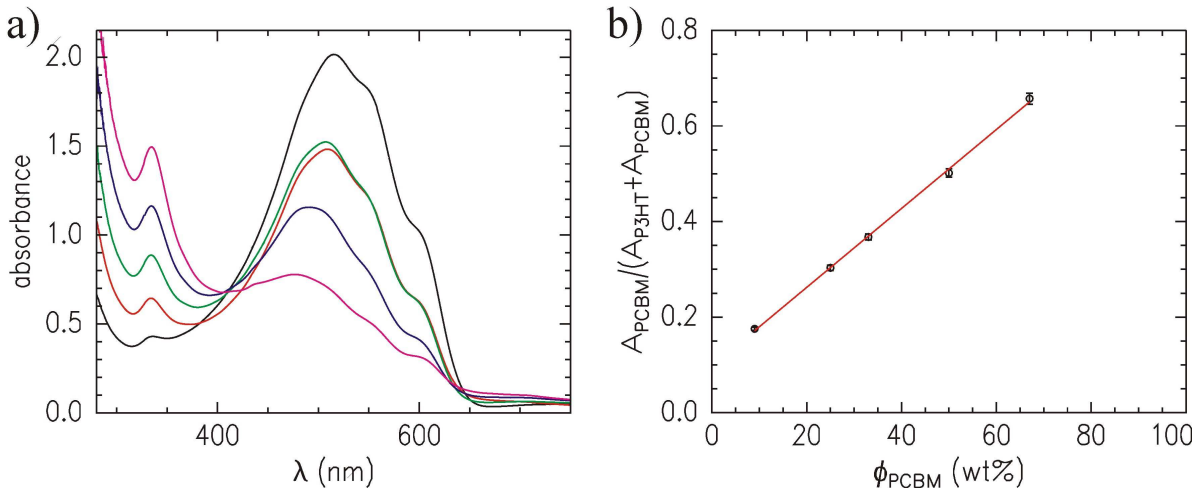

Figure 5.13: *a) Wavelength dependent absorbance spectra of annealed P3HT:PCBM bulk heterojunction films with different PCBM content of 9 wt% (black), 25 wt% (red), 33 wt% (green), 50 wt% (blue) and 67 wt% (magenta). b) The ratio of the PCBM peak intensity at 335 nm compared to the sum of the P3HT and PCBM peak intensities. The uncertanties are obtained from the comparison of absorption data of as-spun and annealed systems. The red line is a linear fit to the data.*

by the presence of PCBM molecules as seen in the shift of the main absorption peak. As already found in the previous section, no additional features appear, so that no significant ground state charge transfer is taking place.[123]

To extract further information on the molecular order of the P3HT chains, the absorbance spectra are analyzed using the weakly coupled H-aggregate model.[23] Details on the H-aggregation of P3HT are discussed in section 2.1.2. The vibronic features, i.e. the shoulders at 550 nm (0-1 transition) and 600 nm (0-0 transition), of the P3HT absorbance spectra are fitted by Gaussian functions. From the ratio of the absorbance peaks, the magnitude of interchain coupling can be estimated within an H-aggregate model.[154] The free exciton bandwidth is found to be about 270 meV for all blend ratios which is high in comparison to other findings.[23] However, the free exciton bandwidth was also found to depend strongly on the solvent used.[155] Therefore, the conjugation length is not altered by the PCBM content but is constant. Consequently, the shift of the main absorbance peak has to be due to a decrease of interchain order as a function of PCBM content. Gao et al. showed that the ratio of aggregated and unaggregated, i.e. amorphous, P3HT phases can be estimated by fitting the vibronic peaks and comparing their areas with the area of the amorphous contribution.[25] The amorphous contribution was obtained by comparing the difference of the absorbance spectrum and the fitting of the vibronic peaks with the absorbance spectrum of a dilute P3HT solution which reveals no crystalline order. Therefore, the spectrum was shifted to the onset of the absorbance spec-

trum. Finally, the spectrum of the solution was fitted by another Gaussian function. The ratio of the areas of the fits of the vibronic and the amorphous fraction is the estimation of the ratio of the aggregated and unaggregated P3HT phases, i.e. the crystallinity.[25]
In this study, the same approach is used to estimate the crystallinity of P3HT in the bulk heterojunction films with different PCBM content. A crystallinity between 60% and 40% is revealed which is decreasing with increasing PCBM content. However, the uncertainty of the estimation is about 15% as the vibronic contributions are no distinct peaks but shoulder-like features. Nevertheless, the decrease in crystallinity explains the blue-shift of the main absorbance peak position nicely. In addition, these crystallinity values are in agreement with literature values.[156]
The studies, mentioned above, found that PCBM does not influence the crystalline organization of P3HT and incorporates only in the amorphous parts of the P3HT phase.[150, 151, 152] However, these studies were performed on layered systems in which the P3HT layer was prepared separately and was able to order undisturbedly. In the bulk heterojunction system discussed here, P3HT and PCBM interact already in the solution and during spin coating. Therefore, a disturbance of the crystalline ordering of P3HT by PCBM is possible. These results are in agreement with findings of Gao et al.[25]
Besides the information on molecular ordering of P3HT the absorbance spectra also confirm the blend ratio of P3HT and PCBM. In figure 5.13b the ratio of the absorbance at 335 nm which is attributed to PCBM and the sum of the P3HT and PCBM peak intensities is shown as a function of the blend ratio. Since the ratios are following a linear function, the actual blend ratio is equal to the blend ratio in the initial solution.

5.3.2 Structural characterization

To probe the detailed morphology of the P3HT:PCBM films with different blend ratios, grazing incidence small angle neutron scattering (GISANS) is chosen. Besides the determination of the structure, special focus is put on molecularly dissolved PCBM in the P3HT phase. The main advantages of using neutron scattering instead of X-ray scattering are that the substrate material, silicon, is transparent for neutrons and also reveals a smaller SLD than PCBM. Therefore, neutron scattering is more sensitive to the material composition of the probed films. In addition, neutrons interact with the atomic nuclei and chemical degeneration of polymers, as it can occur in the case of X-rays, does not take place. The drawback of neutron scattering techniques is the typical low intensity of the primary beam and therefore, counting times in the range of several hours are normal. Due to the high scattering contrast of P3HT and PCBM with SLDs of $0.83{\cdot}10^{-6}$ Å^{-2} and $4.3{\cdot}10^{-6}$ Å^{-2}, respectively, deuteration of one component is not necessary for the

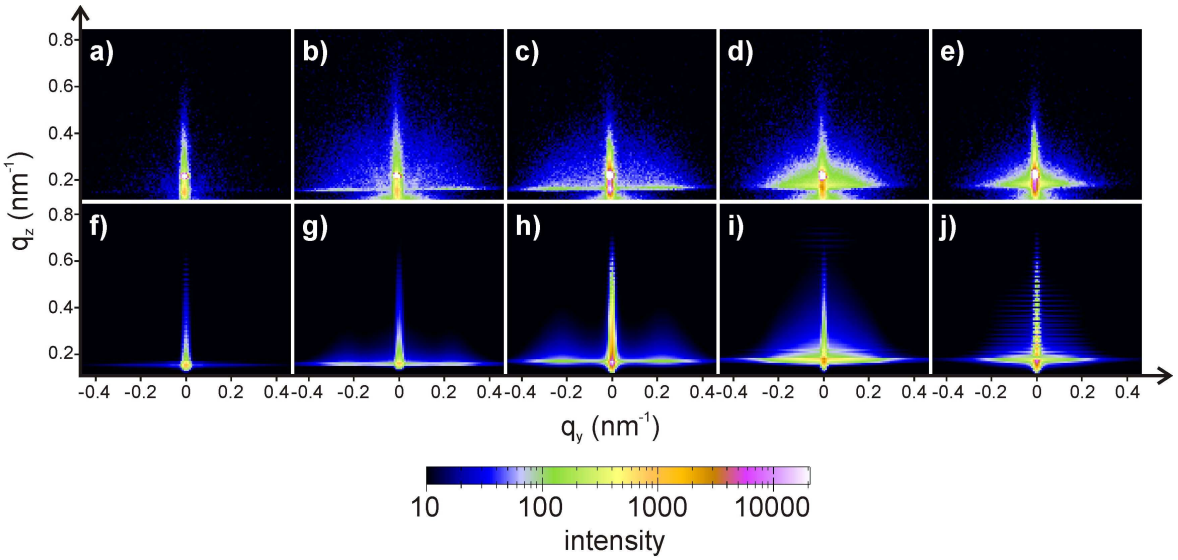

Figure 5.14: *2d GISANS data (a-e) and corresponding IsGISAXS simulations (f-j) of annealed P3HT:PCBM bulk heterojunction films with different PCBM content of 9 wt% (a,f), 25 wt% (b,g), 33 wt% (c,h), 50 wt% (d,i) and 67 wt% (e,j). The same color coding is used for all 2d data.*

investigated system in this study.

In figure 5.14a-e the 2d GISANS scattering data of P3HT:PCBM bulk heterojunction films with different PCBM content are shown. The main changes in intensity occur rather in horizontal than in vertical direction. Therefore, lateral structures alter as a function of the PCBM content. Besides the wing-like features in horizontal direction, also two peaks at $q_y = 0$ are observed. While the peak with the higher intensity is the specular reflection, the second peak is the material sensitive Yoneda peak. The Yoneda peak is shifting to higher q_z values with increasing PCBM content and is therefore probing the P3HT:PCBM material composition.

The program IsGISAXS is used for a detailed quantitative analysis of the scattering data within the DWBA.[85] The simulated 2d IsGISAXS pattern (figure 5.14f-j) are in good agreement with the measured data. PCBM phases in a P3HT matrix are chosen as IsGISAXS model (inclusions encapsulated in a layer on a substrate). The inverted model with P3HT phases in a PCBM matrix is not able to fit the data. In particular, an inverted model revealed a split Yoneda peak instead of a single one as found in the experiment. The layer thickness is set to 300 nm in agreement with the results from the profilometer measurements and the estimations from the absorbance spectra. The PCBM phases are modeled by cylindrical objects which are typically used for polymer blends measured with GISAS due to the rotational isotropy of the samples with respect to rotations around the surface normal.[77] Two form factors describing two different species of PCBM phases and one structure factor are used to fit the GISANS data. Small PCBM objects and

bigger PCBM domains are needed. The scattering data of the P3HT:PCBM films with 25 wt% and 33 wt% PCBM content cannot be fitted by only one PCBM object, but a second, slightly bigger, PCBM object is required. The population of the PCBM domains is found to be below 0.05%. In figure 5.15 the out-of-plane cut of the GISANS data of the P3HT:PCBM film with a PCBM content of 25 wt% with three different fits is shown. The top curve is fitted by a model without the big PCBM domains. Although these domains have a very small population this species is needed to fit the data. Fits with big PCBM domains and one or two smaller PCBM objects are presented in the middle and bottom curves, respectively. It is obvious that for fitting the curve at high q_y values adequately, the second PCBM object is needed.

While the structure factor corresponds to the distance between PCBM objects, the inter-domain distance is not resolved by this GISANS experiment. A one-dimensional paracrystal is used as interference function for the structure factor (section 2.3.3). Gaussian functions are used for the distribution of the structure and the form factors. To account for molecularly dispersed PCBM, the scattering length density of the P3HT phase is fitted. The semicrystalline P3HT phase is treated as one phase in this model as the scattering contrast is low compared to the contrast of P3HT and PCBM. In figure 5.16 a schematic illustration of the used model is shown with PCBM objects of certain size and structural length embedded in a P3HT matrix. The semicrystallinity of P3HT and the big PCBM domains are not depicted. The out-of-plane and detector cuts are fitted simultaneously and the 2d patterns are simulated. The resolution of the instrument used for the GISANS experiments (D22 at ILL) is included by the experimental wavelength

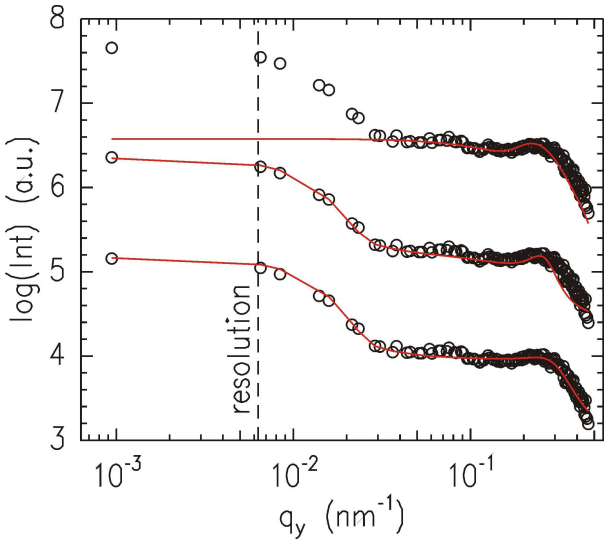

Figure 5.15: *Double-logarithmic plot of out-of-plane cuts taken at the critical angle of PCBM of 2d GISANS measurements from annealed P3HT:PCBM bulk heterojunction films with a PCBM content of 25 wt%. The red lines are fits to the data (black symbols) using different IsGISAXS models. From bottom to top the fits, using the final model with two small objects and one domain, a model with one small object and one domain and a model with only two small domains, are shown. The dashed line indicates the resolution limit. The curves are shifted along the y-axis for clarity.*

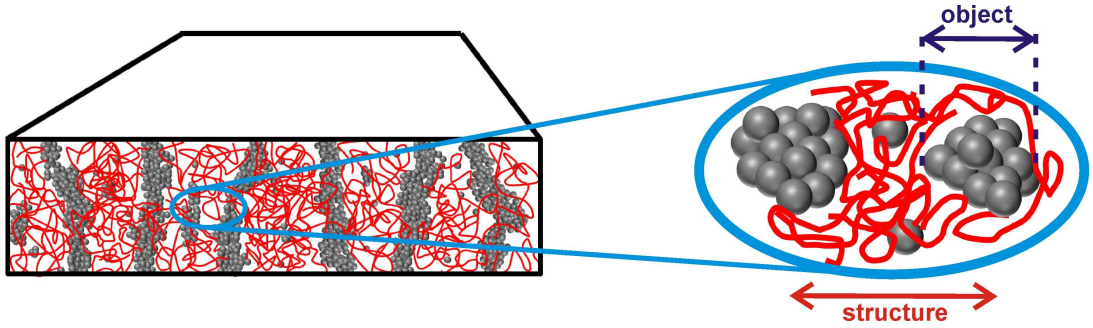

Figure 5.16: *Schematic illustration of the model used for the IsGISAXS simulation. The model consists of objects (PCBM) embedded in a matrix (P3HT) and includes object (blue) and structure (red) sizes. The domains are not shown for clarity. P3HT and PCBM are depicted as red chains and gray spheres, respectively.*

distribution of $\Delta\lambda/\lambda = 10\%$.

The IsGISAXS program was initially developed and used to simulate nanoparticles on a substrate.[85] Therefore, IsGISAXS focuses mainly on lateral structures and misses a possibility to insert an appropriate interface roughness in the models. In addition, multilayer structures cannot be simulated but have to be approximated by only one layer. The Yoneda peak can be fitted sufficiently although it is often not possible to fit the detector cut completely. Moreover, IsGISAXS simulates diffuse scattering only. Therefore, the contributions of the specular reflection and from the transmitted beam are added to the detector cuts by Gaussian functions independent of the IsGISAXS fitting.

The detector and out-of-plane cuts with their corresponding fits are presented in figure 5.17. The fits arise from the complex interplay of the parameters put into the IsGISAXS model described above. In the detector cut the shift of the Yoneda peak (highlighted by an arrow) with increasing overall PCBM content is observed. The shift is due to an increase of the averaged SLD of the P3HT:PCBM bulk heterojunction films and is also represented by the fitting. The exact Yoneda peak position is an interplay of the size and distances of the PCBM phases in the P3HT matrix as well as the P3HT SLD. To fit the Yoneda peak position correctly, the SLD of the P3HT matrix has to be increased in the model used. The increase of the P3HT SLD can only be explained by molecularly incorporated PCBM in the P3HT phase. Therefore, we probe PCBM molecules embedded between P3HT chains. PCBM objects with size as small as 2-3 nm and bigger can already be measured with GISANS and appear in the out-of-plane cut. Since 2-3 nm PCBM objects correspond to an aggregation of three PCBM molecules, the increase in the P3HT SLD is due to single PCBM molecules dispersed in P3HT. The PCBM object sizes and distances as well as the domain sizes contribute mainly to the out-of-plane cuts.

The parameters extracted from the fitting with the IsGISAXS model are summarized in

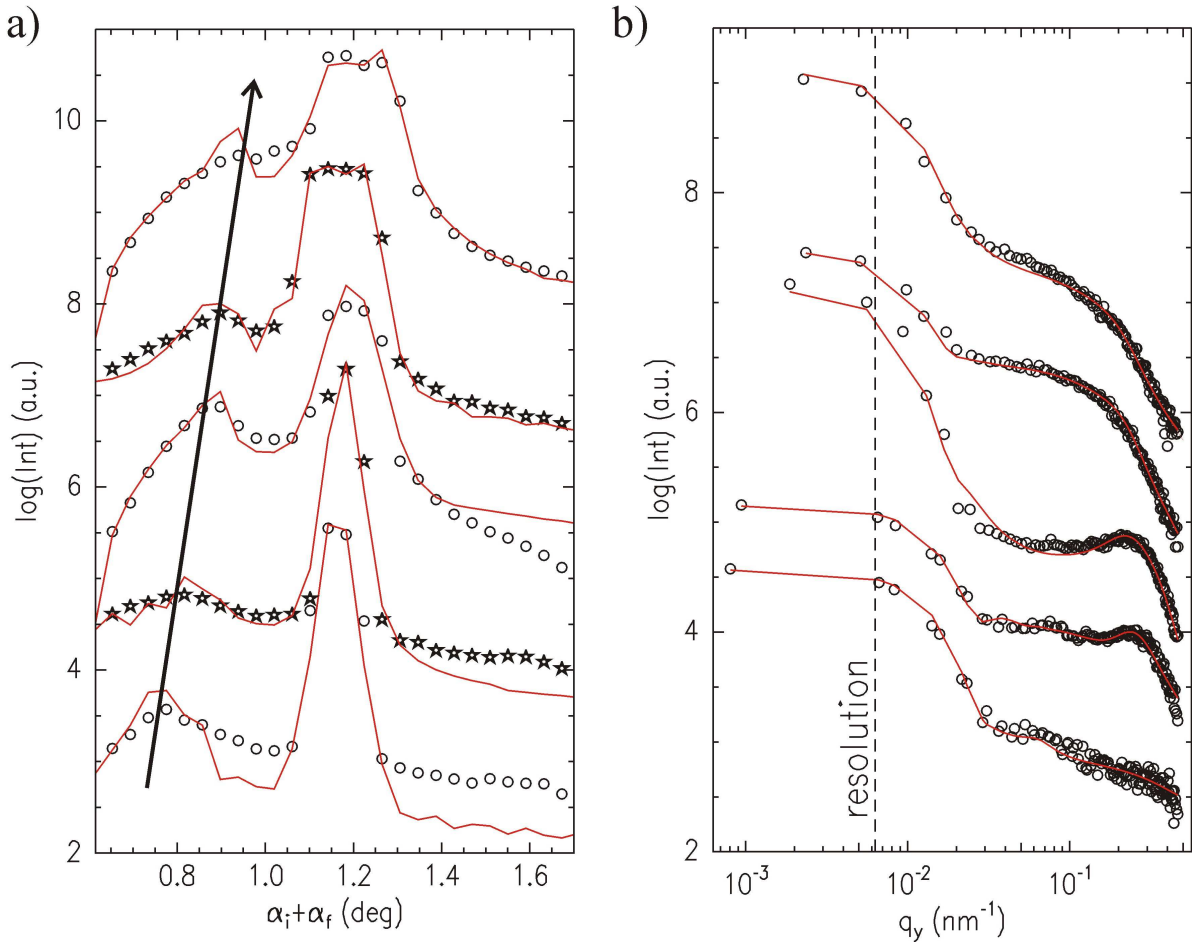

Figure 5.17: *a) Logarithmic plot of detector cuts and b) double-logarithmic plot of out-of-plane cuts taken at the critical angles of PCBM of 2d GISANS measurements from annealed P3HT:PCBM bulk heterojunction films with different PCBM content. The PCBM content of 9 wt%, 25 wt%, 33 wt%, 50 wt% and 67 wt% is increasing from bottom to top. The red lines are fits to the data (black symbols) using IsGISAXS. The arrow and the dashed line indicate the shift of the Yoneda peak and the resolution limit, respectively. The curves are shifted along the y-axis for clarity.*

figure 5.18 as a function of the overall PCBM content. The distribution of the parameters is represented by the error bars (figure 5.18a-c). The dominating PCBM phases are objects with a radius ranging from 3 nm to 10 nm, whereas the largest size is found for the P3HT:PCBM bulk heterojunction films with an overall PCBM content of 50 wt% (figure 5.18a). These objects reveal a population of more than 90%. A second PCBM object with a radius of 18 nm and 16 nm and with a low probability of 1% and 8% is needed to describe the scattering data of the systems with 25 wt% and 33 wt% PCBM content, respectively. A second PCBM object might be required to reproduce the non-equilibirum morphology in such bulk heterojunction systems.

For P3HT:PCBM films with a PCBM content of 9 wt%, a broadly distributed structure

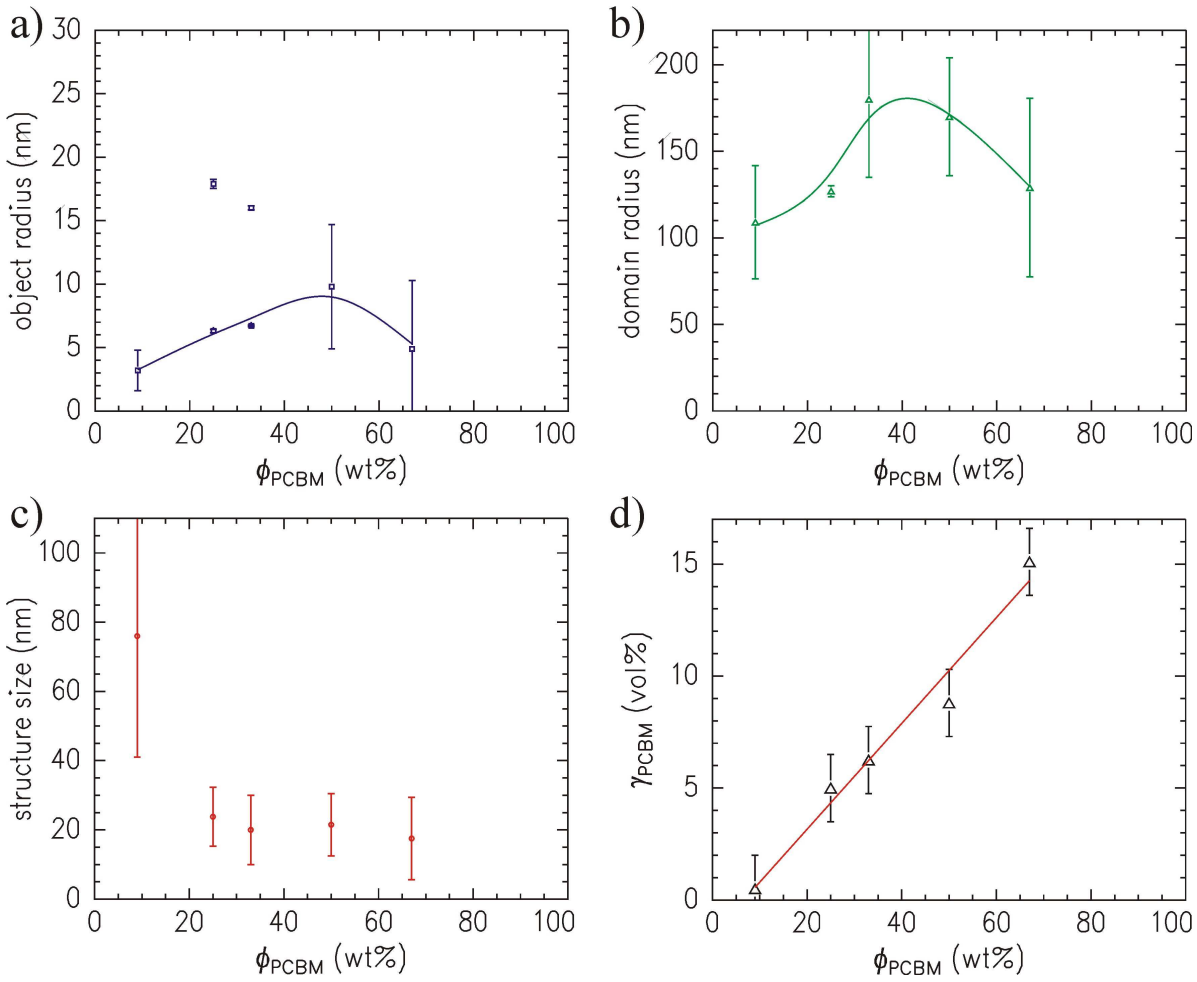

Figure 5.18: *Parameters extracted from the IsGISAXS fitting of the GISANS data shown in figure 5.14. a) Object radius, b) domain radius, c) structure size and d) the fraction of molecularly dispersed PCBM in the P3HT phase depending on the overall PCBM content are shown. The error bars represent the distribution of the length scales (a-c) and the uncertainty (d). The blue (a) and green (b) lines are guide to the eyes and the red line (d) is a linear fit to the data.*

size, i.e. the distance between the PCBM objects, of 80 nm is found. The structure size for the systems with higher PCBM content decreases to about 20 nm independent of the actual blend ratio (figure 5.18a). This structure size is in the range of the exciton diffusion length, thus beneficial for the exciton separation and will finally improve the efficiency. The deviation from the length scale found in section 5.2 for the P3HT:PCBM films made from chlorobenzene is due to the difference of the film thickness. While in this study films with a thickness of 300 nm are characterized, the films in section 5.2 have a thickness of 100 nm. It is well known that structure sizes can change with film thickness.[157] Besides small PCBM objects, also big PCBM domains with a radius of 100 nm to 200 nm are revealed. These domains only have a probability of less than 0.05% and therefore occur

rarely.
In figure 5.18d the volume fraction γ_{PCBM} of molecularly dispersed PCBM in the P3HT phase is depicted as a function of the overall PCBM content. The volume fraction γ_{PCBM} is obtained from the increased SLD of the P3HT matrix needed in the IsGISAXS model to fit the data. For the system with only 9 wt% the PCBM fraction γ_{PCBM} lies in the resolution limit of about 1.5 vol%. With the overall PCBM content, the molecularly dispersed PCBM fraction γ_{PCBM} increases up to 15 vol% for the investigated concentration range.
It was reported by several groups that PCBM does not incorporate in the P3HT crystals but in the amorphous portions of the P3HT phase.[150, 151, 152, 153] Therefore, the actual fraction of molecularly dispersed PCBM in the amorphous part of P3HT is higher. The analysis of the absorbance data revealed a crystallinity between 40% and 60% which is decreasing as a function of the overall PCBM content. Consequently, a molecularly dispersed PCBM fraction γ^*_{PCBM} up to 35 vol% is observed. This limit is in agreement with previous reports[150, 151] and in the range of the miscibility regime ($>$ 42 vol% P3HT) of P3HT:PCBM reported by Kozub et al.[158] In contrast to this, a miscibility limit of 20 vol% was reported by Yin et al. [159] which is challenged by the presented results.

5.3.3 Results

The combination of absorption and GISANS measurements is used to characterize the morphology of P3HT:PCBM bulk heterojunction films as a function of overall PCBM content. Advanced modeling with the weakly coupled H-aggregate model and the DWBA using IsGISAXS reveals detailed knowledge of the P3HT:PCBM film structure. The absorbance spectra exhibit a disturbance of the crystalline (interchain) order of P3HT due to PCBM molecules whereas the conjugation length (intrachain order) stays constant. The crystallinity of P3HT decreases with PCBM content. From the scattering data the inner film morphology is determined. Small PCBM objects and big PCBM domains are found in a P3HT phase. For the blend ratio which typically shows the highest photovoltaic performance (50 wt% PCBM) a structure size fitting the exciton diffusion length is found. In addition, the largest PCBM objects are found for the symmetric blend ratio. Furthermore, the volume fraction of molecularly dispersed PCBM is determined. Together with the crystallinity information from the absorbance analysis a maximum volume fraction of molecularly dispersed PCBM of 35 vol% is found. This finding confirms the results reported on the molecular miscibility of PCBM in conjugated polymers which was found in bilayer and strongly phase separated systems.[150, 151, 152, 153] Moreover, this study extends the previous reports to bulk heterojunction systems.

In general, these findings are of high importance for the modeling of device physics in organic photovoltaic devices. So far, only pure phases were assumed in such modeling.[160] In principal, molecularly dispersed PCBM will improve exciton separation. However, PCBM molecules also can act as traps and will increase geminate recombination. Consequently, additional structural investigations and modeling of the device physics in intermixed phases have to be carried out to understand the influence of molecularly dispersed PCBM.

5.4 Addition of dye

In the previous sections, the influence of external parameters like solvent and blend ratio on the P3HT:PCBM film morphology is detailed. The aim is to understand the influence of external parameters and finally to improve the photovoltaic performance of an organic solar cell by optimizing the morphology. Another approach of enhancing the photovoltaic performance is the introduction of an additional component into the active layer of an organic solar cell. Such an approach results in so-called ternary systems, i.e. a blend of three different materials.
The function of such a third component can be the optimization of the active layer morphology or the change of opto-electronic properties. One of the most common approaches is to broaden the absorption range of the active layer to the IR wavelength range. This is sensible as most polymer:fullerene systems absorb only in a very narrow wavelength range. In the case of P3HT:PCBM systems, for instance, no absorption is taking place above 650 nm (see figure 5.1). One approach to broaden the absorption range is to incorporate particles with plasmonic properties into a bulk heterojunction solar cell.[161, 162] Also the usage of additional organic components with a complementary absorption range in a known donor-acceptor system has been reported. Conjugated polymers as well as organic dyes, such as porphyrins and phthalocyanines, were used as a third component in polymer:fullerene systems.[163, 164, 165, 166, 140, 167, 168] The influence of incorporating a third component on the photovoltaic performance was found to be strongly dependent on the actual component used. Although the absorption range was extended several systems showed a decreased performance. This behavior was related to the aggregation of the dye molecules and an alteration of the morphology which is crucial for the photovoltaic performance. In general, the incorporation of a third component always influences the morphology of the initial system.

5.4.1 Molecular ordering

In this study, the ternary system P3HT:PCBM:OPc with varying OPc content is investigated. The P3HT:PCBM ratio is kept constant at 1:1. Thin films are spin coated from chlorobenzene solution. The absorption coefficient $\alpha(\lambda)$ of the dye OPc reveals three distinct features: at 340 nm and 460 nm characteristic Soret absorption bands and the main absorption at 855 nm (Q-band) with a high absorption coefficient (figure 5.19). With the main absorption peak at 855 nm OPc reveals a complementary absorption range.

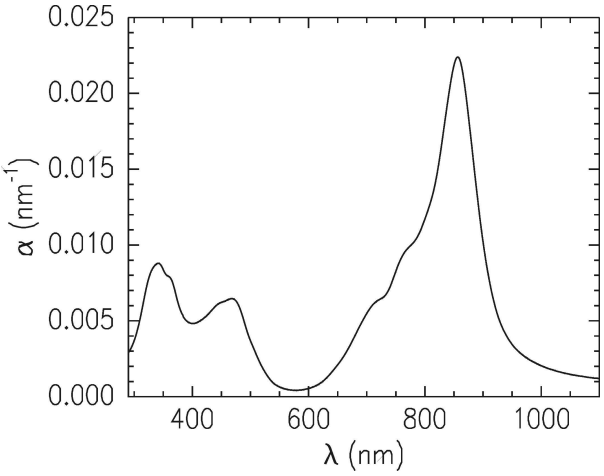

Figure 5.19: *Wavelength dependent absorption coefficient $\alpha(\lambda)$ of the dye OPc.*

Previous reports on the same system revealed that OPc is contributing to the charge carrier generation as seen from external quantum efficiency (EQE) measurements (figure 5.20).[168] For a blend ratio of P3HT:PCBM:OPc = 1:1:0.1, OPc contributed to the charge carrier generation with 10% at 800 nm, determined with EQE. As P3HT and PCBM do not absorb in this region the charge carriers originate from OPc. Besides the additional OPc contribution, also a slight decrease of the EQE in the wavelength range from 400 nm to 650 nm was observed. For higher OPc content the EQE is decreasing dramatically. The authors also performed investigations with transient absorption measurements and suggested a reaction path after the OPc molecule absorbed the incoming light [168]: due to light absorption, an electron is excited on the OPc molecule and directly transferred to a PCBM molecule. The remaining hole is transferred to a P3HT molecule afterwards. Subsequently, the free charge carriers are transported to the electrodes in the P3HT and PCBM phases, respectively. It was concluded that the OPc molecule has to be in contact with both, PCBM and P3HT phases, and therefore resides at the interface of P3HT and PCBM. The strong decrease of the EQE for higher OPc content was related to OPc molecules with no contact to both phases and in addition a disturbed conductivity in P3HT due to the incorporated OPc molecules.[168] However, no additional structural

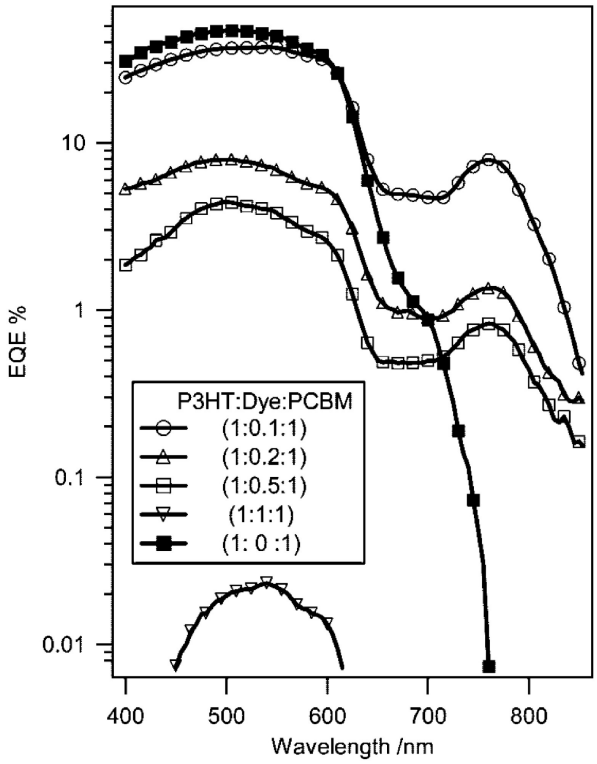

Figure 5.20: *External quantum efficiency of P3HT:PCBM devices with different concentrations of the dye OPc. The figure is taken from reference [168].*

investigations and no further photovoltaic characterization were presented.

The absorption coefficient spectra of as-spun and annealed P3HT:PCBM:OPc ternary blend films (4.8 wt% OPc content) are shown in figure 5.21a. Features of all three components are well represented. In the as-spun case, the P3HT contribution reveals no shoulder-like features as already found for as-spun P3HT:PCBM films (section 5.2). Consequently, P3HT exhibits no or only very low crystallinity. While thermal annealing at 140 °C for 10 min does not change the PCBM features and results in only slight broadening of the OPc peak at 780 nm, the P3HT contribution changes clearly. On the one hand, the main absorption peak is red-shifted which is an indication for increased ordering of the P3HT chains. On the other hand, shoulder-like features appear due to vibrational excitations in P3HT crystals. Consequently, P3HT crystallizes although PCBM and OPc are present. For further analysis, a calculated absorption coefficient spectrum of a ternary film is shown in figure 5.21a. The calculated spectrum is a simple superposition of the as-spun P3HT, PCBM and OPc absorption coefficient spectra weighted with their respective ratios. It is clearly visible that the absorption coefficient of the calculated spectrum is higher compared to the measured ones. This difference in absorption coefficient is attributed to the close interaction of the single molecules which alters the absorption coefficient. Consequently, a simple superposition is not sufficient to estimate the spectra. Nevertheless, the peak position and the shape still reveal information.

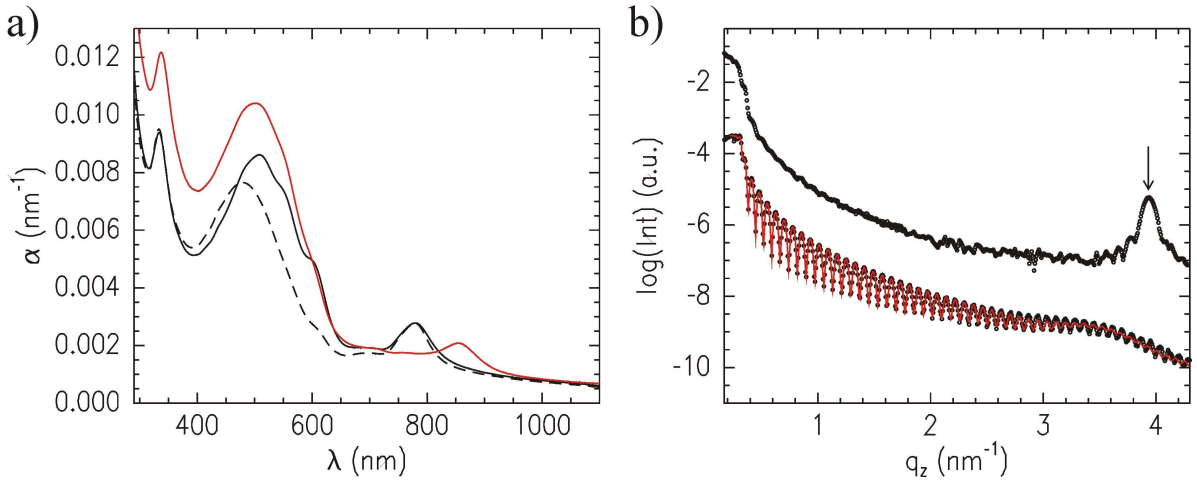

Figure 5.21: *a) Comparison of the measured wavelength dependent absorption coefficient $\alpha(\lambda)$ of as-spun (black dashed line) and annealed (black solid line) P3HT:PCBM:OPc ternary blend films (ratio 1:1:0.1) with the corresponding calculated absorption coefficient (red line). b) X-ray reflectivity data (symbols) with fit (red line) of a ternary blend film (bottom) and an OPc film (top). The Bragg reflection of OPc aggregates is highlighted by the arrow. The curves are shifted along the y-axis for clarity.*

The PCBM contribution at 335 nm stays unchanged when blended with P3HT and OPc regarding peak position and shape. Otherwise the P3HT absorption contribution changes with blending. The position of the main P3HT peak of the calculated spectrum lies between the as-spun and annealed measured spectra. The same is observed for the development of the shoulder-like features representing P3HT crystallization. Consequently, the as-spun ternary film is less ordered than the as-spun P3HT film but thermal annealing reveals an ordering lying between the as-spun and annealed case of pure P3HT. The most remarkable difference of the calculated absorption spectrum and the measured spectra is the large blue shift of the Q-band absorption of OPc from 850 nm to 775 nm. The blue shift is due to a less extended π-electron system. It was reported earlier that the Q-band position is directly connected to the size of the π-conjugated system of the phthalocyanine ring.[169] Due to π-π-stacking of phthalocyanine molecules, i.e. aggregation, the conjugated system is enlarged. In the case of porphyrin aggregates [165] and the confinement of the conducting homopolymer polypyrrole [114], blue shifts were observed.
To probe the film thickness and the ordering of OPc directly, X-ray reflectivity (XRR) is used (figure 5.21b). The thickness is determined to be 64 nm which is extracted from the distances of the Kiessig fringes as the data cannot be fitted due to the high roughness (see section 2.3.2). XRR is typically not applied to detect molecular ordering but to measure film thicknesses. However, XRR is using the same geometry as X-ray diffraction (XRD) measurements just for smaller angles. As the lattice constants of organic crystals are large

in comparison to their inorganic counterparts, the XRR setup used here can detect crystalline order for organic materials with lattice constants above 1.45 nm. In figure 5.21b the XRR curve of an OPc and a ternary blend films are shown. The OPc film reveals a pronounced Bragg reflection at 3.93 nm^{-1} which corresponds to a distance of 1.60 nm. This distance was found for chemically similar phthalocyanine molecules and corresponds to their interstack spacing in aggregates.[170] The XRR curve of the ternary blend film does not reveal a Bragg reflection. So, while OPc aggregates in pure OPc films, no or only little aggregations are formed in the blended films. Consequently, OPc molecules are homogeneously distributed in the ternary film. The vanishing Bragg reflection due to blending is in agreement with the large blue shift of the Q-band found in the absorption spectrum. Thus, the aggregation of OPc can be probed by the Q-band position. The constant Q-band position in the measured absorption spectra of the ternary films (figure 5.21a) is an evidence that OPc does not aggregate even when the system is annealed.

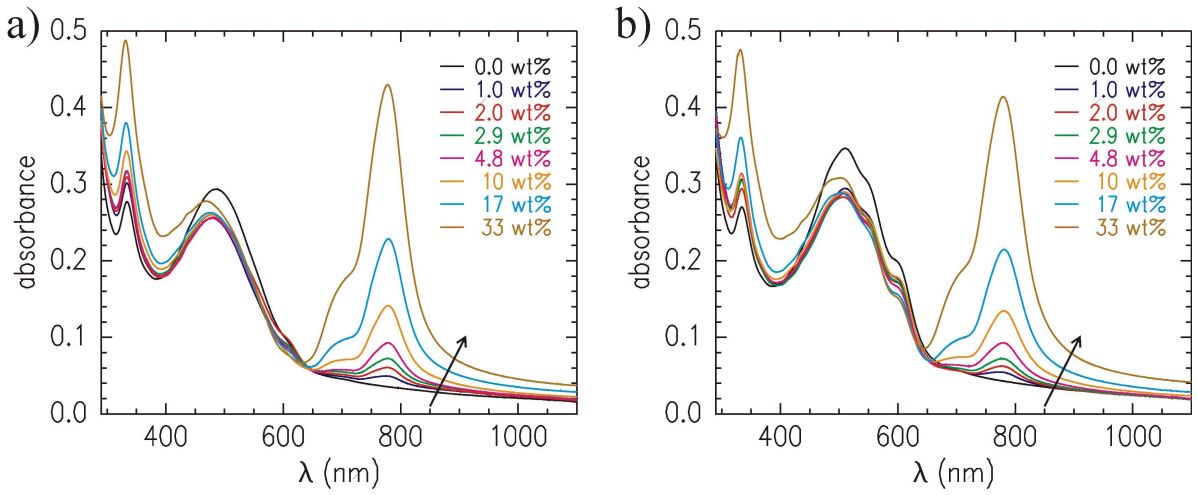

Figure 5.22: *Wavelength dependent absorbance spectra of as-spun (a) and annealed (b) ternary P3HT:PCBM:OPc blend films with different OPc content (from 0 wt% to 33 wt%). The arrows indicate the increasing OPc content.*

The influence of the OPc content up to 33 wt% on the molecular ordering is probed by absorption measurements. In figure 5.22a the absorbance spectra of the as-spun ternary blend films are shown. The OPc Q-band absorption peak increases with the OPc content. In addition, the absorption in the UV-range is enhanced due to the OPc Soret absorption band. The absorption of the P3HT decreases when adding OPc, but then stays unaltered for changing OPc content. The initial drop of the absorbance is due to less P3HT which arises mainly from a smaller film thickness. For the 33 wt% ternary blend film, the absorption peak at 500 nm changes in position and shape which is due to the OPc

absorption. The most remarkable feature is the constant Q-band position which means that OPc forms no or just small aggregates in ternary P3HT:PCBM:OPc films with at least up to 33 wt% OPc content.

Thermal annealing changes the absorbance spectra only partly (figure 5.22b). The major changes are the appearance of shoulder-like features at 550 nm and 600 nm which are due to the crystallization of P3HT. These shoulders do not change with OPc concentration and it therefore seems that OPc does not incorporate inside the P3HT crystals. This finding is in agreement with the results on molecularly dispersed PCBM which are discussed in section 5.3. It was found that PCBM does not embed in the P3HT crystals but in the amorphous P3HT phase.[150, 151, 152] The PCBM contribution stays unaltered as already known from thermal annealing of P3HT:PCBM systems without dye. The OPc Q-band absorption changes only slightly in absorbance and reveals a red shift of about 1 nm. Consequently, also thermal annealing does not result in a significant aggregation of OPc which leads to the conclusion that the dye molecules are homogeneously distributed in the ternary blend.

In figure 5.23 optical micrographs of the ternary P3HT:PCBM:OPc blend films with different OPc content are shown. With increasing dye concentration the overall color of the micrographs changes due to the altered absorption of the films. Except for the change of color, no significant difference are observed. Homogeneous films form independently of the OPc content. In addition, the dye content does not enhance PCBM cluster formation or cluster itself.

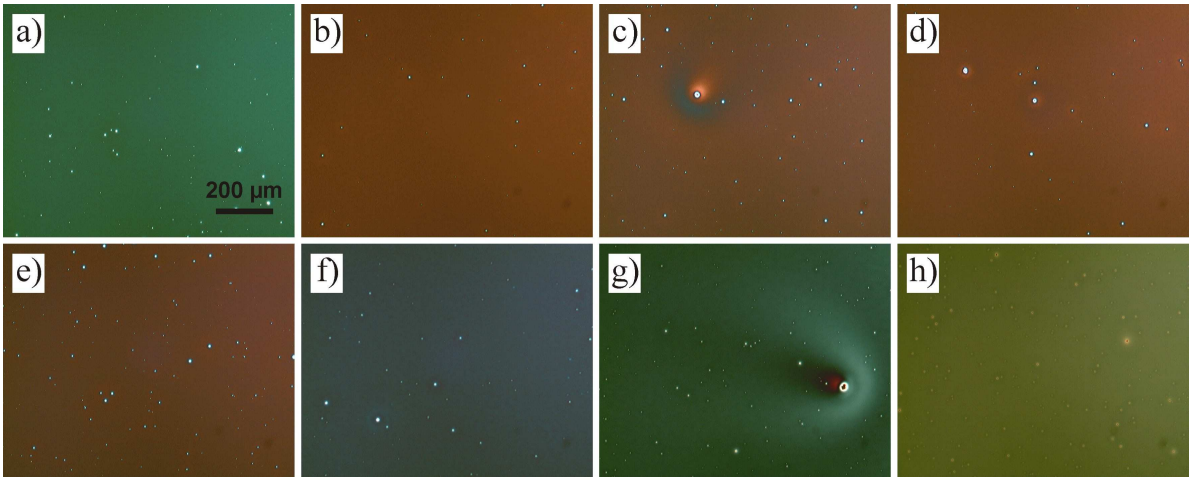

Figure 5.23: *Optical micrographs of as-spun ternary P3HT:PCBM:OPc blend films with 0.0 wt% (a), 1.0 wt% (b), 2.0 wt% (c), 2.9 wt% (d), 4.8 wt% (e), 10 wt% (f), 17 wt% (g) and 33 wt% (h) OPc content. The micrograps are taken at magnifications of 10× (a-d) and 100× (e-h). The scale bars are valid for all micrographs with a magnification of 10×.*

5.4.2 Photovoltaic characterization

P3HT:PCBM:OPc ternary blend solar cells are characterized to determine the photovoltaic performance as a function of the OPc content. While P3HT:PCBM solar cells without dye reached an efficiency of 3.3% under AM1.5G illumination (100 mw/cm^2), already the addition of 0.01 wt% OPc decreases the efficiency. OPc and P3HT compete for photons as both components have an overlap in absorption. However, due to the smaller absorption coefficient in the overlap region and less amount of OPc compared to P3HT this cannot explain the drop in efficiency to 0.6%. In figure 5.24 the open-circuit voltage U_{OC} and the short-circuit current I_{SC} are shown as a function of the OPc content. The decrease of the open-circuit voltage is due to a higher internal resistance in the solar cell. Similar behaviors were already reported for porphyrins and phthalocyanine dyes in ternary systems.[166, 167] Additionally, dye molecules act as traps and increase the recombination and therefore decrease the open-circuit voltage.

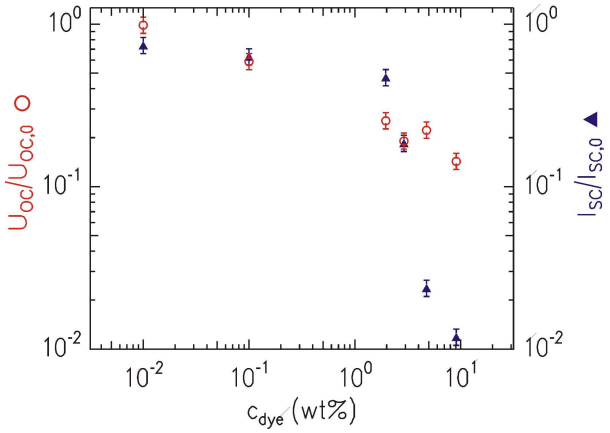

Figure 5.24: *Double-logarithmic presentation of the open-circuit voltage U_{OC} (red open circles) and the short-circuit current I_{SC} (blue filled triangles) as a function of the OPc content c_{dye}.*

The incorporation of OPc in the P3HT:PCBM bulk heterojunction film decreases also the short-circuit current I_{SC}. A two step process is suggested by the initially smaller decrease and the following dramatic drop of the short-circuit current for OPc contents above 2 wt% (figure 5.24). The EQE characterization in figure 5.20 shows besides the additional contribution from OPc also a slight decrease for the P3HT contribution and a drastic reduction over the full wavelength range for higher dye concentrations.[168] Considering the decrease of the photovoltaic performance, it has to be concluded that the gain of additional charge carriers due to OPc absorption cannot compensate the decrease of P3HT and PCBM EQE. Therefore, OPc has to increase the recombination of charge carriers and thus influence the charge transport negatively. From the absorbance data it is concluded that OPc does not incorporate in the ordered P3HT phases. Consequently, OPc is distributed in the amorphous P3HT and in the PCBM phases. The energy levels

of OPc are unknown. However, from the OPc absorption bands in the UV-range (around 3.7 eV), it is concluded that OPc can also act as a trap for charge carriers. Therefore, OPc affects the charge carrier transport and increases recombination. In addition, the influence of already small amounts of OPc on the P3HT:PCBM bulk heterojunction morphology, which influences the photovoltaic performance, cannot be eliminated. The dramatic drop in efficiency might be connected to major morphology changes due to the increasing OPc content. Honda et al. suggested a decreasing absorption due to aggregation of a phthalocyanine dye.[167] However, OPc aggregation does not take place as confirmed by absorption measurements (figure 5.22).

5.4.3 Results

It is shown by XRR measurements that the aggregation of OPc can be probed by the Q-band position of OPC in the absorption spectra. The Q-band is blue-shifted in its unaggregated state. In ternary blend P3HT:PCBM:OPc films, OPc does not aggregate at least up to a OPc content of 33 wt%. Even thermal annealing does not influence OPc aggregation while P3HT does order. From the absorbance data, it can be concluded that OPc does not disturb P3HT ordering and that OPc therefore incorporates preferentially in the PCBM and amorphous P3HT phases. Although EQE characterization by previous reports showed additional charge carrier generation due to OPc (figure 5.20) and the absorption increases with OPc content, the photovoltaic performance in ternary blend P3HT:PCBM:OPc systems is reduced. For small OPc content the reduction in efficiency is attributed to OPc acting as charge carrier traps. Major changes of the bulk heterojunction morphology are suggested as the dominating parameter for the drop in efficiency at high OPc concentration.

5.5 Summary

In this chapter the influence of thermal annealing, solvent and composition on the morphology of P3HT:PCBM bulk heterojunction systems are investigated. The comparison of the exact morphology and the photovoltaic performance of P3HT:PCBM solar cells cast from different solvents reveals that significantly different morphologies can result in similar IV-curves. The favorable structural features, such as length scales in the range of the exciton diffusion length, and the unfavorable morphology, such as small P3HT crystals, cancel each other out. Consequently, it is not possible to gather the morphology of active layers in organic solar cells only from IV-curves and topography measurements. For an entire understanding, the complete morphology has to be determined which is obtained for the first time in this thesis.

For the first time the fraction of molecularly dispersed PCBM in the amorphous P3HT phase of a P3HT:PCBM bulk heterojunction is determined. It is found that the molecularly dispersed PCBM fraction increases linearly with the overall PCBM content. In addition, the detailed morphology, in terms of PCBM objects distributed in a P3HT phase, is obtained. The crystallinity of P3HT is estimated by fitting absorption data by a weakly coupled H-aggregate model. For the most efficient P3HT:PCBM composition of 1:1, the largest PCBM objects with a structure size in the range of the exciton diffusion length are found.

To extend the absorption range of P3HT:PCBM to the IR-range, the dye OPc is added. The dye is homogeneously distributed in the ternary P3HT:PCBM:OPc film independent of the dye fraction. Clustering of the dye does not take place. Although the dye absorption results in additional charges, the total efficiency decreases. The reduction of the photovoltaic performance is explained by a two step process. At low dye concentrations, the dye acts as a trap and decreases the charge carrier mobility. For higher dye content, the efficiency drops dramatically which is attributed to major changes of the morphology.

Chapter 6

Characterization of polymer-polymer systems

Besides the combination of a conjugated polymer with a fullerene derivative, the composition of two conjugated polymers is used as the active layer in organic solar cells.[105] However, these so-called all-polymer systems have suffered from low efficiencies so far. The most efficient solar cells are based on the combination of different polyphenylenevinylenes (PPVs) and polythiophenes and show efficiencies of approximately 2%.[106, 171, 172, 173] The low photovoltaic performance was attributed to the typical low electron mobilities and suboptimal LUMO levels in conjugated polymers. It was stated that the synthesis of new electron-accepting polymers with high electron mobilities and low LUMO levels, which drive the charge separation, would improve the photovoltaic performance.[105]
The advantage of the usage of polymers as electron accepting materials instead of fullerene derivatives is the higher variability in terms of adapting the chemical structure of polymers. Moreover, the mechanism of structure formation in polymer blends is already well understood (see section 2.2.2) and relatively pure phases are achieved in polymer blends. In particular, the fast diffusion of fullerene derivatives in conjugated polymers [151, 153] as discussed in section 5.3 does not take place in all-polymer systems. In addition, it was shown that in the case of the combination of poly((1-methoxy)-4-(2-ethylhexyloxy)-p-phenylene-vinylene) (MEH-PPV) and P3HT a minimum structure size was found at the critical blend ratio calculated from the Flory-Huggins theory.[174]
Similar to polymer:fullerene systems, the morphology formation in all-polymer systems is a self-assembly process and influenced by external parameters.[9] In this chapter, the morphology of all-polymer systems is investigated as a function of the annealing temperature and blend ratio using scattering techniques. The investigated systems contain polyalkylthiophenes as the electron donors and different electron acceptor polymers.
The influence of the annealing time on the internal structure and photovoltaic perfor-

mance of one of the most efficient all-polymer systems, P3HT:F8TBT [173], is examined using by GISAXS (section 6.1). In section 6.2 the polymer blend P3HT:MEH-CN-PPV is investigated. The blend ratio dependent structure formation is probed using grazing incidence RSoXS and imaging methods. Finally, the process of thermal annealing on the morphology and especially the crystallinity of P3OT:CN-PPV is studied (section 6.3). Results of this chapter have been published in references [138, 175].

6.1 Influence of annealing temperature

Organic solar cells made of P3HT and F8TBT have shown an efficiency of 1.8% [173] and are therefore one of the all-polymer systems with the highest photovoltaic performance. Previous investigations revealed an increase in photovoltaic performance due to annealing. This improvement was attributed to a more efficient electron-hole pair separation resulting from an increased hole mobility in P3HT and advanced phase separation. Thereby, higher hole mobilities arise from enhanced P3HT ordering.[176]
In this section, the knowledge about photophysics and photovoltaic performance of these systems is summarized [138] and then compared to GISAXS measurements performed in the framework of this thesis. P3HT:F8TBT films with a thickness of 70-80 nm are spin coated from a 70 °C hot, anhydrous xylene solution. The blend ratio is chosen to be 1:1. The films are thermally annealed at different temperatures (up to 220 °C) for 10 min. The sample preparation is performed in an inert gas atmosphere.

6.1.1 Photophysics and device characteristics

The absorption and photoluminescence (PL) behavior of P3HT is described above (see section 5.1). F8TBT absorbs in the same region as P3HT due to similar band gaps. However, F8TBT revealed a narrower absorption spectrum with no vibronic features. In contrast, F8TBT showed a higher photoluminescence quantum efficiency (PLQE) of 35% compared to 4% for P3HT. In the P3HT:F8TBT blends the PL intensity was quenched below 4%.[138]

The absorption and PL spectra of P3HT:F8TBT blends altered due to annealing. Already at 100 °C vibronic features in the P3HT contribution of the absorption spectrum appeared. Consequently, intermolecular ordering of P3HT chains took place. Also for higher temperatures the vibronic features were observed whereby the vibronic contributions stayed constant. The overall absorption decreased for temperatures above 180 °C. Furthermore, the PL intensity decreased for annealing temperatures below 120 °C due to ordering of P3HT. For higher temperatures the PL spectra was dominated by F8TBT and therefore the PL intensity increased. However, the PLQE was found to be still low

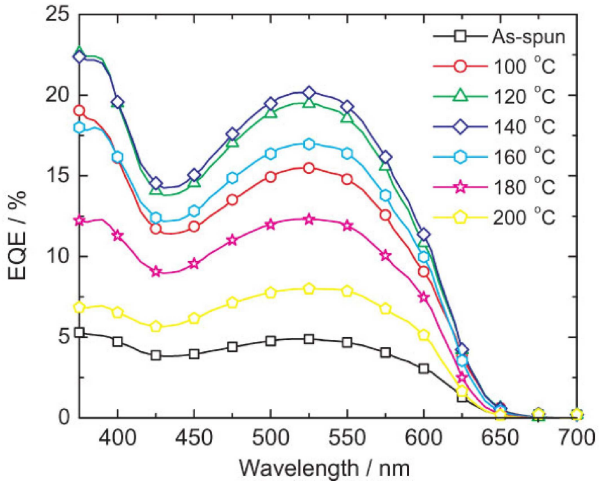

Figure 6.1: *Wavelength dependent external quantum efficiency (EQE) of P3HT:F8TBT photovoltaic devices. EQE curves for devices annealed at different temperatures are shown. The figure is taken from reference [138].*

compared to pure F8TBT which was attributed to F8TBT domains with a size of the exciton diffusion length or a small P3HT content in the F8TBT phases. Therefore, excitons were quenched before radiative recombination.[138]
In figure 6.1 the external quantum efficiencies (EQE) of organic solar cells with an active layer made of P3HT and F8TBT are shown as a function of the annealing temperature. With increasing annealing temperature the EQE increased over the whole wavelength range. A maximum was reached for thermal treatment at 140 °C. For higher temperatures the efficiency decreased again. Also for the photovoltaic performance measured under AM1.5 (100 mW/cm^2) conditions a maximum was found for systems annealed at 140 °C.[138]

6.1.2 Structural characterization

Besides the knowledge on intermolecular ordering of P3HT extracted from the absorption and PL data, the phase separation on mesoscopic length scales is important to understand the obtained photovoltaic behavior. Therefore, GISAXS measurements are performed to probe the inner film morphology. The 2d GISAXS data of as-spun and annealed P3HT:F8TBT films are shown in figure 6.2. A narrowing of the scattering pattern is observed with increasing annealing temperature which is due to a coarsening of the inner film structure. Although the intermolecular ordering, i.e. crystallization, in the polymer blends showed no further development for temperatures above 100 °C as seen in the absorption spectra, phase separation is ongoing with higher temperatures. In addition, the scattering pattern elongates in vertical direction resembling changes perpendicular to the sample surface.

For a quantitative analysis out-of-plane and detector cuts for the as-spun as well as the

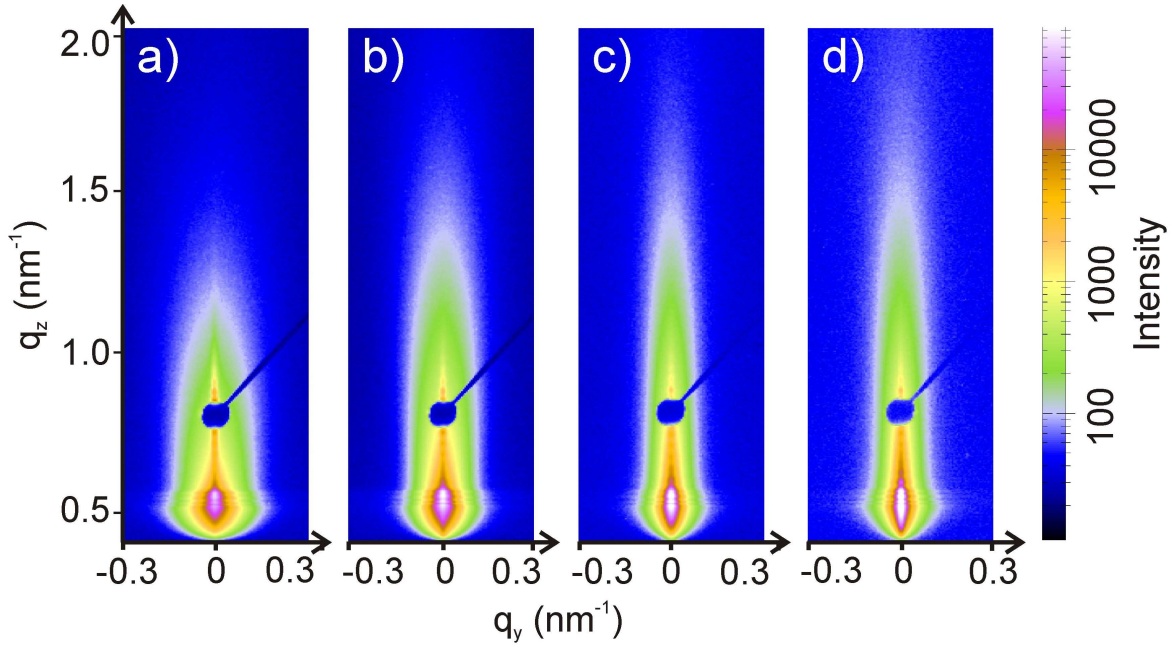

Figure 6.2: *2d GISAXS data of P3HT:F8TBT blend films a) as-spun and annealed at b) 100 °C, c) 140 °C and d) 180 °C for 10 min. The same color coding is used for all images.*

annealed samples are shown (figure 6.3). The out-of-plane cuts (figure 6.3a) are fitted using the effective surface approximation within the DWBA (section 2.3.3). Independent of the annealing temperature a structure size of several hundred nanometers is extracted from the fitting. The distribution of the structure size narrows with annealing temperature. Consequently, these large structures are predominant as the width of the distribution represents the polydispersity of this large structure. For the as-spun film no additional lateral length scale is revealed. However, with annealing a second, smaller structure size appears. This smaller, temperature dependent structure size resembles the evolution of phase separation. For an annealing temperature of 100 °C a structure size of about 25 nm is found. The structure size grows for higher temperatures to 100 nm and 150 nm for 140 °C and 180 °C, respectively. The large structure sizes and the low PLQE for the blends annealed at 180 °C provide evidence that there are still small portions of P3HT in the F8TBT phases and no pure F8TBT phases are formed. The P3HT portion quenches the PL signal of F8TBT resulting in a low PLQE.

The maximum in photovoltaic performance is found for systems annealed at 140 °C although a structure size of 100 nm, which is significantly larger than the exciton diffusion length known for P3HT, is revealed for such a system. For F8TBT a slightly higher exciton diffusion length was suggested.[177] In addition, as the phases in all-polymer systems are purer compared to fullerene-based systems (see previous chapter), the effective exci-

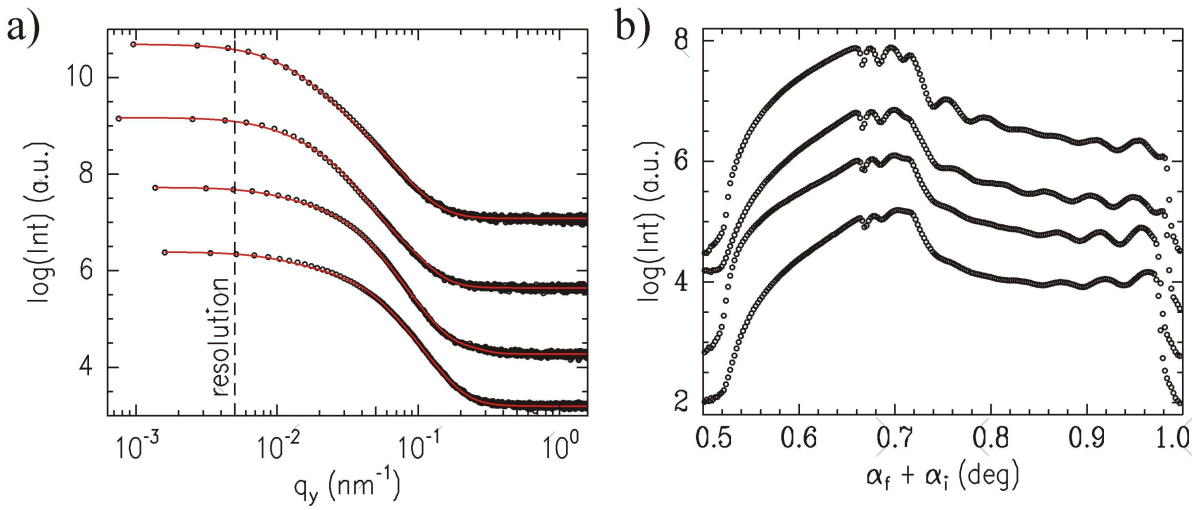

Figure 6.3: *a) Double-logarithmic plot of out-of-plane cuts taken at the critical angle of P3HT and b) logarithmic plot of detector cuts of 2d GISAXS measurements of P3HT:F8TBT blend films. From bottom to top the data for as-spun and annealed at 100 °C, 140 °C and 180 °C films are shown. The red solid lines are fits to the data using the effective surface approximation model. The dashed line indicates the resolution limit. The curves are shifted along the y-axis for clarity.*

ton diffusion length of P3HT in all-polymer systems will be higher than in P3HT:PCBM systems due to fewer recombination sites. Furthermore, structure sizes larger than the exciton diffusion length are favorable as charge carrier recombination during the charge transport to the electrode is reduced.

In figure 6.3b the detector cuts around the Yoneda region of the P3HT:F8TBT GISAXS data are shown. The Yoneda peak position is independent of the annealing temperature as it is defined by the material investigated. Interesting features are the oscillations between the Yoneda peak ($\alpha_f + \alpha_i = 0.72°$) and the specular peak ($\alpha_f + \alpha_i = 1°$). These oscillations represent correlated roughness which means that a layer follows the structure or roughness of an underlying interface. The periodicity of the correlated roughness corresponds to a multiple of the layer thickness. In addition, a beat frequency of the correlated roughness is found. A beat frequency appears when the scattering signal of two layers with similar thicknesses interferes. With annealing temperature the beat frequency changes which is direct evidence for material segregation in vertical direction. Previous investigations with X-ray photoelectron spectroscopy (XPS) of the same system demonstrated the existence of P3HT-rich capping and wetting layers [176] and are therefore consistent with the results presented in this thesis.

6.1.3 Results

GISAXS is used to probe the inner film morphology of the all-polymer system P3HT: F8TBT as a function of annealing temperature and to understand the findings from spectroscopic and photovoltaic characterization. For an annealing temperature of 140 °C a maximum in device performance was found. Intermolecular ordering of P3HT extracted from absorption and PL measurements reached a plateau at 100 °C. GISAXS provided evidence for vertical stratification of the P3HT and F8TBT due to thermal annealing. In addition, a coarsening of the structure in the polymer blend film occurs with annealing. A structure size of 100 nm is found for the system with the maximum photovoltaic performance. An optimal structure size above the exciton diffusion length is a best compromise between effective exciton dissociation and charge extraction. Whereas a small structure size in the range of the exciton diffusion length improves the exciton dissociation, it is also disadvantageous for charge extraction as the probability of charge carrier recombination increases. In contrast, large structures favor charge extraction but excitons will rather recombine than reach an interface for dissociation. So, the highest photovoltaic performance is expected at intermediate length scales.

6.2 Influence of composition and annealing

In this section, the morphology of the all-polymer system P3HT:MEH-CN-PPV as a function of blend ratio is investigated using imaging techniques and soft X-ray scattering (GI-RSoXS). Both materials have been used in the most efficient all-polymer solar cells [106, 173]. However, no study using the combination of both polymers in one system has been published yet. In such a combination, P3HT acts as the electron donor and MEH-CN-PPV as the electron acceptor. After the characterization of the spectral properties of this system, the crystalline properties of pure P3HT and pure MEH-CN-PPV as well as of the corresponding blends are presented. In addition to the investigations of the structure, the options of GI-RSoXS in terms of tuning the X-ray energy are demonstrated.
P3HT:MEH-CN-PPV films are spin coated from chloroform solution with different blend ratios. The ratios are varied from 21 wt%, 28 wt%, 44 wt%, 54 wt% to 70 wt% P3HT content. Annealing is performed at 200 °C for 10 min in air.

6.2.1 Spectral characterization

In figure 6.4a the absorbance spectra of as-spun and annealed (200 °C) P3HT and MEH-CN-PPV homopolymer films are shown. Annealed P3HT reveals vibrational shoulders which is indication for crystalline P3HT as has been discussed in section 5.1. In compar-

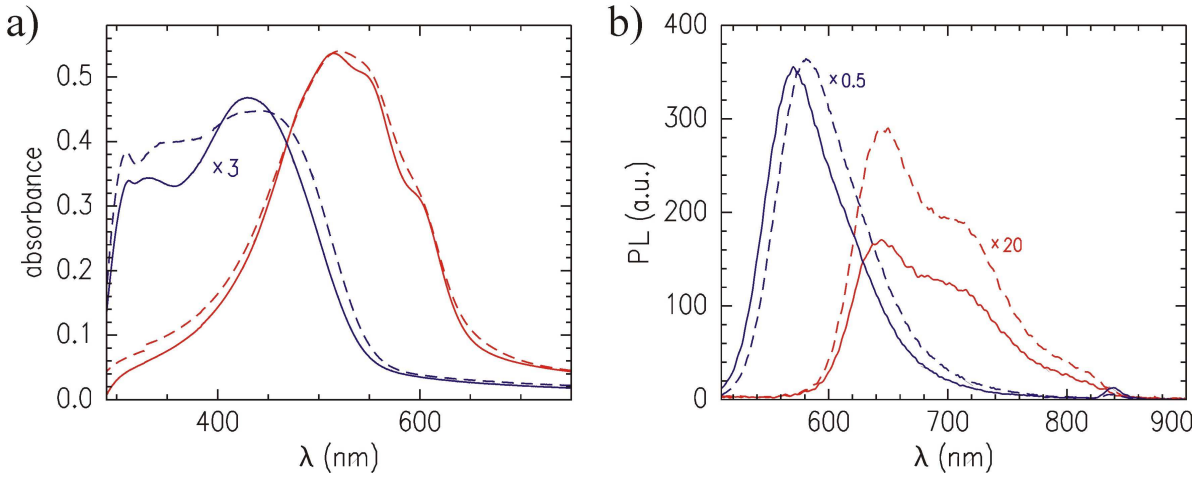

Figure 6.4: *a) Wavelength dependent absorbance spectra and b) photoluminescence (PL) of as-spun (dashed lines) and annealed (solid lines) P3HT (red) and MEH-CN-PPV (blue) thin homopolymer films. The excitation wavelengths are 485 nm and 425 nm for P3HT and MEH-CN-PPV, respectively. The PL spectra of MEH-CN-PPV are corrected for different slit settings. Both absorbance curves and the as-spun PL curve of MEH-CN-PPV are multiplied by 3 and 0.5, respectively. Both PL curves of P3HT are multiplied by 20.*

ison, MEH-CN-PPV shows no features which indicates that no crystalline fractions exist although MEH-CN-PPV has been annealed. However, the main absorption peak narrows which is an evidence for molecular rearrangement due to annealing. In addition, MEH-CN-PPV shows a smaller absorption compared to P3HT. The main absorption takes place from the UV range up to a wavelength of 550 nm. The corresponding PL spectrum exhibits a very high luminescence for as-spun MEH-CN-PPV (figure 6.4b) which diminishes due to annealing. The decrease in PL originates from molecular ordering of the polymer chains whereas no crystallization occurs. Also in the PL spectrum of MEH-CN-PPV no crystalline features such as shoulders are observed. The luminescence of P3HT also decreases due to annealing but not as dramatic as for MEH-CN-PPV.

When P3HT and MEH-CN-PPV are blended (28 wt% P3HT content), the absorbance spectrum follows a linear superposition of the homopolymer absorbance spectra (figure 6.5). Therefore, no significant ground-state charge transfer occurs.[123] Although MEH-CN-PPV is the majority component, the spectra are dominated by the P3HT contribution. Due to annealing shoulder-like features of P3HT representing crystallinity appear. In contrast, the PL spectra are dominated by MEH-CN-PPV. Compared to the PL of the homopolymer films, the blended films reveal a reduced signal which is an indication for exciton dissociation arising from the blending of P3HT and MEH-CN-PPV. Similar to the homopolymer films the PL signal decreases with annealing of the blend film.

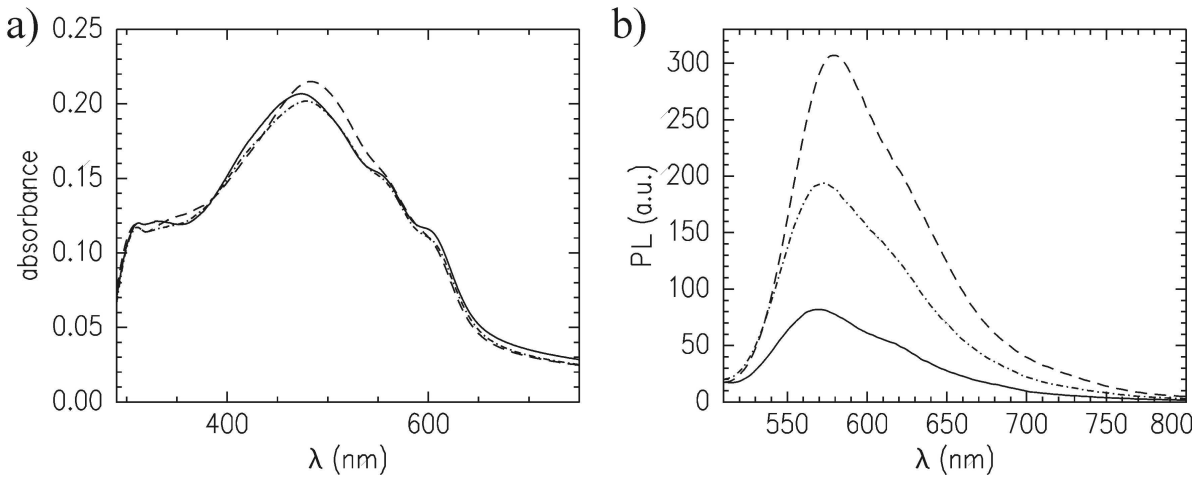

Figure 6.5: *a) Wavelength dependent absorbance spectra and b) photoluminescence (PL) of as-spun (dashed line) and annealed at 140 °C (dotted-dashed line) and 200 °C (solid line) P3HT:MEH-CN-PPV blended films. The P3HT content is 28 wt%. The PL spectra are measured with an excitation wavelength of 485 nm.*

Consequently, blending seems not to hinder the molecular rearrangement of P3HT and MEH-CN-PPV when annealed. In fact, excitons are separated at the polymer-polymer interface.

6.2.2 Crystalline structure

To probe the crystalline order directly, GIWAXS measurements of the P3HT and MEH-CN-PPV homopolymer films are carried out (figure 6.6). The data of MEH-CN-PPV reveal no Bragg peaks even when annealed. Thus, MEH-CN-PPV is amorphous as already indicated by the missing features in the absorbance and PL spectra. The crystallization of MEH-CN-PPV is most probably prevented by the branched side chains and the cyano-groups which are attached to the polymer backbone, but stick out of the conjugation plane (figure 4.1). Thus, both hinder ordering sterically. In contrast, P3HT exhibits already (100) and (010) Bragg peaks in the as-spun case. Furthermore, the Bragg peaks amplify with annealing and higher orders appear. As the (100) and the (010) Bragg peaks are more pronounced in the horizontal and the vertical sector integrals, respectively, than in the other directions, it can be concluded that P3HT orders in a face-on arrangement in this case.

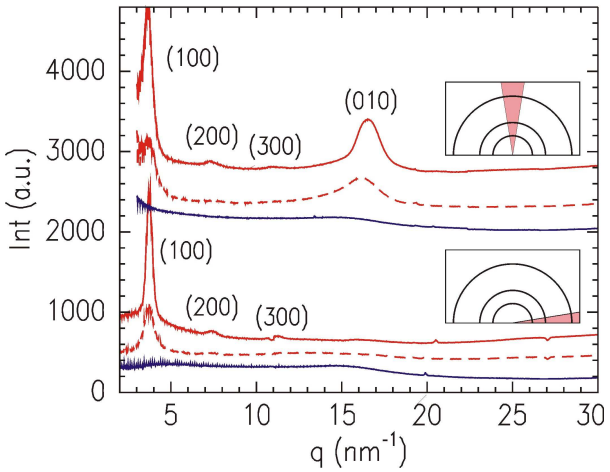

Figure 6.6: *Vertical (upper three curves) and horizontal (lower three curves) sector integrals of GIWAXS measurements of as-spun (dashed lines) and annealed (solid lines) P3HT (red) and MEH-CN-PPV (blue) homopolymer films. Thermal annealing is performed at 160 °C for 10 min. Bragg peaks are indicated. The curves are shifted along the y-axis for clarity. The orientation of the sector integrals is illustrated by the pictograms (inset).*

In figure 6.7a the sector integrals of P3HT:MEH-CN-PPV bulk heterojunction films with different blend ratios are shown. With increasing P3HT content, the Bragg reflections get more pronounced as can be seen from the (100) signal. The increase in intensity is simply due to the higher amount of P3HT. However, the (010) peak intensity depends on the blend ratio which means that the orientation of the P3HT crystals relative to the substrate, i.e. face-on or edge-on orientation, depends on the P3HT content. The systems with 70 wt% and 44 wt% show face-on orientation while P3HT is edge-on oriented in the systems with the other ratios. In the annealed systems, the main orientation of the P3HT crystals is edge-on for all blend ratios (figure 6.7b) which is also found for the P3HT:PCBM system (section 5.2). However, the systems which reveal initial face-on orientation also exhibit a higher portion of face-on oriented crystals after annealing. In addition, for the P3HT:MEH-CN-PPV bulk heterojunction film with a P3HT content of 28 wt% the weakest Bragg reflections are found. Consequently, this blend ratio shows the lowest crystallinity. The orientation of polymer crystals can be altered by changing the substrate cleaning procedure or the introduction of self-assembled monolayers.[178] In the case of the blended P3HT:MEH-CN-PPV films, no artificially modified substrate surface, but the formation of blend ratio dependent enrichment layers might have changed the crystal orientation.

A quantitative analysis of the Bragg peaks is performed via the Scherrer equation (2.64) using the peak position and width. The P3HT (100) and (010) lattice constants are 1.66 nm and 0.38 nm, respectively, and are independent of the blend ratio. These values are in accordance with the values found in section 5.2 and in literature.[130, 131, 132] The (100) crystal size increases slightly from 14 nm to 17 nm with increasing P3HT content. Although MEH-CN-PPV does not influence the lattice constants in a P3HT crystal, the crystal growth is hindered by the presence of MEH-CN-PPV.

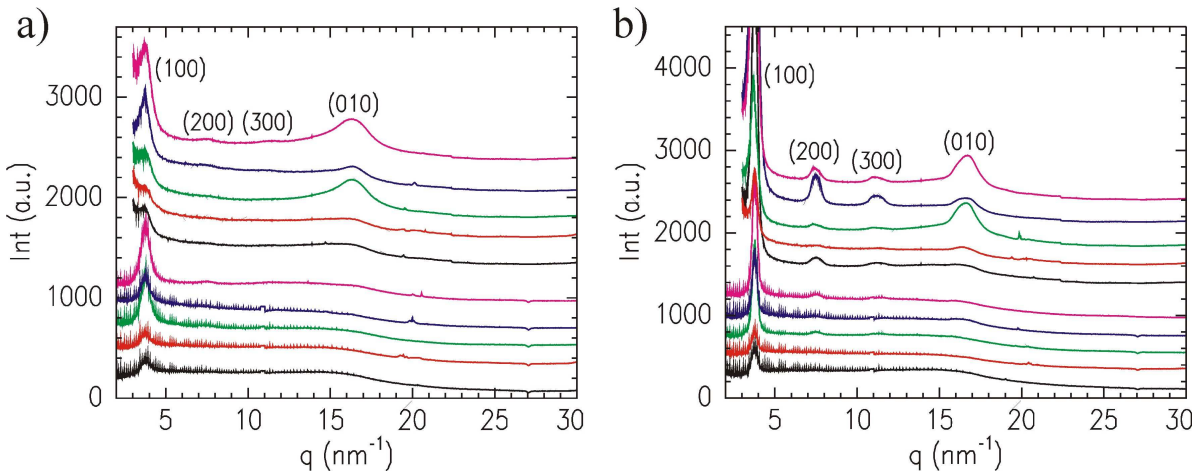

Figure 6.7: *Vertical (upper five curves) and horizontal (lower five curves) sector integrals of GIWAXS measurements of as-spun (a) and annealed (b) P3HT:MEH-CN-PPV bulk hetrojunction films with P3HT content of 21 wt% (black), 28 wt% (red), 44 wt% (green), 54 wt% (blue) and 70 wt% (magenta). Thermal annealing is performed at 200 °C for 10 min. Bragg peaks are indicated. The curves are shifted along the y-axis for clarity.*

There is no crystalline signal corresponding to MEH-CN-PPV. Consequently, the ordering due to annealing deduced from the PL data is an intramolecular order, i.e. an increase in conjugation length, or closer packing of amorphous chains.
Concerning the crystalline orientation of P3HT, changing the blend ratio seems to be a possibility to tune the orientation. In principle, face-on orientation is advantageous as the charge mobility along the (010) direction is higher as compared to the (100) direction because of the π-π-stacking. Thus, in the case of face-on orientation a better contact to the electrodes can be achieved.

6.2.3 Surface structure

While the blend ratio dependence of the crystalline orientation is not discussed in literature so far, the phase separation of two polymers is widely studied and can be described via the Flory-Huggins theory (section 2.2.2). To observe the influence of the blend ratio on the surface structure on the micro- and mesoscale, the topography is investigated by optical microscopy and AFM.
In figure 6.8 optical micrographs of P3HT:MEH-CN-PPV bulk heterojunction films with different blend ratios are shown. All films show structures on the low micrometer scale. However, the structures depend on the blend ratio. The largest structures are revealed for a blend ratio of 44 wt% P3HT content (figure 6.8c). The other ratios show smaller

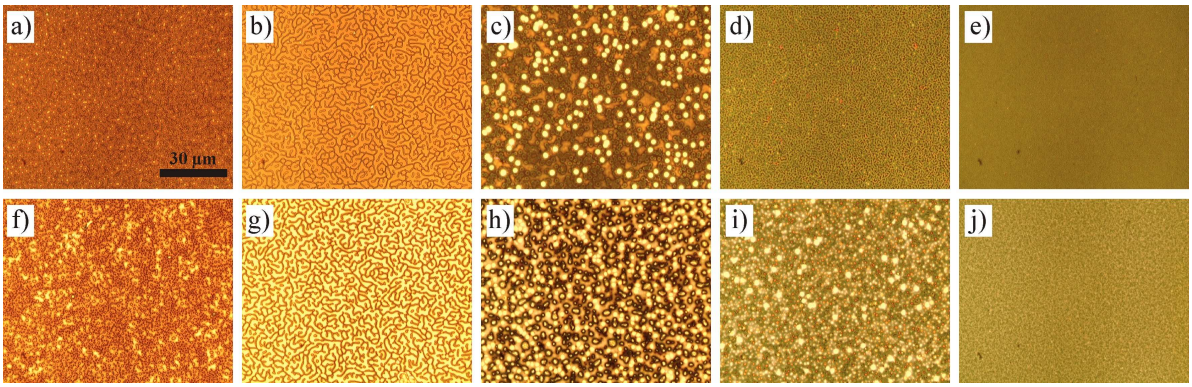

Figure 6.8: *Optical micrographs of as-spun (a-e) and annealed (f-j) P3HT:MEH-CN-PPV bulk heterojunction films with different blend ratios of 21 wt% (a,f), 28 wt% (b,g), 44 wt% (c,h), 54 wt% (d,i) and 70 wt% (e,j) P3HT content. Annealing is performed at 200 °C. The micrographs are taken with 100× magnification.*

structures. While most blend ratios breed an island-like structure, the topography of the 28 wt% system is meander-like or bicontinous. With thermal annealing at 200 °C for 10 min, the structures coarsen except for the film with 28 wt% content. A blend ratio of 28 wt% correponds to the critical blend ratio for this system calculated by equation (2.38) using the molecular weights of P3HT (Rieke Metals Inc.) and MEH-CN-PPV (table 4.1). The critical blend ratio is obtained from the Flory-Huggins theory (section 2.2.2). Although the Flory-Huggins theory is based on bulk systems, it has already been shown that it can also be used to estimate the critical blend ratio for thin films.[174] At the critical blend ratio, the spinodal and binodal phase lines are identical. Consequently, only spinodal phase separation takes place at the critical blend ratio.

The structural stability on the micrometer scale for the thin bulk heterojunction film with 28 wt% might be a reason for the low improvement in crystallinity due to thermal annealing. Obviously, thermal annealing does not coarsen the structure. Nevertheless, the change in the PL spectra suggest molecular rearrangement of the amorphous MEH-

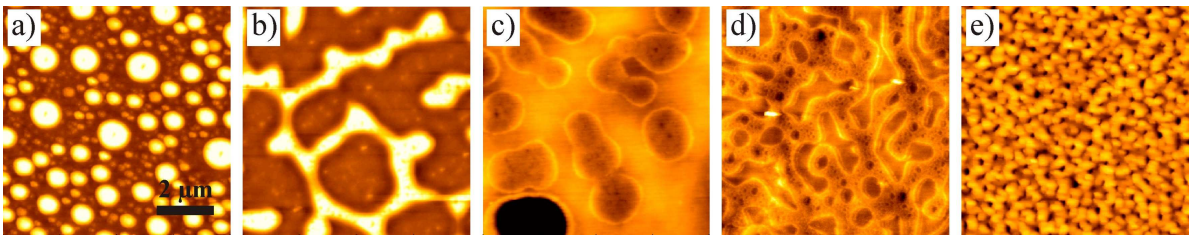

Figure 6.9: *AFM images (8×8 µm^2) of as-spun P3HT:MEH-CN-PPV bulk heterojunction films with different blend ratios of 21 wt% (a), 28 wt% (b), 44 wt% (c), 54 wt% (d) and 70 wt% (e) P3HT content. The color coding spans a height of 60 nm (a,b), 20 nm (c,d) and 30 nm (e).*

CN-PPV. Therefore, purification of the phases most probably takes place. However, the PL decrease upon annealing implies the presence of some P3HT in the MEH-CN-PPV phase acting as quenching state for excitons. A similar observation has been made by McNeill et al. who reported on intermixed phases in all-polymer systems using scanning transmission X-ray microscopy (STXM).[179] The authors found primary purification of the phases due to thermal treatment before coarsening occured. For the P3HT:MEH-CN-PPV system with a 28 wt% P3HT content, at 200 °C the coarsening has not yet set in. Therefore, also the temperature at which coarsening after purification sets in is blend ratio dependent.

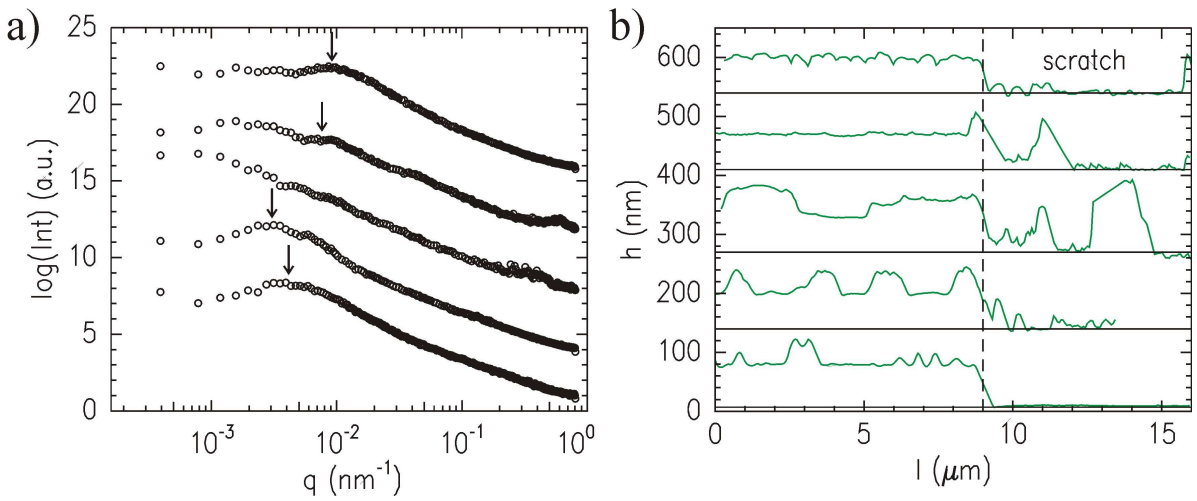

Figure 6.10: *a) Power spectral density curves obtained from AFM images with scan size from 1×1 μm² to 16×16 μm² of as-spun P3HT:MEH-CN-PPV bulk heterojunction films with different blend ratios. The features at $q \approx 0.5$ nm^{-1} are artifacts originating from the AFM measurement. Prominent features are highlighted by arrows. b) Line cuts of AFM images (16×16 μm²) with scratch of as-spun P3HT:MEH-CN-PPV bulk heterojunction films with different blend ratios. The solid and dashed lines indicate the substrate and the edge of the scratch, respectively. The P3HT content of 21 wt%, 28 wt%, 44 wt%, 54 wt% and 70 wt% increases from bottom to top. The curves are shifted in y-direction for clarity.*

To determine the surface structure on the nanometer scale, AFM measurements are carried out. In figure 6.9 the AFM images of the surface of as-spun P3HT:MEH-CN-PPV bulk heterojunction films are presented. The films with a low P3HT content of 21 wt% and 28 wt% reveal pronounced island- and meander-like structures while the systems with higher P3HT content reveal crater-like structures with small height differences. A more homogeneous structure is found for the system with the highest P3HT content. For a quantitative analysis the AFM images are Fourier transformed and so-called power spectral density (PSD) curves are extracted (figure 6.10). Peaks and shoulders in the PSD

curves represent a characteristic length scale. The observed length scales are compared with the results from the scattering data and discussed below (section 6.2.5).
In addition to the structural information, AFM is also used to detect the thicknesses of the films as XRR measurements are not suited for this type of sample due to the large surface structures. Therefore, the polymer films are scratched with a needle and measured with AFM (see section 3.2.2). The corresponding line cuts are shown in figure 6.10b. Both systems with the highest P3HT content reveal a film thickness of about 60 nm without any pronounced surface structures. The rms-roughnesses are found to be 2.8 nm and 4.3 nm for 54 wt% and 70 wt%, respectively. The films with lower P3HT ratio have an homogeneous underlying film with additional structures on top. The films with 21 wt%, 44 wt% and 54 wt% P3HT content reveal film thicknesses plus additional structures of $(70 + 40)$ nm, $(60 + 40)$ nm and $(60 + 30)$ nm, respectively. The uncertainty of the determined film thickness is estimated to be 10 nm by taking several line cuts.
In principle, a structured surface on top of a homogeneous film can be beneficial for photovoltaic applications. Due to this structured surface in an organic solar cell the incoming light is refracted. As a consequence, the light path through the active layer is longer which directly results in more absorbed photons and ultimately in more charge carriers. Typically, such structures are installed artificially by mechanical treatment of the polymer layers of an organic solar cell like imprinting or soft embossing.[180] However, by adapting the blend ratio in the all-polymer system P3HT:MEH-CN-PPV, the surface is directly structured by a self-assembly process without any additional mechanical treatment.

6.2.4 Soft X-ray spectroscopy and scattering

Resonant soft X-ray scattering in grazing incidence geometry (GI-RSoXS) is used to reveal structural information of the P3HT:MEH-CN-PPV bulk heterojunction systems averaged over an area of mm^2 which is orders of magnitudes larger than the areas probed with AFM or optical microscopy. So far, soft X-ray scattering has only been used in transmission geometry investigating a variety of systems also including conjugated polymers.[86, 181, 182, 183]
In figure 6.11a the dispersion δ and the absorption β of P3HT and MEH-CN-PPV as a function of X-ray energy are plotted. The spectra are obtained using near edge X-ray absorption fine structure (NEXAFS) spectroscopy. The calibrated P3HT spectra obtained from the Ade database [184] are plotted for comparison. The measured and the calibrated spectra differ slightly but the main features are present in both spectra. The deviation might result from an insufficient calibration of the beamline. However, the relative difference of the MEH-CN-PPV and P3HT spectra are more important than the absolute values.

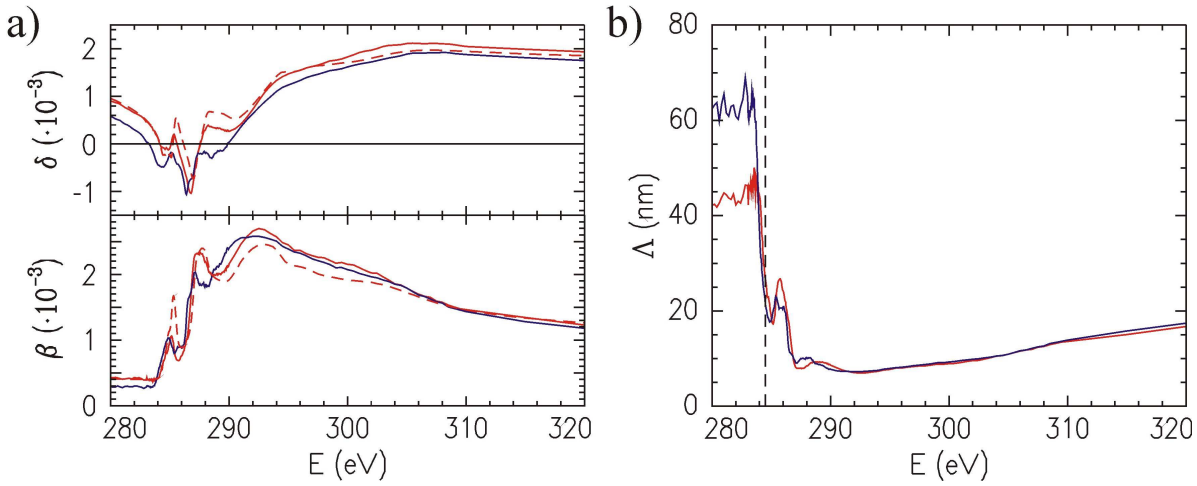

Figure 6.11: *a) The dispersion δ and the absorption β of P3HT (red solid lines) and MEH-CN-PPV (blue solid lines) as a function of the X-ray energy. For comparison the calibrated P3HT spectra from the Ade database (red dashed lines) are plotted.[184] b) The penetration depth Λ of X-rays in P3HT (red) and MEH-CN-PPV (blue) as a function of X-ray energy calculated from the absorption spectra.*

The dispersion δ spectra of P3HT and MEH-CN-PPV reveal positive and negative values and differ strongly depending on the X-ray energy. Therefore, the scattering contrast also depends on the X-ray energy. From the absorption β spectra the penetration depth Λ of the X-rays into P3HT and MEH-CN-PPV is calculated (figure 6.11b). The penetration depth is defined as the depth at which the X-rays have an intensity of $1/e$ of the initial intensity (section 2.3.4). For energies below 284 eV a penetration depth Λ for P3HT and

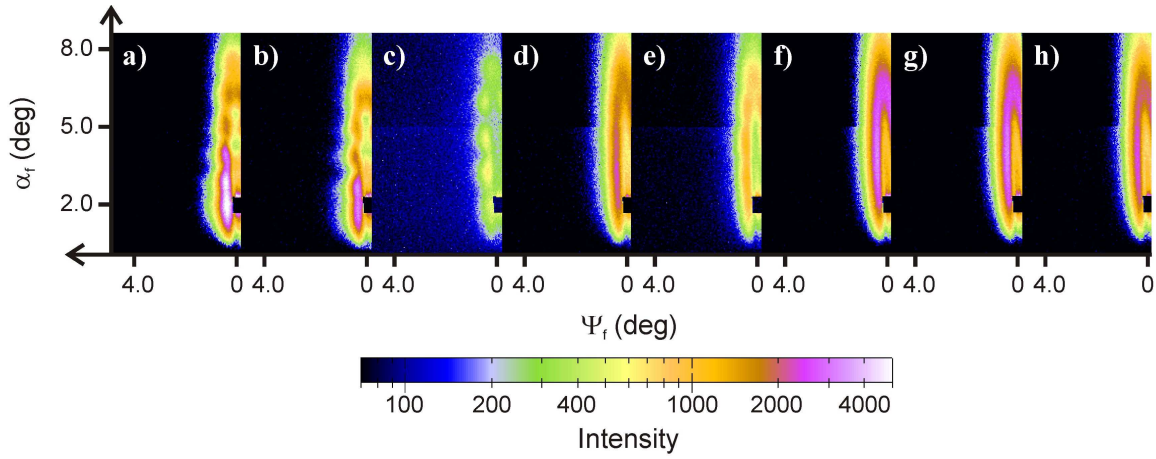

Figure 6.12: *2d GI-RSoXS data of a P3HT:MEH-CN-PPV film with a P3HT content of 70 wt% as a function of X-ray energy. The X-ray energy is changing from 282 eV (a) to 289 eV (h) in steps of 1 eV. The 2d GI-RSoXS data are composites of two measurements with two different detector positions. The specular reflection is shielded with a beam stop. The same color coding is used for all 2d data.*

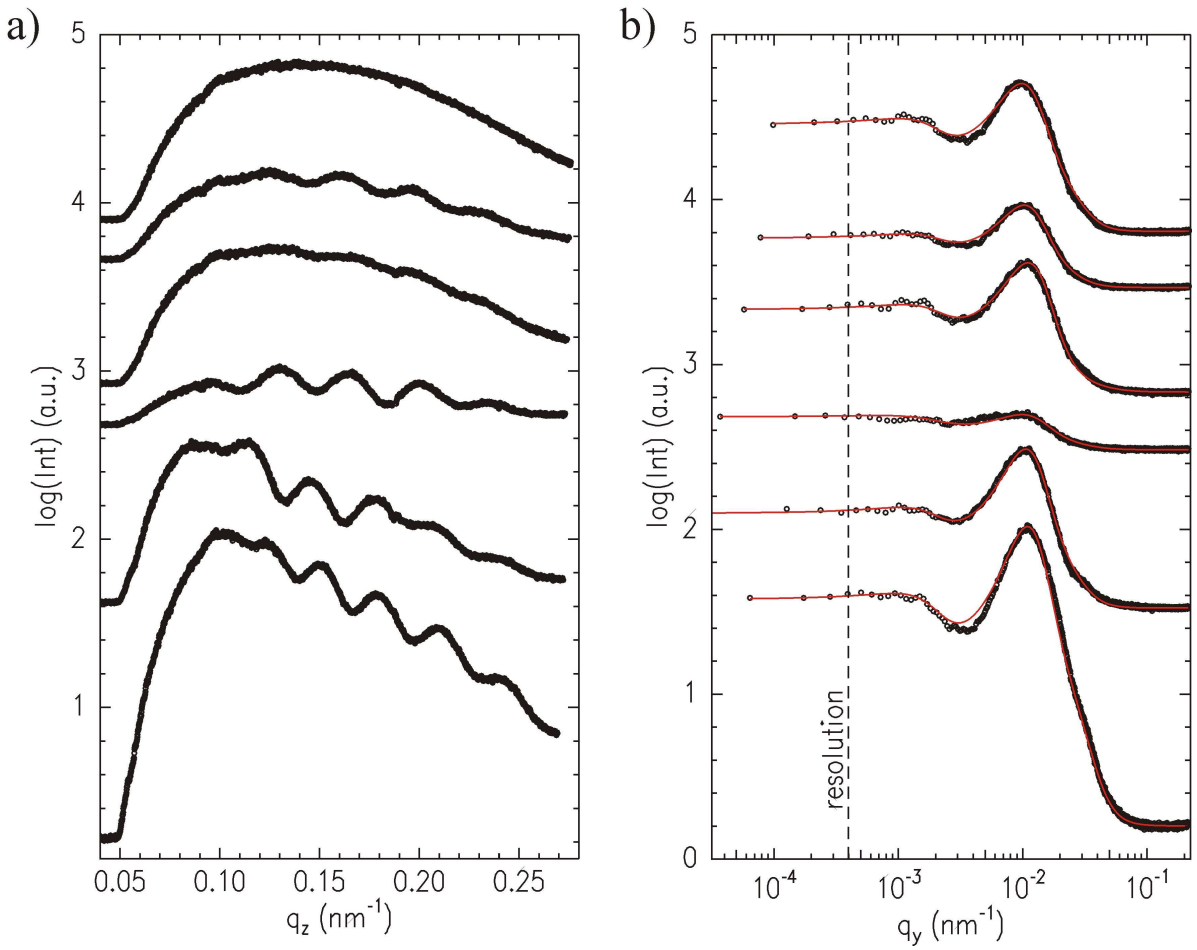

Figure 6.13: *a) Off-detector cuts and b) out-of-plane cuts of GI-RSoXS measurements of a P3HT:MEH-CN-PPV film with a P3HT content of 70 wt% as a function of X-ray energy. The X-ray energy is changing from 280 eV (bottom curve), 283 eV to 287 eV (top curve) in steps of 1 eV. The out-of-plane and the off-detector cuts are taken at an angle above the specular reflection and along the highest intensity in q_z-direction, respectively. b) The red solid lines are fits to the data using three Lorentzian functions. The curves are shifted along the y-axis for clarity.*

MEH-CN-PPV of about 45 nm and 60 nm is obtained, respectively. At higher energies the penetration depth Λ decreases below 20 nm. Consequently, X-rays with an energy above 284 eV cannot penetrate the P3HT:MEH-CN-PPV films completely.

The 2d GI-RSoXS data of P3HT:MEH-CN-PPV bulk heterojunction films with a P3HT content of 70 wt% are shown in figure 6.12 for different X-ray energies from 280 eV to 289 eV. This energy range corresponds to X-ray wavelengths from 4.29 nm to 4.43 nm. Although the energy and accordingly the wavelength are only varied by 3%, the scattering data change dramatically. For energies below 284 eV an intensity oscillation in vertical direction (correlated roughness) is visible. The correlated roughness originates from the interference of scattered X-rays from different interfaces most probably including the sub-

strate. Thus, such a correlated roughness is a strong evidence that the full polymer film is probed. With increasing X-ray energies the correlated roughness vanishes indicating that no scattering signal from the substrate interface is detected and the film is only partly penetrated. These findings are in accordance with the drop in penetration depth above 284 eV (figure 6.11b) and the film thickness of 60 nm (figure 6.10b). In horizontal direction strong intensity features are observed as well. The low intensity of the scattering data with an X-ray energy of 284 eV (figure 6.12c) is due to the very low initial intensity at this energy (section 3.2.4.4).

For a quantitative analysis, off-detector and out-of-plane cuts are presented in figure 6.13. The off-detector cuts are not taken at $q_y = 0$, but along the highest intensity in vertical direction. Due to the different X-ray energies, different q_z ranges are probed. However, the deviations are only 3%. At low energies (280 eV) the dispersion δ is positive and the corresponding off-detector cut reveals a similar shape as known from GISAXS experiments with hard X-rays. However, a distinct Yoneda peak cannot be observed as the incident angle $\alpha_i = 2°$ and the averaged critical angle α_c of the polymer film are similar, i.e. $\alpha_c = 2.3°$ and $1.5°$ for X-ray energies of 280 eV and 283 eV. Consequently, the Yoneda peak is hidden by the specular intensity. No total reflection occurs for higher X-ray energies as the dispersion is negative and therefore no Yoneda peak exists in this energy range. In addition, the correlated roughness is visible. With increasing X-ray energy the overall shape of the curves changes and the correlated roughness vanishes. The frequency of the oscillation for the 280 eV measurement with the largest penetration depth corresponds to a length scale of 213 ± 13 nm which is about 3.6 times the found film thickness.

The out-of-plane cuts (figure 6.13b) reveal a structure peak at 0.01 nm^{-1} which corresponds to a length of 600 nm and is not changing with energy. The structure is obtained by fitting Lorentzian functions to the peaks. Thus, the same structure is detected inde-

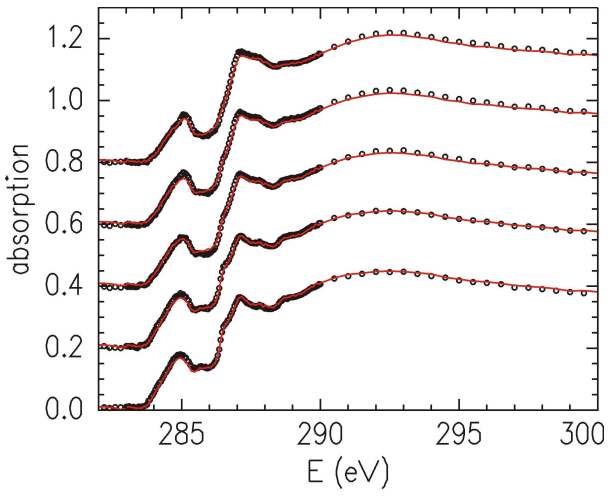

Figure 6.14: *NEXAFS spectra (black symbols) of P3HT:MEH-CN-PPV films with different P3HT contents of 21 wt%, 28 wt%, 44 wt%, 54 wt% and 70 wt% (from bottom to top) and the corresponding sum of P3HT and NEXAFS spectra weighted with the blend ratios (red solid lines). The curves are shifted along the y-axis for clarity.*

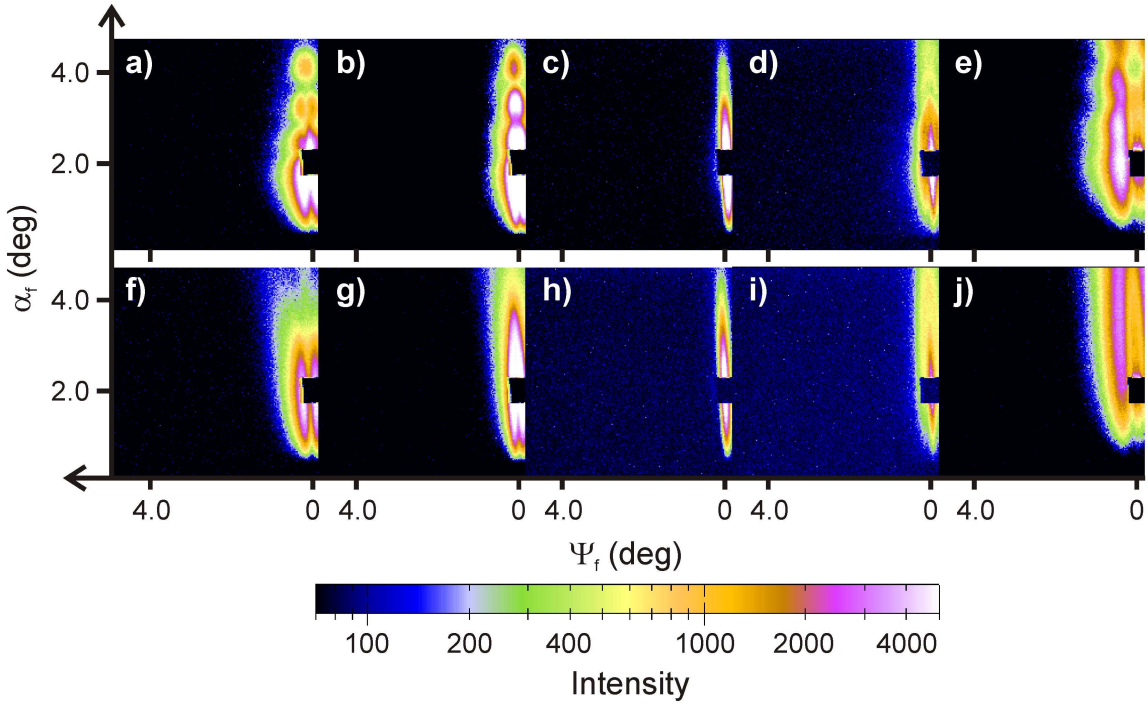

Figure 6.15: *2d GI-RSoXS data of P3HT:MEH-CN-PPV films with different P3HT contents of 21 wt% (a,f), 28 wt% (b,g), 44 wt% (c,h), 54 wt% (d,i) and 70 wt% (e,j) for X-ray energies of 282 eV (a-e) and 288 eV (f-j). The specular reflection is shielded with a beam stop. The same color coding is used for all 2d data.*

pendent of the X-ray energy or rather the penetration depth. Consequently, the same structure sizes are found on the sample surface as also seen in the AFM images and in the film or the scattering is dominated by the surface structures. For more details on the structure, see the next section.

For both, detector and out-of-plane cuts, the overall intensity of the features is changing with energy. These differences are an interplay of the different intensities of the primary beam and the varying scattering contrast depending on the X-ray energies.

6.2.5 Blend ratio dependent morphology

In figure 6.14 the NEXAFS spectra of P3HT:MEH-CN-PPV bulk heterojuntion films with different blend ratios are shown. In addition, the linear superposition of the NEXAFS spectra of P3HT and MEH-CN-PPV homopolymer films weighted with the corresponding blend ratio are plotted. The measured data and the calculated spectra are in good agreement and confirm therefore the blend ratios of the bulk heterojunction films calculated from the polymer solutions which are used initially. The gradually changing blend ratio is well expressed by the superposition. Typically, NEXAFS is used in scanning transmission

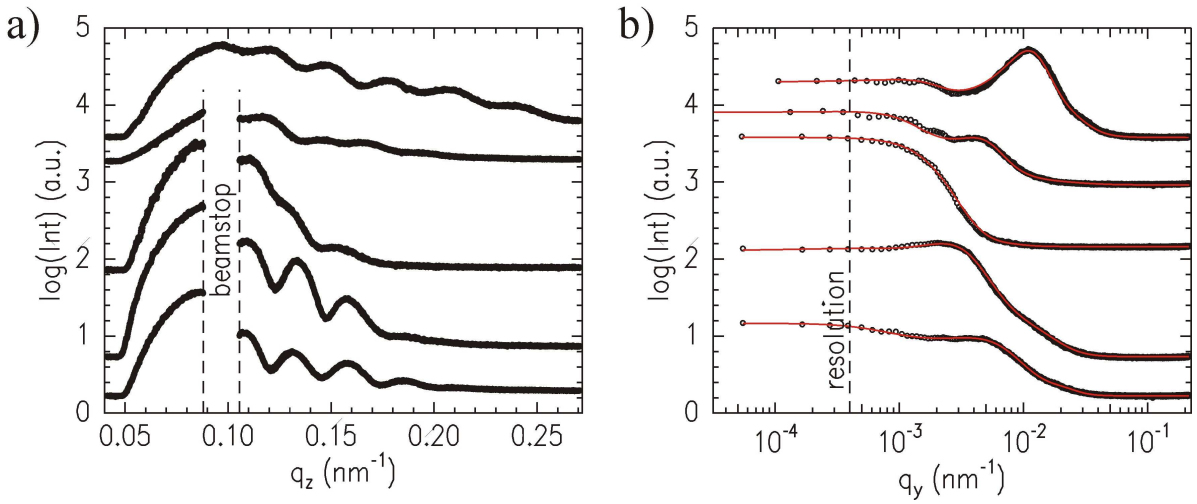

Figure 6.16: *a) Off-detector cuts and b) out-of-plane cuts of GI-RSoXS measurements of P3HT:MEH-CN-PPV films with different P3HT contents of 21 wt%, 28 wt%, 44 wt%, 54 wt% and 70 wt% (from bottom to top) for an X-ray energy of 282 eV. The out-of-plane and the off-detector cuts are taken at an angle above the specular reflection and along the highest intensity in q_z-direction, respectively. b) The red solid lines are fits to the data using three Lorentzian functions. The curves are shifted along the y-axis for clarity.*

X-ray microscopy to map the ratio locally in polymer blend films or also in biological materials.[185, 186]

In the following part, the discussion of scattering data obtained from the P3HT:MEH-CN-PPV bulk heterojunction films with different blend ratios is limited to two X-ray energies. To account for scattering with high and low penetration depths, X-rays with energies of 282 eV and 288 eV are chosen. In figure 6.15 the 2d GI-RSoXS data are shown. Again, the scattering at 282 eV reveals correlated roughness which is not observed for the scattering at 288 eV. The features in q_y direction strongly depend on the blend ratio. While for the system with 70 wt% P3HT content small structures are expected, the scattering data of the 44 wt% does not reveal features in horizontal direction, i.e. structures are not within the resolvable length scale range. The lateral structure information is visible in the scattering data of both energies and therefore for low and high penetration depths.

The corresponding detector and out-of-plane cuts of the GI-RSoXS data obtained at an energy of 282 eV, i.e. the X-rays are probing the whole film, are presented in figure 6.16. For all films correlated roughness is detectable whereas it is most pronounced for P3HT contents of 21 wt% and 28 wt%. These films reveal length scales of about 235 ± 15 nm which is 3.3 and 4.1 times the corresponding film thickness, respectively. The length scales of the other blend ratios are 290 nm, 260 nm and 225 nm for the films with P3HT contents of 44 wt%, 54 wt% and 70 wt%, respectively. These length scales are 4.7, 4.3 and 3.6 times

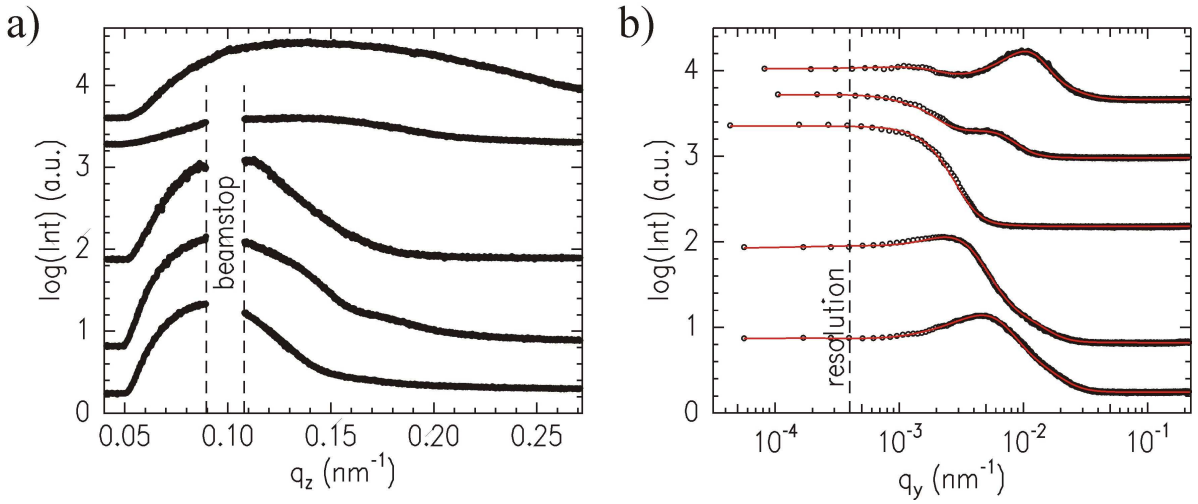

Figure 6.17: *a) Off-detector cuts and b) out-of-plane cuts of GI-RSoXS measurements of P3HT:MEH-CN-PPV films with different P3HT contents of 21 wt%, 28 wt%, 44 wt%, 54 wt% and 70 wt% (from bottom to top) for an X-ray energy of 288 eV. The out-of-plane and the off-detector cuts are taken at an angle above the specular reflection and along the highest intensity in q_z-direction, respectively. b) The red solid lines are fits to the data using three Lorentzian functions. The curves are shifted along the y-axis for clarity.*

the film thicknesses. Although correlated roughness is an evidence that the full polymer film is probed, it is not possible to relate the corresponding length scales clearly to the film thicknesses. Most probably dynamical effects due to scattering at graded interfaces and multiple scattering [73], which cannot be neglected for angles near the critical angle α_c, are the main reason for this deviation. Consequently, also an inner layering of the film influences the correlated roughness. Such a layering has been found before for blended films of standard polymers, like PS and PMMA,[187] and also for related all-polymer bulk heterojunction films (M3EH-PPV:CN-ether-PPV and P3HT:MEH-PPV).[107, 174] The layering is typically solubility driven. During solvent evaporation one component is preferentially transported to the film surface and thus a layering develops. In addition, the surface structures found with AFM (figure 6.9) can influence the correlated roughness. The detector cuts measured at an X-ray energy of 288 eV with low penetration depth show no correlated roughness (figure 6.17a).

In figure 6.16b the out-of-plane cuts for different blend ratios are shown for an X-ray energy of 282 eV. The full polymer film is penetrated. Except for the films with 44 wt% P3HT content, all curves reveal a peak or a pronounced shoulder. The same tendencies are observed in the out-of-plane cuts detected with an X-ray energy of 288 eV, that is, the condition for a low penetration depth (figure 6.17). Therefore, only structures near the surface are probed. The corresponding lateral structure sizes are obtained by fitting

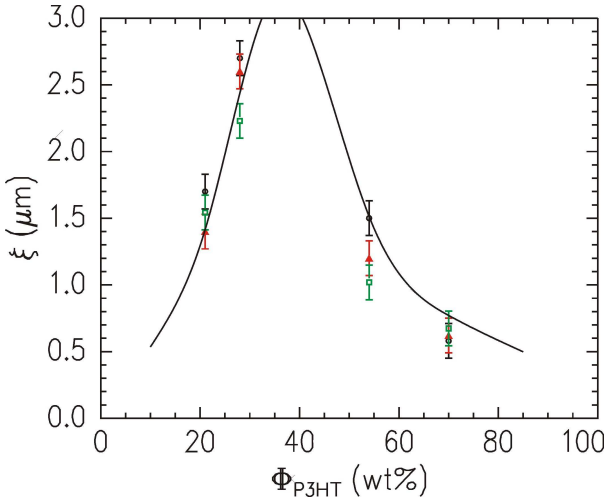

Figure 6.18: *Lateral length scales determined by AFM (green squares) and GI-RSoXS at two different energies, 282 eV (black circles) and 288 eV (red triangles). The solid line is a guide to the eye.*

the data with Lorentzian functions.

The extracted lateral structure sizes obtained from the GI-RSoXS experiments are plotted together with the lateral structure sizes revealed from the AFM measurements (figure 6.10a) in figure 6.18. No characteristic structure size for the P3HT:MEH-CN-PPV bulk heterojunction film with a P3HT content of 44 wt% is detected neither with scattering nor with AFM. This means that this film shows no characteristic length scale in the resolvable range from 30 nm to about 5 µm. For the other blend ratios the structure sizes of the scattering with high and low penetration depth are similar. Moreover, the length scales of the surface structures obtained from AFM measurements also show only little deviations. Consequently, the same structure exists in the film and on the film surface. In addition, no further structural length scales are observed.
In figure 6.19 a schematic morphology describing an all-polymer system with similar inner film and topography structures. Hoppe et al. found a similar morphology for the polymer:fullerene system MDMO-PPV:PCBM.[122] In that case, PCBM clusters surrounded by a MDMO-PPV skin were observed. Nevertheless, the structure in the film and the topography showed similar length scales. However, such a behavior is not a general rule as already discussed in section 5.2 where the topography and the inner film morphology showed large deviations. Consequently, both, topography and inner film morphology, have to be probed to conclude an overall morphology.

6.2.6 Results

The structure of the all-polymer system P3HT:MEH-CN-PPV is characterized on different length scales. Both conjugated polymers were already used in all-polymer solar cells with the highest efficiencies reported so far.[105] The absorption and photolumines-

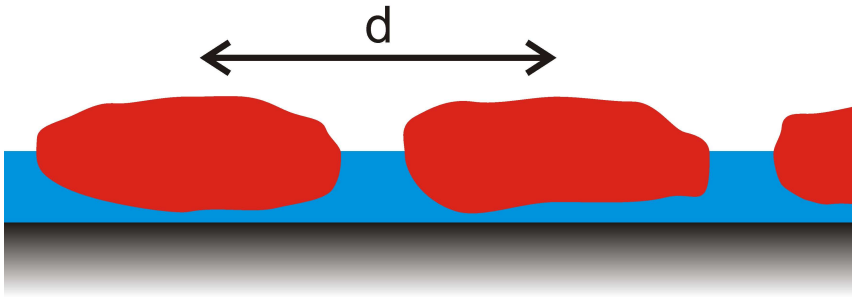

Figure 6.19: *Schematic morphology of an all-polymer film with a structural length scales d. The polymers are depicted in red and blue.*

cence measurements of the homopolymer films revealed features for crystalline ordering of P3HT, but not for MEH-CN-PPV due to annealing. However, the PL of MEH-CN-PPV decreases dramatically which is a sign for a higher packing of the MEH-CN-PPV chains. The GIWAXS results confirm the crystallinity of P3HT, which is increasing with annealing, and shows no indication for crystallinity in MEH-CN-PPV. The branched side chains and the cyano-groups sticking out of the conjugation plane hinder crystallization of MEH-CN-PPV.

The blend ratios of P3HT:MEH-CN-PPV bulk heterojunction films calculated from the initial solutions are confirmed by NEXAFS measurements. Also in the blended films, the absorption and the PL measurements show features related to crystallization and to packing of P3HT and MEH-CN-PPV, respectively, due to thermal annealing. GIWAXS measurements confirm this trend. In addition, GIWAXS measurements reveal a blend ratio dependent orientation of P3HT crystals. While for annealed bulk heterojunction films the main orientation is edge-on for all blend ratios, the portion of face-on oriented crystals is higher for films with 44 wt% and 70 wt% P3HT content. Overall, the crystallinity increases dramatically with thermal annealing with the exception of the film containing 28 wt% P3HT. In this case, only a small increase in crystallinity is observed.

The blend ratio of 28 wt% corresponds to the critical blend ratio calculated from the molecular weights of P3HT and MEH-CN-PPV using the Flory-Huggins theory. Optical microscopy reveals a bicontinous surface structure in the µm-range for this blend ratio. In addition, the bicontinous structure does not change even when annealed to 200 °C while the structure of the systems with other blend ratios coarsens with annealing. Consequently, it seems that the crystallization of the polymer chains and the coarsening processes fo the surface structure are inhibited at the critical blend ratio. Nevertheless, some molecular rearrangement occurs since the PL of MEH-CN-PPV decreases significantly.

The lateral structure sizes are probed using AFM and GI-RSoXS with low and high pen-

etration depths, i.e. the structures near the surface and the morphology in the full film are probed, respectively. Both methods reveal similar lateral structure sizes which depend on the blend ratio. Consequently, the topography and the inner film morphology have the same structural length scales. Further characteristic structures in the film are not observed. The pronounced surface structures can improve the light absorption in an organic solar cell due to light refraction resulting in higher absorption.
In conclusion, on the one hand the blend ratio can be used to tune the orientation of P3HT crystals which is important for charge carrier mobilities. On the other hand surface structures for increased light absorption are also altered with the blend ratio. The origin of the blend ratio dependent crystal orientations might be a result of the formation of enrichment layers which alter the influence of the substrate. However, a final explanation can not be given so far. Further investigations, also with other polymer combinations, are needed to gain further insight in this tuning possibility.

6.3 Influence of blending and annealing

Other polymers of the polythiophene and cyano-PPV groups are P3OT and CN-PPV. P3OT has a similar structure as the above discussed P3HT. The side chains are just extended by two carbon atoms. Therefore, the lattice constants of P3OT crystals are bigger compared to P3HT.[188] CN-PPV and MEH-CN-PPV also differ only in the type of side chain whereas the differences are bigger compared to the polythiophenes. P3OT and CN-PPV are an electron donor and an electron acceptor, respectively, and can be combined and used as an all-polymer system for organic photovoltaics concerning their electronic properties.
In this section, the morphology with special focus on the crystallinity of the homopolymers P3OT and CN-PPV and their blend is investigated. P3OT and CN-PPV are blended with a ratio of 1:2 or 33 wt% P3OT content which is the critical blend ratio for this system. The critical blend ratio is calculated using the molecular weights (table 4.1) and equation (2.38). The molecular weight of CN-PPV is estimated by the spin coating method (section 4.3). For related polythiophene:PPV systems a minimal structure size [174] and a bicontinous morphology (section 6.2) have been found.
The absorption and photoluminescence (PL) of the homopolymers and blended films are presented. In addition, the lateral structures in the blended films are investigated by AFM and GISAXS. Finally, the crystallinity of the homopolymer and the blended films are probed by GIWAXS. The results are discussed with focus on thermal annealing and blending.
P3OT and CN-PPV are dissolved in tetrahydrofuran (THF) by heating to 50 °C. Thin

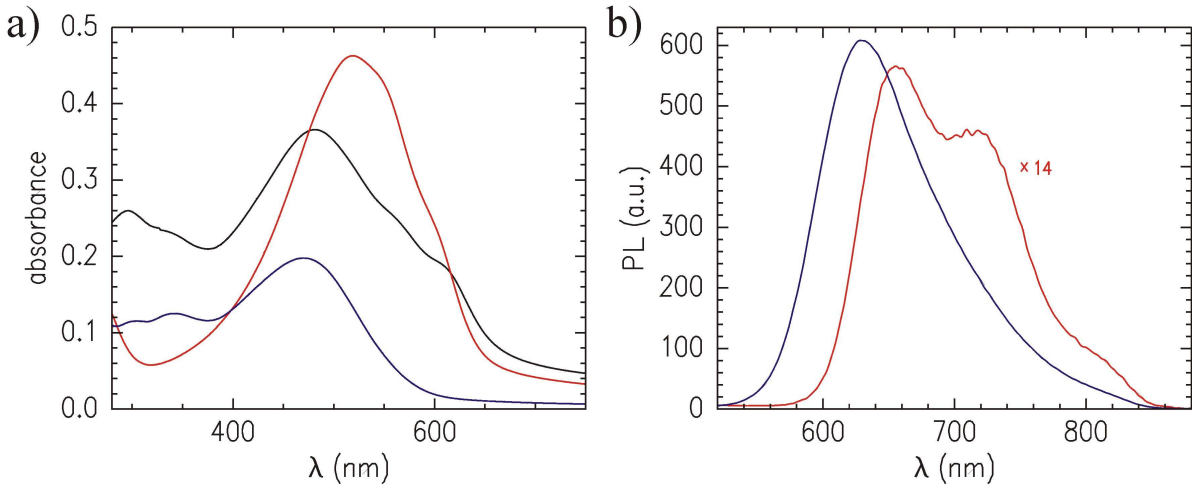

Figure 6.20: *a) Wavelength dependent absorbance spectra and b) photoluminescence PL of as-spun P3OT (red) and CN-PPV (blue) thin homopolymer films. For the blended P3OT:CN-PPV film (black) with 33 wt% P3OT content the absorption spectrum is shown. The PL excitation wavelength is 485 nm. The PL spectrum of P3OT is multiplied by 14 for better visibility.*

films are prepared via spin coating and are annealed at 130 °C for 15 min in vacuum.

6.3.1 Spectral characterization

In figure 6.20a the absorption spectra of P3OT and CN-PPV and their blend are shown. The main absorption peak of P3OT is at 520 nm which is slightly red shifted compared to P3HT. However, the absorption peak positions of P3OT and P3HT films are hardly comparable since the main peak position strongly depends on the molecular packing. The P3OT spectra also reveals vibronic excitation features originating from crystalline P3OT portions at 540 nm and 600 nm. CN-PPV exhibits its main absorption peak at 472 nm and smaller contributions in the near-UV range at 300 nm and 342 nm. However, no additional vibronic features are observed. Thus, both polymers absorb at the maximum of the solar spectrum. When P3OT and CN-PPV are blended, all features are found at the same wavelength, but the intensities change. As peak intensities are related to molecular order, blending influences the molecular ordering of the polymer chains. However, no additional features appear which is an evidence that no significant ground-state charge transfer is taking place.[123]

The PL spectra of the homopolymers are presented in figure 6.20b. Similar to MEH-CN-PPV discussed in section 6.2, CN-PPV has a much higher luminescence than P3OT. In addition, CN-PPV shows no vibronic features which is evidence for the presence of a fully amorphous polymer. P3OT reveals a crystalline contribution comparable to P3HT. The PL spectrum of the P3OT:CN-PPV bulk heterojunction film (figure 6.21) is dominated

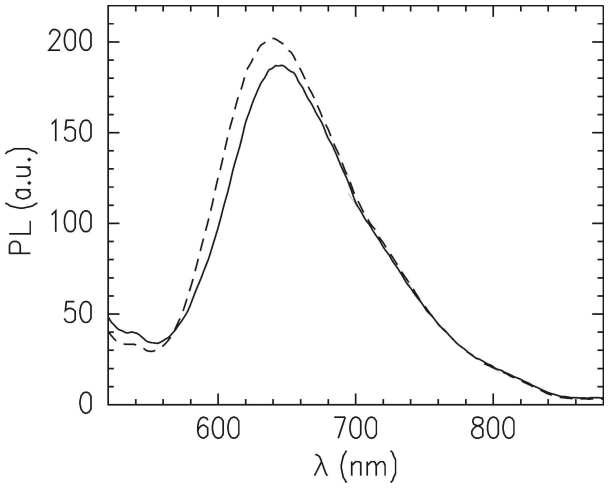

Figure 6.21: *Wavelength dependent photoluminescence (PL) of as-spun (dashed line) and annealed (solid line) of P3OT:CN-PPV bulk heterojunction films with 33 wt% P3OT content. The excitation wavelength is set to 485 nm.*

by CN-PPV which is due to the higher intrinsic PL of CN-PPV and its higher content. Nevertheless, the total PL is quenched compared to the CN-PPV homopolymer PL which is evidence for exciton separation due to blending of P3OT and CN-PPV. Thermal annealing changes the PL of the blend only slightly which is a strong hint that no molecular arrangement is taking place.

6.3.2 Mesoscopic morphology

The surface structures of the P3OT:CN-PPV bulk heterojunction film with 33 wt% P3OT content is investigated using AFM. The surface shows a drop-like structure (figure 6.22a) with a structure size of about 1.4 µm as obtained from the PSD curve (figure 6.23b). In addition, a structure size of several hundred nanometers is apparent. To obtain the film thickness and the height of the drop structure, AFM images are taken from a blend film with a scratch (section 3.2.2). Figures 6.22b and 6.22c show the AFM image of the scratch and the corresponding line cut. The drops have a height of about 70 nm and the underlying film a thickness of 60 nm. This pronounced surface structure can again act as a pattern to diffract light and thus increase light absorption in an organic solar cell.

To obtain information of the inner film morphology GISAXS measurements are performed. The incident angle is set above the critical angles of the material, so that the full film is probed. The detector cuts (figure 6.23a) exhibit no significant changes due to annealing. However, a peak at $q_z = 0.42$ nm^{-1} appears due to the drop structure already detected with AFM. The detector cut gives information on the structure vertical to the film surface. Thus, a pronounced surface structure is observed as a layer with a density averaged over islands and the vacuum/air in between. Consequently, this layer has a

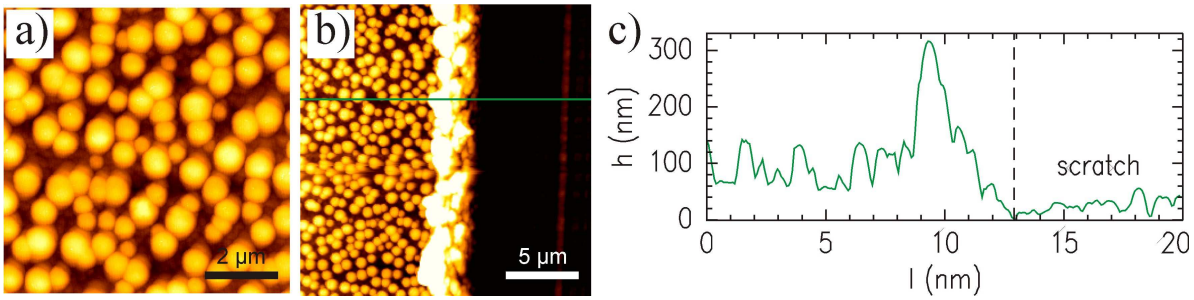

Figure 6.22: *a) AFM image (8×8 µm²) of a P3OT:MEH-CN-PPV bulk heterojunction film with a blend ratio of 33 wt% P3OT content. The color coding spans a heigth of 220 nm. b) AFM image (20×20 µm²) of the same film with a scratch. The green line indicates the position of the taken line cut (c).*

smaller critical angle which appears as an additional peak in the detector cut. From the peak position the surface coverage is determined. The observed peaks exhibit a surface coverage of only 8% and 6% for the as-spun and the annealed films, respectively. This surface coverage is considerably smaller than the one measured with AFM which is 75%. In figure 6.24a the height distribution of the AFM image in figure 6.22a is shown. A surface coverage of 8% corresponds to objects with a height above 168 nm which is depicted in a mask presentation of the AFM image (figure 6.24b). Blue regions illustrate objects with

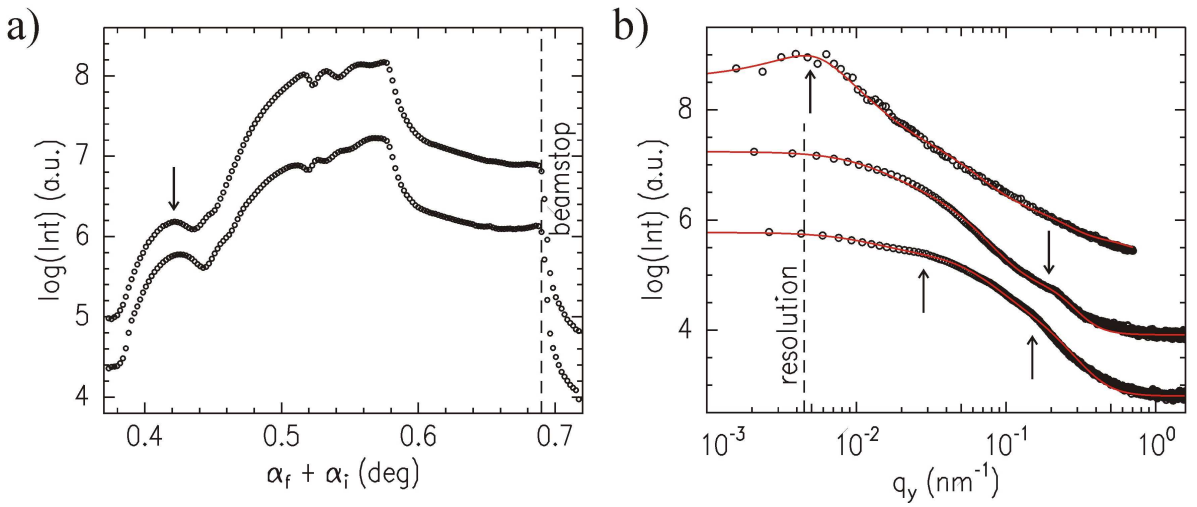

Figure 6.23: *a) Detector cuts and b) out-of-plane cuts of 2d GISAXS data of as-spun (bottom curve) and annealed (upper/middle curve) P3OT:CN-PPV films with 33 wt% P3OT content. The out-of-plane cuts (bottom and middle curves) are taken at the critical angle of P3OT. The data (black symbols) are fitted (red solid line) with the effective surface approximation within the DWBA. The resolution is given by the dashed line. The curves are shifted along the y-axis for clarity. The PSD curve (top curve) obtained from the AFM measurements is plotted for comparison. The data (black symbols) is fitted (red solid line) using two Lorentzian functions. Prominent length scales are highlighted with arrows and discussed in the text.*

a height above 168 nm. Consequently, GISAXS probes not the same surface coverage as seen by AFM but only the top part of the objects which are higher than 168 nm. Nevertheless, the additional peak in the detector cut is direct evidence for surface structures although the surface coverage differs from that measured with AFM.
In figure 6.23b the fitted out-of-plane cuts of the P3OT:CN-PPV films are shown. Fitting reveals a constant structure size of 300 nm for the as-spun and the annealed film. In addition, a smaller length scale of 60 nm in the as-spun case is detected. After thermal annealing this length scale shifts to 35 nm. In addition, the width of the peak which is a sign for polydispersity of the structure decreases due to annealing. Consequently, the 60 nm structure size corresponds to weakly pronounced structures which consist most probably of intermixed phases. Due to annealing, smaller purified structures evolve which correspond to the length scale of 35 nm. These detected length scales are favorable for photovoltaic application as they are in the range of the exciton diffusion length.

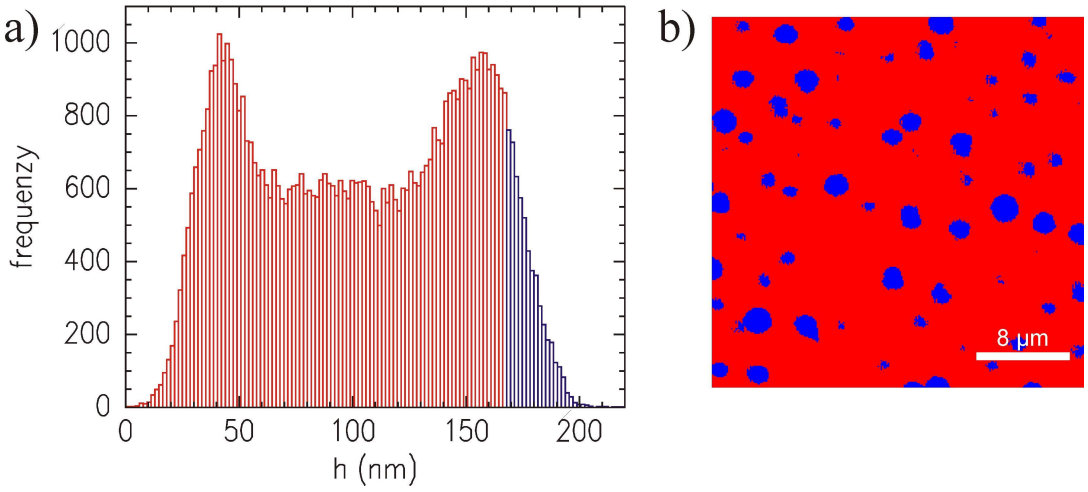

Figure 6.24: *a) Height distribution in the AFM image in figure 6.22a. Heights below and above 168 nm are presented in red and blue, respectively. b) Mask of the AFM image in figure 6.22a with regions of height below (red) and above (blue) 168 nm.*

For comparison the PSD curve obtained from the AFM measurements is shown (figure 6.23b). The 1.4 µm structures found with AFM are not on the resolvable length scale range of the GISAXS experiment and are therefore not detected with GISAXS. At the same time, the structure size of 60 nm observed in GISAXS is not found in the AFM. Hence, these small structures are formed in the polymer film rather than at the surface and both, surface and inner film sensitive techniques are needed to gain full information on the morphology of a bulk heterojunction polymer film.

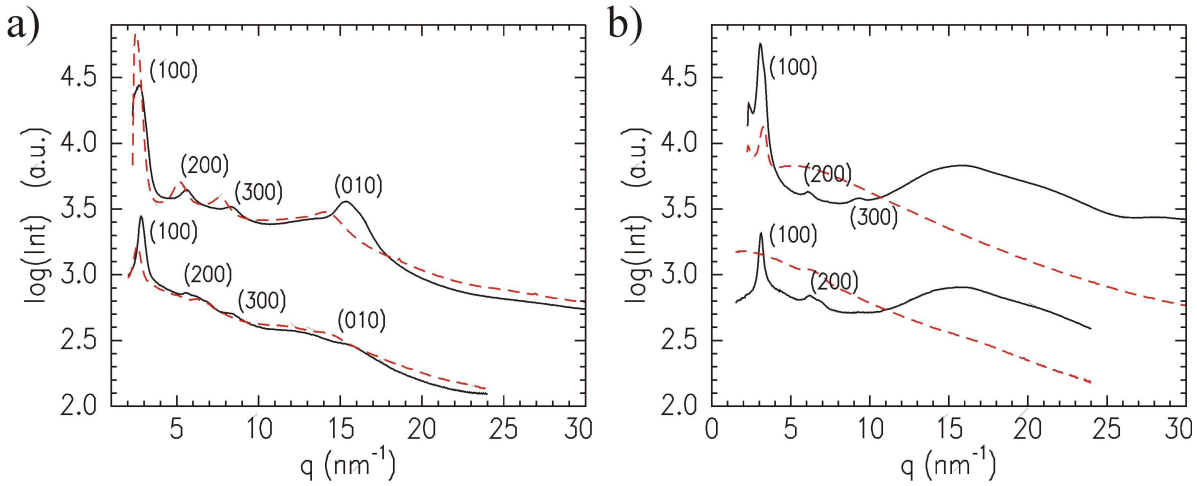

Figure 6.25: *Vertical (upper curves) and horizontal (lower curves) sector integrals derived from 2d GI-WAXS data of as-spun (dashed lines) and annealed (solid lines) P3OT (a) and CN-PPV (b) homopolymer films. Prominent scattering features are indicated.*

6.3.3 Crystalline structure

Besides the morphology on mesoscopic length scales, the molecular ordering is also important for photovoltaic applications, especially for the charge carrier mobility. GIWAXS is used to resolve the crystalline structure of the P3OT and CN-PPV homopolymer films (figure 6.25). The vertical and horizontal sector integrals of P3OT films show already Bragg reflections before thermal annealing whereas the peaks are less pronounced in the horizontal direction. The (100), (200) and (300) as well as the (010) Bragg reflections are detected. This shows that P3OT is already highly crystalline in the as-spun case and reveals edge-on orientation as the main crystal orientation. With thermal annealing the overall crystallinity increases. Furthermore, the distribution of the crystal orientation changes which is seen from the increase of the (010) Bragg reflection and the reduction of the (100) peak in the vertical sector integrals. Accordingly, the fraction of face-on orientated P3OT crystals increases with annealing. The reorientation of the P3OT crystals regarding the substrate is depicted in figure 6.26. In principle, the face-on orientation is favorable for charge carrier transport to the electrodes as the charge carrier mobility along the π-π-stacking is higher than along the (100) direction.

From the peak positions the lattice constants are calculated and shown in table 6.1. The (100) and (010) lattice constants decrease by 9% which is due to higher ordering of the polymer chains with thermal annealing (figure 6.27a). The found values are higher than the values measured for P3HT (section 6.2) originating from the longer side chains. In addition, the lattice constants are also higher than the reported values for P3OT. Urbina et al. used XRD in transmission geometry to detect the crystal properties of P3OT in thick

polymer	**lattice constant [nm]**			
	as-spun		annealed	
	(100)	(010)	(100)	(010)
P3OT	2.47	0.45	2.27	0.41
CN-PPV	1.93	–	2.05	–
blend	2.01	0.39	2.01	0.39

Table 6.1: *Lattice constants of P3OT crystallites in as-spun and annealed P3OT homopolymer and P3OT:CN-PPV blend films. Lattice constants of CN-PPV crystallites in as-spun and annealed CN-PPV homopolymer films. The data are obtained from vertical sector integrals of GIWAXS data. The uncertainty obtained from the Gaussian fits to the Bragg peaks is smaller than 0.1%.*

films and found a lattice constant of 4.13 nm which corresponds to the distance between every second polymer backbone.[189] Also GIXRD measurements revealed smaller lattice constants of 2.05 nm with the conclusion of tilted side chains.[190] The reported values are 10% higher than the values found in this study. These differences result from different preparation techniques. It is well known that the preparation method strongly influences the molecular ordering.[191] While the samples in the XRD study were solution-casted systems, in this study spin coated films are investigated. In addition, also the annealing conditions which alter the crystallization process are different compared to the literature. Finally, various molecular weights and polydispersity of the polymers used also modify the molecular packing.

Contrary to P3OT, as-spun CN-PPV films have only a small (100) Bragg reflection in the vertical sector integral (figure 6.25b). Thus, CN-PPV is less crystalline than P3OT in the as-spun case. After thermal annealing, the (100) Bragg reflection increases and higher orders appear. In addition, also Bragg reflections in horizontal direction are observed. No (010) reflections are detected and therefore no π-π-stacking occurs. This can be explained by the cyano-groups attached to the polymer backbone. These cyano-groups stick out of the conjugation plane and hinder π-π-stacking. Due to the different side chains of

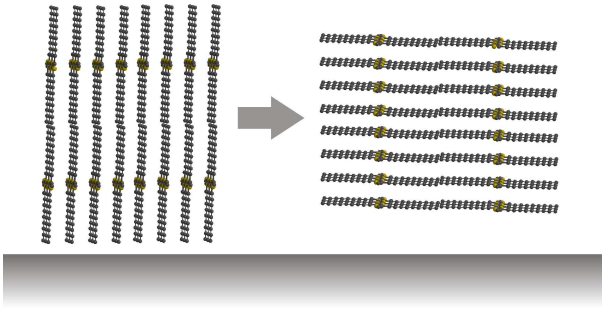

Figure 6.26: *Schematic representation of the reorientation of P3OT crystals from edge-on (left) to face-on (right) arrangement due to annealing.*

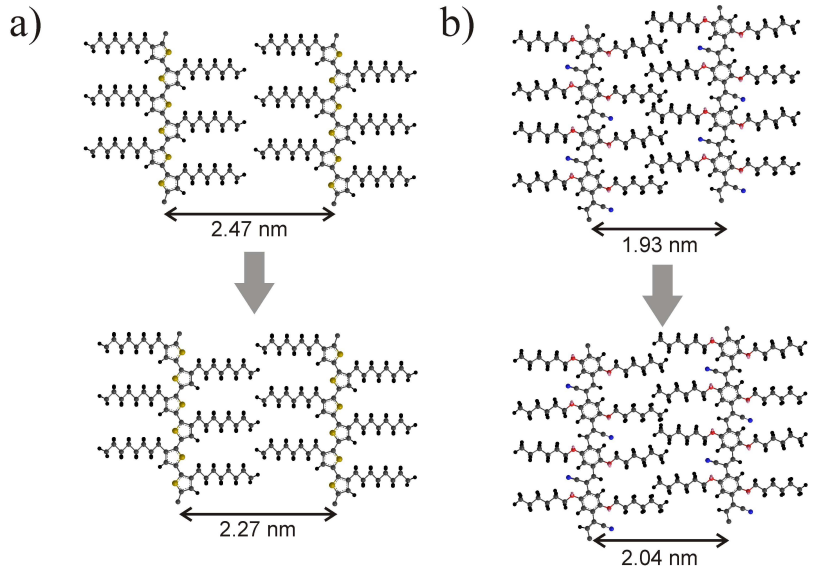

Figure 6.27: *Molecular structure of P3OT (a) and CN-PPV (b) within crystalline domains. The change of the (100) lattice constants due to thermal annealing is depicted.*

MEH-CN-PPV and CN-PPV, CN-PPV shows crystallization in the direction of the side chains, although MEH-CN-PPV is found to be totally amorphous (section 6.2). While CN-PPV has linear alkyl side chains which can order nicely, MEH-CN-PPV has branched side chains which sterically hinder crystallization.

From the ratio of the (100) peak intensities in horizontal and vertical direction, it is concluded that CN-PPV crystals order mainly in edge-on orientation. The (100) lattice constant for CN-PPV increases by 6% due to thermal annealing (table 6.1). The change of the molecular packing of CN-PPV due to annealing is illustrated in figure 6.27b.
In figure 6.28a the sector integrals of 2d GIWAXS data of as-spun and annealed P3OT:CN-PPV bulk heterojunction films are shown. The (100) Bragg reflections with its higher orders is observed for the as-spun films. The (100) intensity is higher in vertical than in horizontal direction as also found for the homopolymer films. Thus, the main portion of the P3OT crystals are edge-on oriented. The P3OT lattice constants are smaller compared to the homopolymer films (table 6.1). In addition, the Bragg reflections are not as pronounced as for the homopolymer films. The differences in molecular packing also influence the absorption behavior and therefore the observed changes in intensity in the absorption spectrum (figure 6.20a). Furthermore, no CN-PPV related feature is observed in the GIWAXS data although CN-PPV is the majority component. Consequently, blending hinders crystallization of both polymers and even influences the crystalline order in terms of the lattice constants (figure 6.28b).
Furthermore, thermal annealing changes the Bragg reflection very little and thus the

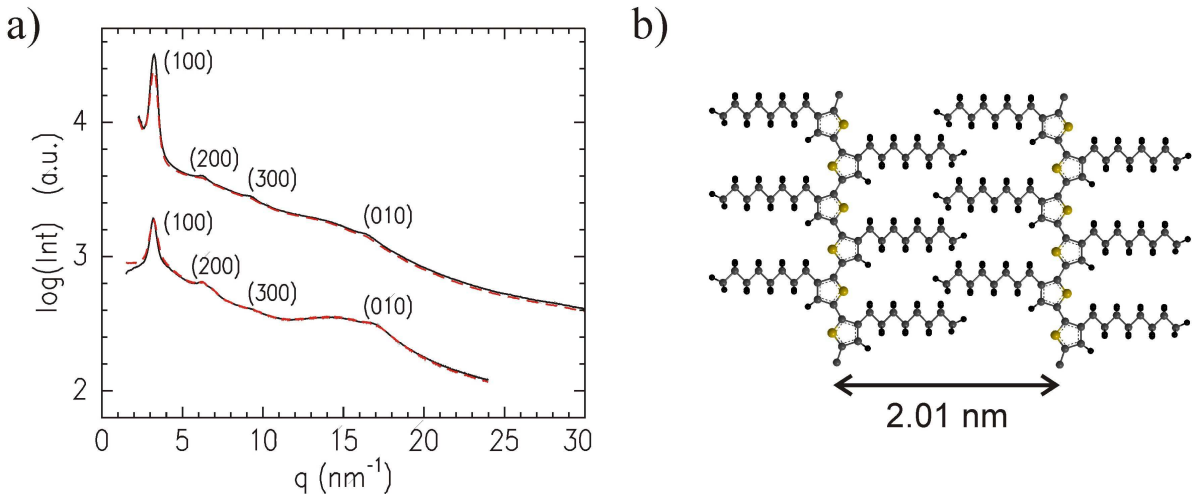

Figure 6.28: *a) Vertical (upper curves) and horizontal (lower curves) sector integrals derived from 2d GIWAXS data of as-spun (dashed lines) and annealed (solid lines) P3OT:CN-PPV bulk heterojunction films with a blend ratio of 33 wt% P3OT content. Prominent scattering features are indicated. b) Molecular structure of P3OT within crystalline domains in the blended film. The (100) lattice constant is depicted.*

crystallinity in the P3OT:CN-PPV bulk heterojunction film increases only slightly. Just the (100) Bragg reflection of the vertical sector integral changes. Consequently, mixing retarded the crystallization process dramatically. In addition, even annealing at 130 °C does not influence the crystallinity significantly. This is in accordance with the PL data of the polymer film which also hardly changes. Due to the phase separation, the volume of the conjugated polymers is reduced and therefore the mobility of the polymer chains is decreased. Even elevated temperatures of 130 °C cannot increase the mobility to allow further crystallization.

A similar behavior is found for the P3HT:MEH-CN-PPV bulk heterojunction system at the critical blend ratio discussed in section 6.2. However, the effect of hindered crystallinity is not as dramatic as for P3OT:CN-PPV. Also, for the system P3HT:F8BT hindered crystallization of P3HT was found.[138] However, the conclusion was drawn from efficiency and absorption measurements and not directly determined as in this study.

6.3.4 Results

The all-polymer system P3OT:CN-PPV with a P3OT content of 33 wt%, which is at the critical blend ratio, is characterized. The homopolymer films show absorption at the maximum of the solar spectrum. GIWAXS measurements reveal already high crystallinity for as-spun P3OT. Due to thermal annealing the crystallinity increases accompanied by a decrease in the lattice constant and a reorientation of the P3OT crystals from edge-on to

face-on. CN-PPV exhibits lower crystallinity even after thermal annealing. Furthermore, π-π-stacking is not taking place due to the sterical hindrance of the cyano group attached to the polymer backbone.
Blending of P3OT and CN-PPV results in polymer films with a pronounced drop-like surface structure. GISAXS reveals a lateral structure size of 60 nm which develops to a more pronounced structure of 35 nm. However, GIWAXS measurements reveal that blending influences the polymer crystallization dramatically. For P3OT lower lattice constants are found which explain the changes in the absorption spectra due to blending. In addition, the crystallization process is hindered. While P3OT shows smaller crystallinity, CN-PPV does not crystallize at all. In addition, thermal annealing alters the crystallinity only very little according the PL data which does not change with thermal annealing.
In conclusion, the retarded crystallization of P3OT and CN-PPV due to blending is the main reason for the low efficiencies of photovoltaic devices made of this combination. The significant lower mobility in amorphous phases prevents charge carrier transport although the lateral mesoscopic structures in the range of the exciton diffusion length would be advantageous for photovoltaics.

6.4 Summary

This chapter discusses the morphologies of all-polymer systems with a polyalkylthiophene as the electron donor material. The electron acceptor polymers are varied.
GISAXS measurements of the all-polymer system P3HT:F8TBT reveals that the optimum structural length scale in an organic solar cell is larger than the exciton diffusion length. While a length scale in or smaller than the range of the exciton diffusion length maximizes the exciton dissociation, such small length scales do not provide sufficient percolation paths for the charge carrier transport to the electrodes. Therefore, the probability for recombination of charge carriers increases for smaller length scales. Consequently, a structural length scale larger than the exciton diffusion length balances exciton dissociation and charge transport and is therefore most efficient.
The possibility of tuning the morphology by changing the blend ratio is investigated for the all-polymer system P3HT:MEH-CN-PPV. Thereby the scattering technique GI-RSoXS is used for the first time. By changing the X-ray energy it is possible to probe the full polymer film or the film surface only without changing the setup. Besides the strong blend ratio dependence of the surface and inner film structure, it is also revealed that the orientation of P3HT crystallites can be altered by the composition. Finally, the morphology on micrometer and crystalline length scales is found to be less sensitive to thermal annealing at the critical blend ratio.

In addition, it is shown that a polymer combination (P3OT:CN-PPV) with fitting energetic properties and optimum structural length scales has a very low photovoltaic performance because blending of these polymers retards the crystallization process. This finding was assumed for other systems [138] but never directly measured before.

Chapter 7

Characterization of block copolymer systems

In the previous chapters the bulk heterojunction concept for polymer-based solar cells is discussed. Bulk heterojunction films consist of a blend of polymers and fullerenes or two polymers. The optimum structure of such a bulk heterojunction for photovoltaic applications is typically a non-equilibrium structure.[9] As detailed in the previous chapters, the preparation processes are crucial for the structure formation. Already small deviations of the preparation process change the bulk heterojunction morphology resulting in a suboptimal morphology.

To obtain nano-structured polymer films with length scales in the range of the exciton diffusion length, diblock copolymers can be used. The resulting structures are typically equilibrated structures and therefore less sensitive to preparation processes. A diblock copolymer consists of two different polymers which are covalently bound together. Due to the repulsion from each other, the two blocks phase separate, but on the nanometer scale as the blocks are covalently bound. Therefore, the phase separation of block copolymers is named micro-phase separation. The structures created by micro-phase separation, such as lamellar, gyroid and hexagonally ordered, cylindric morphologies, are mainly depending on the volume ratio of the two blocks. The phase diagram of coil-coil block copolymers is well understood and theoretically described. A detailed description is found e.g. in references [192, 193, 12].

However, block copolymers containing conjugated polymers behave differently as compared to common coil-coil ones. Already the chemical synthesis has been a major challenge. Furthermore, conjugated polymers tend to crystallize and therefore a competition between micro-phase separation and crystallization occurs.[194] The resulting structure is referred to as supramolecular structure [195] containing crystalline parts which are ordered by micro-phase separation. Nevertheless, there are reports on different types of

diblock copolymers solar cells. However, these solar cells reveal only very low efficiencies so far and a breakthrough has not been achieved yet.[10, 196]
In this chapter, the block copolymer poly(styrene-b-p-phenylene) (P(S-b-PP)) [197] consisting of a standard coil-like polymer and a conjugated polymer is investigated. This block copolymer cannot be used in organic solar cells as it contains only one semiconducting polymer, poly-p-phenylene (PPP). Nevertheless, P(S-b-PP) can be seen as model block copolymer with the coil-like polymer, polystyrene, and a simple conjugated polymer without side chains (PPP). The structure of P(S-b-PP) films made from toluene was investigated previously as a function of film thickness.[198] The authors have shown that the structures are formed from P(S-b-PP) micelles. In addition, the formation of a gold contact on P(S-b-PP) films with micellar structure was probed.[199] It has been found that gold diffuses into a top layer of the P(S-b-PP) film and most probably alters the electronic structure at the contact.
The solvent is changed to tetrahydrofuran (THF) in this thesis to avoid micelle formation. First, the P(S-b-PP) films are characterized with spectroscopic and structural methods (section 7.1). In the second section P(S-b-PP) is used as a template for the incorporation of TiO_2 nanoparticles resulting in a hybrid film. The tuning of the supramolecular structure of P(S-b-PP) by adding an additional polymer is studied in section 7.3.

7.1 Characterization of P(S-b-PP)

The block copolymer P(S-b-PP) is dissolved in tetrahydrofuran (THF) and stirred for 12 h. Before spin coating on HF cleaned silicon substrates, the solution is filtered with a 0.2 µm PTFE filter. To reach structural equilibrium of the P(S-b-PP) films, the films are annealed for 42 h in a saturated THF atmosphere.

In figure 7.1a the absorbance of P(S-b-PP) films made from solutions with different concentrations are shown. With increasing concentration also the absorbance increases which is direct evidence for increasing film thickness. The position of the main absorption peak is 329 nm which is independent of the concentration or rather the film thickness. The absorption is at the edge of the solar spectrum, and thus, disadvantageous for photovoltaic applications. Nevertheless, as P(S-b-PP) is used as a model system for structural characterization, its absorption is secondary. However, PPP can also be doped, with e.g. AsF_5, which extends its absorption range to higher wavelength due to additional electronic states.[200] In this thesis the undoped system is investigated. Only very weak additional features at a wavelength of about 400 nm are observed.

The absorbance at 329 nm follows a linear relation as a function of the concentration up to 10 mg/ml (figure 7.1b). As the absorbance is directly proportional to the film thickness,

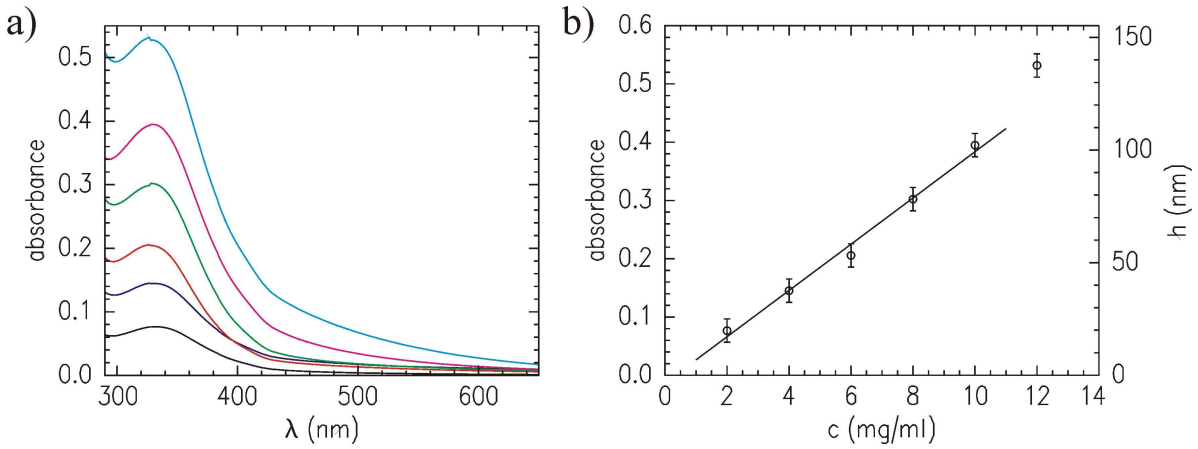

Figure 7.1: *a) Wavelength dependent absorbance of P(S-b-PP) films made from THF solutions with concentrations of 2 mg/ml (black), 4 mg/ml (blue), 6 mg/ml (red), 8 mg/ml (green), 10 mg/ml (magenta) and 12 mg/ml (cyan). b) Concentration dependent absorbance of the maximum at 329 nm. The solid line is a linear fit to the data up to a concentration of 10 mg/ml. The right y-axis corresponds to the film thickness determined from the absorbance.*

the concentration-thickness dependence follows a linear relation which is already known for standard and also conjugated polymers (see section 4.3 and references [112, 113, 174]). The film made from a solution with 12 mg/ml has a higher thickness as expected from the linear relationship between concentration and thickness as shown in figure 7.1b which is in agreement with other polymers and is due to the higher viscosity which starts to influence the film thickness at higher concentrations.[113]
The linear absorbance-thickness dependence can be used to obtain the film thickness if the absorption coefficient $\alpha(\lambda = 329\text{ nm})$ is known. Therefore, a P(S-b-PP) film made from

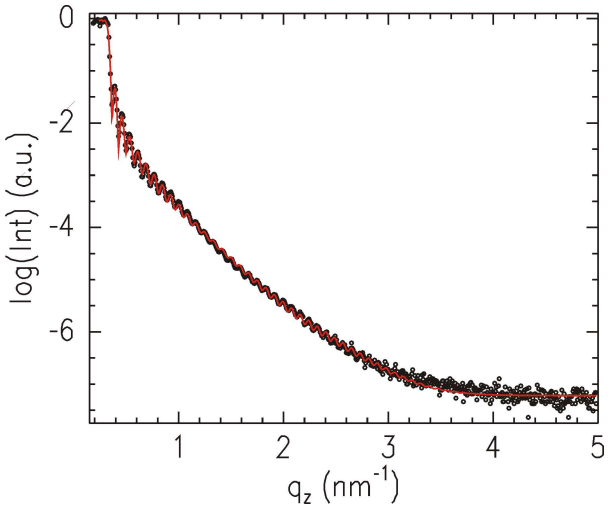

Figure 7.2: *XRR data (black symbols) with fit (red solid line) of a P(S-b-PP) film made from THF solution with a concentration of 8 mg/ml.*

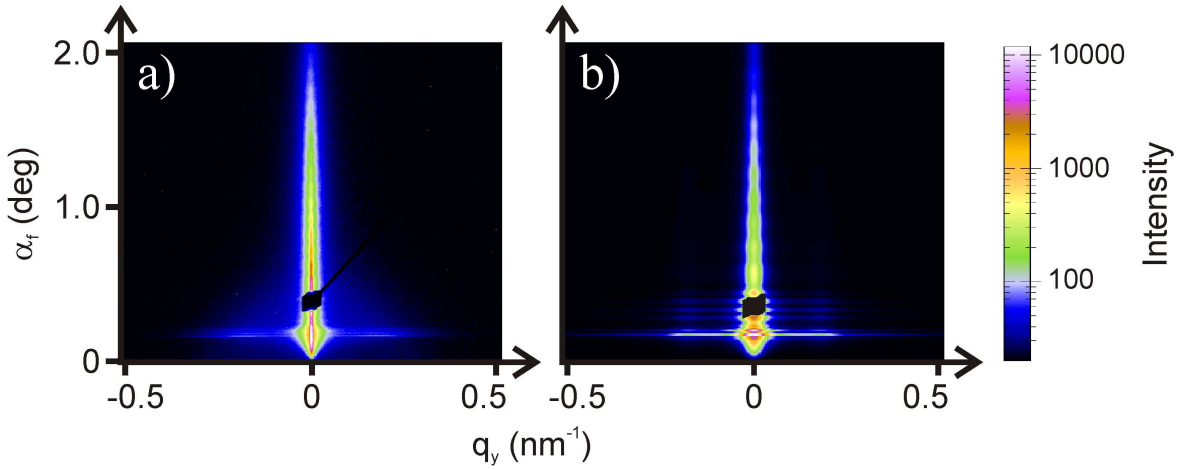

Figure 7.3: *2d GISAXS data (a) and the corresponding 2d IsGISAXS simulation (b) of a solvent-annealed P(S-b-PP) film made from THF solution with a concentration of 8 mg/ml. The intensity color coding is valid for both 2d data.*

a solution with a concentration of 8 mg/ml is measured by X-ray reflectivity (XRR) (figure 7.2) and the thickness h is determined by fitting the data. The thickness is $h = (78 \pm 1)\ nm$. Thus, an absorption coefficient of $\alpha(\lambda = 329\ \text{nm}) = 0.0089\ \text{nm}^{-1}$ results. Hence, a 78 nm thick film absorbs 50 % of the incoming light with a wavelength of 329 nm. In figure 7.1b an additional y-axis with the corresponding thickness h is plotted. For example, a film made from a solution with a concentration of 10 mg/ml is about 100 nm thick.

P(S-b-PP) films with a thickness of 78 nm are chosen for further structural investigations. In figure 7.3a the corresponding 2d GISAXS data is shown. In horizontal direction, wing-like features are visible which are already a sign for lateral phase separation in the nanometer range. In addition, the scattering in vertical direction reveals a modulation which is correlated roughness originating from interference effects of the substrate and the film surface or inner film layering. The corresponding 2d IsGISAXS simulation is shown in figure 7.3b. Both 2d data are in good agreement with each other. The horizontal as well as the vertical features are present. However, the frequency of the vertical modulation differs. This deviation is due to the missing possibility to insert multilayer structures and an appropriate interface roughness in the IsGISAXS model. These limitations give also rise to the additional features next to the beam stop in the simulated 2d pattern. The corresponding line cuts are discussed in the following section.

The model used for the IsGISAXS simulation is presented in figure 7.4. Cylindrical PPP objects with a diameter $2r$ of 10 nm embedded in a PS matrix are used. The distance between the PPP domains is determined to be 16 nm. A second type of PPP domains

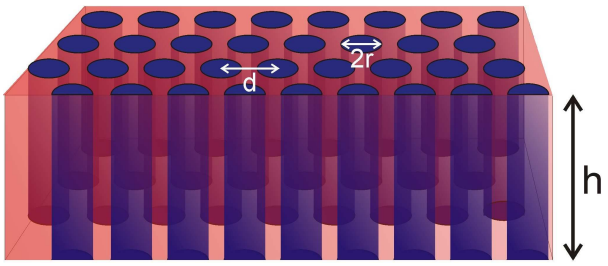

Figure 7.4: *Schematic representation of the IsGISAXS model used for the simulation shown in figure 7.3. The blue and red areas depict PPP and PS, respectively. The radius r of the cylindrical PPP objects, the interparticle distance d and the film thickness h are shown.*

with a diameter of 40 nm and a probability of 0.1% is needed to fit the data. For clarity this second object is not included in the schematic representation. For the arrangement of the PPP domains a 1d paracrystal (1DDL) is used (section 2.3.3). The film thickness is set to 78 nm which is known from the XRR measurements.

Although the material system cannot be used for photovoltaic applications, the revealed structure is promising. The found length scales are on the order of the exciton diffusion length and the structure is most probably near equilibrium due to the solvent annealing of the block copolymer for over 40 h. However, further studies are required to give a conclusion on the equilibrium structure of P(S-b-PP) as the mobility of the polymer chain is decisive when equilibrium is reached, i.e. for a low chain mobility equilibrium might not be reached after 40 h of solvent annealing.

7.2 Nanoparticle incorporation

A new approach to use a diblock copolymer with only one semiconducting block in a photovoltaic device, is to incorporate additional components such as semiconducting nanoparticles (NP). Thus, a donor-acceptor system is obtained which can be used in photovoltaic applications. Due to the combination of organic polymers and inorganic NPs, such as titania, these systems are assigned to the class of hybrid materials. Other hybrid material systems for photovoltaics are the so-called solid state dye sensitized solar cells (ssDSSC) in which inorganic and polymeric semiconductors are combined. In such a ssDSSC, typically a nanostructured titania foam is created by a sol-gel process and the polymer is incorporated after calcination of the titania.[201, 202, 203]

In the combination of block copolymers and NPs, the diblock copolymer acts as the structure determining agent. This combination is already widely studied in the case of standard coil-coil block copolymers and magnetic NPs. In such a combination, the block copolymer defines the structure and the NPs account for the function, e.g. as magnetic storage device. Important is the selective incorporation of the NPs which is achieved with

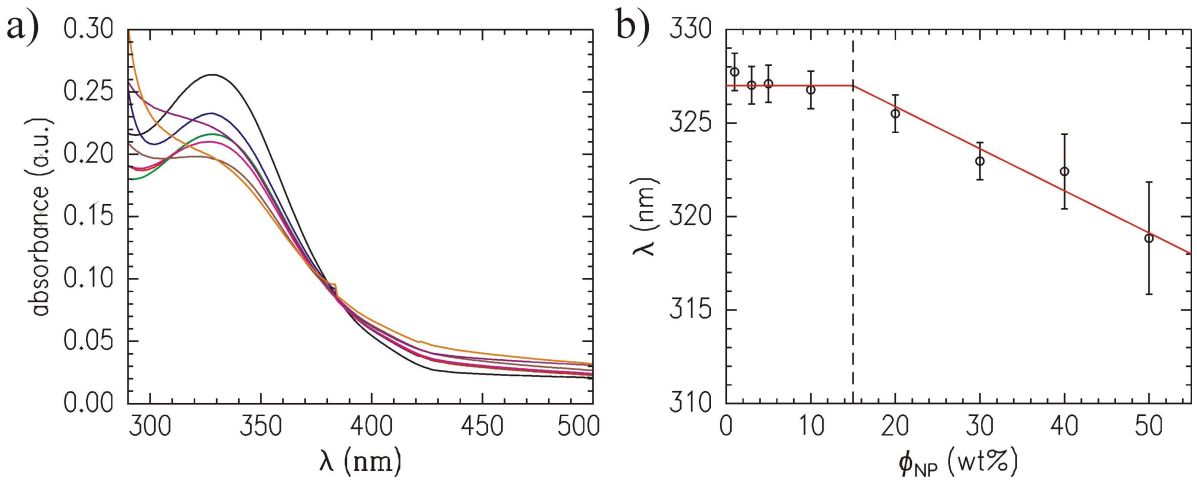

Figure 7.5: *a) Wavelength dependent absorption of P(S-b-PP) films with embedded titania NP with a NP content of 1 wt% (black), 3 wt% (blue), 5 wt% (red), 10 wt% (green), 20 wt% (magenta), 30 wt% (brown), 40 wt% (violet) and 50 wt% (orange). b) The position of the main absorption maximum of P(S-b-PP) as a function of NP content ϕ_{NP}. The dashed line highlights the critical NP concentration. The red solid line is a guide to the eye.*

the surface modification of the nanoparticles.[204, 205] However, only limited reports on semiconducting NPs embedded in a partly semiconducting block copolymer exist. Also, in this case a selective incorporation is crucial to separate the electron and hole conducting materials. In addition, the NP-load has to be sufficiently high to assure charge transport from NP to NP.

In this section, the incorporation of titania NPs in a block copolymer matrix and the influence on the morphology is investigated as a function of the NP content. For this study the model system of titania NPs with 4-tert-butylcatechol (TBC) surface modification and a diameter of 10 nm embedded in P(S-b-PP) is investigated. The surface modification is chosen to prevent agglomeration of NPs. Although the material combination is not ideal for photovoltaic applications, principal knowledge can be extracted.

The film preparation is done by spin coating on HF cleaned silicon substrates with subsequent annealing in a saturated THF atmosphere for 42 h. 8 mg/ml is chosen as the solution concentration to achieve a pure P(S-b-PP) film with a thickness of 78 nm as introduced in the previous section.

7.2.1 Spectral characterization

To probe the selectivity of the NP incorporation, absorption measurements are used. From the absorption spectra the molecular order of the PPP-block is extracted as the position of the main absorption peak is directly related to the molecular order (section 2.1.2) because

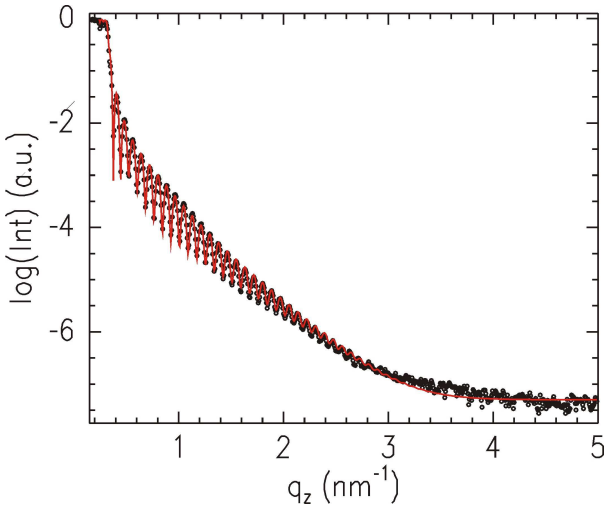

Figure 7.6: *XRR data (black symbols) with fit (red solid line) of a P(S-b-PP) film containing 5 wt% titania NP made from THF solution with a concentration of 8 mg/ml.*

the NPs do not exhibit an absorption maximum in the probed range. In figure 7.5a the absorbance spectra of P(S-b-PP) films with different NP content are shown. The exact peak position is extracted by fitting the spectra by a Gaussian function and plotted in figure 7.5b. The peak position at low NP concentrations is constant at about 327 nm up to at least 10 wt% NP content. Thus, the molecular ordering is not influenced due to NP incorporation which is direct evidence that the titania NP are not located in the PPP phases. For higher NP content the spectra is blue shifted which means that the molecular arrangement off PPP is disturbed.

At lower wavelengths the absorbance increases with increasing NP content which is due to the strong absorption of titania in the UV range.[206] Compared to the absorbance of a pure P(S-b-PP) film (figure 7.1a green line) the absorbance decreases. This reduction is due to less amount of P(S-b-PP) as well as a small decrease in film thickness when the NPs are incorporated. The films with 5 wt% NP content exhibit a film thickness of 74 ± 1 nm as measured by XRR (figure 7.6). In addition to the film thickness, XRR revealed also a 4 nm thick layer near the substrate with increased electron-density due to enrichment of titania NP at the substrate. Also the films with other NP concentrations have smaller film thicknesses as seen from the analysis of the correlated roughness in the GISAXS data (see next section).

7.2.2 Structural characterization

GISAXS is used to probe the influence of the titania NP on the mesoscopic morphology of the P(S-b-PP) film. The 2d GISAXS data of systems with and without different NP contents are shown in figure 7.7. The 2d scattering data without NPs is discussed in the previous section and its IsGISAXS simulation reveals cylindrical PPP objects embedded

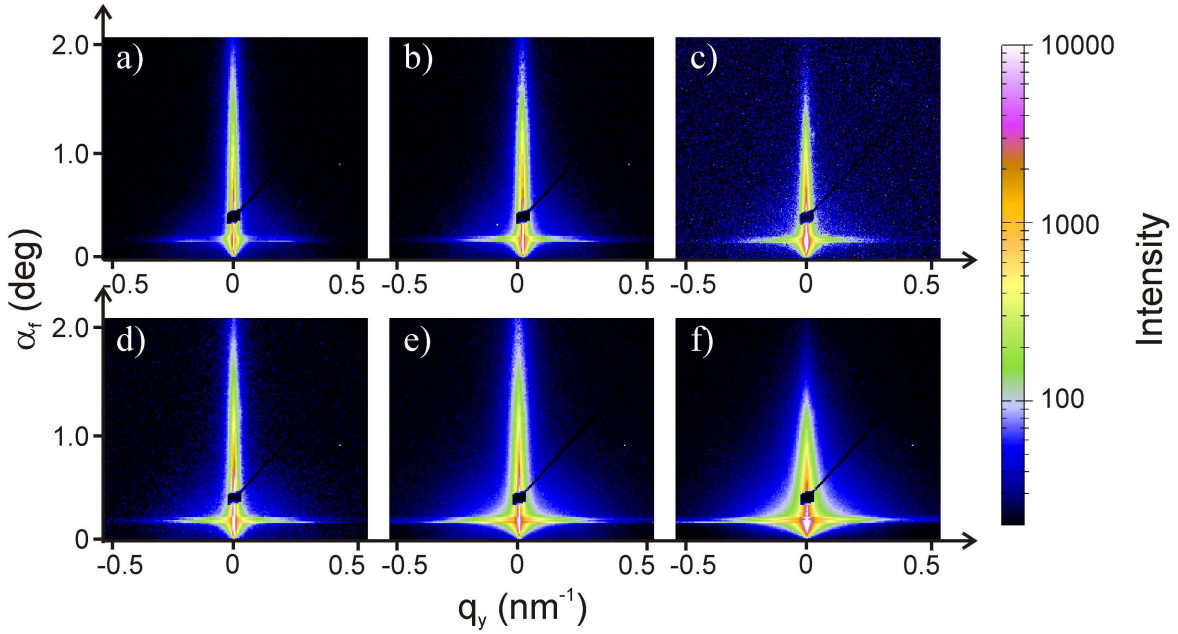

Figure 7.7: *2d GISAXS data of P(S-b-PP) films with embedded titania NP with a NP content of 0 wt% (a), 1 wt% (b), 3 wt% (c), 5 wt% (d), 10 wt% (e) and 20 wt% (f). The intensity color code is valid for all 2d data.*

in a PS matrix. With incorporation of the NPs the 2d data changes. Already for small NP content the intensity of the horizontal scattering at the Yoneda peak increases which is due to the higher contrast between titania and the polymers than between PS and PPP. In addition, a vertical splitting of the horizontal scattering is visible. The lower and upper scattering correspond to the Yoneda peaks of the polymers and titania, respectively. Thus, titania can be resolved by GISAXS in systems with NP content as low as 1 wt%.

The allover shape of the scattering data, in particular in the Yoneda region, stays constant up to a NP concentration of 5 wt%. For higher concentrations the Yoneda peak broadens. Consequently, major structural changes occur at these NP concentrations.

For a quantitative analysis detector and out-of-plane cuts are obtained. The detector cuts are shown in figure 7.8a. The oscillations at angles above $\alpha_f + \alpha_i = 0.8°$, i.e. correlated roughness, correspond to the film thickness of P(S-b-PP). With increasing NP content the correlated roughness is less pronounced which is due to less homogeneous films. The zoom-in into the Yoneda region (figure 7.8b) shows additional oscillations which change with NP content and are therefore an indication that structural changes vertical to the film surface occur. These oscillations correspond to multiples of a layer thickness and are called waveguide effects. For the pure P(S-b-PP) film without NPs the thickness determined by XRR and from the correlated roughness are in good agreement. In addition, the length scale obtained from the waveguide effect is exactly three times the thickness

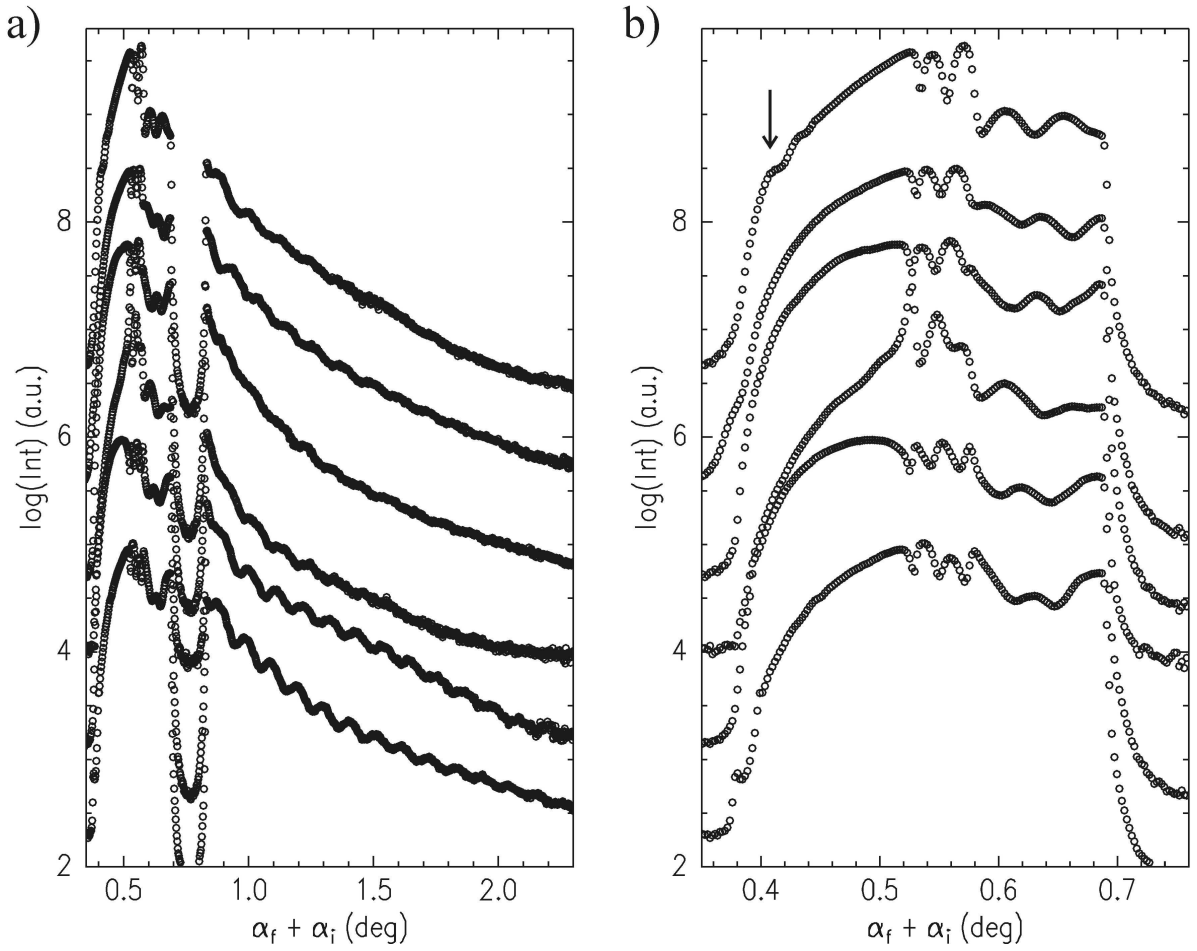

Figure 7.8: *a) Logarithmic plot of detector cuts of P(S-b-PP) films with embedded titania NPs. b) Zoom into the Yoneda region of the detector cuts. The NP contents are 0 wt%, 1 wt%, 3 wt%, 5 wt%, 10 wt% and 20 wt% from bottom to top, respectively. The curves are shifted along the y-axis for clarity.*

value.

In figure 7.9 the length scales obtained from XRR and GISAXS, i.e. the correlated roughness ($\alpha_f + \alpha_i > 0.8°$) and the wave guide effect ($\alpha_f + \alpha_i < 0.8°$), are shown. The length scale retrieved from the wave guide effect is divided by three as this corresponds to the multiple found for the pure P(S-b-PP) film. When NPs are added to the P(S-b-PP) film, the length scales obtained from the correlated roughness decreases. The thickness of films with 5 wt% NP as measured by XRR is in accordance with the length scales obtained from the correlated roughness. The difference of the length scales retrieved from the correlated roughness and the wave guide effects is constant at 7 nm for all films containing NPs, except for the film with 3 wt% NP content which shows a 20 nm difference. As the wave guide effect can originate from interference at interfaces of an inner film layering, it seems that the found difference of these length scales is a measure for enrichment layers.

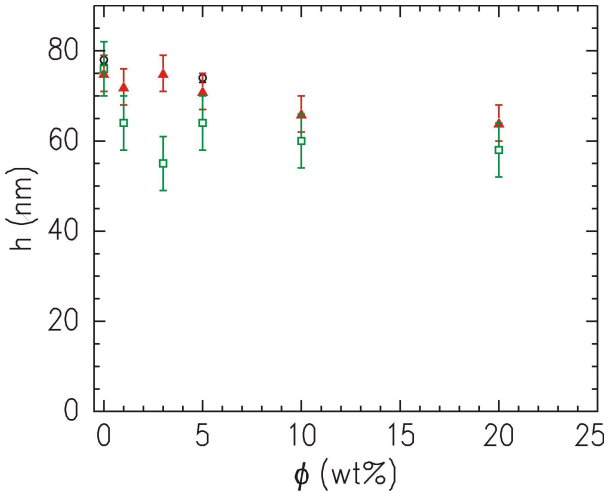

Figure 7.9: *Thicknesses of P(S-b-PP) films as a function of NP content as determined by XRR (black circles), from the correlated roughness at angles above (red triangles) and below (green squares) the specular reflection.*

In addition, the difference of 7 nm is in the range of the 4 nm thick enrichment layer measured by XRR. Thus, the P(S-b-PP) film with NPs has a NP enrichment layer with a constant thickness independent of the NP content, except for the film with 3 wt% NP content. Consequently, the NP have to incorporate into the film as the thickness of the enrichment layer stays constant with increasing NP content.

In the case of 20 wt% NP content, the detector cut reveals additional features at $\alpha_f + \alpha_i \approx 0.4^\circ$ (highlighted by an arrow in figure 7.8b). These features are strong indications for island-like surface structures as discussed in detail in section 6.3.2. For a system with three different components it is impossible to calculate the surface coverage from this feature as long as the composition of the island-like structure is unknown.

Besides the structural information vertical to the sample surface, GISAXS probes also the lateral morphology. The out-of-plane cuts are shown in figure 7.10. For the pure P(S-b-PP) film a pronounced peak is observed. With increasing NP content the peak gets less pronounced which is either due to structural changes or due to decreasing scattering contrast of PS ($\delta_{PS} = 2.9 \cdot 10^{-6}$) and PPP ($\delta_{PPP} = 3.6 \cdot 10^{-6}$). For the latter one, this means that the difference in refractive index has to be decreased. As the dispersion of titania is $\delta_{titania} = 9.48 \cdot 10^{-6}$, the titania NPs have to be incorporated selectively into the PS phase to decrease the contrast. To get no contrast, 10 vol% of NP content in the PS phase, which corresponds to about 19 wt% overall NP content, have to be embedded selectively whereas the block ratio of PS and PPP of 61 vol% (PS-block) or rather 64 wt% (PS-block) is taken into account.

To distinguish between the structural changes and the loss of contrast, the data is fitted using the effective surface approximation within the DWBA (section 2.3.3). For the pure P(S-b-PP) film the fit shows a structural length of 19 nm which is slightly above the structural length found by IsGISAXS (see previous section). Additionally, a structure of

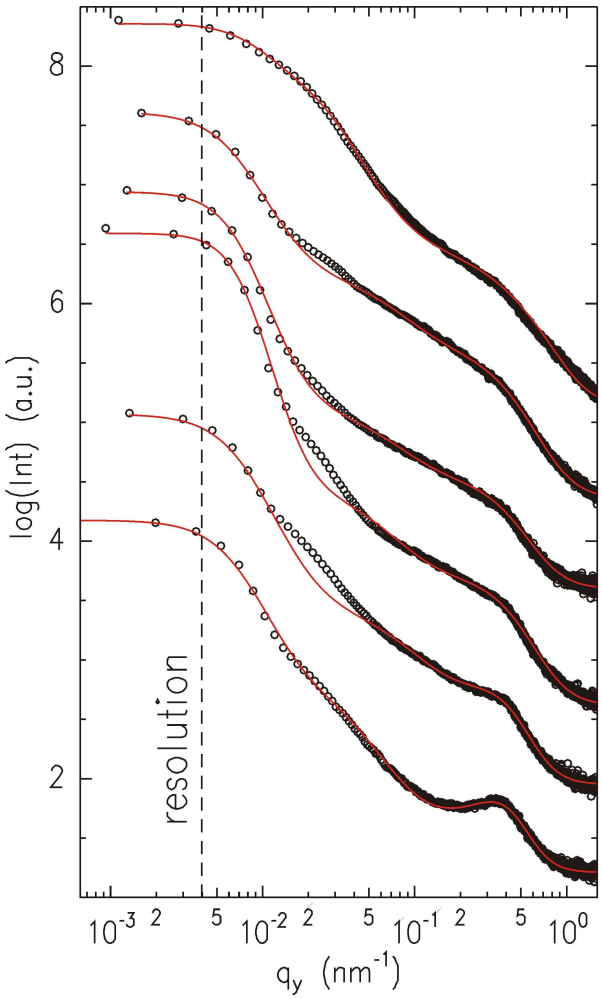

Figure 7.10: *Double-logarithmic plot of out-of-plane cuts (black symbols) with corresponding fits (red solid lines) of P(S-b-PP) films with embedded titania NP. The NP contents are 0 wt%, 1 wt%, 3 wt%, 5 wt%, 10 wt% and 20 wt% from bottom to top, respectively. The effective surface approximation in the framework of the DWBA is used for fitting. The curves are shifted along the y-axis for clarity.*

500 nm is present which is kept constant for all curves. The small structure size increases continuously with increasing NP content from 19 nm up to 50 nm for a NP content of 10 wt%. Furthermore, the distribution of this structure increases. Consequently, the NPs swell the PS phase and the distance between the PPP domains increases. In addition, the long range order is lost as revealed from the increased polydispersity of the structure. For the system with 20 wt% NP content no small structures are resolved but only large structures in the range of 400 nm. At this NP content the contrast between the two phases vanishes if the NPs are only incorporated in the PS phase. However, as seen from the absorption measurements the PPP phase is already perturbed. Consequently, for low content the NPs are selectively incorporated in the PS phase resulting in a swollen structure. With further increase of the NP content the initial morphology is disturbed and NP incorporation is non-selective anymore.

For intermediate q_y values at about 0.02 nm^{-1}, the fits deviate from the data for the P(S-b-PP) films with a NP content from 1 wt% to 10 wt%. This additional structure or

form factor cannot be fitted with the effective surface approximation based on only two structure sizes.
The NPs do not seem to cluster as no additional structure peak corresponding to a length of 10 nm (NP diameter) appears. For magnetic particles such a clustering was found for already low concentrations below 1 %.[205]

7.2.3 Results

The incorporation of inorganic semiconducting nanoparticles in a partly semiconducting diblock copolymer is studied using the model system P(S-b-PP) with titania NPs. The focus is put on the selectivity of incorporation rather than application. GISAXS revealed a morphology of cylindrical PPP objects in a PS phase. When adding titania NPs, the main absorption peak of PPP stays constant for low NP contents. Thus, the NPs do not disturb the molecular ordering of PPP and are selectively incorporated in the PS phase. As a consequence the PS phase swells and the distance of the PPP phases increases. Additionally, the scattering features get less pronounced due to loss in scattering contrast with selective incorporation. Besides the surface modification, the selective incorporation is most probably driven by the crystallization of the PPP phase. During crystallization of polymers, impurities, which includes also the NP, are ejected from the crystalline phase. XRR data and the analysis of the correlated roughness and the waveguide effect observed in the GISAXS data suggest a thin enrichment layer of titania NPs at the substrate interface which is independent of the NP content. Such an additional layer acting as a type of blocking layer would be favorable in the case of application.

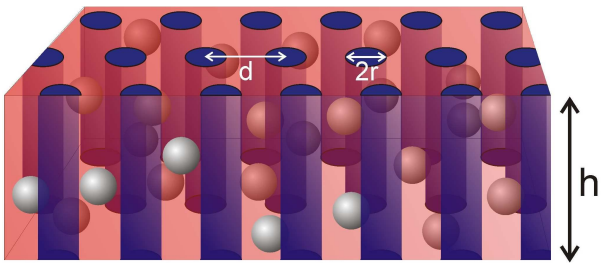

Figure 7.11: *Schematic representation of the suggested model extracted from the scattering data. The blue and red areas depict PPP and PS, respectively. The gray spheres represent the titania NP. The radius r of the cylindrical PPP objects, the interparticle distance d and the film thickness h are shown.*

In figure 7.11 a model of selectively incorporated titania NPs in a P(S-b-PP) film in the case of low NP content is presented. The enrichment of NPs at the substrate interface is not shown for enhanced clarity.
For high NP content, the absorption of PPP changes and the molecular order is influenced

by the NPs. This is a strong indication that the NPs are incorporated in both phases. In addition, the distance of the PPP phases cannot be resolved which is due to the decreased contrast and the loss of structure.
To use this new approach in photovoltaic applications, further structural investigations, such as topographical characterizations, on the model system and finally, photovoltaic characterizations are needed. Most probably, a different material combination with an absorption in the main part of the solar spectrum may be required.

7.3 Swelling of P(S-b-PP)

In the previous section, P(S-b-PP) is used as the structure determining agent. In principle, the structure resulting from a diblock copolymer is defined by the ratio of the two blocks. Thus, the block ratio has to be changed chemically to alter the structure. Such a chemical modification is tedious work, in particular for copolymers containing conjugated blocks. Besides chemical modifications, it is also possible to add a homopolymer which is identical to one of the two blocks. By adding the homopolymer the corresponding block swells which is equivalent to a change of the block ratio. Consequently, the resulting structure will be modified. The homopolymer has to be a low molecular weight homopolymer to avoid the destruction of the initial structure due to large scale phase separation. This swelling approach to modify the morphology of block copolymers has been applied for several other systems before.[207, 208, 209, 210, 211, 212] Perlich et al., for example, used the swelling approach to tune the structure of titania obtained from a sol-gel process for photovoltaic applications.[212]
A fully deuterated polystyrene d8-PS homopolymer with a molecular weight of $M_W = 2.4$ kg/mol is chosen to be incorporated in P(S-b-PP). The d8-PS content is set to 1 wt%, 5 wt%, 10 wt%, 25 wt% and 50 wt%. The polymer is spin coated from a THF solution with 25 mg/ml on HF cleaned silicon and solvent cleaned FTO substrates. The resulting films are thermally annealed at 150 °C, which is well above the glass transition temperature of PS ($T_{g,PS}$ =100 °C), for 48 h. Due to the deuteration of the homopolymer the contrast in neutron scattering experiments is enhanced and the d8-PS can be probed directly.

7.3.1 Surface structure

In figure 7.12 scanning electron microscopy (SEM) images of P(S-b-PP) films with different d8-PS contents are shown. Large round structures with a diameter of 100 nm to 200 nm are visible for films with 1 wt%, 5 wt% and 10 wt% d8-PS content. These large structures reveal a white rim. Between the large domains, smaller structures in the range

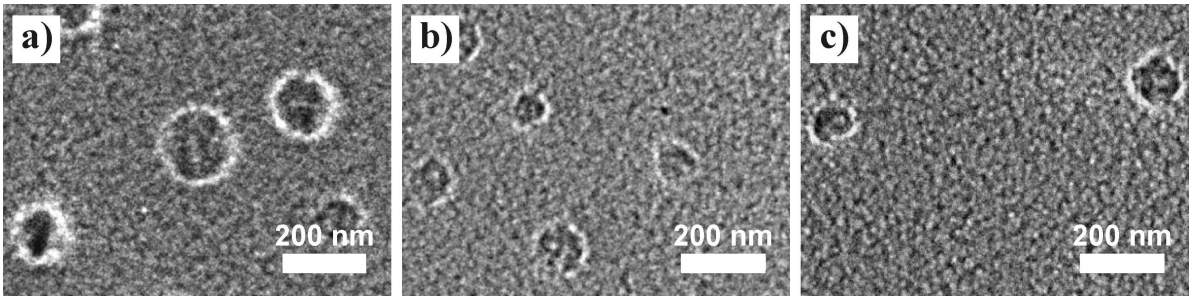

Figure 7.12: *Scanning electron microscopy images of P(S-b-PP) films swollen with different d8-PS contents of 1 wt% (a), 5 wt% (b) and 10 wt% (c). The images are obtained with a field-emission SEM (FESEM, Zeiss LEO 1530 Gemini) operating at an accelerating voltage of 1 kV.*

of 10 nm to 20 nm are observed. This structure size is in good aggreement with the length scales seen for P(S-b-PP) in the previous sections. Thus, also in thicker, thermally annealed P(S-b-PP) films structures on the nanometer scale are formed.

Since it is not possible to distinguish between hole- and island-like structures in the SEM images additional AFM images are taken (figure 7.13). The round objects found in the SEM are also visible in the AFM images and are identified as holes with a depth of up to 20 nm. It seems that the surface coverage of holes is decreasing with d8-PS content at least for the 25 wt% d8-PS films. The 1 wt% d8-PS film reveals a hole density of 10% while for the 25 wt% d8-PS film only a density of 7% is found. For diblock copolymer films a surface with holes or islands is common and is due to deficit or excess of material to fill the next layer. For the film with the higher d8-PS content the addition of d8-PS compensates the missing material and therefore, the hole density is decreased. The small structures observed in the SEM images are not resolved with AFM at the chosen magnification.

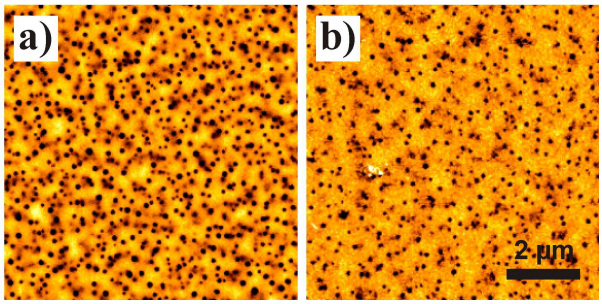

Figure 7.13: *AFM images (8×8 μm^2) of P(S-b-PP) films swollen with different d8-PS contents of 1 wt% (a) and 25 wt% (b). The scale bar is valid for both images. The color coding spans a height of 20 nm (a) and 12 nm (b)*

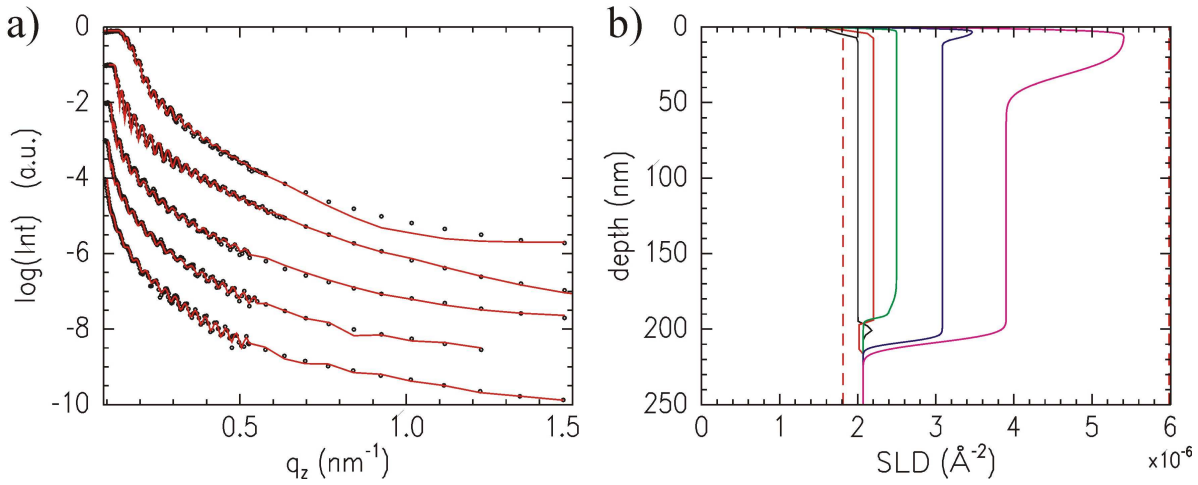

Figure 7.14: *a) Neutron reflectivity data (black symbols) with fits (red solid lines) of P(S-b-PP) films swollen with different d8-PS contents of 1 wt%, 5 wt%, 10 wt%, 25 wt% and 50 wt%. The d8-PS is increasing from bottom to top. The curves are shifted along the y-axis for clarity. b) Scattering length density (SLD) profiles of P(S-b-PP) films swollen with different d8-PS contents of 1 wt% (black), 5 wt% (red), 10 wt% (green), 25 wt% (blue) and 50 wt% (magenta). The left and right red dashed lines represent the SLDs of P(S-b-PP) and d8-PS, respectively.*

7.3.2 Vertical material composition

To probe the vertical distribution of d8-PS, neutron reflectivity experiments are performed (figure 7.14a). Due to the lower SLD of the silicon substrate ($2.08 \cdot 10^{-6}$ Å) compared to d8-PS ($5.99 \cdot 10^{-6}$ Å), the critical edge in the reflectivity data is defined by the polymer. With increasing d8-PS content the edge shifts to higher q_z values. In addition, Kiessig fringes are observed which reveal the film thickness. At higher q_z values a lower resolution is chosen for the measurements.

Vertical scattering length density (SLD) profiles are extracted from the fitting of the reflectivity data (figure 7.14b). The top of the graph (depth = 0 nm) corresponds to the film surface. As the films consist of three components, PS, PPP and d8-PS, with different SLDs, a non-ambiguous material composition profile cannot be calculated from the SLD profile. For clarification the averaged SLD of P(S-b-PP) ($1.81 \cdot 10^{-6}$ Å) and the SLD of d8-PS ($5.99 \cdot 10^{-6}$ Å) are depicted as red dashed lines. The SLD of the substrate is unchanged for all systems. The film thickness is constant at about 220 nm for all systems except for the film with 10 wt% which revealed a slightly lower thickness of 200 nm. With increasing d8-PS content the SLD in the film increases. In the bulk of the film the SLD is constant which is direct evidence that the d8-PS is incorporated homogeneously. Only for the system with 1 wt% d8-PS content a thin enrichment layer of 10 nm is found at the substrate. In addition, a depletion layer near the surface with a SLD below the SLD

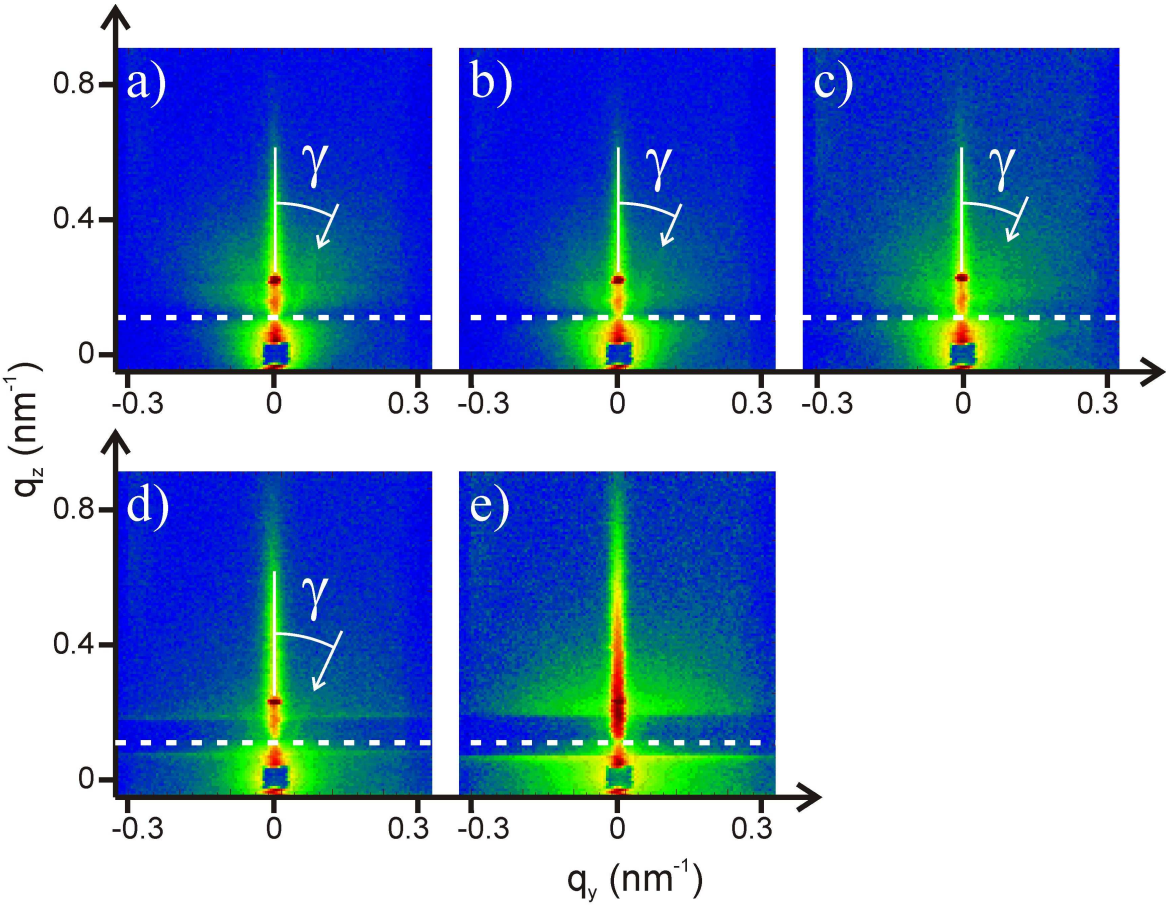

Figure 7.15: *2d GISANS data of P(S-b-PP) films swollen with different d8-PS contents of 1 wt% (a), 5 wt% (b), 10 wt% (c), 25 wt% (d) and 50 wt% (e). Inclined scattering features are highlighted by γ. The reflection (upper) and transmission (lower) scattering are seperated by a dashed white line.*

of P(S-b-PP) is found. This can be explained by the holes already observed in the AFM and SEM images which result in a top layer with an average SLD below P(S-b-PP). This low SLD corresponds to a hole density of 5% surface coverage under the assumption of a pure P(S-b-PP) film. The hole density is lower than the value of 10% as obtained by AFM. However, taking the presence of d8-PS with a higher SLD into account a hole density of 10% is obtained with 2 wt% d8-PS content in the top layer. This d8-PS content is slightly larger than the d8-PS content in the full film. Consequently, already a small d8-PS enrichment exists at the film surface of the 1 wt% film.

AFM and SEM show also holes for films with higher d8-PS content. However, the corresponding layer in the SLD profile cannot be distinguished anymore as the overall SLD increases due to the higher d8-PS content and the hole density decreases. In addition, a d8-PS enrichment layer on the film surface forms for higher d8-PS contents. These effects

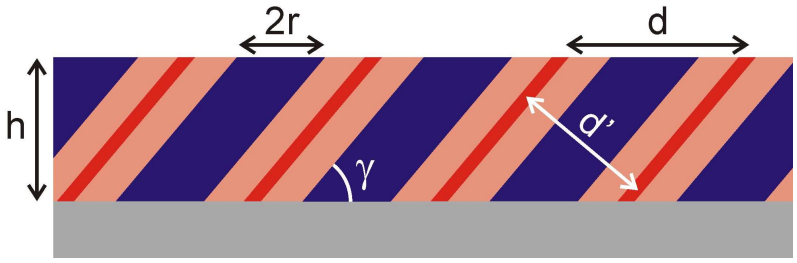

Figure 7.16: *Schematic representation of the model explaining inclined scattering features. The PPP, PS and d8-PS phases are depicted in blue, light red and red, respectively. The gray box represents the substrate. The radius r of the cylindrical PPP objects, the measured and the corrected interparticle distances d and d′ and the film thickness h are shown.*

contribute to the SLD of the very top layer and make it difficult to resolve a thin depletion layer.
The formation of the d8-PS enrichment layer is found for d8-PS contents of 25 wt% and 50 wt%. For these films the excess d8-PS is rejected from the block copolymer. It seems that for systems with lower d8-PS content the homopolymer is fully incorporated in the P(S-b-PP). Concerning photovoltaic applications an enrichment layer at the substrate interface or the film surface is favorable as it acts as a blocking layer and, thus, avoids short cuts.

7.3.3 Lateral structure

In figure 7.15 2d GISANS data of P(S-b-PP) films with different d8-PS contents on silicon are shown. As silicon is almost transparent for neutrons the transmitted signal is also observed. However, due to refraction of the neutron beam this transmitted signal is not comparable with standard SANS experiments in transmission geometry. In the following, the data analysis focuses on the reflected signal.
The scattering data show the specular reflection as well as the material sensitive Yoneda peak. In addition, broad diffuse scattering is observed. For the films with low d8-PS content the 2d data look very similar but change for the higher d8-PS contents (25 wt% and 50 wt%). In particular, for the system with 50 wt% d8-PS content the scattered signal increases dramatically which is due to the higher scattering contrast of the deuterated homopolymer.

The scattering data reveal additional inclined features with an inclination of $\gamma = (23 \pm 2)^\circ$ independent of the d8-PS content. For the film with 50 wt% d8-PS content no inclined feature is visible. This inclined scattering originates from tilted structures with a base angle of $\gamma = (23 \pm 2)^\circ$. Starting from the cylindrical morphology found for the pure

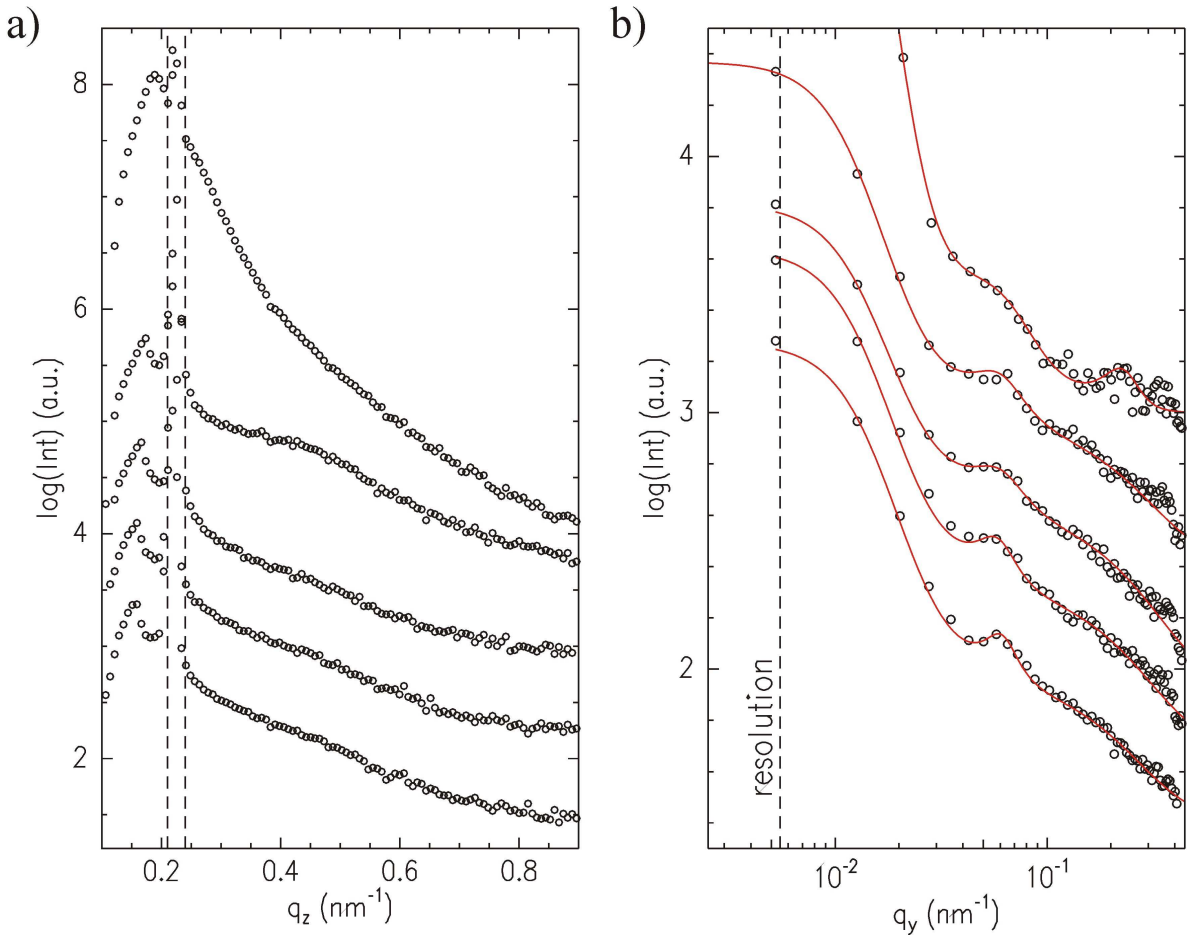

Figure 7.17: *a) Logarithmic plot of detector cuts and b) double-logarithmic plot of out-of-plane cuts of 2d GISANS measurements of P(S-b-PP) films swollen with different d8-PS contents of 1 wt%, 5 wt%, 10 wt%, 25 wt% and 50 wt% from bottom to top. The dashed lines indicate the specular reflection in a) and the resolution limit in b). b) The red solid lines are fits to the data using the effective surface approximation model. The curves are shifted along the y-axis for clarity.*

P(S-b-PP) film, in figure 7.16 a schematic model with inclined structures is presented. The homopolymer is incorporated in the PS phase and consequently increases the size of the PS domains. The structures, including the PPP and PS phases, are tilted with the base angle γ. Similar tilted scattering features were already found for channel structures with inclined walls in the case of mechanically nanostructured PEDOT:PSS.[213]

The detector cuts of the swollen P(S-b-PP) films are shown in figure 7.17a. The material sensitive Yoneda peak shifts to higher q_z values with increasing d8-PS content as the average SLD value is also increasing. This observation is in agreement with the shift of the critical edge observed in the neutron reflectivity data (figure 7.14a). For the systems with d8-PS content up to 10 wt% the detector cuts exhibit a very similar shape without any additional features which is in good agreement with the neutron reflectivity data

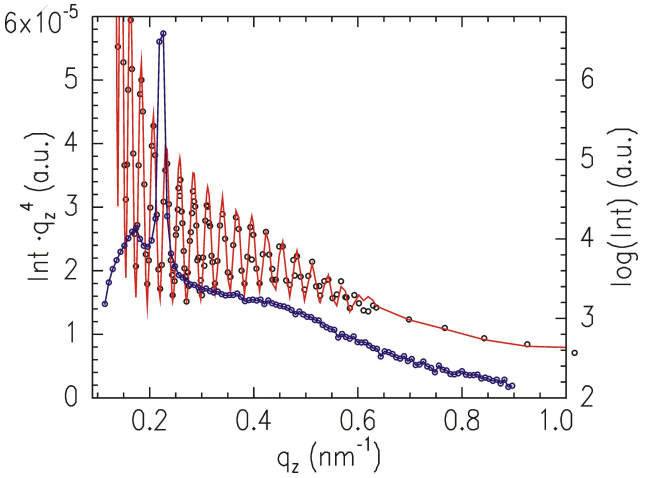

Figure 7.18: *Plots of the neutron reflectivity data (black circles) with fit (red solid line) in the Fresnel normalized presentation and the detector cut (blue circles) of a P(S-b-PP) film with a d8-PS content of 25 wt%.*

revealing no strong layering. The detector cut of the film with 25 wt% d8-PS content reveals a shoulder-like feature which is an indication of an enrichment layer. For the same film neutron reflectivity shows a d8-PS enrichment layer at the sample surface. To confirm that the shoulder-like feature is originated from the same enrichment layer, the detector cut and the reflectivity curve are plotted in figure 7.18. The reflectivity curve is displayed in the Fresnel normalized presentation, i.e. the intensity is multiplied by q_z^4, which is used to enhance weak features. It is clearly visible that both curves exhibit a schoulder-like feature with similar length. Consequently, the feature in the detector cut represents the same enrichment layer as revealed with neutron reflectivity. The detector cut of the P(S-b-PP) film with 50 wt% d8-PS content has much higher intensity as already observed in the 2d data. However, a clear feature representing an enrichment layer is not observed.

Due to the inclined structures and therefore inclined scattering features, it is not possible to extract exact lateral length scales from the out-of-plane cuts (figure 7.17b). A 2d simulation would be necessary to achieve this. Unfortunately, IsGISAXS, which is typically used for 2d simulations (section 5.3), can only simulate objects with tilted walls but not fully tilted objects. Nevertheless, the out-of-plane cuts give an idea on the rough structure sizes but it is important to keep in mind that the extracted length scales are estimated values. To obtain the estimated structure sizes, the effective surface approximation model (section 2.3.3) is used for fitting the out-of-plane cuts.

The out-of-plane cuts exhibit a pronounced lateral length scale d which increases from 104 nm to 130 nm with increasing d8-PS content. To account for the tilt in the structure, the structure size has to be corrected with $d' = d \sin\gamma$. The resulting length scale d' changes from 41 nm to 51 nm with increasing d8-PS content. These values are more than double the structure sizes found for the pure P(S-b-PP) film by GISAXS and observed

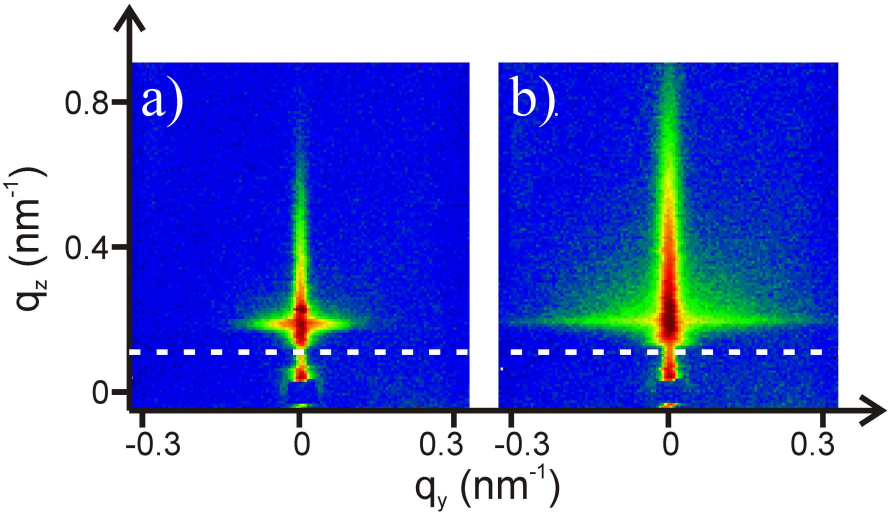

Figure 7.19: *2d GISANS data of P(S-b-PP) films swollen with different d8-PS contents of 5 wt% (a) and 50 wt% (b) on FTO substrates. The reflection (upper) and transmission (lower) scattering are seperated by a dashed white line.*

for the swollen films with SEM. Nevertheless, these values are on the same order of magnitude, particularly keeping in mind that this is just an estimate. The increase in the length scale is a strong evidence that swelling of the PS block due to the incorporation of d8-PS is taking place.
Besides the mentioned length scale of the tilted structures, a broadly distributed length scale of 200 nm is found for P(S-b-PP) film with a d8-PS content up to 25 wt% which is in good agreement with the length scales of the hole-like structure obtained by AFM. The system with the highest d8-PS content (50 wt%) exhibits another pronounced feature corresponding to a size of 28 nm which cannot be assigned to a particular structure so far.

7.3.4 Influence of substrate

Up to now, P(S-b-PP) films on HF cleaned silicon substrates are characterized. To probe the influence of the type of substrate on the structure, P(S-b-PP) films with 5 wt% and 50 wt% d8-PS content are prepared on solvent cleaned FTO substrates. FTO is a transparent conducting oxide which is typically used as electrode in organic solar cells.
In figure 7.19 the 2d GISANS data is shown. In comparison to the 2d data of P(S-b-PP) films on silicon (figure 7.15), the 2d data of the films on FTO exhibit less transmitted signal due to the thicker FTO substrate. Furthermore, higher intensities are observed, in

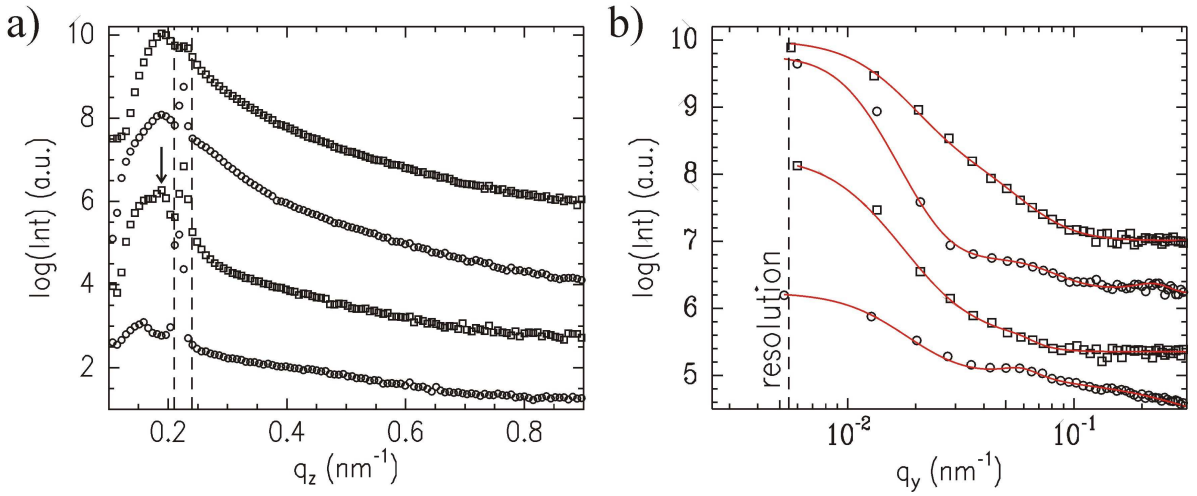

Figure 7.20: *a) Logarithmic plot of detector cuts and b) double-logarithmic plot of out-of-plane cuts of 2d GISANS measurements of P(S-b-PP) films swollen with different d8-PS contents of 5 wt% (lower two curves) and 50 wt% (upper two curves) on Si substrates (cricles) and FTO substrates (squares). The dashed lines indicate the specular reflection in a) and the resolution limit in b). b) The red solid lines are fits to the data using the effective surface approximation model. The curves are shifted along the y-axis for clarity.*

particular, in the Yoneda region. Altogether, the rough FTO surface [214] dominates the scattering signal and thus, the inclined scattering features are not observed.

For a detailed analysis detector and out-of-plane cuts are obtained and compared with the corresponding data of the films made on silicon (figure 7.20). An additional Yoneda peak appears in the detector cut of the P(S-b-PP) film with 5 wt% d8-PS which is due to FTO (arrow in figure 7.20a). For higher d8-PS content the new Yoneda peak is not observed as it is superimposed by the Yoneda peak of d8-PS. Furthermore, the specular intensity decreases for the systems on FTO substrates due to the increased roughness of FTO. The overall shape of the detector cuts does not change when replacing the smooth silicon substrate with the rough FTO.

The out-of-plane cuts containing information on lateral length scales are shown in figure 7.20b. The scattering is dominated by the FTO substrate as already seen in the 2d data. However, there are still features originating from the P(S-b-PP) films visible. Fitting the scattering data using the effective surface approximation exhibits the same length scales as for the films on silicon substrates. This includes the constant structure size of 200 nm, which is most probably related to the hole-like surface structures, and the increasing structure size, which corresponds to the distance between PPP domains. Only the 28 nm length scale found for the P(S-b-PP) film with 50 wt% d8-PS content is not observed on the FTO substrate. In summary, the substrate type does not influence the

structure formation of P(S-b-PP) in this case.
The influence of the FTO substrate on the morphology of nanostructured titania has previously been studied. In that case, the structure changed depending on the underlying substrate material.[215] However, the material system differed from the copoylmer used in this thesis. Thus, the influence of the substrate on the structure depends on the material system used.

7.3.5 Results

Swelling of the PS block of P(S-b-PP) with different d8-PS contents is used to tune the morphology of P(S-b-PP). Imaging techniques (AFM and SEM) reveal hole-like surface structures with a depth up to 20 nm. This perforated top layer appears in the neutron reflectivity data as a layer with decreased SLD. However, the reflectivity data exhibit a homogeneous distribution of d8-PS throughout the 220 nm thick films. For the systems with high d8-PS content (25 wt% and 50 wt%), d8-PS enrichment layers at the sample surface are observed. These enriched layers form most probably due to excess material of d8-PS which can no longer be incorporated in the PS domains as this would destroy the overall morphology. The existence of the enrichment layer is confirmed by GISANS measurements. Such enrichment layers are favorable as blocking layers regarding application in organic electronics if a fully conjugated diblock copolymer instead of the model system P(S-b-PP) is used.
The lateral structure is probed by GISANS. The main difference of the morphology found in the P(S-b-PP) films swollen by d8-PS compared to pure P(S-b-PP) films (section 7.1) is the inclined structure with a tilt angle of about 23°. The inclination is already present for d8-PS contents of only 1 wt%. The inclination results either from the addition of d8-PS or from the increased film thickness of about 220 nm. The inclined structures would require a full 2d simulation of the scattering data to obtain exact length scales. Nevertheless, standard GISANS analysis using the effective surface approximation gives an estimate on the length scales. The increase of the structure size with addition of d8-PS gives direct evidence that the morphology is succesfully swollen by incorporation of d8-PS.
Finally, the influence of the substrate material is investigated. It is found that the morphology does not change when the silicon substrate is replaced by FTO. Thus, the results obtained for the P(S-b-PP) films on silicon can be transferred to other substrates, in particular to FTO.

7.4 Summary

The morphology of the diblock copolymer P(S-b-PP) consisting of the standard coil-like polystyrene (PS) and the semiconducting rod-like poly-p-phenylene (PPP) is investigated as a model system for photovoltaic applications. The advantage of block copolymers compared to polymer blends is that the optimum morphology is the equilibrium structure. Thus, these systems are more stable concerning structural aging.
It is found that P(S-b-PP) fulfills a linear concentration-thickness dependence in the case of spin coating like other homopolymers. A 78 nm thick P(S-b-PP) film forms cylindrical PPP objects embedded in a PS phase. The radius of the cylinders is 10 nm, which fits the typical exciton diffusion length.
The combination of semiconducting titania NPs selectively incorporated in the PS phase of P(S-b-PP) is used as a new approach which might work for hybrid organic photovoltaic devices in future. In this case, the block copolymer is the structure determining agent. The NPs form a constant 7 nm thin enrichment layer which is revealed by the correlated roughness and the wave guide effect in the GISAXS measurements. From the absorption data, in particular the peak position of the main absorption maximum of PPP, it is revealed that the molecular order of PPP is not disturbed by the incorporation of the NPs up to a content of 10 wt%. Thus, the NPs are selectively embedded in the PS phase. These findings are confirmed by GISAXS as the scattering contrast between PS and PPP is balanced by the NP incorporation. In addition, the dominant structural length increases with increasing NP content which is due to the swelling of the PS phase. In summary, up to a critical concentration the NPs incorporate selectively in the PS phase which is attributed to the NP modification and the crystallization of the PPP block ejecting the NPs. This approach is used for the first time and might be sucessfully applied for block copolymers and NPs which fit better concerning electronic properties and absorption spectra.
Additionally, the morphology of P(S-b-PP) is tuned by swelling the PS block by a PS homopolymer with a low molecular weight. For the homopolymer the deuterated derivative d8-PS is used to increase the contrast for neutron scattering experiments. The swollen P(S-b-PP) films reveal inclined structures which increase with increasing homopolymer content. Thus, the selective swelling of a single block of the block copolymer is successful. In addition, an enrichment of the homopolymer near the surface forms. Such a morphology would generally be favorable for photovoltaic applications as the lateral length scales are in the range of the exciton diffusion length and additionally an enrichment layer, which could act as a blocking layer, exists. Finally, it is revealed that the found morphology is independent of the substrate used, at least for silicon and FTO substrates. Consequently, this system can be characterized on silicon and the information directly transferred to FTO substrates.

Chapter 8

Conclusion and outlook

Material combinations resembling the different possible classes in organic photovoltaics for the active layer of an organic solar cell are investigated in this thesis. For all systems the modification of an external parameter results in an altered morphology. It is comprehensively shown that these structures are highly sensitive to the environmental conditions and control parameters. Furthermore, it is found that gaining knowledge on the detailed morphology needs a combination of several complementary investigation techniques. Scattering techniques in addition to imaging techniques provide an excellent possibility to probe surface morphology and buried structures without destroying the sample and the results have a similar statistical relevance as the photovoltaic characteristics obtained from measuring IV-curves. Therefore, the comparison of structure obtained from scattering with the photovoltaic performance is powerful for gaining fundamental understanding.

The standard system today in organic photovoltaics, P3HT:PCBM, is investigated in the first part of this thesis. The bulk heterojunction morphology of this polymer-fullerene system is fully characterized as a function of the solvent used. Despite similar photovoltaic characteristics, the morphologies differ significantly. Variations in lateral structure sizes, vertical material composition and crystallinity are found. These differences cancel each other out regarding photovoltaic performance. Furthermore, surface imaging reveals surface structures with different length scales than found in the bulk of the film. Consequently, the exact determination of the morphology is necessary to obtain a complete understanding of an organic solar cell. Probing only the solar cell topography and its electronic properties is insufficient and can result in misinterpretations.
Moreover, in this thesis the novel concept of fullerenes being dissolved in the P3HT matrix is confirmed for bulk heterojunction systems for the first time. The molecularly dispersed fullerene ratio is determined. It increases linearly with the overall fullerene content. These findings are crucial for the modeling of charge carrier transport processes in organic solar

cells, since so far in simulations only pure phases have been taken into account.
One step towards a further improvement of organic solar cells is the extension of the absorption range of the active layer. This is realized by the addition of a dye with a complementary absorption range. Although the dye contributes to the charge carrier generation, the overall photovoltaic performance decreases for the system under investigation. The reduction of efficiency is attributed to the dye acting as a trap for low dye concentrations and initializing major changes of the morphology for higher dye content. Therefore, including an additional component to an organic photovoltaic system can cause a change in morphology and thereby influence the photovoltaic performance.

Besides standard polymer-fullerene systems, polymer-polymer bulk heterojunction films have the potential for high performance organic solar cells. In a first step, one of the most efficient material combinations, P3HT:F8TBT, is investigated. It is found that the optimum structural length scale in the active layer of an organic solar cell is larger than the actual exciton diffusion length. While small length scales are ideal for exciton dissociation, the charge carrier transport is hindered due to increased recombination. At the observed length scale these effects are balanced and thus the most efficient solar cell is obtained.
Moreover, a new scattering technique (GI-RSoXS) is applied to probe the morphology of the polymer-polymer system, P3HT:MEH-CN-PPV, with varying blend ratio. The advantage of changing the film depth sensitivity without changing the setup is highlighted. The observed structures are present at the film surface and inside the film, as well. Besides the strong influence of composition on the mesoscopic structures, it is shown that the main crystal orientation of the polymer also depends on the blend ratio. At the critical blend ratio the structural changes are less sensitive to annealing. Polymer-polymer bulk heterojunction systems offer a good possibility to tune the morphology on different length scales by adjusting the composition.
Finally, the widely used assumption that blending of some polymers can retard the crystallization process and therefore result in very inefficient devices is directly proven for the first time. Although the investigated samples match concerning electronic properties and mesoscopic length scales, the missing crystallinity is the limiting factor in this system.

The optimum morphology of the systems summarized so far is mostly not in structural equilibrium and therefore in a potentially unstable state. Therefore, diblock copolymers are studied which can form equilibrated structures favorable for photovoltaic applications. The diblock copolymer P(S-b-PP) consisting of a semiconducting and a non-conducting polymer is characterized as a model system for photovoltaic applications in this thesis.
The combination of inorganic, semiconducting nanoparticles and the diblock copolymer is presented as a novel approach for photovoltaic applications. To obtain two separated

phases of the nanoparticle and the semiconducting block, the nanoparticles have to be embedded selectively. It is shown that up to a nanoparticle content of 10 wt% the initial block copolymer structure is preserved and the nanoparticles are embedded in the non-conducting polymer phase. The selectivity is attributed to the nanoparticle modification and the crystallization of the semiconducting block.
The morphology of a diblock copolymer mainly depends on its block ratio. Thus, the block ratio has to be changed to tune the morphology. Besides synthesizing a new polymer, the selective swelling of a single block with an identical homopolymer is used in this thesis. Due to this swelling, the structure size in the block copolymer films increases and the phases are tilted. However, the length scales are still in the range of the exciton diffusion length. In addition, the homopolymer is ejected for higher concentrations and forms an enrichment layer near surface which would act as a favorable blocking layer in photovoltaic applications. Additionally, the structures are found to be independent of the substrate used.

It is found that all investigated systems are sensitive to changes in the preparation history concerning the morphology and the photovoltaic performance. Although this gives the possibility to tune the structure and therefore optimize the solar cell efficiency, these systems are also vulnerable to unintentional changes. In principle, bulk heterojunction systems have the best photovoltaic performance if structural length scales are in the range or slightly above the exciton diffusion length, crystalline fractions exist and a correct vertical material distribution forms. Nevertheless, in detail every material combination behaves differently to modifications and thus no exact general rule can be extracted. Hence, new material combinations have to be optimized individually.
In summary, this thesis demonstrates possible effects on the morphology for different material combinations and proves widely used assumptions by direct measurements.

Future projects concerning the morphology of the active layer in organic solar cells should include its long term structural stability. In particular, in the case of bulk heterojunction systems which are not in equilibrium, structural changes will most probably occur on longer timescales. Local heating due to solar radiation, which is not contributing to charge carrier generation, can induce mobility of the polymer chains and result in structural changes. The main challenge will be to distinguish the effect of structural degradation from chemical aging of the polymer and to develop an analytic mechanism accordingly. Finally, this mechanism has to be related to the change in photovoltaic performance. Especially, the high diffusivity of fullerenes has to be taken into account. The observation that structural changes in polymer-polymer systems are retarded at the critical blend

ratio is promising, as this might open a possibility to reduce structural degradation.

Bibliography

[1] M. A. Green, K. Emery, Y. Hishikawa, W. Warta, and E. D. Dunlop. Solar cell efficiency tables (version 39). *Prog. Photovolt: Res. Appl.*, 20:12–20, 2012.

[2] Herbert Naarmann. *Polymers, Electrically Conducting.* Wiley-VCH Verlag GmbH & Co. KGaA, 2000.

[3] H. Shirakawa, E. J. Louis, A. G. MacDiarmid, C. K. Chiang, and A. J. Heeger. Synthesis of electrically conducting organic polymers: halogen derivatives of polyacetylene, (CH). *J. Chem. Soc., Chem. Commun.*, pages 578–580, 1977.

[4] D. Mühlbacher, M. Scharber, M. Morana, Z. Zhu, D. Waller, R. Gaudiana, and C. Brabec. High photovoltaic performance of a low-bandgap polymer. *Adv. Mater.*, 18:2884–2889, 2006.

[5] G. Yu, C. Zhang, and A. J. Heeger. Dual-function semiconducting polymer devices: light-emitting and photodetecting diodes. *Appl. Phys. Lett.*, 64:1540–1542, 1994.

[6] N. S. Sariciftci, D. Braun, C. Zhang, V. I. Srdanov, A. J. Heeger, G. Stucky, and F. Wudl. Semiconducting polymer-buckminsterfullerene heterojunctions: Diodes, photodiodes, and photovoltaic cells. *Appl. Phys. Lett.*, 62:585–587, 1993.

[7] G. Yu, J. Gao, J. C. Hummelen, F. Wudl, and A. J. Heeger. Polymer photovoltaic cells: enhanced efficiencies via a network of internal donor-acceptor heterojunctions. *Science*, 270:1789–1791, 1995.

[8] J. J. M. Halls, C. A. Walsh, N. Greenham, E. A. Marseglia, R. Friend, S. C. Moratti, and A. Holmes. Efficient photodiodes from interpenetrating polymer networks. *Nature*, 376:498–500, 1995.

[9] M. A. Ruderer and P. Müller-Buschbaum. Morphology of polymer-based bulk heterojunction films for organic photovoltaics. *Soft Matter*, 7:5482–5493, 2011.

[10] R. A. Segalman, B. McCulloch, S. Kirmayer, and J. J. Urban. Block copolymers for organic optoelectronics. *Macromolecules*, 42:9205–9216, 2009.

[11] S. H. Park, A. Roy, S. Beaupre, S. Cho, N. Coates, J. S. Moon, D. Moses, M. Leclerc, K. Lee, and A. J. Heeger. Bulk heterojunction solar cells with internal quantum efficiency approaching 100%. *Nat. Photonics*, 3:297–303, 2009.

[12] G. Strobl. *The Physics of Polymers*. Springer-Verlag Berlin Heidelberg, 3rd edition, 2007.

[13] S. Barth and H. Bässler. Intrinsic photoconduction in PPV-type conjugated polymers. *Phys. Rev. Lett.*, 79:4445–4448, 1997.

[14] D. Hertel and H. Bässler. Photoconduction in amorphous organic solids. *ChemPhysChem*, 9:666–688, 2008.

[15] C. Deibel, D. Mack, J. Gorenflot, A. Schöll, S. Krause, F. Reinert, D. Rauh, and V. Dyakonov. Energy levels and exciton binding energy in the conjugated polymer poly(3-hexyl thiophene). *Phys. Rev. B*, 81:085202–1 – 085202–4, 2010.

[16] C. Deibel and V. Dyakonov. Polymer-fullerene bulk heterojunction solar cells. *Rep. Prog. Phys.*, 73:096401, 2010.

[17] C. Deibel, V. Dyakonov, and C. J. Brabec. Organic bulk-heterojunction solar cells. *IEEE J. Sel. Top. Quantum Electron.*, 16:1517–1527, 2010.

[18] G. Yu and A. J. Heeger. Charge seperation and photovoltaic conversion in polymer composites with internal donor/acceptor heterojunctions. *J. Appl. Phys.*, 78:4510, 1995.

[19] M. Pope and C. E. Swenberg. *Electronic processes in organic crystals and polymers*. Oxford University Press, 2nd edition, 1999.

[20] F. C. Spano. The spectral signatures of Frenkel polarons in H- and J-aggregates. *Acc. Chem. Res.*, 43:429–439, 2010.

[21] J. Cornil, D. Beljonne, Z. Shuai, T. W. Hagler, I. Campbell, D. D. C. Bradley, J. L. Bredas, C. W. Spangler, and K. Müllen. Vibronic structure in the optical absorption spectra of phenylene vinylene oligomers: a joint experimental and theoretical study. *Chem. Phys. Lett.*, 247:425–432, 1995.

[22] L. Lüer, H.-J. Egelhaaf, D. Oelkrug, G. Cerullo, G. Lanzani, B.-H. Huisman, and D. de Leeuw. Oxygen-induced quenching of photoexcited states in polythiophene films. *Org. Electron.*, 5:83, 2004.

[23] J. Clark, C. Silva, R. H. Friend, and F. C. Spano. Role of intermolecular coupling in the photophysics of disordered organic semiconductors: Aggregate emission in regioregular polythiophene. *Phys. Rev. Lett.*, 98:206406, 2007.

[24] P. J. Brown, D. S. Thomas, A. Köhler, J. S. Wilson, J.-S. Kim, C. M. Ramsdale, H. Sirringhaus, and R. H. Friend. Effect of interchain interactions on the absorption and emission of poly(3-hexylthiophene). *Phys. Rev. B*, 67:064203, 2003.

[25] Y. Gao, T. P. Martin, E. T. Niles, A. J. Wise, A. K. Thomas, and J. K. Grey. Understanding morphology-dependent polymer aggregation properties and photocurrent generation in polythiophene/fullerene solar cells of variable compositions. *J. Phys. Chem. C*, 114:15121–15128, 2010.

[26] W. J. D. Beenken. Excitons in conjugated polymers: Do we need a paradigma change? *Phys. Status Solidi A*, 206:2750–2756, 2009.

[27] P. E. Shaw, A. Ruseckas, and I. D. W. Samuel. Exciton diffusion measurements in poly(3-hexylthiophene). *Adv. Mater.*, 20:3516–3520, 2008.

[28] D. Kurrle and J. Pflaum. Exciton diffusion length in the organic semiconductor diindenoperylene. *Appl. Phys. Lett.*, 92:133306, 2008.

[29] P. Peumans, A. Yakimov, and S. R. Forrest. Small molecular weight organic thin-film photodetectors and solar cells. *J. Appl. Phys.*, 93:3693, 2003.

[30] N. S. Sariciftci, L. Smilowitz, A. J. Heeger, and F. Wudl. Photoinduced electron-transfer from a conducting polymer to buckminsterfullerenes. *Science*, 258:1474, 1992.

[31] I.-W. Hwang, D. Moses, and A. J. Heeger. Photoinduced carrier generation in P3HT/PCBM bulk heterojunction materials. *J. Phys. Chem. C*, 112:4350–4354, 2008.

[32] L. Onsager. Initial recombination of ions. *Phys. Rev.*, 54:554–557, 1938.

[33] C. L. Braun. Electric field assisted dissociation of charge transfer states as a mechanism of photocarrier production. *J. Chem. Phys.*, 80:4157–4161, 1984.

[34] R. A. Marcus. On the theory of oxidation-reduction reactions involving electron transfer: I. *J. Chem. Phys.*, 24:966, 1956.

[35] R. A. Marcus. Electron transfer reactions in chemistry: theory and experiment. *Rev. Mod. Phys.*, 65:599, 1993.

[36] A. Miller and E. Abrahams. Impurity conduction at low concentrations. *Phys. Rev.*, 120:745, 1960.

[37] W. F. Pasveer, J. Cottaar, C. Tanase, R. Coehoorn, P. A. Bobbert, P. W. M. Blom, D. M. de Leeuw, and M. A. J. Michels. Unified description of charge-carrier mobilities in disordered semiconducting polymers. *Phys. Rev. Lett.*, 94:206601, 2005.

[38] H. Houili, E. Tutis, I. Batistic, and L. Zuppiroli. Investigation of the charge transport through disordered organic molecular heterojunctions. *J. Appl. Phys.*, 100:033702, 2006.

[39] G. Schönherr, R. Eiermann, H. Bässler, and M. Silver. Dispersive exciton transport in a hopping system with gaussian energy distribution. *Chem. Phys.*, 52:287, 1980.

[40] H. Bässler. Charge transport in disordered organic photoconductors - a Monte Carlo simulation study. *Phys. Status Solidi b*, 175:15, 1993.

[41] A. J. Mozer and N. S. Sariciftci. Negative electric field dependence of charge carrier drift mobility in conjugated, semiconducting polymers. *Chem. Phys. Lett.*, 389:438, 2004.

[42] S. M. Tuladhar, M. Sims, J. Kirkpatrick, R. C. Maher, A. J. Chatten, D. D. C., J. Nelson, P. G. Etchegoin, C. B. Nielsen, P. Massiot, W. N. George, and J. H. G. Steinke. Influence of alkyl chain length on charge transport in symmetrically substituted poly(2,5-dialkoxy-p-phenylenevinylene) polymers. *Phys. Rev. B*, 79:035201, 2009.

[43] V. D. Mihailetchi, L. J. A. Koster, J. C. Hummelen, and P. W. M. Blom. Photocurrent generation in polymer-fullerene bulk heterojunctions. *Phys. Rev. Lett.*, 93:216601, 2004.

[44] R. Sokel and R. C. Hughes. Numerical analysis of transient photoconductivity in insulators. *Journal of Applied Physics*, 53:7414–7424, 1982.

[45] J. C. Scott and G. G. Malliaras. Charge injection and recombination at the metal-organic interface. *Chem. Phys. Lett.*, 299:115 – 119, 1999.

[46] P. Langevin. Recombinaison et mobilites des ions dans les gaz. *Ann. Chim. Phys.*, 28:433, 1903.

[47] A. Salleo, T. W. Chen, and A. R. Völkel. Intrinsic hole mobility and trapping in a regioregular poly(thiophene). *Physical Review B*, 70:115311, 2008.

[48] C. Fougnies, M. Dosiére, M. H. J. Koch, and J. Roovers. Morphological study and melting behavior of narrow molecular weight fractions of poly(aryl ether ether ketone) (PEEK) annealed from the glassy state. *Macromolecules*, 31:6266, 1998.

[49] J. D. Hoffman, G. T. Davis, and J. I. Lauritzen. *Treatise on Solid State Chemistry*, volume 3. Plenum, New York, 1976.

[50] G. Strobl. From the melt via mesomorphic and granular crystalline layers to lamellar crystallites: A major route followed in polymer crystallization? *Eur. Phys. J. E*, 3:165, 2000.

[51] B. Lotz. What can polymer crystal structure tell about polymer crystallization processes? *Eur. Phys. J. E*, 3:185, 2000.

[52] S. Z. D. Cheng, C. Y. Li, and L. Zhu. Commentary on polymer crystallization: Selection rules in different length scales of a nucleation process. *Eur. Phys. J. E*, 3:195, 2000.

[53] M. Muthukumar. Commentary on theories of polymer crystallization. *Eur. Phys. J. E*, 3:199, 2000.

[54] A. Kundagrami and M. Muthukumar. Continuum theory of polymer crystallization. *J. Chem. Phys.*, 126:144901, 2007.

[55] G. Strobl. Colloquium: Laws controlling crystallization and melting in bulk polymers. *Rev. Mod. Phys.*, 81:1287, 2009.

[56] M. V. Massa and K. Dalnoki-Veress. Homogeneous crystallization of poly(ethylene oxide) confined to droplets: The dependence of the crystal nucleation rate on length scale and temperature. *Phys. Rev. Lett.*, 92:255509, 2004.

[57] R. Becker. Die Keimbildung bei der Ausscheidung in metallischen Mischkristallen. *Ann. Physik*, 32:128, 1938.

[58] F. P. Price. *Nucleation*. Dekker, New York, 1969.

[59] W. Hu. *Progress in Understanding of Polymer Crystallization*. Springer-Verlag Berlin Heidelberg, 2007.

[60] B. Wunderlich. *Macromolecular Physics: 2 Crystal Nucleation, Growth, Annealing*. Academic Press, New York, 1976.

[61] A. T. Fromhold. Stress in dielectric contact layers on metals. *Surf. Sci.*, 22:396–410, 1972.

[62] G. Strobl. Crystallization and melting of bulk polymers: New observations, conclusions and a thermodynamic scheme. *Prog. Polym. Sci.*, 31:398, 2006.

[63] P. J. Flory. Thermodynamics of high polymer solutions. *J. Chem. Phys.*, 10:51, 1942.

[64] M. L. Huggins. Theory of solutions of high polymers. *J. Phys. Chem.*, 64:1712, 1942.

[65] H.S. Lee, H.C. Jung, M.S. Han, C.S. Lee, and W.N. Kim. Compatibility studies of blends of a thermotropic liquid crystalline polymer and flexible chain polymers by application of Flory's lattice theory. *Polymer*, 42:2177–2184, 2001.

[66] H. Tanaka and T. Nishi. New types of phase separation behavior during the crystallization process in polymer blends with phase diagram. *Phys. Rev. Lett.*, 55:1102–1105, 1985.

[67] M. Tolan. *X-Ray Scattering from Soft-Matter Thin Films*. Springer-Verlag Berlin Heidelberg, 1999.

[68] P. Müller-Buschbaum. *Polymer Surfaces and Interfaces: Characterization, Modification and Applications*. Springer-Verlag Berlin Heidelberg, 2008.

[69] L. G. Parratt. Surface studies of solids by total reflection of x-rays. *Phys. Rev.*, 95:359, 1954.

[70] L. Nevot and P. Croce. Characterization of surfaces by grazing x-ray reflection–application to the study of polishing of some silicate glasses. *Rev. Phys. Appl.*, 15:761, 1980.

[71] H. Kiessig. Interferenz von Röntgenstrahlen an dünnen Schichten. *Ann. Phys.*, 10:769–788, 1931.

[72] C. Braun. *Parratt32*. HMI Berlin, 2002.

[73] G. Renaud, R. Lazzari, and F. Leroy. Probing surface and interface morphology with grazing incidence small angle x-ray scattering. *Surf. Sci. Rep.*, 64:255–380, 2009.

[74] I. Grillo. *Soft Matter Characterization*. Springer-Verlag Berlin Heidelberg, 2008.

[75] J. Lekner. Reflection theory and the analysis of neutron reflection data. *Physica B*, 173:99–111, 1991.

[76] S. H. Anastasiadis, T. P. Russell, S. K. Satija, and C. F. Majkrzak. Neutron reflectivity studies of surface-induced ordering of diblock copolymer films. *Phys. Rev. Lett.*, 62:1852–1855, 1989.

[77] P. Müller-Buschbaum. *A basic introduction to grazing incidence small angle X-ray scattering*. Springer, Berlin, 2009.

[78] S. K. Sinha, E. B. Sirota, S. Garoff, and H. B. Stanley. X-ray and neutron scattering from rough surfaces. *Phys. Rev. B*, 38:2297–2311, 1988.

[79] V. Holý and T. Baumbach. Nonspecular x-ray reflection from rough multilayers. *Phys. Rev. B*, 49:10668–10676, 1994.

[80] Y. Yoneda. Anomalous surface reflection of x-rays. *Phys. Rev.*, 131:2010–2013, 1963.

[81] P. Müller-Buschbaum. Grazing incidence small-angle x-ray scattering: an advanced scattering technique for the investigation of nanostructured polymer films. *Anal. Bioanal. Chem.*, 376:3–10, 2003.

[82] A. Naudon, D. Babonneau, D. Thiaudière, and S. Lequien. Grazing-incidence small-angle x-ray scattering applied to the characterization of aggregates in surface regions. *Physica B*, 283:69–74, 2000.

[83] R. Hosemann, W. Vogel, D. Weick, and F. J. Baltá-Calleja. Novel aspects of the real paracrystal. *Acta Cryst.*, A37:85–91, 1981.

[84] M. Rauscher, T. Salditt, and H. Spohn. Small-angle x-ray scattering under grazing incidence: The cross section in the distorted-wave Born approximation. *Phys. Rev. B*, 52:16855–16863, 1995.

[85] R. Lazzari. IsGISAXS: a program for grazing-incidence small-angle x-ray scattering analysis of supported islands. *J. Appl. Cryst.*, 35:406–421, 2002.

[86] H. Ade and A. P. Hitchcock. NEXAFS microscopy and resonant scattering: Composition and orientation probed in real and reciprocal space. *Polymer*, 49:643–675, 2008.

[87] H. Ade and H. Stoll. Near-edge x-ray absorption fine-structure microscopy of organic and magnetic materials. *Nat. Mater.*, 8:281–290, 2009.

[88] V. Lucarini, J. J. Saarinen, K.-E. Peiponen, and E. M. Vartiainen. *Kramers-Kronig Relations in Optical Materials Research*. Springer-Verlag Berlin Heidelberg, 2005.

[89] B. L. Henke, E. M. Gullikson, and J. C. Davis. X-ray interactions: photoabsorption, scattering, transmission, and reflection at E=50-30000 ev, Z=1-92. *Atomic Data and Nuclear Data Tables*, 54:181–342, 1993.

[90] J. Stöhr and D. A. Outka. Determination of molecular orientations on surfaces from theoretical angular dependence of near-edge x-ray-absorption fine-structure spectra. *Phys. Rev. B*, 36:7891–7905, 1987.

[91] A. Guinier. *X-ray diffraction in crystals, imperfect crystals, and amorphous bodies*. Dover Publications, 1994.

[92] C. Kittel. *Einführung in die Festkörperphysik*. Oldenbourg, 14. edition, 2006.

[93] T. Hippler, S. Jiang, and G. Strobl. Block formation during polymer crystallization. *Macromolecules*, 38:9396–9397, 2005.

[94] J. L. Baker, L. H. Jimison, S. Mannsfeld, S. Volkman, S. Yin, V. Subramanian, A. Salleo, A. P. Alivisatos, and M. F. Toney. Quantification of thin film crystallographic orientation using x-ray diffraction with an area detector. *Langmuir*, 26:9146–9151, 2010.

[95] J. S. Bendat and A. G. Piersol. *Random Data: Analysis and Measurement Procedures*. Wiley-Interscience, New York, 1971.

[96] J. S. Gutmann, P. Müller-Buschbaum, and M. Stamm. Complex pattern formation by phase separation of polymer blends in thin films. *Faraday Discuss.*, 112:285, 1999.

[97] A. Diethert. *Near-surface composition of pressure sensitive adhesive films and its impact on adhesion*. PhD thesis, Fakultät für Physik der Technischen Universität München, 2011.

[98] R. Kampmann, V. Deriglazov, M. Haese-Seiller, M. Marmotti, M. Tristl, and E. Sackmann. REFSANS: a novel reflectometer for analyses of liquid and soft surfaces at the new research reactor FRM-II in Munich/Germany. *Physica B*, 276:212, 2000.

[99] R. Kampmann, M. Haese-Seiller, M. Marmotti, J. Burmester, V. Deriglazov, V. Syromiatnikov, A. Okorokov, F. Frisius, M. Tristl, and E. Sackmann. The novel reflectometer REFSANS for analyses of liquid and soft surfaces at the new research reactor FRM-II in Munich, Germany. *Appl. Phys. A*, 74:S249, 2002.

[100] S. V. Roth, R. Döhrmann, M. Dommach, M. Kuhlmann, I. Kröger, R. Gehrke, H. Walter, C. Schroer, B. Lengeler, and P. Müller-Buschbaum. The small-angle options of the upgraded USAXS beamline BW4 at HASYLAB. *Rev. Sci. Instrum.*, 77:085106, 2006.

[101] J. Perlich, J. Rubeck, S. Botta, R. Gehrke, S. V. Roth, M. A. Ruderer, S. M. Prams, M. Rawolle, Q. Zhong, V. Körstgens, and P. Müller-Buschbaum. Grazing incidence wide angle x-ray scattering at the wiggler beamline BW4 of HASYLAB. *Rev. Sci. Instrum.*, 81:105105, 2010.

[102] E. Metwalli, J.-F. Moulin, R. Gebhardt, R. Cubitt, A. Tolkach, U. Kulozik, and Müller-Buschbaum P. Hydration behavior of casein micelles in thin film geometry: A GISANS study. *Langmuir*, 25:4124–4134, 2009.

[103] C. Wang, A. Hexemer, J. Nasiatka, E. R. Chan, A. T. Young, H. A. Padmore, W . F. Schlotter, J. Lüning, S. Swaraj, B. Watts, E. Gann, H. Yan, and H. Ade. Resonant soft X-ray scattering of polymers with a 2d detector: Initial results and system developments at the Advanced Light Source. *IOP Conf. Ser.: Mater. Sci. Eng.*, 14:012016, 2010.

[104] J. Stöhr. *NEXAFS spectroscopy*. Springer, Berlin, 2003.

[105] C. R. McNeill and N. Greenham. Conjugated-polymer blends for optoelectronics. *Adv. Mater.*, 21:3840, 2009.

[106] M. Granström, K. Petritsch, A. C. Arias, A. Lux, M. R. Andersson, and R. H. Friend. Laminated fabrication of polymeric photovoltaic diodes. *Nature*, 395:257, 1998.

[107] T. Kietzke, H.-H. Hörhold, and D. Neher. Efficient polymer solar cells based on M3EH-PPV. *Chem. Mater.*, 17:6532, 2005.

[108] B. C. O'Regan, I. Lopez-Duarte, M. V. Martinez-Diaz, A. Forneli, J. Albero, A. Morandeira, E. Palomares, T. Torres, and J. R. Durrant. Catalysis of recombination and its limitation on open circuit voltage for dye sensitized photovoltaic cells using phthalocyanine dyes. *J. Am. Chem. Soc.*, 130:2907, 2008.

[109] Johann Szeifert. *Mesoporous Titania Materials - Tuning and Optimizing Nanostructures and Porous Morphologies*. PhD thesis, LMU München: Fakultät für Chemie und Pharmazie, 2011.

[110] P. Müller-Buschbaum, N. Hermsdorf, S. V. Roth, J. Wiedersich, S. Cunis, and R. Gehrke. Comparative analysis of nanostructured diblock copolymer films. *Spectrochimica Acta Part B*, 59:1789, 2004.

[111] P. Müller-Buschbaum. Influence of surface cleaning on dewetting of thin polystyrene films. *Euro. Phys. J. E*, 12:443, 2003.

[112] D. W. Schubert. Spin coating as a method for polymer molecular weight determination. *Pol. Bull.*, 38:117, 1997.

[113] D. W. Schubert and T. Dunkel. Spin coating from a molecular point of view: its concentration regimes, influence of molar mass and distribution. *Mat.Res. Innovat.*, 7:314, 2003.

[114] M. A. Ruderer, M. Hirzinger, and P. Müller-Buschbaum. Photoactive nanostructures of polypyrrole. *ChemPhysChem*, 10:2692, 2009.

[115] C. J. Brabec, S. Gowrisanker, J. J. M. Halls, D. Laird, S. Jia, and S. P. Williams. Polymer-fullerene bulk-heterojunction solar cells. *Adv. Mater.*, 22:3839–3856, 2010.

[116] Y. Liang, Z. Xu, J. Xia, S.-T. Tsai, Y. Wu, G. Li, C. Ray, and L. Yu. For the bright future-bulk heterojunction polymer solar cells with power conversion efficiency of 7.4%. *Adv. Funct. Mater.*, 22:E135, 2010.

[117] B. A. Collins, J. R. Tumbleston, and H. Ade. Miscibility, crystallinity, and phase development in organic solar cells: Towards an enlightened understanding of device morphology and stability. *J. Phys. Chem. Lett.*, 2:3135–3145, 2011.

[118] M. A. Ruderer, S. Guo, R. Meier, H.-Y. Chiang, V. Körstgens, J. Wiedersich, J. Perlich, S. V. Roth, and P. Müller-Buschbaum. Solvent-induced morphology in polymer-based systems for organic photovoltaics. *Adv. Funct. Mater.*, 21:3382–3391, 2011.

[119] M. A. Ruderer, R. Meier, L. Porcar, R. Cubitt, and Müller-Buschbaum P. Phase separation and molecular intermixing in polymer-fullerene bulk heterojunction thin films. *J. Phys. Chem. Lett.*, 3:683–688, 2012.

[120] M. A. Ruderer, M. Hinterstocker, and Müller-Buschbaum P. Structure in ternary blend systems for organic photovoltaics. *Synth. Met.*, 161:2001–2005, 2011.

[121] S. E. Shaheen, C. J. Brabec, N. S. Sariciftci, F. Padinger, T. Fromherz, and J. C. Hummelen. 2.5% efficient organic plastic solar cells. *Appl. Phys. Lett.*, 78:841–843, 2001.

[122] H. Hoppe, M. Niggemann, C. Winder, J. Kraut, R. Hiesgen, A. Hinsch, D. Meissner, and N. S. Sariciftci. Nanoscale morphology of conjugated polymer/fullerene based bulk-heterojunction solar cells. *Adv. Funct. Mater.*, 14:1005–1011, 2004.

[123] M. M. Wienk, J. M. Kroon, W. J. H. Verhees, J. Knol, J. C. Hummelen, P. A. van Hal, and R. A. J. Janssen. Efficient methano[70]fullerene/MDMO-PPV bulk heterojunction photovoltaic cells. *Angew. Chem.*, 115:3493–3497, 2003.

[124] A. C. Arias, J. D. MacKenzie, R. Stevenson, J. J. M. Halls, M. Inbasekaran, E. P. Woo, D. Richards, and R. H. Friend. Photovoltaic performance and morphology of polyfluorene blends: A combined microscopic and photovoltaic investigation. *Macromolecules*, 34:6005–6013, 2001.

[125] M. T. Rispens, A. Meetsma, R. Rittberger, C. J. Brabec, N. S. Sariciftci, and J. C. Hummelen. Influence of the solvent on the crystal structure of PCBM and the efficiency of MDMO-PPV:PCBM 'plastic' solar cells. *Chem. Commun.*, pages 2116–2118, 2003.

[126] Andrew R. Campbell, Justin M. Hodgkiss, Sebastian Westenhoff, Ian A. Howard, Robert A. Marsh, Christopher R. McNeill, Richard H. Friend, and Neil C. Greenham. Low-temperature control of nanoscale morphology for high performance polymer photovoltaics. *Nano Lett.*, 8:3942–3947, 2008.

[127] J. Moule and K. Meerholz. Controlling morphology in polymer-fullerene mixtures. *Adv. Mater.*, 20:240–245, 2008.

[128] C. Uhrich, R. Schueppel, A. Petrich, M. Pfeiffer, K. Leo, E. Brier, P. Kilickiran, and P. Baeuerle. Organic thin-film photovoltaic cells based on oligothiophenes with reduced bandgap. *Adv. Funct. Mater.*, 17:2991–2999, 2007.

[129] D. M. DeLongchamp, B. M. Vogel, M. C. Jung, Y.and Gurau, C. A. Richter, O. A. Kirillov, J. Obrzut, D. A. Fischer, S. Sambasivan, L. J. Richter, and E. K. Lin. Variations in semiconducting polymer microstructure and hole mobility with spin-coating speed. *Chem. Mater.*, 17(23):5610–5612, 2005.

[130] S. Hugger, R. Thomann, T. Heinzel, and T. Thurn-Albrecht. Semicrystalline morphology in thin films of poly(3-hexylthiophene). *Colloid. Polym. Sci.*, 282:932–938, 2004. 10.1007/s00396-004-1100-9.

[131] Zhiyong Wu, Albrecht Petzold, Thomas Henze, Thomas Thurn-Albrecht, Ruth H. Lohwasser, Michael Sommer, and Mukundan Thelakkat. Temperature and molecu-

lar weight dependent hierarchical equilibrium structures in semiconducting poly(3-hexylthiophene). *Macromolecules*, 43:4646–4653, 2010.

[132] K. Sethuraman, S. Ochiai, K. Kojima, and T. Mizutani. Performance of poly(3-hexylthiophene) organic field-effect transistors on cross-linked poly(4-vinyl phenol) dielectric layer and solvent effects. *Appl. Phys. Lett.*, 92:183302, 2008.

[133] L. Chang, H. W. A. Lademann, J.-B. Bonekamp, K. Meerholz, and A. J. Moule. Effect of trace solvent on the morphology of P3HT:PCBM bulk heterojunction solar cells. *Adv. Funct. Mater.*, 21:1779–1787, 2011.

[134] H. Zhong, X. Yang, B. deWith, and J. Loos. Quantitative insight into morphology evolution of thin PPV/PCBM composite films upon thermal treatment. *Macromolecules*, 39:218–223, 2006.

[135] D. Kronholm and J. Hummelen. Fullerene-based n-type semiconductors in organic electronics. *Material Matters*, 2:16–20, 2007.

[136] P. A. Troshin, H. Hoppe, J. Renz, M. Egginger, J. Y. Mayorova, A. E. Goryachev, A. S. Peregudov, R. N. Lyubovskaya, G. Gobsch, N. S. Sariciftci, and V. F. Razumov. Material solubility-photovoltaic performance relationship in the design of novel fullerene derivatives for bulk heterojunction solar cells. *Adv. Funct. Mater.*, 19:779–788, 2009.

[137] C. R. McNeill, B. Watts, L. Thomsen, H. Ade, N. C. Greenham, and P. C. Dastoor. X-ray microscopy of photovoltaic polyfluorene blends: Relating nanomorphology to device performance. *Macromolecules*, 40:3263–3270, 2007.

[138] C. R. McNeill, A. Abrusci, I. Hwang, M. A. Ruderer, P. Müller-Buschbaum, and N. C. Greenham. Photophysics and photocurrent generation in polythiophene/polyfluorene copolymer blends. *Adv. Funct. Mater.*, 19:3103–3111, 2009.

[139] Manfred Stamm, Günter Reiter, and Klaus Kunz. The use of x-ray and neutron reflectometry for the investigation of polymeric thin films. *Physica B*, 173:35–42, 1991.

[140] K. B. Burke, W. J. Belcher, L. Thomsen, B. Watts, C. R. McNeill, H. Ade, and P. C. Dastoor. Role of solvent trapping effects in determining the structure and morphology of ternary blend organic devices. *Macromolecules*, 42:3098–3103, 2009.

[141] J. Perlich, V. Körstgens , E. Metwalli, L. Schulz, R. Georgii, and P. Müller-Buschbaum. Solvent content in thin spin-coated polystyrene homopolymer films. *Macromolecules*, 42:337–344, 2009.

[142] A. Diethert, Y. Peykova, N. Willenbacher, and P. Müller-Buschbaum. Near-surface composition profiles and the adhesive properties of statistical copolymer films being model systems of pressure sensitive adhesive films. *ACS Appl. Mater. Interfaces*, 2:2060–2068, 2010.

[143] G. Kaune and P. Müller-Buschbaum. Gradient-doping of a conductive polymer film with a layer-by-layer approach. *Phys. Status Solidi RRL*, 4:52–54, 2010.

[144] C. M. Björström, S. Nilsson, A. Bernasik, A. Budkowski, M. Andersson, K. O. Magnusson, and E. Moons. Vertical phase separation in spin-coated films of a low bandgap polyfluorene/PCBM blend-effects of specific substrate interaction. *Appl. Surf. Sci.*, 253:3906–3912, 2007.

[145] X. Wang, T. Ederth, and O. Inganäs. In situ wilhelmy balance surface energy determination of poly(3-hexylthiophene) and poly(3,4-ethylenedioxythiophene) during electrochemical doping-dedoping. *Langmuir*, 22:9287–9294, 2006. PMID: 17042544.

[146] A. Kumar, G. Li, Z. Hong, and Y. Yang. High efficiency polymer solar cells with vertically modulated nanoscale morphology. *Nanotechnology*, 20:165202, 2009.

[147] A. J. Parnell, A. D. F. Dunbar, A. J. Pearson, P. A. Staniec, A. J. C. Dennison, H. Hamamatsu, M. W. A. Skoda, D. G. Lidzey, and R. A. L. Jones. Depletion of PCBM at the cathode interface in P3HT/PCBM thin films as quantified via neutron reflectivity measurements. *Adv. Mater.*, 22:2444–2447, 2010.

[148] J. W. Kiel, B. J. Kirby, C. F. Majkrzak, B. B. Maranville, and M. E. Mackay. Nanoparticle concentration profile in polymer-based solar cells. *Soft Matter*, 6:641–646, 2010.

[149] M. Campoy-Quiles, T. Ferenczi, T. Agostinelli, P. G. Etchegoin, Y. Kim, T. D. Anthopoulos, P. N. Stavrinou, D. D. C. Bradley, and J. Nelson. Morphology evolution via self-organization and lateral and vertical diffusion in polymer:fullerene solar cell blends. *Nat. Mater.*, 7:158–164, 2008.

[150] B. A. Collins, E. Gann, L. Guignard, X. He, C. R. McNeill, and H. Ade. Molecular miscibility of polymer-fullerene blends. *J. Phys. Chem. Lett.*, 1:3160–3166, 2010.

[151] N. D. Treat, M. A. Brady, G. Smith, M. F. Toney, E. J. Kramer, C. J. Hawker, and M. L. Chabinyc. Interdiffusion of PCBM and P3HT reveals miscibility in a photovoltaically active blend. *Adv. Energy Mater.*, 1:82–89, 2011.

[152] D. Chen, F. Liu, C. Wang, A. Nakahara, and T. P. Russell. Bulk heterojunction photovoltaic active layers via bilayer interdiffusion. *Nano Lett.*, 11:2071–2078, 2011.

[153] B. A. Collins, Z. Li, C. R. McNeill, and H. Ade. Fullerene-dependent miscibility in the silole-containing copolymer PSBTBT-08. *Macromolecules*, 44:9747–9751, 2011.

[154] F. C. Spano. Modeling disorder in polymer aggregates: The optical spectroscopy of regioregular poly(3-hexylthiophene) thin films. *J. Chem. Phys.*, 122:234701, 2005.

[155] Jenny Clark, Jui-Fen Chang, Frank C. Spano, Richard H. Friend, and Carlos Silva. Determining exciton bandwidth and film microstructure in polythiophene films using linear absorption spectroscopy. *Appl. Phys. Lett.*, 94:163306, 2009.

[156] O. F. Pascui, R. Lohwasser, M. Sommer, M. Thelakkat, T. Thurn-Albrecht, and K. Saalwächter. High crystallinity and nature of crystal-crystal phase transformations in regioregular poly(3-hexylthiophene). *Macromolecules*, 43:9401–9410, 2010.

[157] M. A. Meier, R.and Ruderer, A. Diethert, G. Kaune, V. Körstgens, S. V. Roth, and P. Müller-Buschbaum. Influence of film thickness on the phase separation mechanism in ultrathin conducting polymer blend films. *J. Phys. Chem. B*, 115:2899–2909, 2011.

[158] D. R. Kozub, K. Vakhshouri, L. M. Orme, C. Wang, A. Hexemer, and E. D. Gomez. Polymer crystallization of partially miscible polythiophene/fullerene mixtures controls morphology. *Macromolecules*, 44:5722–5726, 2011.

[159] W. Yin and M. Dadmun. A new model for the morphology of P3HT/PCBM organic photovoltaics from small-angle neutron scattering: Rivers and streams. *ACS Nano*, 5:4756–4768, 2011.

[160] W. Ma, A. Gopinathan, and A. J. Heeger. Nanostructure of the interpenetrating networks in poly(3-hexylthiophene)/fullerene bulk heterojunction materials: Implications for charge transport. *Adv. Mater.*, 19:3656–3659, 2007.

[161] D. Duche, P. Torchio, L. Escoubas, F. Monestier, J.-J. Simon, F. Flory, and G. Mathian. Improving light absorption in organic solar cells by plasmonic contribution. *Sol. Energy Mater. Sol. Cells*, 93:1377–1382, 2009.

[162] A. P. Kulkarni, K. M. Noone, K. Munechika, S. R. Guyer, and D. S. Ginger. Plasmon-enhanced charge carrier generation in organic photovoltaic films using silver nanoprisms. *Nano Lett.*, 10:1501–1505, 2010. PMID: 20235514.

[163] C.-H. Chen, C.-H. Hsieh, M. Dubosc, Y.-J. Cheng, and C.-S. Hsu. Synthesis and characterization of bridged bithiophene-based conjugated polymers for photovoltaic applications: Acceptor strength and ternary blends. *Macromolecules*, 43:697–708, 2010.

[164] M. Koppe, H.-J. Egelhaaf, G. Dennler, M. C. Scharber, C. J. Brabec, P. Schilinsky, and C. N. Hoth. Near IR sensitization of organic bulk heterojunction solar cells: Towards optimization of the spectral response of organic solar cells. *Adv. Funct. Mater.*, 20:338–346, 2010.

[165] W.J. Belcher, K.I. Wagner, and P.C. Dastoor. The effect of porphyrin inclusion on the spectral response of ternary P3HT:porphyrin:PCBM bulk heterojunction solar cells. *Sol. Energy Mater. Sol. Cells*, 91(6):447–452, 2007.

[166] P. C. Dastoor, C. R. McNeill, H. Frohne, C. J. Foster, B. Dean, C. J. Fell, W. J. Belcher, W. M. Campbell, D. L. Officer, I. M. Blake, P. Thordarson, M. J. Crossley, N. S. Hush, and J. R. Reimers. Understanding and improving solid-state polymer/C60-fullerene bulk-heterojunction solar cells using ternary porphyrin blends. *J. Phys. Chem. C*, 111:15415–15426, 2007.

[167] S. Honda, T. Nogami, H. Ohkita, H. Benten, and S. Ito. Improvement of the light-harvesting efficiency in polymer/fullerene bulk heterojunction solar cells by interfacial dye modification. *ACS Appl. Mater. Interfaces*, 1:804–810, 2009.

[168] E. M. J. Johansson, A. Yartsev, H. Rensmo, and V. Sundström. Photocurrent spectra and fast kinetic studies of P3HT/PCBM mixed with a dye for photoconversion in the near-ir region. *J. Phys. Chem. C*, 113:3014–3020, 2009.

[169] A. Ogunsipe, D. Maree, and T. Nyokong. Solvent effects on the photochemical and fluorescence properties of zinc phthalocyanine derivatives. *J. Mol. Struct.*, 650:131–140, 2003.

[170] Z. G. Ji, K. W Wong, P. K. Tse, R. W. M. Kwok, and W. M. Lau. Copper phthalocyanine film grown by vacuum deposition under magnetic field. *Thin Solid Films*, 402:79 – 82, 2002.

[171] Marc M. Koetse, Jörgen Sweelssen, Kornel T. Hoekerd, Herman F. M. Schoo, Sjoerd C. Veenstra, Jan M. Kroon, Xiaoniu Yang, and Joachim Loos. Efficient polymer:polymer bulk heterojunction solar cells. *Appl. Phys. Lett.*, 88:083504, 2006.

[172] S. C. Veenstra, J. Loos, and J. M. Kroon. Nanoscale structure of solar cells based on pure conjugated polymer blends. *Prog. Photovolt. : Res. Appl.*, 15:727–740, 2007.

[173] C. R. McNeill, A. Abrusci, J. Zaumseil, R. Wilson, M. J. McKiernan, J. H. Burroughes, J. J. M. Halls, N. C. Greenham, and R. H. Friend. Dual electron donor/electron acceptor character of a conjugated polymer in efficient photovoltaic diodes. *Appl. Phys. Lett.*, 90(19):193506, 2007.

[174] M. A. Ruderer, E. Metwalli, W. Wang, G. Kaune, S. V. Roth, and P. Müller-Buschbaum. Thin films of photoactive polymer blends. *ChemPhysChem*, 10:664–671, 2009.

[175] M. A. Ruderer, S. M. Prams, M. Rawolle, Q. Zhong, J. Perlich, S. V. Roth, and P. Müller-Buschbaum. Influence of annealing and blending of photoactive polymers on their crystalline structure. *J. Phys. Chem. B*, 114:15451–15458, 2010.

[176] C. R. McNeill, J. J. M. Halls, R. Wilson, G. L. Whiting, S. Berkebile, M. G. Ramsey, R. H. Friend, and N. C. Greenham. Efficient polythiophene/polyfluorene copolymer bulk heterojunction photovoltaic devices: Device physics and annealing effects. *Adv. Funct. Mater.*, 18(16):2309–2321, 2008.

[177] X. He, F. Gao, G. Tu, D. G. Hasko, S. Hüttner, N. C. Greenham, U. Steiner, R. H. Friend, and W. T. S. Huck. Formation of well-ordered heterojunctions in polymer:PCBM photovoltaic devices. *Adv. Funct. Mater.*, 21(1):139–146, 2011.

[178] D.-H. Kim, Y.-D. Park, Y. Jang, H. Yang, Y.-H. Kim, J.-I. Han, D.-G. Moon, S. Park, T. Chang, C. Chang, M. Joo, C.-Y. Ryu, and K. Cho. Enhancement of field-effect mobility due to surface-mediated molecular ordering in regioregular polythiophene thin film transistors. *Adv. Funct. Mater.*, 15:77–82, 2005.

[179] C. R. McNeill, B. Watts, S. Swaraj, H. Ade, L. Thomsen, W. Belcher, and P. C. Dastoor. Evolution of the nanomorphology of photovoltaic polyfluorene blends: sub-100 nm resolution with x-ray spectromicroscopy. *Nanotechnol.*, 19:424015, 2008.

[180] R. Meier, F. Markl, C. Birkenstock, and P. Müller-Buschbaum. Film thickness controllable wet-imprinting of nanoscale channels made of conducting or thermoresponsive polymers. *J. Mater. Chem.*, 22:192–198, 2012.

[181] S. Swaraj, C. Wang, T. Araki, G. Mitchell, L. Liu, S. Gaynor, B. Deshmukh, H. Yan, C. R. McNeill, and H. Ade. The utility of resonant soft x-ray scattering and reflectivity for the nanoscale characterization of polymers. *Eur. Phys. J. Special Topics*, 167:121–126, 2009.

[182] C. Wang, D. H. Lee, A. Hexemer, M. I. Kim, W. Zhao, H. Hasegawa, H. Ade, and T. P. Russell. Defining the nanostructured morphology of triblock copolymers using resonant soft x-ray scattering. *Nano Lett.*, 11(9):3906–3911, 2011.

[183] H. Yan, B. A. Collins, E. Gann, C. Wang, Ha. Ade, and C. R. McNeill. Correlating the efficiency and nanomorphology of polymer blend solar cells utilizing resonant soft x-ray scattering. *ACS Nano*, 6:677–688, 2012.

[184] B. Watts, S. Swaraj, D. Nordlund, J. Lüning, and H. Ade. Calibrated NEXAFS spectra of common conjugated polymers. *J. Chem. Phys.*, 134:024702, 2011.

[185] H Ade, X Zhang, S Cameron, C Costello, J Kirz, and S Williams. Chemical contrast in x-ray microscopy and spatially resolved XANES spectroscopy of organic specimens. *Science*, 258:972–975, 1992.

[186] C. R. McNeill, B. Watts, L. Thomsen, W. J. Belcher, N. C. Greenham, and P. C. Dastoor. Nanoscale quantitative chemical mapping of conjugated polymer blends. *Nano Lett.*, 6:1202–1206, 2006.

[187] S. Walheim, M. Böltau, J. Mlynek, G. Krausch, and U. Steiner. Structure formation via polymer demixing in spin-cast films. *Macromolecules*, 30(17):4995–5003, 1997.

[188] Y. D. Park, D. H. Kim, Y. Jang, J. H. Cho, M. Hwang, H. S. Lee, J. A. Lim, and K. Cho. Effect of side chain length on molecular ordering and field-effect mobility in poly(3-alkylthiophene) transistors. *Org. Electron.*, 7:514 – 520, 2006.

[189] A. Urbina, E. Palacios-Lidon, C. Miguel, B. Perez-Garcia, R. Garcia-Valverde, J. Abellan, and J. Colchero. Electronic and structural properties of poly-(3-octylthiophene) and graphitic nanoparticle blends. *J. Eur. Phys. J. Appl. Phys.*, 37:283–286, 2007.

[190] T. J. Prosa, M. J. Winokur, Jeff Moulton, Paul Smith, and A. J. Heeger. X-ray structural studies of poly(3-alkylthiophenes): an example of an inverse comb. *Macromolecules*, 25:4364–4372, 1992.

[191] J.-M. Verilhac, G. LeBlevennec, D. Djurado, F. Rieutord, M. Chouiki, J.-P. Travers, and A. Pron. Effect of macromolecular parameters and processing conditions on supramolecular organisation, morphology and electrical transport properties in thin layers of regioregular poly(3-hexylthiophene). *Synth. Met.*, 156:815 – 823, 2006.

[192] F. S. Bates and G. H. Fredrickson. Block copolymer thermodynamics: Theory and experiment. *Annu. Rev. Phys. Chem.*, 41:525, 1990.

[193] F. S. Bates and G. H. Fredrickson. Block copolymers-designer soft materials. *Phys. Today*, 52:32–38, 1999.

[194] B. D. Olsen and R. A. Segalman. Self-assembly of rod-coil block copolymers. *Mater. Sci. Eng., R*, 62:37 – 66, 2008.

[195] M. Lee, B.-K. Cho, and W.-C. Zin. Supramolecular structures from rod-coil block copolymers. *Chem. Rev.*, 101:3869–3892, 2001.

[196] S. B. Darling. Block copolymers for photovoltaics. *Energy Environ. Sci.*, 2:1266–1273, 2009.

[197] G. Widawski, M. Rawiso, and B. Francois. Self-organized honeycomb morphology of star-polymer polystyrene films. *Nature*, 369:387–389, June 1994.

[198] M. Al-Hussein, M. A. Ruderer, E. Metwalli, V. Körstgens, U. Vainio, S. V. Roth, R. Döhrmann, R. Gehrke, R. Gebhardt, M. Burghammer, and P. Müller-Buschbaum. Determination of the ordered structure in conjugated-coil diblock copolymers films from a thickness gradient prepared by spin-coated drop technique. *Macromolecules*, 42(12):4230–4236, 2009.

[199] M. A. Ruderer, V. Körstgens, E. Metwalli, M. Al-Hussein, U. Vainio, S. V. Roth, R. Döhrmann, R. Gehrke, R. Gebhardt, M. Burghammer, and P. Müller-Buschbaum. Determination of the local gold contact morphology on a photoactive polymer film using nanobeam GISAXS. *NIMB*, 268:403–410, 2010.

[200] Y. Pelous, G. Froyer, C. Herold, and S. Lefrant. Chemical p doping of PPP thin films: Optical investigations. *Synth. Met.*, 29:17–22, 1989.

[201] H. Tokuhisa and P.T. Hammond. Solid-state photovoltaic thin films using TiO2, organic dyes, and layer-by-layer polyelectrolyte nanocomposites. *Adv. Funct. Mater.*, 13:831–839, 2003.

[202] J. Das, F. S. Freitas, I. R. Evans, A. F. Nogueira, and D. Khushalani. A facile nonaqueous route for fabricating titania nanorods and their viability in quasi-solid-state dye-sensitized solar cells. *J. Mater. Chem.*, 20:4425–4431, 2010.

[203] M. Rawolle, M. A. Niedermeier, G. Kaune, J. Perlich, P. Lellig, M. Memesa, Y.-J. Cheng, J. S. Gutmann, and P. Müller-Buschbaum. Fabrication and characterization of nanostructured titania films with integrated function from inorganic-organic hybrid materials. *Chem. Soc. Rev.*, 2012.

[204] Y. Lin, A. Boker, J. He, K. Sill, H. Xiang, C. Abetz, X. Li, J. Wang, T. Emrick, S. Long, Q. Wang, A. Balazs, and T. P. Russell. Self-directed self-assembly of nanoparticle/copolymer mixtures. *Nature*, 434:55–59, 2005.

[205] M. M. Abul Kashem, J. Perlich, A. Diethert, W. Wang, M. Memesa, J. S. Gutmann, E. Majkova, I. Capek, S. V. Roth, W. Petry, and P. Müller-Buschbaum. Array of magnetic nanoparticles via particle co-operated self-assembly in block copolymer thin film. *Macromolecules*, 42:6202–6208, 2009.

[206] M. A. Niedermeier, D. Magerl, Q. Zhong, A. Nathan, V. Körstgens, J. Perlich, S. V. Roth, and Müller-Buschbaum P. Combining mixed titania morphologies into a complex assembly thin film by iterative block-copolymer-based sol-gel templating. *Nanotechnol.*, 23, 2012.

[207] D. J. Kinning, K. I. Winey, and E. L. Thomas. Structural transitions from spherical to nonspherical micelles in blends of poly(styrene-butadiene) diblock copolymer and polystyrene homopolymers. *Macromolecules*, 21:3502–3506, 1988.

[208] K. I. Winey, E. L. Thomas, and L. J. Fetters. Swelling of lamellar diblock copolymer by homopolymer: influences of homopolymer concentration and molecular weight. *Macromolecules*, 24:6182–6188, 1991.

[209] M. D. Whitmore and T. W. Smith. Swelling of copolymer micelles by added homopolymer. *Macromolecules*, 27:4673–4683, 1994.

[210] M. W. Matsen. Phase behavior of block copolymer/homopolymer blends. *Macromolecules*, 28:5765–5773, 1995.

[211] N. Ouarti, P. Viville, R. Lazzaroni, E. Minatti, M. Schappacher, A. Deffieux, and R. Borsali. Control of the morphology of linear and cyclic PS-b-PI block copolymer micelles via PS addition. *Langmuir*, 21:1180–1186, 2005.

[212] J. Perlich, L. Schulz, M. M. Abul Kashem, Y.-J. Cheng, M. Memesa, J. S. Gutmann, S. V. Roth, and P. Müller-Buschbaum. Modification of the morphology of P(S-b-EO) templated thin TiO2 films by swelling with PS homopolymer. *Langmuir*, 23:10299–10306, 2007.

[213] R. Meier, H.-Y. Chiang, M. A. Ruderer, S. Guo, V. Körstgens, J. Perlich, and P. Müller-Buschbaum. In situ film characterization of thermally treated microstructured conducting polymer films. *J. Polym. Sci., Part B: Polym. Phys.*, 2012.

[214] F.Z. Dahou, L. Cattin, J. Garnier, J. Ouerfelli, M. Morsli, G. Louarn, A. Bouteville, A. Khellil, and J.C. Bernede. Influence of anode roughness and buffer layer nature on organic solar cells performance. *Thin Solid Films*, 518:6117–6122, 2010.

[215] P. Müller-Buschbaum, J. Perlich, M. M. Abul Kashem, L. Schulz, S. V. Roth, Y. J. Cheng, and J. S. Gutmann. Combinatorial investigation of nanostructures formed in a titanium dioxide based nanocomposite film on top of fluor-doped tin oxide layers. *phys.stat.sol. (RRL)*, 1:119–121, 2007.

List of publications

Publications related to the dissertation

- M. A. Ruderer, R. Meier, L. Porcar, R. Cubitt, P. Müller-Buschbaum: Phase separation and molecular intermixing in polymer - fullerene bulk heterojunction thin films; *Phys. Chem. Lett.* **2012**, *3*, 683-688.

- M. A. Ruderer, M. Hinterstocker, P. Müller-Buschbaum: Structure in ternary blend systems for organic photovoltaics; *Synth. Met.* **2011**, *161*, 2001-2005.

- M. A. Ruderer, S. Guo, R. Meier, H.-Y. Chiang, V. Körstgens, J. Wiedersich, J. Perlich, S. V. Roth, P. Müller-Buschbaum: Solvent induced morphology in polymer-based systems for organic photovoltaics; *Adv. Funct. Mater.* **2011**, *21*, 3382-3391.

- M. A. Ruderer and P. Müller-Buschbaum: Morphology of polymer-based bulk heterojunction films for organic photovoltaics; *Soft Matter* **2011**, *7*, 5482-5493.

- M. A. Ruderer, S. M. Prams, M. Rawolle, Q. Zhong, J. Perlich, S. V. Roth, P. Müller-Buschbaum: Influence of annealing and blending of photoactive polymers on their crystalline structure; *J. Phys. Chem. B* **2010**, *114*, 15451-15458.

- M. A. Ruderer, V. Körstgens, E. Metwalli, M. Al-Hussein, U. Vainio, S. V. Roth, R. Döhrmann, R. Gehrke, R. Gebhardt, M. Burghammer, P. Müller-Buschbaum: Determination of the local gold contact morphology on a photoactive polymer film using nanobeam GISAXS; *NIMB* **2010**, *268*, 403-410.

- M. A. Ruderer, M. Hirzinger, P. Müller-Buschbaum: Photoactive nanostructures of polypyrrole; *ChemPhysChem* **2009**, *10*, 2692 - 2697.

- C. R. McNeill, A. Abrusci, I. Hwang, M. A. Ruderer, P. Müller-Buschbaum and N. C. Greenham: Photophysics and photocurrent peneration in polythiophene/polyfluorene copolymer blends; *Adv. Funct. Mater.* **2009**, *19*, 3103-3111.

- M. A. Ruderer, E. Metwalli, W. Wang, G. Kaune, S. V. Roth, P. Müller-Buschbaum: Thin Films of Photoactive Polymer Blends; *ChemPhysChem* **2009**, *10*, 664 - 671.

Further publications

- R. Meier, H.-Y. Chiang, M. A. Ruderer, S. Guo, V. Körstgens, J. Perlich, P. Müller-Buschbaum: In situ film characterization of thermally treated microstructured conducting polymer films; *J. Polym. Sci. Part B: Polym. Phys.* **2012**, *50*, 631-641.

- X. Xia, E. Metwalli, M. A. Ruderer, V. Körstgens, P. Busch, P. Böni, P. Müller-Buschbaum: Nanostructured diblock copolymer films with embedded magnetic nanoparticles; *J. Phys. Condens. Matter* **2011**, *23*, 254203.

- M. Rawolle, M. A. Ruderer, S. M. Prams, Q. Zhong, D. Magerl, J. Perlich, S. V. Roth, P. Lellig, J. S. Gutmann, P. Müller-Buschbaum: Nanostructuring of titania thin films by combination of micro-fluidics and block copolymer based sol-gel templating; *Small* **2011**, *7*, 884-891.

- R. Meier, M. A. Ruderer, A. Diethert, G. Kaune, V. Körstgens, S. V. Roth, P. Müller-Buschbaum: Influence of Film Thickness on the Phase Separation Mechanism in Ultrathin Conducting Polymer Blend Films; *J. Phys. Chem. B* **2011**, *115*, 2899-2909.

- E. Metwalli, J.-F. Moulin, M. Rauscher, G. Kaune, M. A. Ruderer, U. van Bürck, M. Haese-Seiler, R. Kampmann, P. Müller-Buschbaum: Structural investigation of diblock copolymer thin films using TOF-GISANS; *J. Appl. Cryst.* **2011**, *44*, 84-92.

- J. Perlich, J. Rubeck, S. Botta, R. Gehrke, S. V. Roth, M. A. Ruderer, S. M. Prams, M. Rawolle, Q. Zhong, V. Körstgens, P. Müller-Buschbaum: Grazing incidence wide angle X-ray scattering at the wiggler beamline BW4 of HASYLAB; *Rev. Sci. Instr. 2010*, *81*, 105105.

- G. Kaune, M. Memesa, R. Meier, M. A. Ruderer, A. Diethert, S. V. Roth, M. D'Acunzi, J. S. Gutmann, P. Müller-Buschbaum: Hierarchically structured titania films prepared by polymer/colloidal templating; *ACS Appl. Mater. Interfaces* **2009**, *1*, 2862-2869.

- G. Kaune, M. A. Ruderer, E. Metwalli, W. Wang, S. Couet, K. Schlage, R. Röhlsberger, S. V. Roth, P. Müller-Buschbaum: In situ GISAXS study of gold film growth on conducting polymer films; *ACS Appl. Mater. Interfaces* **2009**, *1*, 353-360.

- M. Al-Hussein, M. A. Ruderer, E. Metwalli, V. Körstgens, U. Vainio, S. V. Roth, R. Döhrmann, R. Gehrke, R. Gebhardt, M. Burghammer, P. Müller-Buschbaum: Determination of the ordered structure in conjugated-coil diblock copolymers films from a thickness gradient prepared by spin-coated drop technique; *Macromolecules* **2009**, *42*, 4230-4236.

- G. Kaune, W. Wang, E. Metwalli, M. Ruderer, R. Roßner, S. V. Roth P. Müller-Buschbaum: Layered TiO2:PVK nano-composite thin films for photovoltaic applications; *Eur. Phys. J. E* **2008**, *26*, 73-79.

- W. Wang, K. Troll, G. Kaune, E. Metwalli, M. Ruderer, K. Skrabania, A. Laschewsky, S. V. Roth, C. M. Papadakis, P. Müller-Buschbaum: Thin films of poly(N-isopropylacrylamide) end-capped with n-butyltrithiocarbonate; *Macromolecules* **2008**, *41*, 3209-3218.

- E. Metwalli, S. Couet, K. Schlage, R. Röhlsberger, V. Körstgens, M. Ruderer, W. Wang, G. Kaune, S. V. Roth, P. Müller-Buschbaum: In situ GISAXS investigation of gold sputtering onto a polymer template; *Langmuir* **2008**, *24*, 4265-4272.

Scientific reports

- M. A. Ruderer, C. Wang, A. Hexemer, P. Müller-Buschbaum: Resonant soft X-ray scattering on conducting polymer films; *Lehrstuhl für Funktionelle Materialien, Annual report 2011.*

- M. A. Ruderer and P. Müller-Buschbaum: Grazing incidence resonant soft X-ray scattering on conducting polymer blend films; *International Graduate School CompInt, Annual report 2011.*

- M. A. Ruderer, R. Meier, L. Porcar, R. Cubitt, P. Müller-Buschbaum: Morphology of active layer materials for photovoltaic applications; *Experimental report for the Institute Laue-Langevin (ILL), 2011.*

- M. A. Ruderer, R. Cubitt, P. Müller-Buschbaum: Electronic materials with variable conductivities via block copolymer-homopolymer blend films; *Experimental report for the Institute Laue-Langevin (ILL), 2011.*

- M. A. Ruderer, S. M. Prams, J. Perlich, S. V. Roth, P. Müller-Buschbaum: Influence of annealing and blending of photoactive polymers on their crystalline structure; *Lehrstuhl für Funktionelle Materialien, Annual report 2010.*

- M. A. Ruderer, M. Al-Hussein, U. Vainio, S. V. Roth, R. Döhrmann, R. Gehrke, R. Gebhardt, M. Burghammer, P. Müller-Buschbaum: Determination of the local gold contact morphology on a photoactive polymer film using nanobeam GISAXS; *Lehrstuhl für Funktionelle Materialien, Annual report 2010.*

- M. A. Ruderer and P. Müller-Buschbaum: Influence of annealing and blending of photoactive polymers on their crystalline structure; *International Graduate School CompInt, Annual report 2010.*

- C. R. McNeill, A. Abrusci, I. Hwang, M. A. Ruderer, P. Müller-Buschbaum, N. C. Greenham: Photophysics and photocurrent generation in polythiophene/polyfluorene copolymer blends; *Lehrstuhl für Funktionelle Materialien, Annual report 2009.*

- M. A. Ruderer and P. Müller-Buschbaum: Controlled embedding of semiconducting nanoparticles in a conducting polymer template; *Lehrstuhl für Funktionelle Materialien, Annual report 2009.*

- M. A. Ruderer and P. Müller-Buschbaum: Controlled embedding of semiconducting nanoparticles in a conducting polymer template; *International Graduate School CompInt, Annual report 2009.*

- M. A. Ruderer, S. M. Prams, W. Wang, Q. Zhong, S. V. Roth, P. Müller-Buschbaum: Controlled embedding of semiconducting nanoparticles in a conducting polymer template; *HASYLAB, Annual report 2009.*

- M. A. Ruderer, R. Cubitt, P. Müller-Buschbaum: Structure control of conjugated block copolymers via adding a homopolymer; *Lehrstuhl für Funktionelle Materialien, Annual report 2008.*

- M. A. Ruderer, A. Diethert, R. Meier, G. Kaune, A. Timmann, S. V. Roth, P. Müller-Buschbaum: Temperature influence on photoactive polymer blend films; *HASYLAB, Annual report 2008.*

- M. A. Ruderer, S. V. Roth, P. Müller-Buschbaum: Nanostructuring of thin semiconducting polymer ?lms for photovoltaic applications; *Lehrstuhl für Funktionelle Materialien, Annual report 2007.*

- M. A. Ruderer and P. Müller-Buschbaum: Nanostructures of hybridmaterials for photovoltaics; *Lehrstuhl für Funktionelle Materialien, Annual report 2006.*

Conference talks

- M. A. Ruderer: Morphology of bulk heterojunction systems for polymer-based photovoltaics; *Complex Matter and Biophysics Seminar*, Raleigh, NC (USA), December 2011.
- M. A. Ruderer, S. M. Prams, M. Rawolle, G. Kaune, W. Wang, Q. Zhong, E. Metwalli, J. Perlich, S. V. Roth, P. Müller-Buschbaum: Morphology of bulk heterojunction systems for polymer-based photovoltaics; *1st Colloquium of the Munich School of Engineering*, Garching (Germany), July 2011.
- M. A. Ruderer, S. M. Prams, M. Rawolle, Q. Zhong, J. Perlich, S. V. Roth, P. Müller-Buschbaum: Influence of annealing and blending of photoactive polymers on their crystalline structure; *APS March Meeting*, Dallas, TX (USA), March 2011.
- M.A. Ruderer, S. M. Prams, J. Perlich, S. V. Roth, P. Müller-Buschbaum: Morphologies of bulk heterojunctions for polymer based photovoltaics; *HASYLAB-TUM Kolloquium*, Hamburg (Germany), November 2010.
- M.A. Ruderer and P. Müller-Buschbaum: Polymers for applications in organic photovoltaics; *SEEIT - Photovoltaic Workshop*, Freiburg (Germany), September 2010.
- M. A. Ruderer, S. Guo, R. Meier, H.-Y. Chiang, V. Körstgens, J. Wiedersich, J. Perlich, S. V. Roth, P. Müller-Buschbaum: Investigations of structural changes by modification of polymer systems for photovoltaic applications; *P.2010*, Halle (Saale) (Germany), September 2010.
- M. A. Ruderer, S. M. Prams, W. Wang, Q. Zhong, R. Meier, S. V. Roth, J. Szeifert, T. Bein, P. Müller-Buschbaum: Controlled embedding of semiconducting nanoparticles in a conducting polymer template; *DPG Frühjahrstagung*, Dresden (Germany), March 2010.
- M. A. Ruderer: Controlled embedding of semiconducting nanoparticles in a conducting polymer template; *CompInt Winterschool*, Antholz (Italy), March 2010.
- M. A. Ruderer, R. Meier, P. Müller-Buschbaum: Enhanced light harvesting in semiconducting nanoparticle/polymer composites; *Nanoworkshop*, Prague (Czech Republic), September 2009.
- M. A. Ruderer, R. Meier, J. Perlich, G. Kaune, R. Cubitt, M. Haese-Seiler, R. Kampmann, P. Müller-Buschbaum: Electronic materials with variable conductivities via block copolymer-homopolymer blend films; *FRM-II Workshop on Neutron Scattering*, Burg Rothenfels (Germany), June 2009.

- M. A. Ruderer: A neutron study of photoactive rod-coil diblock copolymer films; *CompInt Winterschool*, Antholz (Italy), March 2009.
- M. A. Ruderer, S. V. Roth, P. Müller-Buschbaum: Structure and Morphology of Conducting Polymer Films for Photovoltaic Applications; *Winterschool on Organic Electronics: The Role of Interfaces*, Planneralm (Austria), January 2008.
- M. A. Ruderer: Characterization of semi-conducting polymer blend thin films for photovoltaic applications; *3rd FRM-II Workshop on Neutron Scattering*, Burg Rothenfels (Germany), July 2007.

Conference poster presentations

- M. A. Ruderer, C. Wang, A. Hexemer, P. Müller-Buschbaum: Resonant soft X-ray scattering on conducting polymer systems; *International Workshop of Advances in Photovoltaics and Photocatalysis*, Garching (Germany), July 2011.
- M. A. Ruderer, C. Wang, A. Hexemer, P. Müller-Buschbaum: Resonant soft X-ray scattering on conducting polymer systems; *5th FRM-II Workshop on Neutron Scattering*, Burg Rothenfels (Germany), June 2011.
- M. A. Ruderer, S. M. Prams, M. Rawolle, S. Guo, J. Perlich, S. V. Roth, P. Müller-Buschbaum: Internal morphology of BHJ solar cells probed in-situ with GISAXS during operation; *HASYLAB User Meeting*, Hamburg (Germany), January 2011.
- M.A. Ruderer, S. Guo, R. Meier, H.-Y. Chiang, J. Wiedersich, V. Körstgens, J. Perlich, S.V. Roth, P. Müller-Buschbaum: Investigations of structural changes by modification of polymer systems for photovoltaic applications; *SPP1355 Workshop*, Dresden (Germany), October 2010.
- M. A. Ruderer, S. M. Prams, W. Wang, Q. Zhong, R. Meier, S. V. Roth, P. Müller-Buschbaum: Enhanced light harvesting in semiconducting nanoparticle/polymer composites; *GISAS*, Hamburg (Germany), September 2009.
- M. A. Ruderer, R. Meier, J. Perlich, G. Kaune, R. Cubitt, M. Haese-Seiler, R. Kampmann, P. Müller-Buschbaum: Structure control of conjugated block copolymers via adding a homopolymer; *SAS*, Oxford (UK), September 2009.
- M. A. Ruderer, R. Meier, J. Perlich, G. Kaune, R. Cubitt, M. Haese-Seiler, R. Kampmann, P. Müller-Buschbaum: Structural control of conjugated block copolymer films via addition of homopolymer; *FRM II Usermeeting*, Garching (Germany), May 2009.

- M. A. Ruderer, R. Meier, J. Perlich, G. Kaune, R. Cubitt, M. Haese-Seiler, R. Kampmann, P. Müller-Buschbaum: Structure control of conjugated block copolymers via adding a homopolymer; *DPG Frühjahrstagung*, Dresden (Germany), March 2009.

- M. A. Ruderer, S. M. Prams, A. Diethert, R. Meier, G. Kaune, S. V. Roth, P. Müller-Buschbaum: Temperature influence on photoactive polymer blend films; *HASYLAB Usermeeting*, Hamburg (Germany), January 2009.

- M. A. Ruderer, R. Meier, E. Metwalli, J.-F. Moulin, P. Müller-Buschbaum: Structural investigations of polymer blend films for photovoltaic applications; *Deutsche Neutronenstreutagung*, Garching (Germany), September 2008.

- M. A. Ruderer, E. Metwalli, W. Wang, G. Kaune, S.V. Roth, P. Müller-Buschbaum: Structure and morphology of conducting polymer films for photovoltaic applications; *DPG Frühjahrstagung*, Berlin (Germany), February 2008.

Acknowledgements

I would like to thank Prof. Dr. P. Müller-Buschbaum for giving me the opportunity to continue my work in the field of organic photovoltaics after my diploma thesis. His critical view on my scientific work and his outstanding experience in the field of scattering and polymer science were essential for my success during my PhD studies. I benefited from the extended discussions for which he always had time despite his busy schedule.

The International Graduate School 'Materials Science of Complex Interfaces' (CompInt) of the Elite Network of Bavaria is gratefully acknowledged for funding. In addition, I would like to thank Prof. A. Bausch for organizing the winterschools, seminars etc. in the framework of CompInt and the members of CompInt for the great time during these activities, in particular, Dr. T. Einert, M. Hauf, R. Jungmann, S. Neubauer, K. Schmoller, F. Sedlmeier and U. Zinth.

My time as visiting research student at the University of Cambridge and the Lawrence Berkeley National Laboratory was a great experience on a scientific as well as on a personal level. I thank Prof. Dr. Neil Greenham who gave me the opportunity to work and learn in his group at the Cavendish Laboratories (Cambridge) as well as Dr. T. Brenner and Dr. B. Friedel who instructed me in the labs at the beginning.
I want to thank Dr. A. Hexemer for his warm welcome to his group at the ALS (Berkeley). I will never forget the team meeting with oysters and tritip at Point Reyes as well as our trip to the APS March meeting in Dallas, TX. I enjoyed the stay very much, thanks to S. Alvarez-Rivera, Dr. E. Chan, X. Gu and Dr. C. Wang. I would further like to acknowledge the opportunity to perform the sample preparation in Berkeley in the labs of Prof. Dr. T. Xu at the UCB with the help of P. Bai.

The main results in this thesis were gathered in many demanding but successful beamtimes. The success is owed to the excellent teamwork during every beamtime. I want to thank Dr. A. Diethert, Dr. G. Kaune, Dr. V. Körstgens, Dr. R. Meier, Dr. E. Metwalli, Dr. J.-F. Moulin, A. Nathan, M. Niedermeier, S. M. Prams, M. Rawolle, W. Wang and Q. Zhong. In addition, I thank H.-Y. Chiang, S. Guo and D. Magerl for measuring my samples although I did not join the corresponding beamtimes.

As the local support at the beamlines is as important as the teamwork, I want to acknowledge the beamline scientists Dr. J. Perlich, Dr. S. V. Roth, Dr. A. Timmann (HASYLAB, BW4), Dr. R. Cubitt, Dr. L. Porcar (ILL, D22), Dr. R. Kampmann, Dr. J.-F. Moulin (FRM2, REFSANS), Dr. M. Skoda (ISIS, SURF), Dr. C. Wang (ALS, 11.0.1.2), Dr. E. Schaible (ALS, 7.3.3) and Dr. A. Hexemer (ALS). For the important technical support I thank the workshop at the Lehrstuhl für Funktionelle Materialien (R. Jahrstorfer and R. Funer).

I also want to acknowledge the help from other chairs and facilities here in Munich: first, Prof. Dr. P. Böni and B. Russ who provided the possibility to use the X-ray reflectometer at the Lehrstuhl E21. Furthermore, I want to thank S. Schoell from the WSI for helping me with the HF cleaning of my substrates and Dr. J. M. Szeifert and Prof. Dr. T. Bein (LMU) for providing the titania nanoparticles.

Special thanks go to 'my' diploma and master, bachelor and working students S. Prams, A. Nathan, S. Guo, M. Hirzinger, M. Krawczyk, M. Hinterstocker, R. Roßner and N. Hörmann. My dissertation benefits from their high motivation and support. I wish them all the best for their futures.

I want to thank Dr. M. Al-Hussein for the interesting discussions during his visits at the Lehrstuhl für Funktionelle Materialien.

Moreover, I am very thankful to the people who read the manuscript and contributed to its improvement: Dr. A. Diethert, A. M. Herzig, Dr. E. M. Herzig, Dr. V. Körstgens, D. Magerl, M. Niedermeier, M. Rawolle, K. Sarkar and M. Schindler.

I enjoyed the time being at the Lehrstuhl für Funktionelle Materialen very much. Besides doing science in a very well equipped and productive environment, I liked the many opportunities for presenting and discussing my ongoing research. Here I want to thank Dr. M. Abul-Kashem, Dr. V. Körstgens, Dr. E. Metwall, Dr. J.-F. Moulin and Dr. J. Perlich who introduced me to everything at the beginning of my stay at our chair and further on. Special thanks go also to Dr. R. Meier with whome I started my PhD. For the good atmosphere I want to thank my office mates of my first years in the big office and Dr. A. Diethert and M. Niedermeier for the great time together in the small office.

Besides the scientific work, I enjoyed the many activities we did together as a group. I will leave the group with fond memories of our hiking days, soccer matches, conference trips and internal workshops. Not to forget the famous celebrations at the Oktoberfest or the Nockherberg. Also the team members I did not mention so far contributed a lot to the very kind atmosphere: Dr. J. Adelsberger, A. Ammara, C. Birkenstock, C. Brandt, S. Busch, H. Choe, Dr. G. DePaoli Dr. Z. Di, P. Douglas, S. Ener, E. Faber, S. Fink, Dr. A. Golosova, S. Guo, M. He, W. Hefter, T. Hoppe, S. Jaksch, Dr. A. Meier-Koll, D.

Müller, A. Naumann, A. Omran, C. Palumbiny, Prof. Dr. C. Papadakis, Dr. N. Paul, Dr. M. Philipp, S. Raith, Prof. Dr. W. Schirmacher, K. Scherer, A. Sepe, K. Wagenbauer, M. Waletzki, W. Wang, X. Xia, Y. Yuan and Dr. J. Zhang.

I apologize to my friends, particularly to S. Lippacher, who might have missed me during the time I was busy writing this thesis. Missing all the spectacular trips to the mountains was the hardest challenge.

The biggest thank-you goes to my family, on which I can always rely. I dedicate this thesis to them.

Finally, I thank my gorgeous Eva for all her support and all her patience during the last year.